A FRAMEWORK FOR MULTIPHASE HEAT AND MASS TRANSPORT IN POROUS MEDIA WITH APPLICATIONS TO FOOD PROCESSES

A Dissertation

Presented to the Faculty of the Graduate School

of Cornell University

in Partial Fulfillment of the Requirements for the Degree of

Doctor of Philosophy

by

Amit Halder

May 2010

A FRAMEWORK FOR MULTIPHASE HEAT AND MASS TRANSPORT IN POROUS MEDIA WITH APPLICATIONS TO FOOD PROCESSES

Amit Halder, Ph.D.

Cornell University 2010

A framework of porous media multiphase models has been developed which can be applied to a wide range of thermal food processes. The developed models are easily implementable in commercial software and therefore has wider usage. The development of fundamental physics-based models of food processes and their implementation in commercial software is not trivial and it requires physical as well as mathematical insight into the material and the process. Experiments are conducted to study the flow of water through cellular structures. Two pathways of moisture migration have been found to exist. At temperatures below 55^{o}C, intracellular pathway is dominating and at higher temperatures, extracellular pathway is dominating. Heat and mass transfer coefficients required in the mathematical model have been studied in details by solving a conjugate model (porous media and outside atmosphere together). The developed model was applied to a food application, deep-fat frying, and validated with experimental results from literature. Finally, a tool that predicts the safety and risk parameters for many different food processes is developed by integrating the versatile fundamental-based simulation of food processes with the best known prediction models available for microbiological growth and inactivation.

BIOGRAPHICAL SKETCH

Amit Halder was born in Asansol, West Bengal in India. He went to elementary, middle and high school in Bokaro Steel City in Jharkhand, India. He was admitted in Indian Institute of Technology Kharagpur in July 2000 for his undergraduate education. In 2004, he completed his Bachelor's degree in Agricultural and Food Engineering. During his stay at IIT, Amit pursued a number of projects and courses related to mathematical modeling of food processes, which got him interested in the field of mathematical modeling with applications to food processing. In August 2004, he joined the Department of Biological and Environmental Engineering at Cornell University, Ithaca, to pursue his graduate studies in this field under Professor Ashim K. Datta.

To my parents, Satyabrata Halder and Ruma Halder, and sister, Sumita.

ACKNOWLEDGEMENTS

First of all, I would like to thank my advisor, Professor Ashim K. Datta, for his support and guidance throughout my stay at Cornell for the last five years. The successful completion of this work as well as other projects would not be possible without the numerous discussion with him, his encouragement and optimism about the projects. I am highly indebted to him for all the time he devoted for the discussions with me that has helped me develop academically as a researcher and will help me in my future career.

I would also like to acknowledge Professors Kenneth Torrance and Martin Wiedmann for their role on my Special Committee. I sincerely thank Professor Roger Spanswick for the numerous discussions related to transport of water in plant tissues that helped me understand the finer details of the topic. I would also like to thank Professor P. Michael Davidson at University of Tennessee, Knoxville for the discussions and guidance while developing the microbial kinetic database and the food safety predictor software and also for hosting me at their facility.

A special thanks to my colleagues in the research group, Vineet Rakesh and Ashish Dhall, for their technical support that helped me in the most difficult times as well as their assistance and company. I am also thankful to Dr. Glenn Black (Ph.D. from University of Tennessee and now in Grocery Manufacturer's Association) for the invaluable discussions while developing the microbial kinetic database. Finally, I would like to thank my family and friends for their love and support throughout the work.

TABLE OF CONTENTS

LIST OF TABLES

LIST OF FIGURES

CHAPTER 1

INTRODUCTION

Mathematical modeling and simulation have not been able to contribute to the faster development of food processing industries, as they have done in the case of the mechanical and chemical industries. The primary reason for this is that foods are complex and non-homogenous, and the physics that occurs during processing is still not clearly established. Society has a critical need to automate food processing (both in industry and at home), while improving its quality and making it safe. Product, process and equipment design in food manufacturing requires as detailed an understanding of food processes as possible through physics-based modeling. The development of fundamental physics-based models of food processes is not trivial, as it requires physical as well as mathematical insight into the material and the process.

1.1 Food as hygroscopic porous media

A porous material is a solid matrix consisting of interconnected pores or voids filled with fluids (liquids or gases). A hygroscopic solid is a material that can attract moisture and therefore the vapor pressure surrounding the solid is a function of the moisture content and temperature of the solid. In food systems, an enormous range of thermal processes can be viewed as involving transport of energy, moisture and, in some cases, fat through a hygroscopic porous medium. Examples include extraction, drying, deep-fat frying, microwave heating, meat roasting and rehydration. In the vast majority of food systems, proteins or carbohydrates form a porous skeleton that has water and/or fat physically and chemically bound to it. During a heating process, water and fat can transport in-

side the solid matrix or can be released into the pore space and then transported through the porous medium. Other important phenomena that can occur include rapid evaporation due to intensive heating, melting of ice or fat when starting from a frozen state and shrinkage due to physicochemical changes in the porous matrix. No model in the literature considers all these physics together, and as part of a general framework that can also be easily implemented in commercial software for widespread use.

1.2 Challenges in the development of a fundamental physics-based model

In food processing, simulation technology has remained relatively underdeveloped, outside of its use in research. The most prevalent models are simple heat and mass transfer models, which have several empirical constants, making them useful for a particular process and material. These models do not yield any insight into transport during the process but they can give accurate results for the identical processing conditions and material properties (for which the empirical constants were measured). When process and product change, as is frequently the situation, a fundamental physics-based model can accommodate such changes more easily, but developing such a model is not trivial and the challenges in developing it are discussed next.

1.2.1 Fundamental understanding of heat and mass transport inside cellular structures is needed

For accurate prediction of temperature and moisture content in cellular tissues during thermal processing, it is critical to understand where water is located inside the cellular tissue and the various resistive pathways it can follow during a thermal process. Cellular foods, like fruits, vegetables and meat, have complex structures and, depending on the extent of dehydration, liquid water is found in the pores or as intracellular water. The resistance to flow faced by liquid water in the pores is different from that faced by intracellular water. A predictive model that can be used to simulate drying processes of cellular foods generally uses a lumped model with effective diffusivity as a function of moisture content to describe moisture migration ([1], [2]). Such an effective diffusivity is an average of all the resistive pathways— it is empirical and specific to a process and food material. The effective diffusivities for the purpose of modeling drying processes should be based on the properties of cellular structures in addition to the moisture content of the tissue ([3], [4]). At present, there are no studies that relate pore sizes and cellular structure to transport properties so as to facilitate mathematical modeling.

1.2.2 Properties and parameters required in the transport model are limited

There are complex, porous media models of frying and drying processes ([36], [6], [21]) in which distinct phases of water are considered but the availability of

transport properties for such models is limited. The accuracy of a mathematical model, with respect to the physical phenomena it represents, depends on the availability of proper transport properties. Material properties, such as the permeability of water and gas in a medium and capillary pressure, and parameters, such as heat and mass transfer coefficients at the boundary, are not available for most materials and processes. Input parameters, such as heat and mass transfer coefficients, are difficult to measure directly through experiments and require a different formulation of the simulation. Due to the non-availability of properties, researchers use their estimated values in complex models, which can lead to large errors in final solutions. Thus, there is a critical need to systematically obtain the properties and parameters needed in the simulations.

1.2.3 Solver limitations

Previous detailed physics-based models of frying ([36], [6]) have been solved by user-developed codes. These codes are either publicly unavailable, have limited capabilities or are difficult to use for anyone but the creator. Implementation of the same process in commercial code will make the power of simulation capability more widely available for designing products and processes. However, the governing equation and boundary conditions, which are unique to food processes, do not match the available equations in a commercial software that is typically built for non-food applications. Therefore, the models developed for food processes can require significant reformulations to be successfully implemented in commercial software.

1.3 Objectives

The objective of this work is to develop a framework for porous media models that is easily implementable in commercial software and can be applied over a wide range of food processes. This would be accomplished through the following steps:

(1) To experimentally study where water is located inside cellular tissue and how changes in structure and subsequent changes in flow pathways during thermal processing affect transport.

(2) To develop a general multiphase model for hygroscopic biological materials that can be used for various thermal processes and can be implemented in a typical commercially available software.

(3) To obtain the heat and mass transfer coefficients at the porous media surface that are needed as boundary conditions in the models. This would be done by solving a conjugate problem of microwave heating, containing both the porous material and the outside environment.

(4) To apply the developed model to simulate deep fat frying and validate the results.

(5) To integrate the most powerful and versatile fundamentals-based simulation of food processes with the best known prediction models available for microbiological growth and inactivation, in order to provide a tool that predicts safety parameters for many different food processes.

1.4 Organization of the dissertation

The dissertation is organized into seven chapters. An overview of the chapters are given below.

Chapter 1: Introduction This chapter provides an introduction to the dissertation and its overall objectives.

Chapter 2: Water transport in cellular tissues In this chapter, the location of water inside the cellular tissues was determined using various experimental techniques. Using a combination of permeability measurement, pore size distribution analysis and bioimpedance analysis, it is shown that water in a cellular tissue is mostly intracellular at the lower temperatures at which cell membranes are intact. During drying at high temperatures, cell membranes are damaged and the moisture transport pathway is primarily extracellular (through intercellular spaces and the lacunae created by the killed cells), with a much lower resistance to water transport. Based on the experiments, it is concluded that there are two pathways of moisture migration, extracellular pathways and intracellular pathways, depending upon the cell structure of the biological tissue. The difference in diffusivity between the two pathways has been estimated to be three orders of magnitude. Therefore, transport properties measured or predicted at low temperatures cannot be used for high temperatures because they correspond to distinct moisture migration pathways.

Chapter 3: A comprehensive transport model in porous media with phase change In this paper, a general multiphase model for hygroscopic food mate-

rials that can be used for many thermal processes (e.g., deep-fat frying, meat cooking, baking, microwave heating, etc.) is developed. The model can be implemented in commercial software that will facilitate wider usage. In the model, the food material is treated as a porous medium, and heat and mass transfer inside the porous material during thermal processing are described using equations for mass and energy conservation that include binary diffusion, capillary and convective modes of transport, physicochemical changes in the solid matrix that include phase changes such as melting of fat and water, and evaporation-condensation of water. Evaporation-condensation is considered to be distributed throughout the domain and is described by a novel non-equilibrium formulation that has been discussed in detail.

Chapter 4: Boundary conditions in multiphase, porous media, transport models of thermal processes with rapid evaporation In this paper, the exchange of heat and moisture at the porous surface is investigated. A conjugate domain, including both the porous media (food) and the outside environment (air) during microwave heating, is solved so that there is no need to provide separate boundary conditions at the porous media surface (it becomes an internal boundary). From the simulation results, the effect of blowing velocity on the boundary layer and the factors affecting the heat and mass transfer coefficients are studied. A general conclusion is that blowing effects are very small due to the small blowing parameter values.

Chapter 5: Application to Deep-Fat Frying. Part I: Model Development and Input Parameters In this paper, an improved multiphase porous media model involving heat and mass transfer has been developed and solved numerically

with careful consideration given to the selection of input parameters. A non-equilibrium formulation for evaporation is used, which describes the physics more accurately and is easier to implement in a typical CFD software as such a formulation can explicitly provide the evaporation rate in terms of concentration of vapor and temperature. External heat and mass transfer coefficients are estimated to accurately reflect multiple frying stages – the non-boiling stage, the surface boiling stage, and the falling rate stage.

Chapter 6: Application to Deep-Fat Frying. Part II: Results, Validation and Sensitivity Analysis The multiphase porous media model for frying, developed in Chapter 5, has been applied to frying of a restructured potato slice to obtain temperature, pressure, moisture, oil content, acrylamide content and evaporation rate profiles, providing valuable insight into the frying process. The model is validated by comparing temperature, moisture content and crust thickness profiles from experimental results in the literature. Post-frying cooling is included through appropriate changes in boundary conditions. Sensitivity analyses of the surface mass transfer coefficient, evaporation rate constant and oil diffusivity show that they all have significant effects on the process.

Chapter 7: A user-friendly general-purpose predictive software package for food safety In this paper, development of a powerful, state-of-the-art interactive software package, which provides customized answers concerning food safety for many production-to-consumption situations, is presented. In the software, process models for a number of food processes (e.g., frying, sterilization, etc.) are integrated with various databases such as the USDA Nutrient database to determine the composition of food, a food property database and a chemi-

cal and microbiological kinetics database. A user-friendly GUI is built on top of the commercial software (COMSOL Multiphysics) to make the software interactive and easy to use for food processing problems. The integration with various databases and the user-friendly interface makes the software unique and a useful tool for a much broader user base covering design, research, education and Extension. This is a major step toward making food process simulation technology accessible to a broad community for food product and process design with improved quality and safety.

1.5 Co-authorship

The dissertation is organized into seven chapters. Co-authorship of individual chapters is indicated below.

Chapter 1: Introduction This chapter provides an introduction to the work and the overall objectives.

Chapter 2: Water transport in cellular tissues All the experiments and analysis shown in this chapter have been done by Amit Halder under the supervision of Professor Ashim Datta and Professor Roger Spanswick.

Chapter 3: A comprehensive transport model in porous media with phase change In this work, Amit Halder and Ashish Dhall worked together under the supervision of Professor Ashim Datta. In addition to developing the comprehensive model, Amit Halder worked on the details of implementing the

evaporation formulation and implemented the comprehensive model for the frying process. Ashish Dhall implemented the comprehensive model for the meat cooking process with help from Amit Halder.

Chapter 4: Boundary conditions in multiphase, porous media, transport models of thermal processes with rapid evaporation Model development and analysis was done by Amit Halder under the supervision of Professor Ashim Datta.

Chapter 5: Application to Deep-Fat Frying. Part I: Model Development and Input Parameters Amit Halder is the primary contributor to this work. Ashish Dhall, also a co-author of the journal publication, has some contribution in model development. The work was done under the supervision of Professor Ashim Datta.

Chapter 6: Application to Deep-Fat Frying. Part II: Results, Validation and Sensitivity Analysis Amit Halder is the primary contributor to this work. Ashish Dhall, also a co-author in the journal publication, has some contribution in model development. The work was done under the supervision of Professor Ashim Datta.

Chapter 7: A user-friendly general-purpose predictive software package for food safety This was a collaboration between Cornell University and University of Tennessee, Knoxville. Amit Halder is the primary contributor in this software development project with Professor Ashim Datta as the Principal Investigator. Amit Halder developed the frying and microwave heating models

in the software. Ashish Dhall developed the formulation used to calculate thermal properties from the composition of food. Amit Halder worked closely with Dr. Glenn Black and Professor P. Michael Davidson in developing the microbial growth/ death kinetic database. Amit Halder also worked closely with Dr. Jessie Li and Professor Svetlana Zivanovic in developing the chemical kinetic database. In addition to the above, Amit Halder designed and developed the GUI of the software with Pavan Boob.

BIBLIOGRAPHY

[1] Ateba, P. and Mittal G.S., 1994, Modeling the Deep-Fat Frying of Beef Meatballs, *International Journal of Food Science and Technology*, 29(4): 429-440.

[2] Ikediala, J.N., Correia, L.R., Fenton, G.A. and BenAbdallah N., 1996, Finite element modeling of heat transfer in meat patties during single-sided pan-frying, *Journal of Food Science*, 61(4): 796-802.

[3] King, C.J., 1968, Rates of moisture sorption and desorption in porous, dried foodstuffs, *Food Technology*, 22(4): 165-171.

[4] Rotstein, E., 1987, The prediction of diffusivities and diffusion-related transport properties in the drying of cellular foods, *Physical properties of Foods 2*, 131-145.

[5] Ni, H. and Datta, A.K., 1999, Moisture, oil and energy transport during deep-fat frying of food materials, *Food and Bioproducts Processing*, 77(C3): 194-204.

[6] Yamsaengsung, R. and Moreira, R.G., 2002, Modeling the transport phenomena and structural changes during deep fat frying - Part 1: model development, *Journal of Food Engineering*, 53(1): 1-10.

[7] Halder, A., Dhall, A. and Datta, A.K., 2007, An improved, easily implementable, porous media based model for deep-fat frying - Part I: Model development and input parameters, *Food and Bioproducts Processing*, 85(C3): 209-219.

CHAPTER 2

WATER TRANSPORT IN CELLULAR TISSUES DURING THERMAL PROCESSING

Accurate modeling of water transport in food materials requires knowledge of how transport properties depend on the material structure. Water transport in a cellular tissue depends on its pathway (intracellular vs. extracellular), which in turn depends on temperature. Using a combination of permeability measurement, pore size distribution analysis and bioimpedance analysis, it is shown that water in a cellular tissue is mostly intracellular at the lower temperatures at which cell membranes are intact. During drying at high temperatures, cell membranes are damaged and the moisture transport pathway is primarily extracellular (through intercellular spaces and the lacunae created by the killed cells), with a much lower resistance to water transport. The difference in diffusivity for the two pathways has been estimated to be three orders of magnitude. Therefore, transport properties measured or predicted at low temperatures cannot be used for high temperatures because they correspond to different moisture migration pathways.

Keywords: food, pores, bioimpedance, extracellular, intracellular, permeability

Nomenclature

a	water activity
c	concentration, kg m^{-3}
C	Capacitance, Farad
d	Diameter of pore, m
D	Diffusivity, m^2 s^{-1}
F	Flow rate, m^3 s^{-1}
f	frequency of signal, Hz
J	flux, kg m^{-2} s^{-1}
k	permeability, m^2
L	length of the channel, m
M	moisture content (dry weight basis), kg water / kg dry weight
N	total number of pores
n	number of pores
p	pressure, Pa
R	resistance, ohms
t	thickness of cell membrane, m
V	volume, m^3
X	reactance, ohms
Z	impedance, ohms

Greek Symbols

β	electrical resistivity, Ohm m
γ	surface tension, N m^{-1}
κ	ratio of electrical resistivity
μ	viscosity, Pa s
ω	angular frequency, Hz
ϕ	chemical potential, J mol^{-1}
ρ	density, kg m^{-3}
θ	contact angle between liquid water and surface

Subscripts

a	air
e	extracellular
eff	effective
i	intracellular
w	water
0	zero frequency
cap	capillary
ECW	Extracellular water
ICW	Intracellular water
inf	infinite frequency

2.1 Introduction

For accurate prediction of temperature and moisture content in cellular tissues during thermal processing, it is of utmost importance to understand the differ-

ent pathways that water can take during the process. The resistance to moisture migration offered by different pathways depends on the structure and composition of the tissue. Cellular foods like fruits, vegetables and meat have complex structures and, depending on the extent of dehydration, water is found as liquid water in the pores or inside the cells. The resistance faced by liquid water in the pores is different from that faced by water inside the cells. A predictive model to simulate drying or other water removal processes in cellular foods generally uses an effective diffusivity as a function of moisture content to describe the moisture migration ([1], [2]). Such an effective diffusivity is an average of all the resistive pathways and is completely empirical, specific to a process and food material. But for the purpose of modeling drying processes, effective diffusivities should be based on the properties of cellular structures in addition to the moisture content of the tissue ([3],[4]). In more complex models of frying and drying processes ([36], [6], [7]), where various transport modes of different phases of water are considered, the availability of transport properties is limited, thus reducing the usefulness of such models. It therefore becomes critical to understand how transport properties relate to the structure of materials and how they change as materials transform during the process.

The outline of this paper is as follows: The literature review is followed by the objectives of the paper. The theories behind capillary pressure, pore size distribution and bioelectrical impedance analysis are discussed, followed by the experimental setups used. Finally, the experimental results are discussed, leading to identification of moisture migration pathways and explanation of relationship between moisture diffusivity and the structure of a cellular food material.

2.1.1 Literature review

To reach our goal of understanding water transport in a cellular tissue, we can start by considering the tissue as a porous medium and look into how cellular structure affects such transport. The capillary pressure and permeability measurement experiments help us to understand the porous medium. As will be shown later, it is also important to know what fraction of water is inside the cell. For this, we will use bioelectrical impedance analysis.

Capillary pressure, permeability and pore size distribution measurement

Capillary pressure has been routinely measured for soil structures in the field of soil science and hydrology ([8], [9], [10]) and for rocks in petroleum engineering ([11],[12] and [13]). The most common method for measuring capillary pressure is using the pressure plate technique, in which external pressure is applied to force water out of a saturated sample. Another common technique for measuring capillary pressure, in the case of rocks, is the centrifuge technique, in which water is forced out of the saturated sample by centrifugal force [13]. These experimental methods work well for rigid, non-cellular and homogenous materials but need major modifications for measurements in soft and cellular tissues due to their non-homogeneity and deformation under high pressures. Capillary pressure in green softwood was measured using the centrifuge technique [14]. Due to the lack of such data for food materials, the data for softwood has been extensively used in modeling of water transport in potatoes during frying [6]. This approach is based on the assumption that the structure of potato tubers and softwood are similar and therefore their capillary pressure should also be similar. There is no measured capillary pressure data whatsoever as we move

away from wood and potato tissue into other biomaterials. Therefore, there is an acute need to develop an experimental procedure for measuring capillary pressure in food materials to facilitate the modeling of water transport during drying processes.

Permeability can be used to estimate resistance to flow offered by a pathway. Unlike capillary pressure data, there are some permeability data available for potatoes [15] and ground beef [16]. The permeability of water was measured by forcing water through the material and recording the resistance based on the flow rate coming out of the other end of the sample. Since the tissues are non-homogenous and there is a huge difference between the largest and the smallest pores, there is significant variation in the permeabilities through these pores. The above-mentioned experiments give the permeability of the least resistant pathway or the largest pores. Therefore, to get the proper estimate of permeability, we must know the pore size distribution of the food material.

Several studies have estimated porosity (volume of air to total volume) using gas pycnometry in the case of chicken [17] and mercury porosimetry for chicken meat [18], but the pore size distribution is still largely unavailable for most food materials. Quantitative characterization of porous media, as shown in breads [19], has been rare for other products. The relationship of pore size distribution to transport properties is also not available.

Bioelectrical impedance analysis

Bioelectrical impedance analysis (BIA) gives the fraction of the water in a tissue that is intracellular. BIA measures the opposition of a tissue to an applied

low-strength alternating current and, based on the measured impedance to an electrical current, estimates of intracellular water content are made. A tissue is an imperfect conductor of electrical current. The concept of using electrical resistance or impedance to assess physiological aspects of the body dates back over 100 years, but the period of intense research in BIA started in 1985 [20], when he demonstrated that this technology could be used to detect various immune diseases in humans. Since then, BIA has been used extensively to estimate the physiological state of various biological tissues because of its simplicity and because it can be done *in situ* without cutting or crushing. The first successful validation of measurement of extracellular and intracellular water inside animal tissues using BIA was reported 1992 [21]. Now, measurement of intracellular and extracellular water in live animals using BIA is routine for detecting immunological diseases.

In the case of plant tissues (e.g., fruits, vegetables, roots, leaves, etc.), BIA has been used extensively in physiological investigation such as injury due to freeze-thaw cycles in potato tubers and carrot roots [22] and to estimate the extent of bruising in apples [23]. The electrical impedance of ripe and unripe nectarine fruits were compared to develop a fruit maturity index [24]. The relationship between the electrical and rheological properties of potato tuber tissue was also shown using BIA [25]. The impedance analysis was also used to study the effect of drying and freezing-thawing treatments on eggplants [26]. In all these studies, qualitative assessment of rheological properties was based on the measured impedance. Neither the estimate of intracellular water (ICW) content nor any information regarding transport of water inside the cellular tissue was available.

2.1.2 Objectives

The objectives of this present study are: 1) to quantify the amount of water present in the capillaries and cells of two tissues (potato and eggplant) at different temperatures; 2) to establish different pathways of moisture transport in a cellular tissue under different processing conditions; 3) to discuss the implications of these microstructural aspects on water transport in such tissues.

2.2 Theory behind the measurements

2.2.1 Capillary pressure

Capillary pressure is the difference in pressure across the interface between two immiscible fluids, a non-wetting fluid and a wetting fluid. When the wetting fluid is liquid water and the non-wetting fluid is air, the capillary pressure, p_{cap}, is given by

$$p_{cap} = p_a - p_w \tag{2.1}$$

where p_a is the air pressure and p_w is the liquid water pressure. In the case of food materials (e.g., potato, meat, etc.), what is referred to as the capillary pressure is essentially the lumped effect of surface tension, immiscibility, the presence of microscopic scale fluid-fluid interfaces, fluid viscosity, the wettability of solid surfaces, grain size distribution, microscale and macroscale heterogeneities, solid matrix deformation, and fluid composition [27]. Although processes determining the capillary pressure of water are extremely complicated,

the main theoretical and practical tool currently in use for characterizing this is an empirical relationship between capillary pressure and moisture content, given by

$$p_{cap} = p_{cap}(M) \tag{2.2}$$

where M is the moisture content (dry weight basis) of the porous material.

Experiments conducted to calculate capillary pressure as a function of moisture content assume that all the liquid water is present in the capillaries and that it flows as long as the applied gas pressure (p_a) exceeds the capillary pressure (p_{cap}). As soon as the applied gas pressure is equal to the capillary pressure of the food material at that moisture content, the liquid water stops flowing and capillary pressure is determined from the applied gas pressure. This pressure is then related to the moisture content of the material at that point, to find the relation given by Eq. 2.2. By extending this to a number of applied pressures, a capillary pressure curve, which relates capillary pressure to moisture content, is generated.

Pressure plate experiment

The simplest way to force water through a porous medium is to run a pressure plate experiment [28]. The schematic of the experimental set-up is shown in Figure 2.1. The potato slice is placed on a saturated porous polycarbonate membrane of pore sizes of 0.1 microns (Sterlitech Corporation, Kent, WA) in the pressure chamber. The air pressure is applied from the top. If the base of the potato slice is in good contact with the porous membrane then the liquid water

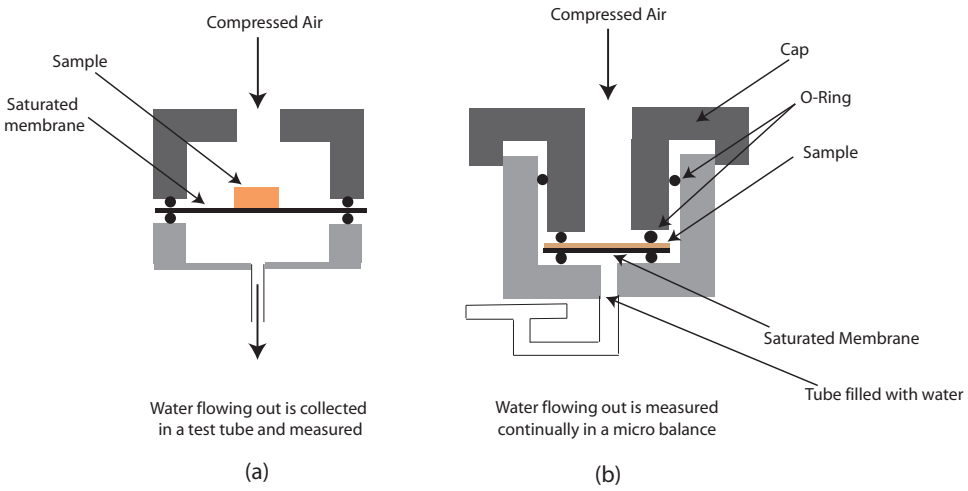

Figure 2.1: Schematic of the experimental setup for capillary pressure measurement : a) Pressure plate experiment; b) Liquid extrusion porosimeter in Porous Materials Inc. (Ithaca, NY).

in the potato slice is in continuum with the liquid water in the polycarbonate membrane. In that case, the bottom surface of the potato slice is at atmospheric pressure and there is a pressure difference between the top and bottom surfaces (equal to the magnitude of the applied gas pressure). The largest pore size of the polycarbonate membrane is smaller than the smallest pore size of the potato slice, so the air cannot push out water from the polycarbonate membrane before it pushes it from the potato slice. When water is pushed out of the potato slice, it replaces the water in the polycarbonate membrane which flows out into a receiver where its volume is measured.

Liquid extrusion porosimetry

A Liquid Extrusion Porosimeter (Porous Materials Inc., Ithaca, NY) was used to measure the capillary pressure of the potato sample at different moisture contents. Unlike the pressure plate experiment, the pressure was raised every hour

in this equipment. The maximum pressure that can be applied using this equipment is 0.7 MPa and the pressure step size used was 0.025 MPa. The amount of water drained from the potato is collected in a microbalance (0.001 gm accuracy) and measured at regular intervals. The initial moisture content of the potato slice is known, so its transient moisture content is calculated from the measured drained water.

2.2.2 Largest pore size and pore size distribution

Largest pore size

A pore size distribution experiment gives the fraction of void volume that is occupied by different pore sizes. The schematic of the pore size distribution experimental setup is shown in Figure 2.2. The pores of the sample are assumed to be filled with water initially. Air pressure on the top surface of the sample is slowly increased so as to displace the liquid from the pores and thereby increase gas flow through the sample at the other end. The gas can displace the liquid from the pores only when the applied pressure exceeds the capillary pressure on the liquid. The differential pressure, p_{cap}, required for displacement of liquid water in a cylindrical pore is given by [45]:

$$p_{cap} = 4\frac{\gamma cos\theta}{d} \tag{2.3}$$

where γ is the surface tension of liquid water, d is the diameter of the pore and θ is the contact angle between liquid water and the surface. The pressure required to empty a pore is smallest for the largest pore (also known as the bubble point diameter) and can be estimated from Eq. 2.3.

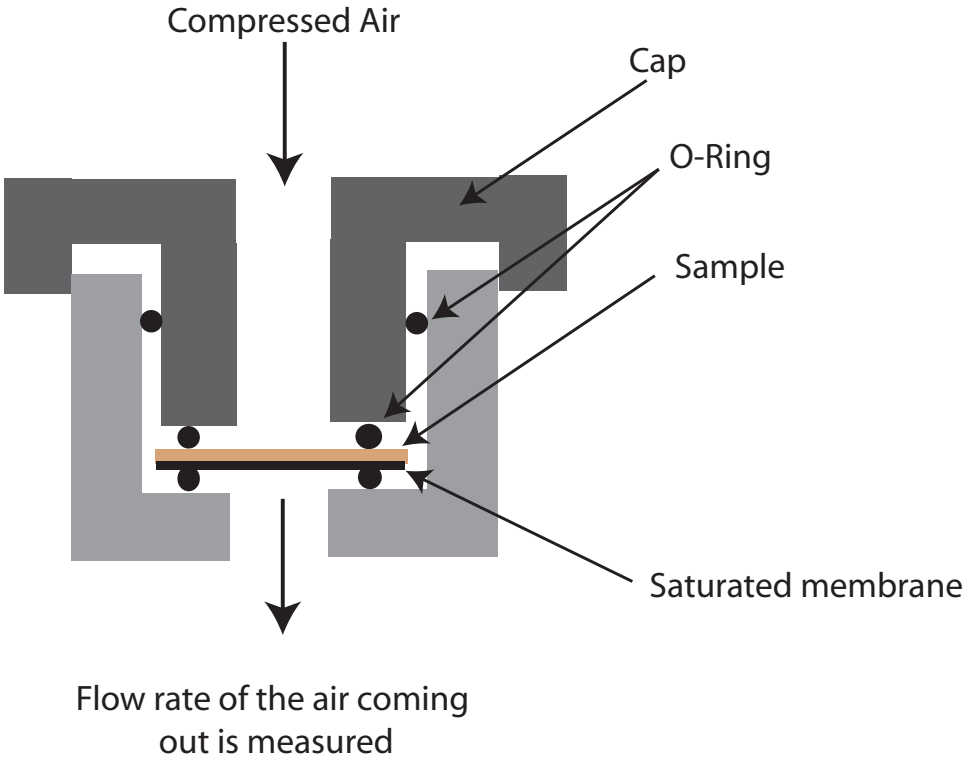

Figure 2.2: Schematic of the experimental setup for pore size distribution measurement.

Pore size distribution

To calculate the pore size distribution, flow rates through wet and dry samples are determined. A wet sample is one that is initially saturated with water and, during the experiment, the water is pushed out of the sample by pressurized air. A dry sample is one that is completely dry and the pore channels are filled with air. Therefore, a wet curve (flow rate versus time for a wet sample) provides the flow rate through all the open pores at any given pressure, while a dry curve provides flow rate through all the pores (since all pores are open).

Assuming viscous flow, at a given temperature, the flow rate, F, through a porous channel is given by the product of velocity (from the Poiseuille equation)

and area, shown as:

$$\begin{aligned} F &= \text{area} \times \text{velocity} \\ &= \frac{\pi d^2}{4} \times \frac{d^2}{32\mu} \frac{dp}{dx} \\ &= \frac{\pi d^2}{4} \times \frac{d^2}{32\mu} \frac{p}{L} \end{aligned} \tag{2.4}$$

Therefore, the flow rate through N number of pores can be written as [30]:

$$\begin{aligned} F &= \frac{\pi}{128\mu L} \sum_{i=1}^{N} n_i {d_i}^4 \times p \\ &= g(d, N) \times f(p) \end{aligned} \tag{2.5}$$

So, flow rate through a porous medium is a function of pressure and the pore characteristics of the sample (e.g., the diameter of the pores, d, and the number of pores, N). For viscous flow, the pressure variable is separable from the other variables and can be expressed as a product of two functions, $f(p)$ and $g(d, N)$, as shown in Eq. 2.5.

Therefore, the ratio of flow rates through a wet and dry sample at the same applied pressure is given by:

$$[F_{wet,p}/F_{dry,p}] = [f(p) \times g(d, N)]_{wet,p}/[f(p) \times g(d, N)]_{dry,p} \tag{2.6}$$

The function $f(p)$ is the same for wet and dry samples and therefore the ratio of flow rates is a function of pore structure only and is given by:

$$[F_{wet,p}/F_{dry,p}] = [g(d, N)]_{wet,p}/[g(d, N)]_{dry,p} \tag{2.7}$$

Therefore, the fraction of flow through pores with diameters between D_j and D_{j+1} is

$$\triangle F = [F_{wet,p}/F_{dry,p}]_{j+1} - [F_{wet,p}/F_{dry,p}]_j \tag{2.8}$$

The fraction of flow through a diameter range is equal to the fraction of pore volume in that diameter range, thus providing the pore size distribution.

2.2.3 Bioelectrical impedance analysis

Bioelectrical impedance analysis (BIA) is performed to determine the fraction of water in a tissue that is intracellular. The technology is based on the principle that electricity is conducted through a tissue by electrolyte-containing fluids and will take the path of least resistance. The simplified equivalent circuit for current flow through a tissue is proposed by [22] and shown in Figure 2.3. The total impedance, Z, can be broken down into two parts: 1) the real part, known as resistance; 2) the complex part, known as reactance. The electrical current inside the tissue experiences opposition from 1) the fluids in the tissue (extracellular and intracellular fluids); 2) the cell membrane, which has a high resistance but acts as a capacitor (storing up electrical charge for a given electrical potential). In Figure 2.3, the resistance due to extracellular fluid is shown as R_e and that due to intracellular fluid (in the cytoplasm) as R_i; the impedance due to cell membrane capacitance is given as:

$$Z_c = \frac{1}{j\omega C} \tag{2.9}$$

where Z_c is the impedance due to cell membrane capacitance, $\omega = 2\pi f$, with f being the frequency of the signal, and C is the capacitance of the cell membrane. Therefore, the total impedance of the electrical circuit is:

$$Z = \frac{R_e \left(R_i + \frac{1}{j\omega C} \right)}{R_e + R_i + \frac{1}{j\omega C}} \tag{2.10}$$

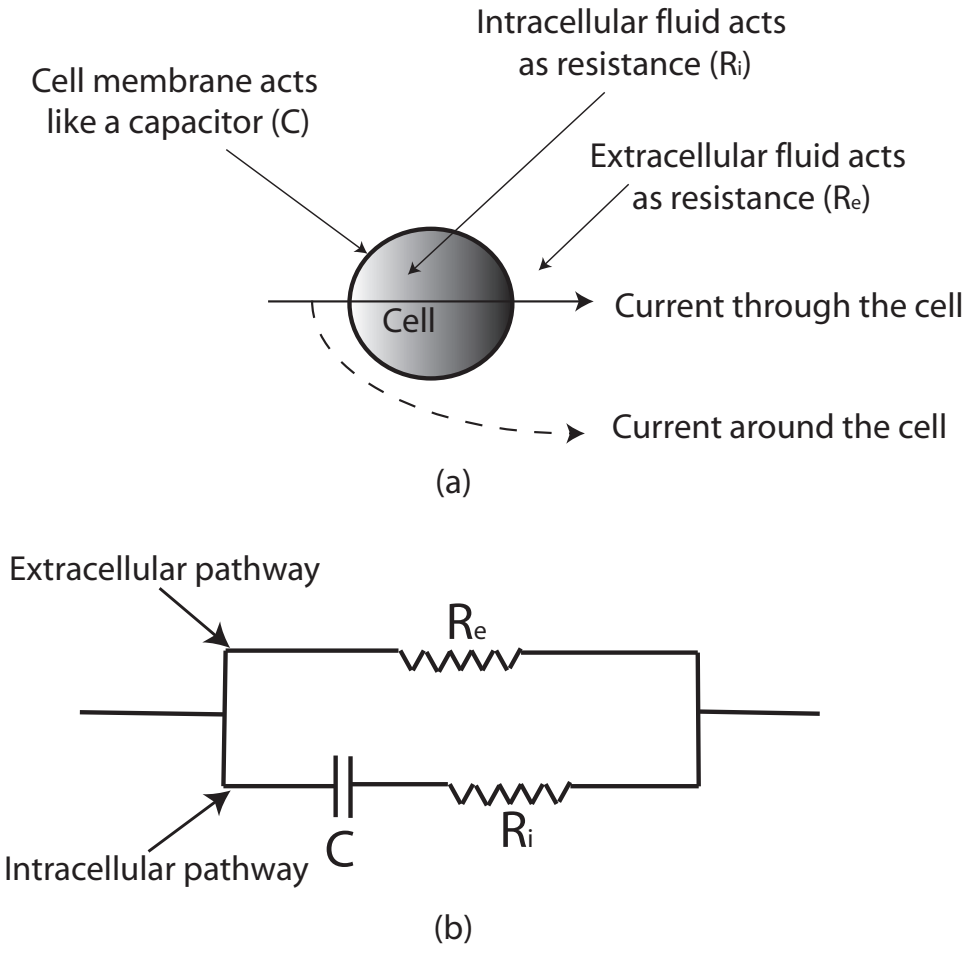

Figure 2.3: a) Schematic of a cell with extracellular fluid and two pathways that a current can take (through the cell and around the cell) is shown; b) The equivalent circuit for current through cell and extracellular fluid is shown. This is a parallel circuit as the current can go either through the extracellular fluid or through the cell (cell membrane and intracellular fluid). The resistance of the plasma membrane, which is in parallel with the membrane capacitance, is ignored due to its relatively high value.

Bioelectrical impedance at low frequencies

As shown in Figure 2.4, at low frequencies the current applied to the tissue will travel predominantly through the extracellular fluid and only a portion of the applied current will be opposed by the cell membranes of the tissues. This is because, at low frequencies, cell membranes have high electrical resistance because the RC time constant of the cells is small. The potential gradients across the cell membranes will closely follow the external potential gradient and therefore the magnitude of the current into the cell capacitor will be small. A major part of the current goes through the extracellular compartment. R_0 is the resistance measured at zero frequency (e.g., a direct current). It is the best theoretical value of impedance of the extracellular space as almost all the current travels through this space.

Bioelectrical impedance at high frequencies

As the frequency increases, the impedance of the membrane (a capacitor) decreases, allowing more current to flow into the intracellular compartments. Because of the change in polarity due to the AC current, the cell membrane charges and discharges at the rate of the frequency. At higher frequencies, the rate of charge and discharge becomes such that the impedance due to the capacitor diminishes to insignificant proportions, and the current flows through both the extracellular and intracellular compartments in proportions that depend on their relative conductivities and volumes [31]. Thus, R_{inf} is the impedance measured at infinite frequency and is the best theoretical value of impedance due to the extracellular and intracellular fluid. Note that the infinite frequency current will not be affected by interaction with the cell membranes and that it will pass

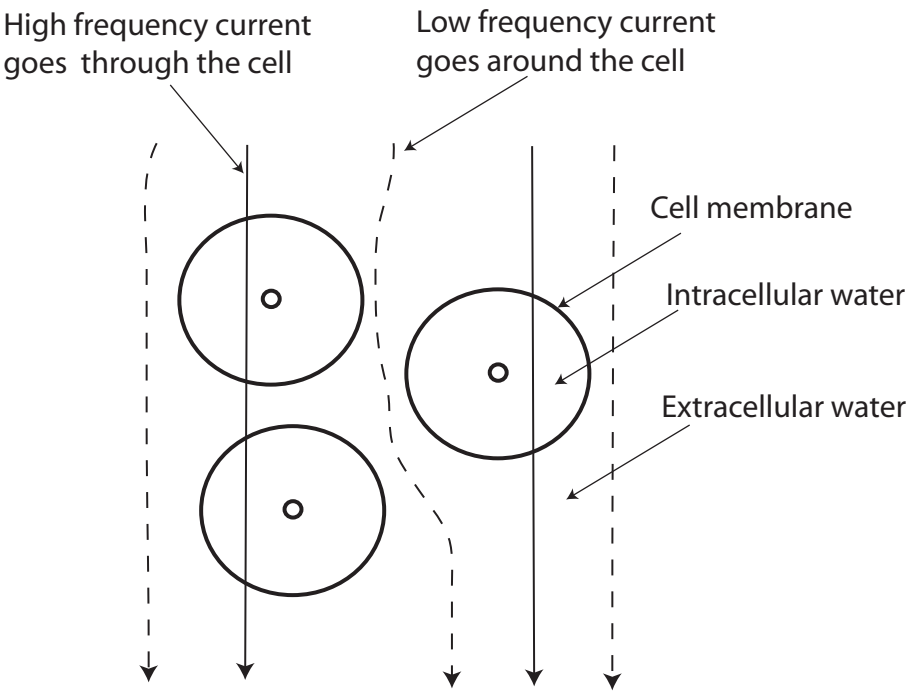

Figure 2.4: The responses of different frequency signals in a biological tissue are shown. A high frequency signal can go through both the cell membrane and intracellular fluid. The low frequency signal cannot penetrate the cell membrane and therefore goes around the cell.

directly through the cell membranes. Hence, at this frequency the reactance component of the impedance vector is zero. In this way the impedance at R_{inf} is the impedance due to the total tissue water (intracellular and extracellular) and is given by

$$R_{inf} = \frac{R_i R_e}{R_i + R_e} \tag{2.11}$$

Cole-Cole plot

The impedance of the equivalent circuit (shown in Figure 2.3) at an angular frequency, ω, can be rewritten in terms of R_0 and R_{inf} as:

$$\begin{aligned} Z &= R + jX \\ &= R_{inf} + \frac{R_0 - R_{inf}}{1 + j\omega C} \\ &= \left(R_{inf} + \frac{R_0 - R_{inf}}{1 + \omega^2 C^2} \right) + j\omega C \left(\frac{R_{inf} - R_0}{1 + \omega^2 C^2} \right) \end{aligned} \tag{2.12}$$

A plot of reactance (X) versus resistance (R) of a tissue for various frequencies, known as a Cole-Cole plot and shown in Figure 2.5, gives a semi-circle. The semi-circular nature of the plot allows the determination of R_{inf} (a theoretical value) that cannot be measured directly. In practice, resistance (R) and reactance (X) are measured for a number of frequencies (between 5 kHz and 1 MHz) and the Cole-Cole plot is constructed and extrapolated at the ends (to touch the R-axis) to yield R_{inf} and R_0.

Ratio of intracellular water to extracellular water

The ratio of intracellular water volume (V_{ICW}) to extracellular water volume (V_{ECW}) was predicted from the modeled R_0 and R_{inf} using equations formulated from theory [32] that describes the effect that a concentration of nonconductive material has on the apparent resistivity of the surrounding conductive fluid. The ratio is determined by the following equation [33]:

$$\left(1 + \frac{V_{ICW}}{V_{ECW}} \right)^{5/2} = \frac{R_e + R_i}{R_i} \left(1 + \kappa \frac{V_{ICW}}{V_{ECW}} \right) \tag{2.13}$$

where

$$\kappa = \frac{\beta_{ICW}}{\beta_{ECW}} \tag{2.14}$$

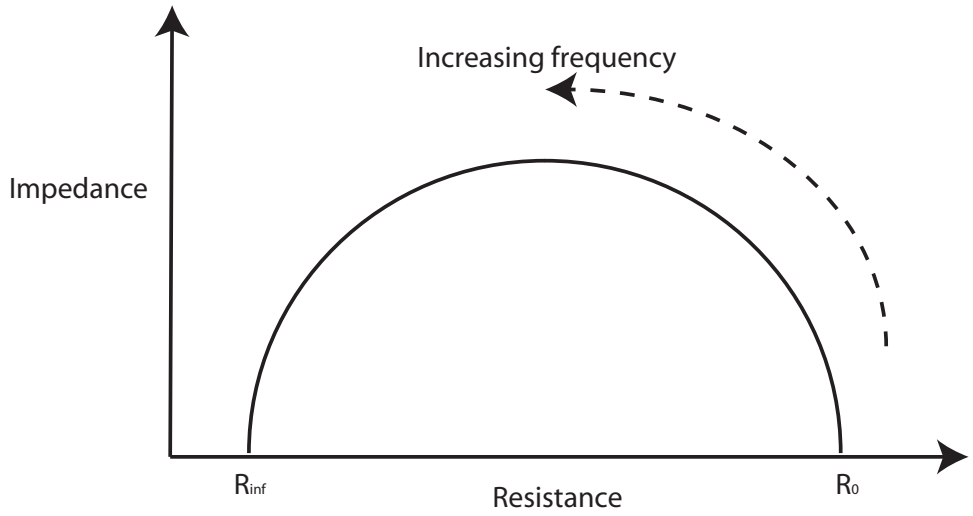

Figure 2.5: A Cole-Cole plot. In practice, the resistance (R) and reactance (X) is measured for a number of frequencies (between 5 kHz and 1 MHz) and Cole-Cole plot is constructed. The ends are then extrapolated to touch the R-axis to get R_{inf} and R_0.

Equation 2.13 can be written in terms of R_0 and R_{inf} using Equation 2.11 as:

$$\left(1 + \frac{V_{ICW}}{V_{ECW}}\right)^{5/2} = \frac{R_0}{R_{inf}}\left(1 + \kappa\frac{V_{ICW}}{V_{ECW}}\right) \tag{2.15}$$

The parameter κ is the ratio of electrical resistivity in intracellular fluid to electrical resistivity in extracellular fluid, and has been determined for animal cells to be between 3.2 and 3.71 [33]. For higher plant cells, it is not possible to measure this parameter. For animal cells it was determined that conductivity in extracellular fluid is always more than that in the intracellular fluid. In plant structures, there are Donnan free spaces that contain a high concentration of negative charges that are associated with mobile cations [34], thereby conferring a high electrical conductance on the extracellular region. Therefore, we use a conservative value of κ equal to 3.2. This will give the lowest estimate of intracellular water volume.

2.3 Materials and Methods

2.3.1 Capillary pressure measurements

As will be discussed later, pressure driven flow was difficult to achieve, and consequently two separate experimental setups were tried to measure the capillary pressure of a potato sample (Russet white Idaho type) as the moisture content changes.

Setup 1: Classical pressure plate experiment

Cylindrical potato samples (diameter 3 cm and thickness 2 cm) were placed in the pressure chamber (as shown in Figure 2.1a) at an applied pressure (0.1 MPa; 0.3 MPa; 0.5 MPa and 1.5 MPa) for 5 days and was allowed to come to equilibrium. After 5 days, the sample was taken out of the chamber and its weight was measured (the difference between the initial and final weight of the potato slice should be equal to the weight of water collected during the experiment). The relative humidity inside the chamber was at 100%. Each time, a sample was also placed outside the chamber at 60% RH and atmospheric pressure during the course of the experiment to estimate moisture loss that would happen without applied pressure, due to evaporation.

Setup 2: Liquid Extrusion Porosimetry experiment

Cylindrical potato samples (diameter 3 cm and thickness 2 cm) were placed in the pressure chamber (as shown in Figure 2.1b). The pressure in the chamber

was increased by 0.025 MPa every hour until it reached 0.7 MPa (the maximum for the equipment). The relative humidity inside the chamber was 100%. Each time, a sample was also placed outside the chamber at 60% RH and atmospheric pressure during the course of the experiment, as explained in the previous paragraph.

2.3.2 Pore size distribution measurements

Five samples of potato tissue (diameter 3 cm and thickness 2 cm) were analyzed for pore size distribution. Each sample was placed in the pressure chamber (as shown in Figure 2.2) and the applied pressure was slowly increased from 0.0 to 0.7 MPa in 4 hours. The air flow sensor at the other end recorded the total air flowing out of the potato sample during the course of the experiment. At the end of the experiment, the air flow rate was plotted against the applied pressure for the wet and dry samples (a dry sample is the slice at the end of the pore size experiment from which the water has been forced out) and the pore size distribution was estimated as explained before in the theory section.

2.3.3 Bioelectrical impedance analysis

The bioelectrical impedance analysis was performed using the IMP SFB7 body composition meter (Impedimed Inc., San Diego, CA). It is a single-channel, tetra-polar bioimpedance spectroscopy device that scans 256 frequencies between 4 kHz and 1000 kHz for the estimation of impedances in tissues. The equipment was calibrated using the calibration cell provided. Needle electrodes

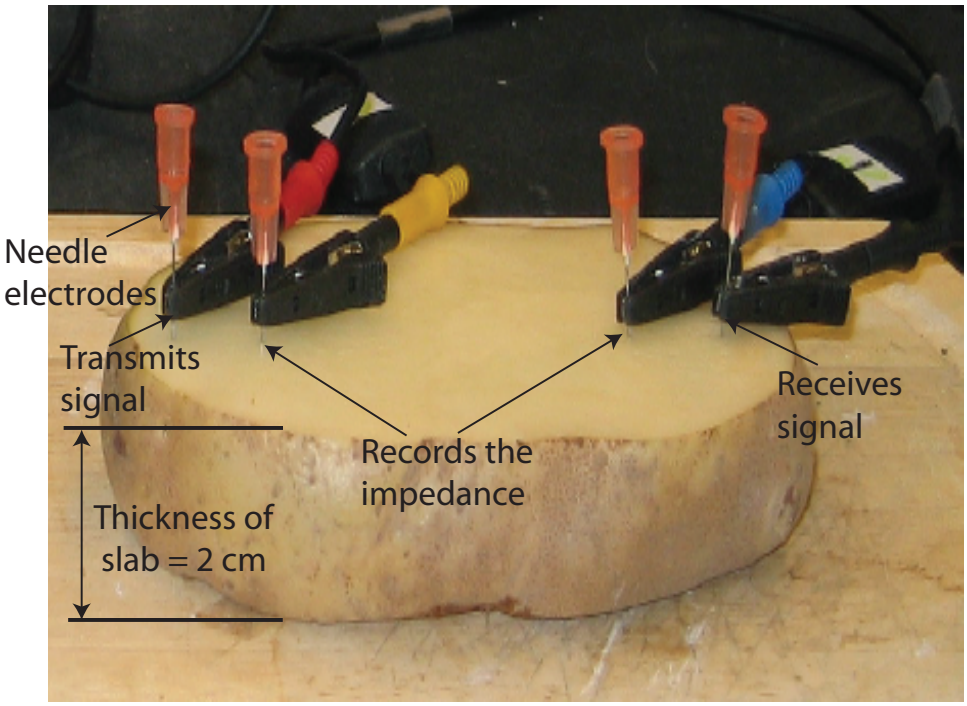

Figure 2.6: Picture of the experimental setup for bioelectrical impedance analysis. The needle electrodes are connected to the instrument (not shown in the picture).

(0.5 mm thick and made of stainless steel) were used. A $200\mu A$ RMS AC current flowed through the electrodes. The experimental procedure can be divided into four cases:

Case 1: Five different kinds of fruits and vegetables (apples, eggplants, cucumbers, tomatoes and potatoes) were analyzed. Three samples of each kind were tested for intracellular water content at 22°C. Each sample was cut in the shape of a slab of 2 cm thickness. The electrodes were placed 4 cm apart as shown in Fig. 2.6.

Case 2: Three potato samples (in a slab shape of 2 cm thickness) are placed in an oven with the air temperature at: a) 45°C; b) 55°C; c) 70°C; d) 90°C. The weights of the samples and the resistances, R_0 and R_{inf}, were measured once every hour for 24 hours of drying upon removal from the oven for a short time.

Case 3: Three eggplant samples (in a slab shape of 2 cm thickness) are placed in an oven with the air temperature at: a) 55°C; b) 90°C. The weights of the samples and the resistances, R_0 and R_{inf}, were measured once every hour for 24 hours of drying upon removal from the oven for a short time.

Case 4: Three potato samples (in a slab shape of 2 cm thickness) are placed in a 2 kW microwave oven. The weights of the samples and the resistances, R_0 and R_{inf}, were measured every 20 seconds of heating upon removal from the microwave oven for a short time. The total cumulative heating time is 2 minutes.

2.4 Results and Discussion

2.4.1 Is the water present in the capillaries (intercellular spaces)?

Both experimental setups for the measurement of capillary pressure, the classical pressure plate experiment and liquid extrusion porosimetry, yielded similar results, that is, they produced little flow even at very high pressures. The pres-

sure plate experiment did not register any water flowing out of the potato for applied pressures between 0.1 to 0.5 MPa, and only 2% of the water flowed out at an applied pressure of 1.5 MPa (the highest possible pressure for this apparatus). The liquid extrusion porosimeter also gave similar results as only 2% of the total water flowed out at an applied pressure of 0.7 MPa (the highest possible pressure for this apparatus). The two different experimental setups, pressure plate and extrusion porosimetry, provide two different approaches to obtaining the pressure-driven flow, and therefore together these results demonstrate that only 2% of total water can be driven out by pressures up to 1.5 MPa.

Of course, we know that raw potato loses water when left in the atmosphere. A quick measurement showed that the same potato slices (as in the previous paragraph) left open to ambient air at atmospheric pressure lost approximately 80% of their water over 5 days. This contrasts with the low pressure-driven flow for pressures up to 1.5 MPa. The plausible reasons for this can be: 1) the rest of the water is not present in the capillaries; 2) the capillary pressure (which is negative or attractive) is higher than the applied pressure and therefore water cannot flow out of the pores; 3) the water is present in the blind pores (explained in Figure 2.7), therefore no water flows out, but in that case the moisture migration during drying at atmospheric pressure is not pressure-driven (since pores are not connected). To better understand the pore sizes and structures, pore size distribution experiments were performed, which are described in the next section.

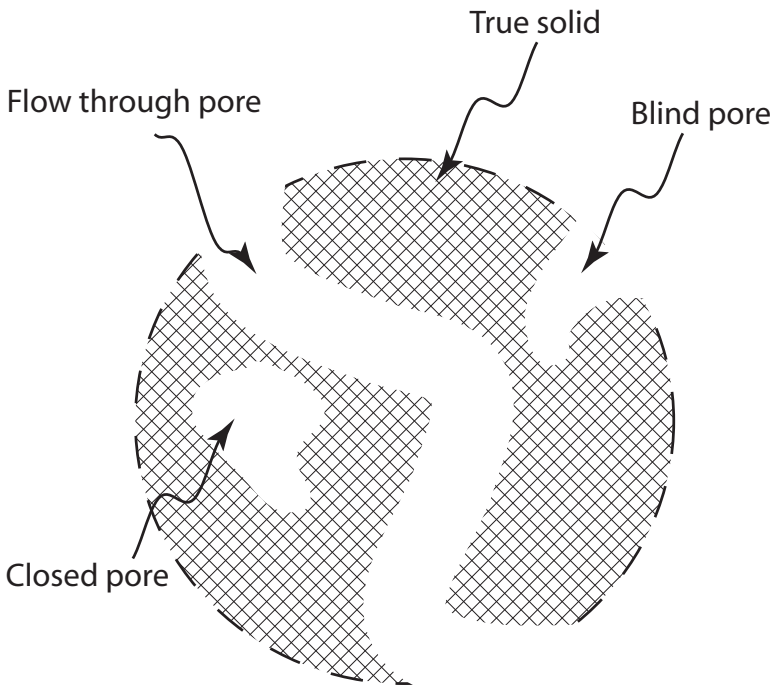

Figure 2.7: Schematic showing three different types of pores that can be present in a porous material.

2.4.2 What is the nature of the capillaries?

As explained in Section 2.2.2, for the theory behind pore size distribution, as gas pressure is slowly increased, liquid water is drained out from progressively smaller pores, starting with the largest pores. The flow rate of gas through the dry and wet potato samples at various applied pressures is shown in Figure 2.8. As can be seen, when drying a wet sample (the wet curve), there is no gas flow initially because the gas cannot displace liquid completely from the pores at this applied pressure. As the pressure is slowly increased on one side of the sample, the gas pressure reaches a point at which it is slightly greater than the surface tension force of the water and displaces it from the largest pores and thus gas starts to flow out from the other end. As shown in Figure 2.8, this occurs at

Table 2.1: Summary of pore size distribution experiment of 5 potato samples

Sample number	Largest pore diameter (microns)	Average pore diameter (microns)
1	5.736	0.389
2	0.915	0.440
3	5.761	0.554
4	1.267	0.875
5	5.745	0.453
Average	3.885	0.542

around 0.23 MPa. The pore diameter corresponding to this pressure (calculated using Eq. 2.3) is the largest pore diameter of the sample. For the sample shown in Figure 2.8, the largest pore diameter is estimated at 0.92 microns and its pore size distribution is shown in Figure 2.9. The average pore and smallest pore diameters are 0.53 microns and 0.35 microns, respectively. A total of five samples of potato were tested for pore size distribution and Table 1 gives the largest and average pore diameter of each of the five samples of the same potato type (Russet white Idaho potatoes). The average over the five samples gives the largest and average pore diameter in this potato type as 3.88 microns and 0.542 microns, respectively. The implications of these are provided in the following paragraph.

Thus, the pore size distribution study demonstrates that: 1) Pores are not initially empty (since gas does not flow through at low pressures), which leads to two possibilities—either the pores are filled with water (requiring higher pressure) or they are blind pores. 2) Pores are not all blind and there are channels through which water and gas can flow. This is true, since the flow of gas does

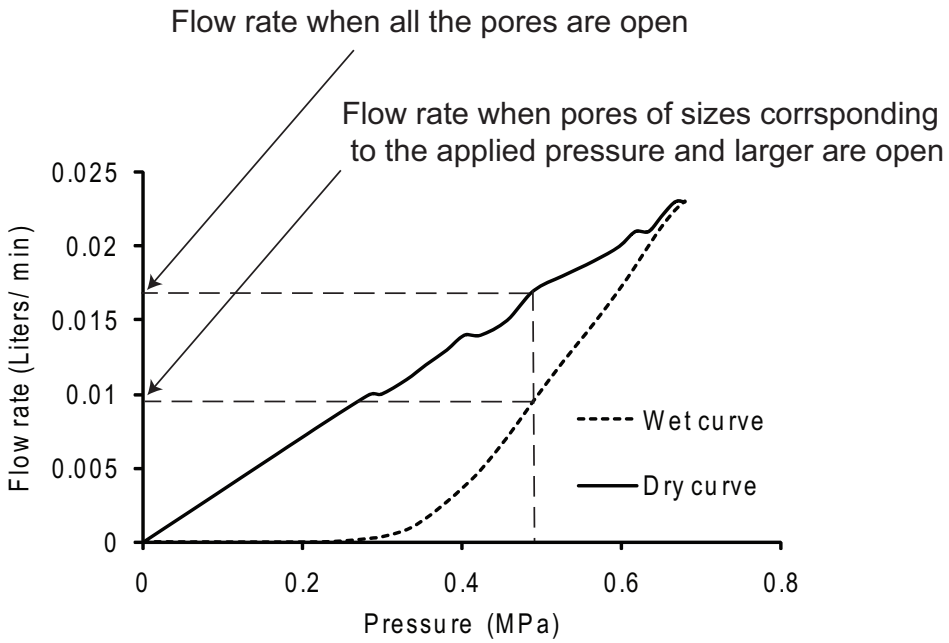

Figure 2.8: Wet and dry curves obtained during the pore size distribution experiment of a potato slice. A wet curve gives the flow rate at applied pressures when the sample is partially filled with water and the rest consists of empty channels filled with air which allow air to pass. A dry curve gives the flow rate at various applied pressures when the sample is completely dry and all the pore channels are filled with air and allow air to pass through them.

occur once the liquid is forced out as gas pressure is increased beyond a certain threshold (the bubble point). 3) Pore sizes up to 0.35 micron contain only 2% of the total water (that is all the water flowing out for pressures up to 0.7 MPa, a pressure that corresponds to a 0.35 micron diameter pore). This leads to the conclusion that either most of the water (98%) is in pores smaller than 0.35 micron in diameter, it is in blind pores, or it is not in pores at all (it is in the cells?). This is discussed in the following section.

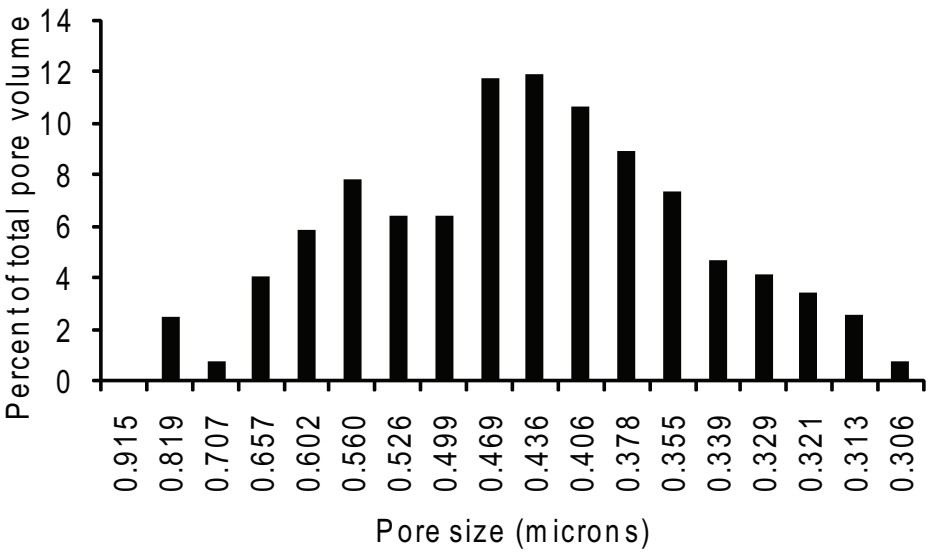

Figure 2.9: Pore size distribution of a potato slice. Largest pore diameter measured was 0.915 microns and smallest was 0.306 microns. Average pore diameter for the slice is 0.499 microns.

2.4.3 If not in the capillaries, is the water present inside cells?

Only a small amount of water can be contained in the intercellular spaces. For example, only 1-2% of the total volume of water occupies intercellular spaces in potato tubers [35]. Therefore, it is unlikely that there is a significant amount of water remaining in the intercellular spaces that can be drained out by applying still higher external pressures. So, the question is, where is the water if it is not in the pores (intercellular spaces)? The biology literature states that at least 70% of the water is intracellular in meat [36] and vegetables ([37], [38]) at room temperature. Intracellular water flow would require cell membranes to rupture at high pressure (a value of 3 MPa for the rupture of cell walls and cell membranes in carrots was reported by [39] that is above the values used for capillary pressure measurements. It appears critical to quantify the amount of intracel-

lular water, which we accomplished using bioelectrical impedance analysis on potatoes and eggplants, as described in the next section.

2.4.4 How much water is intracellular?

Using bioelectrical impedance analysis, intracellular water content (ICW) at room temperature was measured for five different vegetables, as shown in Table 2. Potatoes and eggplants have high ICW at around 95% and tomatoes have relatively lower ICW at around 80%. The experimental results reported in Table 2 closely match the data on intracellular water content in the literature as measured using other experimental procedures, such as freezing [38].

As potato has around 95% intracellular water at room temperature, only 5% of the water in the pores would be forced out by applied pressure (in the range discussed in Section 4.1). This is consistent with what occurred during the capillary pressure measurement and pore size distribution experiments, where 2% of the water could be driven out on the application of pressure at 0.7 MPa.

Figure 2.10 shows the Cole-Cole plot for a sample measured at different times while drying at 90°C. The resistance at zero frequency, R_0, which is inversely proportional to extracellular water content, decreases with an increase in temperature. The value of R_0 for a raw potato is 2300 ohms, which decreases to 1100 ohms after 30 minutes and 150 ohms after 105 minutes of drying. A decrease in R_0 means an increase in extracellular water content and this can be explained if cell membranes are damaged and intracellular water is released into the matrix.

Table 2.2: Intracellular water content (%) of different cellular products at room temperature (22°C)

Sample	Intracellular water content (%)
Cucumber (Sample 1)	95.3
Cucumber (Sample 2)	95.8
Tomato (Sample 1)	84.7
Tomato (Sample 2)	78.7
Apple (Sample 1)	90.2
Apple (Sample 2)	89.9
Eggplant (Sample 1)	96.8
Eggplant (Sample 2)	97.3
Potato (Sample 1)	95.3
Potato (Sample 2)	96.0

That cell membrane damage releases water into the extracellular matrix is further illustrated in Figure 2.11 which shows the variation with the temperature in resistance and reactance of the sample at the same signal frequency. From this figure, the temperature range in which the cells get damaged and release water in the matrix can be estimated. As the temperature increases from 20°C to 50°C, the resistance decreases slightly with the temperature due to an

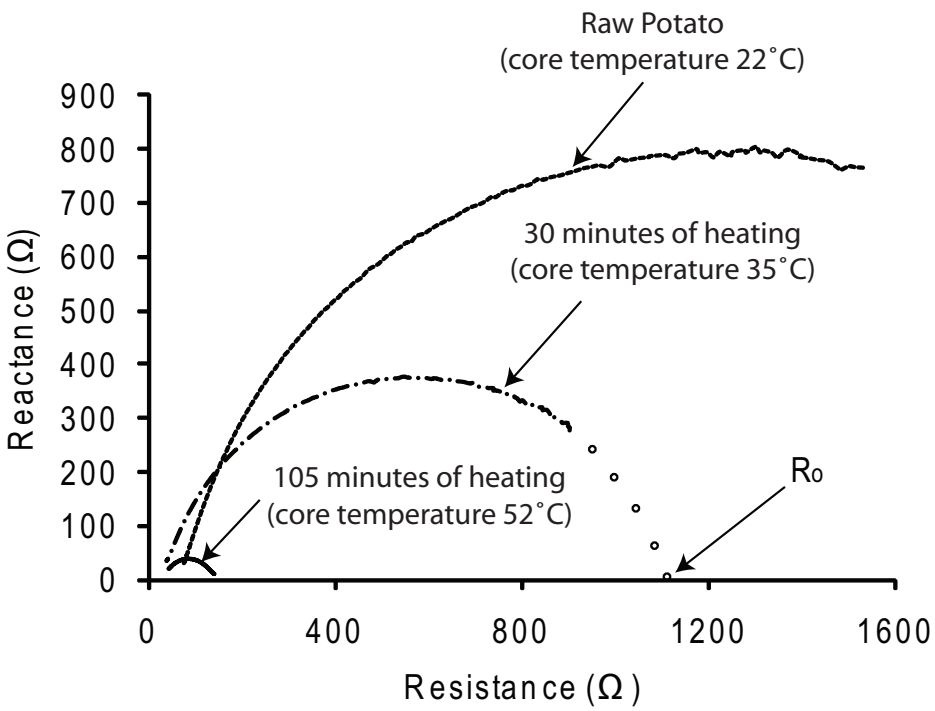

Figure 2.10: Cole-Cole plot for a potato slice, heated at 90°C, is obtained from BIA. The semi-circular nature of the plot allows the determination of R_{inf} and R_0 by extrapolation to touch the horizontal axis. As temperature increases inside the potato (with drying time), R_0 decreases, signifying increased pathways through the extracellular water (thus increased amount of extracellular water)

increase in conductance of the fluids. Similar observations were also made during bioelectrical impedance analysis of skin [40]. The capacitance of the cell increases with the temperature [41] and this should lead to a decrease in reactance, as also shown in Figure 2.11. Between 52°C and 60°C, there is a sharp drop in resistance and reactance. Resistance decreases suddenly because, as the cell membrane ruptures, the cross-sectional area through which the current is passing increases significantly, thus reducing the resistance (resistance is inversely proportional to cross-sectional area). The damage to the cell also causes a reduction in the potential across the membrane produced by the applied cur-

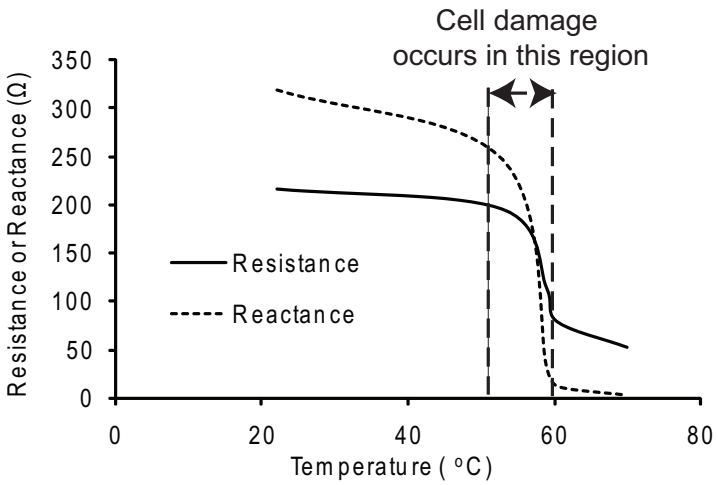

Figure 2.11: Variation of resistance and reactance with temperature at 50 kHz. The temperature range where resistance and reactance drops sharply (between 52°C and 60°C) is identified as the range where the cell membranes get damaged.

rent, thus reducing the current flowing into the membrane capacitance.

Bioelectrical impedance analysis in low temperature drying

The potato samples were dried in an oven for 24 hours at two temperatures (45°C and 55°C) to estimate the range of temperatures within which the cell damage takes place and the intracellular water is released into the intercellular space. Figure 2.12a and 2.12b give the variations in moisture content (kg water /kg dry weight), temperature and the percentage of intracellular water content (ICW) of potato slice while drying at 45°C. In Figure 2.12a, it can be seen that, during the drying process, the potato samples lose water significantly (moisture content dropped from 4.35 to 2.75). Figure 2.12b shows that the temperature inside the potato always remains below 42°C and ICW remains stable at around 96% throughout the drying process. This means that the cells lose water to the

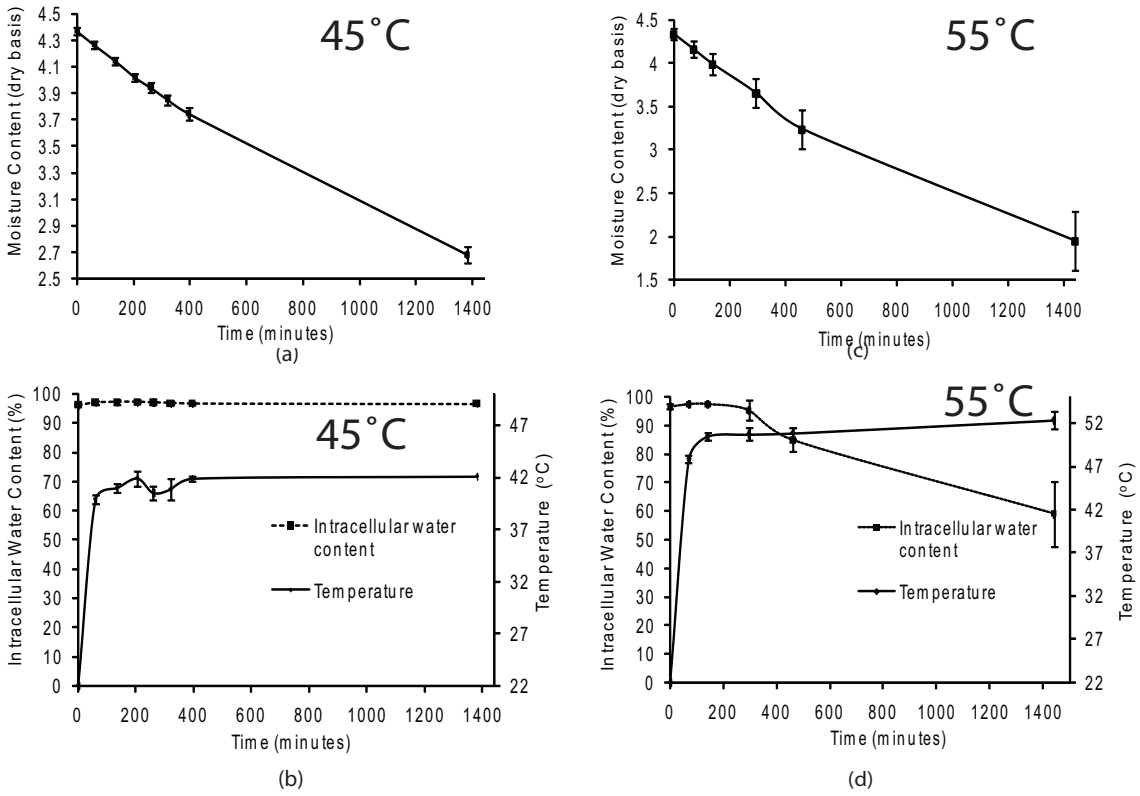

Figure 2.12: Moisture content (kg water/ kg dry weight) versus time for drying of potato slice at a) 45°C and c) 55°C. Intracellular water content(%) and core temperature versus time for drying of potato slice at at b) 45°C and d) 55°C.

outside during the process but they are not damaged and the cell membranes remain intact throughout. So, the water migration pathway during this process can be called an intracellular pathway, as shown in Figure 2.17a, where water migrates through three different zones in series: cell membranes, cell walls and intercellular spaces.

During the drying of potato slices at 55°C (shown in Figure 2.12c and 2.12d), the ICW remains stable at 96% until the temperature nears 50°C (300 minutes of drying). As the temperature rises above 50°C, the ICW drops slowly and reaches 60% after 24 hours of drying. Based on these results it can be said that

the cell membrane remains intact until the temperature reaches about 50°C and is ruptured as the temperature rises above that temperature, thereby releasing water into the intercellular space and increasing the fraction of extracellular water. The sample loses water significantly during this higher temperature period (shown in Figure 2.12c). The water migration during the initial period of drying (in the first 300 minutes when the cells are intact) would proceed through the intracellular pathways (just as when drying the slices at 45°C). When the cell membrane ruptures, the released water travels through intercellular space and this is called an extracellular pathway (shown in Fig 2.17b). In an extracellular pathway, the migrating water experiences no resistance from cell membranes. Thus, when drying potato slices at 55°C, during the initial period the moisture migrates primarily through intracellular pathways. During the later stages, when the cell membranes rupture, some of the water migrates through extracellular pathways but the movement is still primarily intracellular as ICW remains above 60%.

Similar observations were also made from the low temperature drying experiments with eggplant (e.g., eggplant dried at 55°C). As can be seen in Fig 2.13, the ICW remains constant at around 97% until the temperature reaches about 50°C and then decreases slowly to 75% at the end of 24 hours of drying (during which time the temperature remains above 50°C). In Figure 2.13a, it can be seen that the eggplant loses a significant amount of water (moisture content dropped from 15.9 to 5.01) during this period. The moisture migration in eggplant during drying at 55°C is similar to what occurs in potato drying at 55°C: moisture migrates almost exclusively along intracellular pathways in the initial stages, followed by both intracellular and extracellular pathways, although 75% of the water migration is still intracellular.

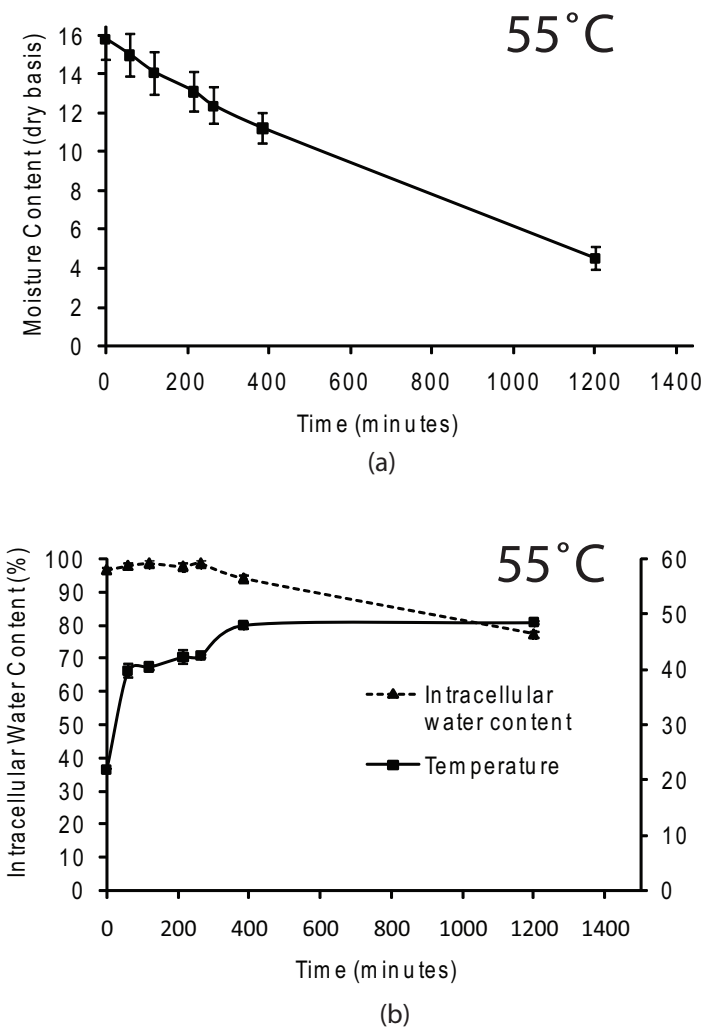

Figure 2.13: (a) Moisture content (kg water/ kg dry weight) and (b) Intracellular water content(%) and core temperature versus time for drying of eggplant slice at 55°C.

Bioelectrical impedance analysis in high temperature drying

Potato and eggplant slices were dried at high temperatures and their ICW values were measured at regular time intervals to see how higher temperatures affect ICW. The potato samples were dried and analyzed at two temperatures (70°C and 90°C), the results of which are shown in Figure 2.14. The ICW starts

decreasing as soon as the core temperature rises above 50°C. But in the case of high temperature drying, the time required to reach 50°C is short and the sample is under the effect of high temperatures for a longer period of time and therefore shows lower ICW after 24 hours of drying. Water migration primarily follows extracellular pathways during high temperature drying. As in the case of drying at 90°C (shown in Figure 2.14d), after 200 minutes there is no intracellular water. In the case of drying at 70°C, the migration primarily follows intracellular pathways initially (until 100 minutes) but primarily extracellular pathways in the last 300 minutes. In between, the migration is dominated by both intracellular and extracellular pathways. Similar results were observed in the case of drying eggplant at 90°C (shown in Figure 2.15).

Bioelectrical impedance analysis in microwave heating of potatoes

Microwaves heat more rapidly and possibly more uniformly, which should lead to differences in ICW during the heating process. In microwave heating of a potato sample, ICW remained constant until the temperatures were below 62°C and then declined sharply to 40% after 2 minutes of heating (as shown in Figure 2.16b). Microwave heating is rapid and cell membranes at high temperatures do not rupture instantaneously. Therefore, by the time most cell membranes rupture inside the potato, the sample temperature rises to 62°C. This explains why cell membrane rupture is observed at higher temperature than when drying. As shown in Figure 2.16a, moisture content does not change much during the 2 minutes of microwave heating, and the ICW drops to 40%. Therefore, initially (in the first two minutes) the moisture migration proceeds through both intracellular and extracellular pathways but the amount of water

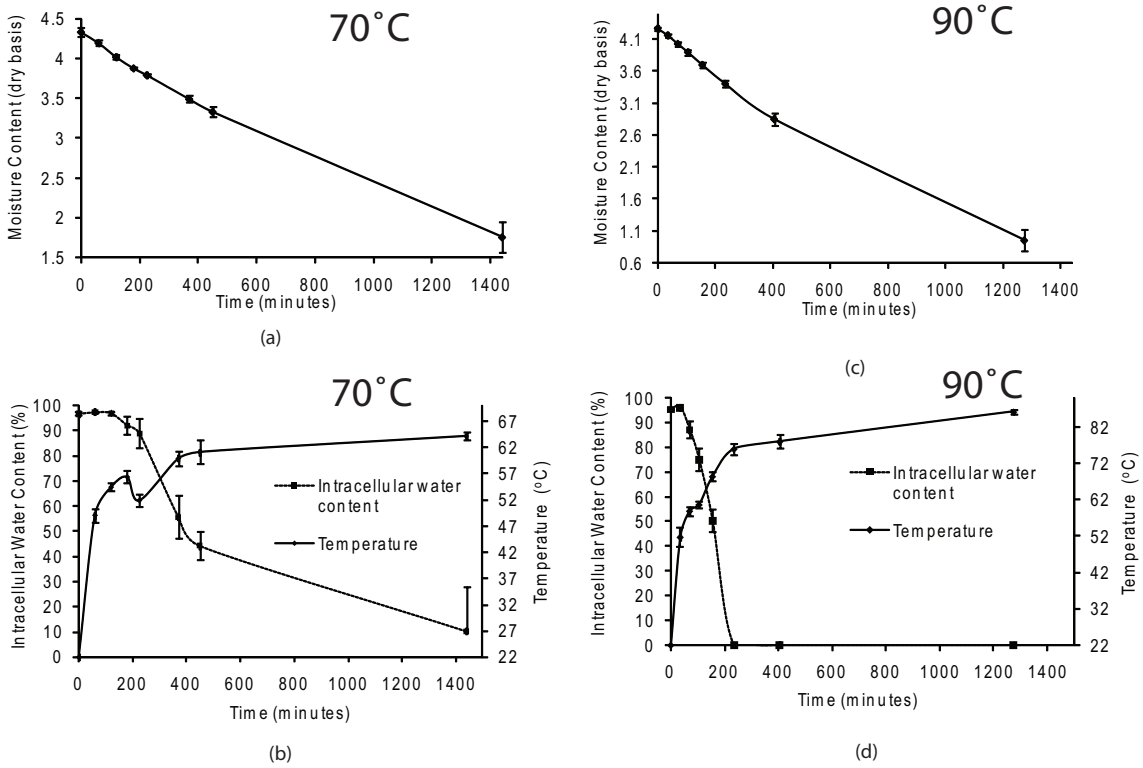

Figure 2.14: Moisture content (kg water/ kg dry weight) versus time for drying of potato slice at a) 70°C and c) 90°C. Intracellular water content(%) and core temperature versus time for drying of potato slice at at b) 70°C and d) 90°C.

lost during this time is less than 5%. In the later stages of microwave heating (after 2 minutes and not shown in the figure), when most of the moisture loss takes place, the cell membranes are damaged and the water is released into the matrix, leading to an extracellular pathway. Note that, at a temperature of 62°C, pressure generated due to evaporation from microwave heating is unlikely to have any significant effect on cell membrane rupture.

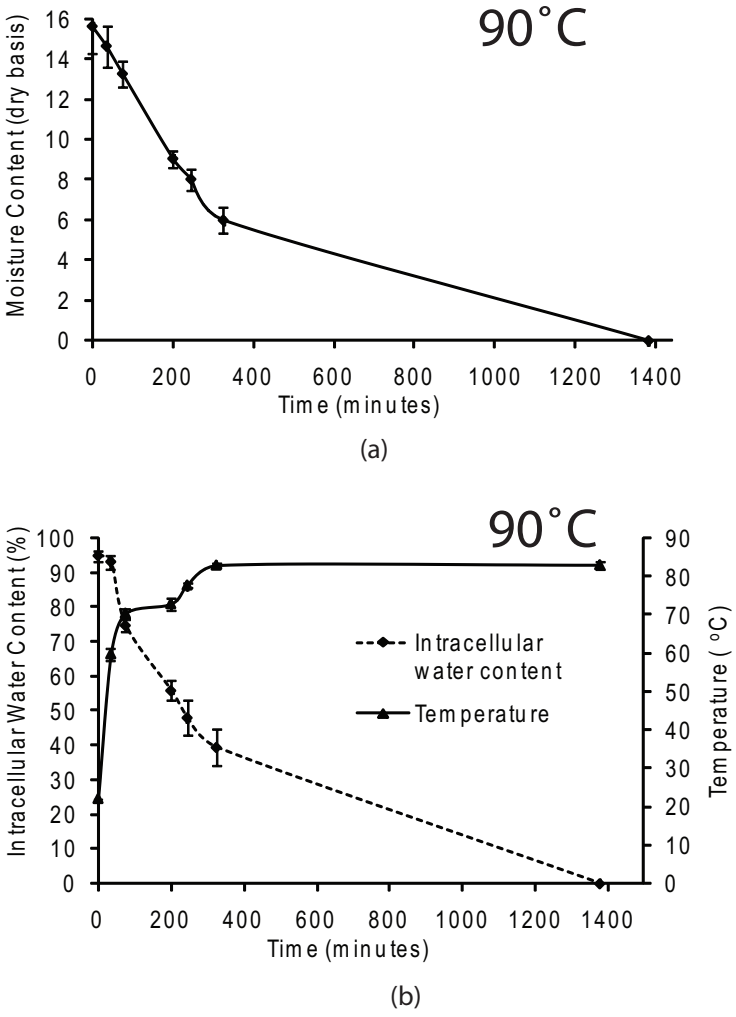

Figure 2.15: (a) Moisture content (kg water/ kg dry weight) and (b) Intracellular water content(%) and core temperature versus time for drying of eggplant slice at 90°C.

2.4.5 A summary of where the water is

Based on the porosimetry and bioimpedance analyses, it can be concluded that most of the water is not in the pores but in the cells. In fact, more than 90% of the water inside the potato tissue is intracellular at 22°C. At temperatures in the range of 52–60°C, the cell membrane is ruptured (intracellular water content

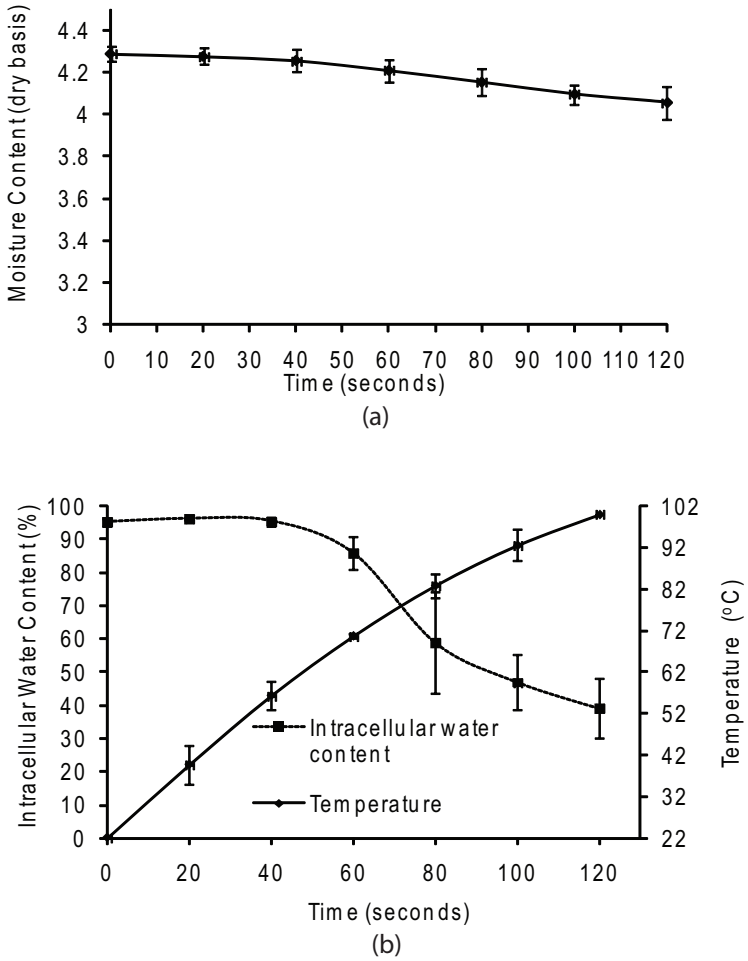

Figure 2.16: (a) Moisture content (kg water/ kg dry weight) and (b) Intracellular water content(%) and core temperature versus time for drying of potato slice during microwave heating.

decreases drastically) and water is released into the extracellular matrix. This conclusion is consistent with our porosimetry measurements where flow did not occur at the lower temperatures for very high pressures. In carrots, for example, the pressure required to rupture cell walls and cell membranes is 3 MPa [39] and the pressures used (0.7 MPa) in our capillary pressure and pore size distribution measurements were not sufficient to rupture the cell walls and cell membranes and drive out the intracellular water. Although one obvious pos-

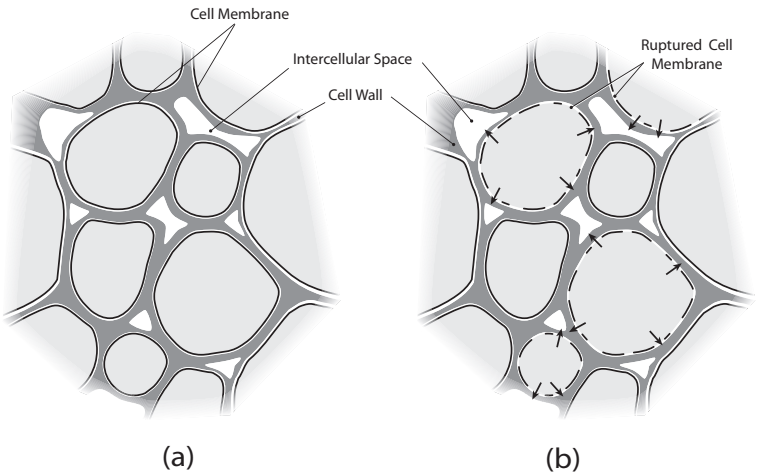

Figure 2.17: Schematic showing the cell membrane structure at a) temperatures below 52ºC (low temperatures); b) temperatures above 52ºC (high temperatures). At low temperatures, the moisture migration faces resistance from cell membranes, cell walls and intercellular spaces. At high temperatures, the cell membrane is ruptured. The moisture migration faces resistance from cell walls and intercellular spaces.

sibility is to repeat the pressure-driven flow experiments for potatoes at higher temperatures, the available instrument does not permit this measurement due to the softness of the potato at higher temperatures. In the next two sections, we discuss the implications of the location of water on its transport.

2.4.6 Water transport at low temperatures: Cell membrane is intact

The main source of water in a tissue is the cell. As shown in the experiments with BIA, more than 90% of the water inside potato tissue is intracellular at 22°C. At low temperatures (between 22°C and 50°C), the cell membranes remain intact and the transport of water out of the tissue involves migration

through both the cells and extracellular space. The main pathway, as shown in Figure 2.17a, can be described in terms of water moving from inside the cells through the cell membranes and then the cell walls into the intercellular space. This moisture transport takes place due to the gradient of water potential between cells and the intercellular spaces. The migrating moisture meets resistance from the cell membranes, cell walls and the intercellular spaces—whichever offers maximum resistance controls the transport.

Next, we compute the flux of water from inside the cell to the outside. The water potential (the driving force for water transport) inside and outside the cell can be expressed as

$$\begin{aligned} \phi_{w,intra} &= \phi_{w,0} + RT \ln(a_{w,intra}) \\ \phi_{w,extra} &= \phi_{w,0} + RT \ln(a_{w,extra}) \end{aligned} \tag{2.16}$$

Therefore, the water potential difference driving the flow of water from inside the cell to outside is given by

$$\triangle \phi_w = RT \ln(a_{w,intra}) - RT \ln(a_{w,extra}) \tag{2.17}$$

The relationship of water activity, a_w, to moisture content at constant temperature is known as a moisture isotherm and is readily available for many different food materials. The difference in pressure due to the water potential difference can be expressed as [8]:

$$\triangle p_w = \frac{RT}{V_w} \ln(a_{w,intra}) - \frac{RT}{V_w} \ln(a_{w,extra}) \tag{2.18}$$

where p_w is referred to as capillary pressure in the food literature but is essentially the lumped effect of all the surface forces acting on the fluid (discussed in section 2.2.1). Assuming Darcy's flow, the water flux through the tissue can be

written as

$$J_w = -\rho_w \frac{k_{eff}}{\mu_w} \frac{\triangle p_w}{\triangle x} \tag{2.19}$$

where k_{eff} is the effective permeability through the tissue (a lumped parameter including the effect of transport through cell walls, cell membranes and intercellular spaces). Equation 2.19 is analogous to the water flux equation, $J_w = \rho_w L_w \, (\triangle p_w)$, commonly used in the plant physiology field. The relationship between hydraulic conductivity (L_w used in plant physiology literature) and permeability (k used in this manuscript) can be written as:

$$L_w = \frac{k_{eff}}{\mu_w \triangle x} \tag{2.20}$$

Next, we compute the individual permeabilities ($L_w \mu_w t$ or k) offered by cell walls, cell membranes and intercellular spaces to migrating moisture. The literature has recorded only a small amount of permeability (k) data for water through various biological tissues, cell walls, and cell membranes. In *tissues*, permeability is reported to be on the order of 10^{-18} m^2 for potato and beef [15] and in the range of 10^{-18} m^2 to 10^{-16} m^2 for ground beef [16]. Based on our interpretation of the measurement techniques used in these studies, we strongly feel that these data (for potato and beef) represent permeability through the largest of the pores in the intercellular space. For *cell walls*, permeability in fruits and vegetables is not available but permeability of water through cell walls of spruce heartwoods was found to be between 4.03×10^{-21} m^2 and 67.5×10^{-21} m^2 [42], which can be representative of the values in fruits and vegetables because both are plant cells and the cell walls exhibit similar structure. The value of 5×10^{-20} m^2 found for Nitella (a plant) cell walls (converted from $L_w = 30$ μm min^{-1} atm^{-1} in [43] using Eq. 2.20 and thickness of cell wall as 10^{-5} m) is in the same range observed by [42] for spruce heartwoods. For *cell membranes*, the permeability for potato cells has been reported as 10^{-24} m^2

(converted from $L_w = 10^{-13}$ m s^{-1} Pa^{-1} in [44] using Eq. 2.20 and thickness of cell membrane as 10^{-8} m). Because the cell membrane exhibits three orders of magnitude lower permeability, it is likely to be the controlling resistance to transport at lower temperatures.

In continuum mechanics treatment of flow in an unsaturated porous media, flux given by Eq. 2.19 is rewritten in terms of a concentration gradient as (see, e.g., [45])

$$\begin{aligned} J_w &= -\rho_w \frac{k_{eff}}{\mu_w} \frac{\triangle p_w}{\triangle c_w} \frac{\triangle c_w}{\triangle x} \\ &= -D_w \nabla c_w \end{aligned} \tag{2.21}$$

where D_w is the capillary diffusivity (not molecular diffusivity) of water through the cell membrane and, from Eq. 2.21, it can be written as

$$D_w = \rho_w \frac{k_{eff}}{\mu_w} \frac{\triangle p_w}{\triangle c_w} = \rho_w \frac{k_{eff}}{\mu_w} \frac{\partial p_w}{\partial c_w} \tag{2.22}$$

In practice, D_w is treated as an effective diffusivity, that includes all transport mechanisms, including capillarity. Equation 2.22 shows that D_w depends on the permeability. Based on the discussion in the previous paragraph, that cell membrane permeability is the controlling resistance for low temperature drying (since the cell membranes are not ruptured at lower temperatures), the relevant permeability in moisture diffusivity, D_w, is the cell membrane permeability. Using the moisture isotherm data for potato tissue [45] and the cell membrane permeability of potato tissue [44], the diffusivity is computed (using Eq. 2.22) to be on the order of 10^{-11} m^2/s. Experimentally measured diffusivity of water through potatoes is on the order of 10^{-11} m^2/s for air drying at 30°C [46], showing the same order of magnitude as our predicted results. At this temperature, cell membranes are intact and the diffusivity value obtained corresponds to the intracellular pathway.

2.4.7 Water transport at high temperatures: Cell membrane is destroyed

At high temperatures, cell membranes rupture and release water into the extracellular space (schematic in Figure 2.17b) and therefore the transport of water to the outside occurs predominantly through the extracellular space. Applying Darcy's law in the intercellular space, the water flux can be written as

$$J_w = -\rho_w \frac{k_{out}}{\mu_w} \frac{\triangle p_w}{\triangle x} \tag{2.23}$$

Therefore, similar to Eq. 2.22, D_w for migration at high temperatures can be written as

$$D_w = -\rho_w \frac{k_{out}}{\mu_w} \frac{\partial p_w}{\partial c_w} \tag{2.24}$$

The main difference between the diffusivity value at high temperature and that at low temperature is found in the corresponding permeability values. For high temperature, the permeability is that of intercellular spaces, approximated from literature studies as 10^{-18} m^2 (see discussion in section 4.6), in contrast with the much lower value of 10^{-24} m^2 for low temperatures discussed in the previous section, where it is attributed to permeability of cell membranes. The diffusivity calculated for a permeability of 10^{-18} m^2 is on the order of 10^{-7} m^2/s. The water diffusivity in potato tissues has been reported as 10^{-9} m^2/s during drying at 70 °C [47]. At this temperature, around 20–30% of water may still be intracellular (as shown in Figure 2.14b), which explains the reduced diffusivity value observed in the experiments. Drying at 70 °C is in the mid range and perhaps explains the diffusivity of 10^{-9} m^2/s between the two extremes.

2.5 Conclusions

Transport of water in a cellular tissue depends on its pathway (intracellular vs. extracellular), which in turn depends on temperature. Using a combination of permeability measurement, pore size distribution analysis and bioimpedance analysis, it is shown that water in a cellular tissue is mostly intracellular at lower temperatures when cell membranes are intact. This explains why very little water ($\sim$ 2%) can be pushed out by applying pressures up to 1.5 MPa. Using bioelectrical impedance analysis, it was observed that $\sim$ 95% of the water is intracellular in potato tissue at lower temperatures, and this water becomes extracellular at temperatures above 52°C when the cell membranes rupture. Also, data in the literature shows that cell membrane permeabilities are at least three orders of magnitude lower than those in the cell walls and other extracellular space. Therefore, when drying at lower temperatures, cell membranes are not damaged, the pathway of moisture transport is intracellular, and resistance to transport is dominated by cell membranes—resulting in a lower moisture diffusivity value. During drying at high temperatures, cell membranes are damaged and the moisture transport pathway is primarily extracellular (through intercellular space and the lacunae created by killed cells), which offers lower resistance, leading to a higher moisture diffusivity value. The difference in diffusivity for the two pathways has been estimated to be three orders of magnitude, consistent with experimental data reported in the literature. Thus, transport properties measured or predicted at low temperatures cannot be used for high temperatures because the processes correspond to different moisture migration pathways.

Acknowledgment

This research was partially supported by the United States Department of Agriculture Regional Project NC 1023 and the United States Department of Agriculture National Integrated Food Safety Project 2004-51110-02167. The authors would like to thank Professor Apostolos Kantzas in Chemical and Petroleum Engineering, University of Calgary, and Dr. Akshaya Jena in Porous Materials Inc., Ithaca, for assistance with the discussion of capillary pressure measurement techniques. The authors would also like to thank Josh Powers and Terry Murray in Porous Materials Inc., Ithaca, and Robert Schindelbeck in Crop and Soil Sciences, Cornell University, for all their help during the experiments.

BIBLIOGRAPHY

[1] Ateba, P. and Mittal G.S., 1994, Modeling the Deep-Fat Frying of Beef Meatballs, *International Journal of Food Science and Technology*, 29(4): 429-440.

[2] Ikediala, J.N., Correia, L.R., Fenton, G.A. and BenAbdallah N., 1996, Finite element modeling of heat transfer in meat patties during single-sided pan-frying, *Journal of Food Science*, 61(4): 796-802.

[3] King, C.J., 1968, Rates of moisture sorption and desorption in porous, dried foodstuffs, *Food Technology*, 22(4): 165-171.

[4] Rotstein, E., 1987, The prediction of diffusivities and diffusion-related transport properties in the drying of cellular foods, *Physical properties of Foods 2*, 131-145.

[5] Ni, H. and Datta, A.K., 1999, Moisture, oil and energy transport during deep-fat frying of food materials, *Food and Bioproducts Processing*, 77(C3): 194-204.

[6] Yamsaengsung, R. and Moreira, R.G., 2002, Modeling the transport phenomena and structural changes during deep fat frying - Part 1: model development, *Journal of Food Engineering*, 53(1): 1-10.

[7] Halder, A., Dhall, A. and Datta, A.K., 2007, An improved, easily implementable, porous media based model for deep-fat frying - Part I: Model development and input parameters, *Food and Bioproducts Processing*, 85(C3): 209-219.

[8] Gee, G.W., Campbell, M.D., Campbell, G.S. and Campbell, J.H., 1992, Rapid measurement of low soil water potentials using a water activity meter, *Soil Science Society American Journal*, 56: 1068-1070.

[9] Conca, J.L. and Wright, J., 1998, The UFA method for rapid, direct measurements of unsaturated transport properties in soil, sediment, and rock, *Australian Journal of Soil Research*, 36, 291-315.

[10] Khanzode, R.M., Vanapalli, S.K. and Fredlund, D.G., 2002, Measurement of soil-water characteristic curves for fine-grained soils using a small-scale centrifuge, *Canadian Geotechnical Journal*, 39(5): 1209-1217.

[11] Hassler, G.L. and Brunner, E., 1945, Measurement of Capillary Pressures in Small Core Samples, *Transactions of the American Institute of Mining and Metallurgical Engineers*, 160, 114-123.

[12] Reitsma, S. and Kueper, B.H., 1994, Laboratory Measurement of Capillary-Pressure Saturation Relationships in a Rock Fracture, *Water Resources Research*, 30(4): 865-878.

[13] Chen, Z.A. and Ruth, D.W., 1997, Ramp-up centrifugation of capillary pressure experiments, *AIChE Journal*, 43(8): 2133-2136.

[14] Spolek, G.A. and Plumb O.A., 1981, Capillary pressure in softwoods, *Wood Science Technology*, 15:189-199.

[15] Datta, A.K., 2006, Hydraulic permeability of food tissues, *International Journal of Food properties*, 9: 767-780.

[16] Oroszvari, B.K., Rocha, C.S., Sjoholm, I. and Tornberg, E., 2006, Permeability and mass transfer as a function of the cooking temperature during the freezing of beefburgers, *Journal of Food Engineering*, 74(1): 1-12.

[17] Farkas, B.E. and Singh, R.P., 1991, Physical-Properties of Air-Dried and Freeze-Dried Chicken White Meat, *Journal of Food Science*, 56(3): 611-615.

[18] Kassama, L.S. and Ngadi, M.O., 2004, Pore development in chicken meat during deep-fat frying, *Lebensmittel-Wissenschaft Und-Technologie-Food Science and Technology*, 37(8): 841-847.

[19] Datta, A.K., Sahin, S., Sumnu, G. and Keshin, S.O., 2007, Porous media characterization of breads baked using novel heating modes, *Journal of Food Engineering*, 79(1): 106-116.

[20] Lukaski, H.C., Johnson, P.E., Bolonchuk, W.W. and Lykken, G.L., 1985, Assessment of fat-free mass using bioelectrical impedance measurements of the human body, *Journal of Clinical Nutrition*, 41: 810-817.

[21] Matthie, J.R., Withers, P.O., Van Loan, M.D. and Mayclin, P.L., 1992, Development of a commercial complex bio-impedance spectroscopic (CBIS) system for determining intracellular water (ICW) and extracellular (ECW) volumes, *Proceedings of the 8th International Conference on Electrical Bioimpedance Kuopio Finland 1992, Kuopio, Finland, University of Kuopio*, 203-205.

[22] Zhang, M.I.N., Stout, D.G. and Willison, J.H.M., 1990, Electrical-impedance analysis in plant-tissues - symplasmic resistance and membrane capacitance in the Hayden model, *Journal of Experimental Botany*, 41(224): 371-380.

[23] Cox, M.A., Zhang, M.I.N. and Willison, J.H.M., 1993, Apple bruise assessment through electrical-impedance measurements, *Journal of Horticultural Science*, 68(3): 393-398.

[24] Harker, F.R. and Dunlop, J., 1994, Electrical impedance studies of nectarines during coolstorage and fruit ripening, *Postharvest Biology and Technology*, 4, 125-134.

[25] Dejmek, P. and Miyawaki, O., 2002, Relationship between the electrical and rheological properties of potato tuber tissue after various forms of processing, *Bioscience Biotechnology and Biochemistry*, 66(6): 1218-1223.

[26] Wu, L., Ogawa, Y. and Tagawa, A., 2008, Electrical impedance spectroscopy analysis of eggplant pulp and effects of drying and freezing-thawing treatments on its impedance characteristics, *Journal of Food Engineering*, 87(2): 274-280.

[27] Hassanizadeh, S.M. and Gray, W.G., 1993, Thermodynamic basis of capillary pressure in porous media, *Water Resources Research*, 29(10): 3389-3405.

[28] Gardener, W.R., 1956, Calculation of capillary conductivity from pressure plate outflow data, *Soil Science Society of America Proceedings*, 20: 317-320.

[29] Bear, J., 1972, Dynamics of fluids in porous media, American Elsevier Publishing Company, Inc., New York.

[30] Gupta, N. and Jena, A., 2001, Determining the pore structure of individual layers of multi-Layered ceramic composites, *Ceramic Industry*, 151(2): 24-29.

[31] Cole, K.S., 1972, Membranes, ions and impulses: A chapter of classical biophysics. Los Angeles: UCLA press.

[32] Hanai, T., 1968, Electrical properties of emulsions, In: Emulsion Science, edited by P.H. Sherman. London: Academic, p. 354-477.

[33] De Lorenzo, A., Andreoli, A., Matthie, J. and Withers, P., 1997, Predicting body cell mass with bioimpedance by using theoretical methods: a technological review, *Journal of Applied Physiology*, 82(5): 1542-1548.

[34] Dainty J. and Hope A.B., 1961, The electric double layer and the Donnan equilibrium in relation to plant cell walls, *Australian Journal of Plant Physiology*, 14, 541-551.

[35] Hudson, D.E., 1975, Relationship of Cell-Size, Intercellular Space, and Specific Gravity to Bruise Depth in Potatoes, *American Potato Journal*, 52(1): 9-14.

[36] Honikel, K.O. and Hamm, R., 1994, Measurement of water-holding capacity and juiciness, Quality attributes in meat, poultry and fish products, Blackie Academic and Professional Publication, 125-161.

[37] Nobel, P.S., 2009, Cells and diffusion, Physicochemical and Environmental Plant Physiology, 4-th edition, 3-42.

[38] Asquith, M.H., Kirk, E., Kirkland, M., Morrey, S.M., Ormerod, A.P., Ralfs, J.D., Sharp, D.G. and Sidebottom, C.M., January 30 2007, Freezing vegetables, US Patent 7169426.

[39] Carpita, N.C., 1985, Tensile strength of cell walls of living cells, *Plant Physiology*, 79: 485-488.

[40] Cornish, B.H., Thomas, B.J. and Ward, L.C., 1998, Effect of temperature and sweating on bioimpedance measurements, *Applied Radiation and Isotopes*, 49(5/6): 475-476.

[41] Leuchtag, H.R., 1995, Fit of the dielectric anomaly of squid axon membrane near heat-block temperature to the ferroelectric Curie-Weiss law, *Biophysical Chemistry*, 53(3): 197-205.

[42] Palin, M.A. and Petty, J.A., 1983, Permeability to water of the wood cell wall and its variation with temperature, *Wood Science Technology*, 17: 187-193.

[43] Kamiya, N., Tazawa, M. and Takata, T., 1962, Water permeability of the cell wall in Nitella, *Plant and Cell Physiology*, 3: 285-292;

[44] Rotstein, E. and Cornish, A.R.H., 1978, Influence of cellular membrane permeability on drying behavior, *Journal of Food Science*, 43: 926-939.

[45] Ratti, C., Crapiste, G.H. and Rotstein, E., 1989, A New Water Sorption Equilibrium Expression for Solid Foods Based on Thermodynamic Considerations, *Journal of Food Science*, 54(3): 738-742.

[46] Saravacos, G.D., 1967, Effect of drying method on the water sorption of dehydrated apple and potato, *Journal of Food Science*, 32: 81-84

[47] Mulet, A., 1994, Drying modeling and water diffusivity in carrots and potatoes, *Journal of Food Engineering*, 22(1-4): 329-348.

CHAPTER 3

A COMPREHENSIVE TRANSPORT MODEL IN POROUS MEDIA WITH PHASE CHANGE

3.1 Abstract

Background. Fundamental, physics-based modeling of complex food processes is still in the developmental stages. This lack of development can be attributed to complexities in both the material and the transport processes. Society has a critical need for automating food processes (both in industry and at home), while improving quality and making food safe. Product, process and equipment design in food manufacturing requires the more detailed understanding of food processes that is possible only through physics-based modeling. The objectives of this paper are to: 1) develop a general multicomponent and multiphase modeling framework that can be used for different thermal food processes and can be implemented in commercially available software (for wider use); and 2) apply the model to the simulation of deep-fat frying and hamburger cooking processes, and validate the results.

Model details. Treating food material as a porous medium, heat and mass transfer inside such material during its thermal processing is described using equations for mass and energy conservation that include binary diffusion, capillary and convective modes of transport, physicochemical changes in the solid matrix that include phase changes such as melting of fat and water, and evaporation/ condensation of water. Evaporation/condensation is considered to be distributed throughout the domain and is described by a novel non-equilibrium formulation whose parameters have been discussed in detail.

Results. Two complex food processes, deep-fat frying and contact heating of a hamburger patty, representing a large group of common food thermal processes with similar physics, have been implemented using the modeling framework. The predictions are validated with experimental results from the literature. As the food (a porous hygroscopic material) is heated from the surface, a zone of evaporation moves from the surface to the interior. Mass transfer due to the pressure gradient (from evaporation) is significant. As temperature rises, properties of the solid matrix change and the phases of frozen water and fat become transportable, thus affecting the transport processes significantly.

Conclusion. Because the modeling framework is general and formulated in a manner that makes it implementable in commercial software, it can be very useful in computer-aided food manufacturing. Beyond its immediate applicability in food processing, such a comprehensive model can be useful in medicine (for thermal therapies such as laser surgery), soil remediation, nuclear waste treatment and other fields where heat and mass transfer take place in porous media with significant evaporation and other phase changes.

Keywords: multiphase, porous-media, evaporation, non-equilibrium

Nomenclature

b	number of components in the solid phase
c	concentration, kg m^{-3}
c_p	specific heat capacity, J $kg^{-1}K^{-1}$
C_g	molar density, kmol m^{-3}
$D_{eff,g}$	effective gas diffusivity, m^2s^{-1}
D	diffusivity, m^2 s^{-1}
$\mathbf{g}$	acceleration due to gravity, kg m^{-3}
h	heat transfer coefficient, W m^{-2} K^{-1}
h_m	mass transfer coefficient of vapor, m s^{-1}
$\dot{I}$	volumetric evaporation rate, kg m^{-3} s^{-1}
k	thermal conductivity, W m^{-2} K^{-1}
k^p	permeability, m^2
K	non-equilibrium evaporation constant, s^{-1}
$K_{i,j}$	non-equilibrium constant for interphase mass transfer from i to j, s^{-1}
L	length scale, m
m	overall mass fraction
M_a, M_v	molecular weight of air and vapor
n	total number of phases
$\mathbf{n}$	total flux, kg m^{-2} s^{-1}
P	gas pressure, Pa
p_v	vapor pressure, Pa
$\mathbf{q}$	heat flux, J m^{-2} s^{-1}
R	universal gas constant, J $kmol^{-1}$ K^{-1}
$\dot{R_{i,j}}$	rate of mass transfer from i to j, kg m^{-3} s^{-1}
S	saturation

t	time, s
T	temperature
u	velocity, m s^{-1}
V	volume, m^3
x	mole fraction

Greek Symbols

ρ	density, kg m^{-3}
λ	latent heat of vaporization, J kg^{-1}
ω_v, ω_a	mass fraction of vapor and air in relation to total gas
ϕ	porosity
μ	dynamic viscosity, Pa s

Subscripts

amb	ambient
a, g, o, s, v, w	air, gas, oil, solid, vapor, water
bw, bf	water, fat in solid phase
cap	capillary
eff	effective
eq	equilibrium
f	final
i	i^{th} liquid phase, initial
in	intrinsic
ini	initial
j	j^{th} component in solid phase
0	at time $t = 0$

r	relative, residual
sat	saturation
$surf$	surface
T	temperature
tot	total

3.2 Introduction

Mathematical modeling has not been able to contribute as much to the development of food processing industries as it has with respect to the mechanical and chemical industries. The primary reason for this is that foods are complex and non-homogenous, and the physics that could explain what happens during processing is still not clearly established. The time and cost involved limit the number of experiments that can be done to achieve this. Looking at recent trends towards the automation of food processes and production of minimally processed healthier foods, it can be said that there is a need to develop accurate mathematical models of these food processes which can be extensively used for equipment design or to ensure food safety. The development of fundamental physics-based models of food processes is not trivial, as it requires physical as well as mathematical insight into the material and the process.

In food systems, an enormous range of thermal processes can be viewed as involving transport of energy, moisture and, in some cases, fat through a hygroscopic porous medium. Examples include extraction, drying, deep fat frying, microwave heating, meat roasting and rehydration. In the vast majority of food systems, proteins or carbohydrates form a porous skeleton which has water and/or fat physically and chemically bound to it. During heating, water and

fat can transport inside the solid matrix or can be released into the pore space and then transported through the porous medium. Other important phenomena that can occur are rapid evaporation due to intensive heating, the melting of ice or fat during the processing of frozen food, and shrinkage due to physicochemical changes in the porous matrix. There is no single model that considers all of these physics together and that can also be implemented in a software application for wide usage.

The existing models of thermal processes can be broadly divided into four groups. The first group consists of totally lumped models for heat and mass transport that do not include any important physics [1, 2, 3, 4, 5]. Such models are based entirely on empirical data, are suited for a specified product and processing condition and, therefore, cannot be used for even a slightly different situation. The second group consists of slightly improved models that assume conductive heat transfer for energy and diffusive transport for moisture, solving a transient diffusion equation using experimentally determined effective diffusivity [6, 7, 8, 9, 10]. Lumping together all modes of water transport as diffusion cannot be justified under all situations, especially when other phenomena such as pressure-driven flow due to intensive heating or transport due to physicochemical changes in the porous medium become important. Also, the use of effective diffusivity does not yield insights into the prevalent transport mechanisms. These models might provide good matches with experimental results but they cannot be generalized to other conditions.

The third group of models, with a significantly improved formulation compared with those of simple diffusion models, assumes a sharp moving boundary separating the dry and the wet region (e.g., deep-fat frying models [4, 3, 13]).

This assumption is analogous to that made in freezing and thawing models of a pure material [14], where a sharp front separates the frozen and unfrozen regions. In contrast to sharp boundary models, distributed evaporation models assume evaporation occurs over a zone rather than at an interface [15, 13, 13]. In a given situation, it is possible that the real evaporation zone is very narrow, closer to the sharp interface, and that a distributed evaporation formulation will, in fact, predict such narrow evaporation zone.

Evaporation of water in intensive heating food processes, such as deep-fat frying and baking, has usually been implemented using an equilibrium formulation wherein liquid water present in the food is always assumed to be in equilibrium with water vapor present in the pore space [15, 13, 18]. There's no detailed study of this equilibrium assumption for hygroscopic materials such as food. Only qualitative description of the conditions under which either equilibrium or non-equilibrium assumptions can hold is available [23]. As will be explained later, a non-equilibrium formulation that can also be used to enforce equilibrium is a more general approach and appears to be the obvious alternative. Furthermore, significant effort is required to implement the equations resulting from an equilibrium formulation in the framework of most commercial software, whereas implementation of a non-equilibrium formulation is straight forward.

Overall, accurate models of food processes, which include all the physics, still do not exist. Multiphase porous media models have been used with success in other fields and applications to describe physics that is similar to that involved in food processing. A multiphase porous media approach with conservation equations for relevant components, appropriately including the effect

of various phenomena particular to food, has been developed for some food applications [5, 17, 14, 18]. However, none of these models is general enough to be applied to many different processes. Moreover, these models have been formulated in such a way that they are very difficult to manipulate and implement in commercial software, and have been solved by user-developed codes. These codes are either publicly unavailable, have limited capabilities or are difficult to use by anyone other than the creator. A general framework applicable to the majority of food processes, which is implementable in commercial software, has not been developed yet. This development is not trivial and requires significant reformulations or in some cases developing a new model altogether. The present study aims to do this.

Some of the physics involved in food processes can be seen in other applications such as geoscience [23], nuclear waste storage and management [24], groundwater contamination [25], [26]), and thermal treatment of tumors or drug delivery in bio-medical engineering [27]. However, food processing applications, involving thermal treatment of heterogeneous materials, are extremely complex. A fundamental physics-based model developed for food processes, which accounts for all the relevant phenomena, can be applied to other fields with simplifications.

The objectives of this study are: (1) to develop a general multiphase model for hygroscopic biological materials that can be used for various thermal processes and can be implemented in commercially available software; (2) to apply the model to simulate deep-fat frying and hamburger cooking processes and validate the results.

The outline of the paper is as follows: A comprehensive mathematical

model, which can be used to simulate a large number of thermal processes, is presented first, followed by detailed discussion of a non-equilibrium approach to implementing evaporation/condensation phase change. Two food processes, deep-fat frying of a restructured potato slab and contact heating of a hamburger patty, are modeled using the set of equations developed to show the model's effectiveness in solving different types of thermal food processes. The paper concludes with a discussion of the importance of this comprehensive modeling framework in food processing.

3.3 Mathematical model

A multiphase porous media model is developed that describes heat and mass transfer inside a food material during thermal processing. Mass and energy conservation equations are developed that, depending on the process, may include binary diffusion, capillary and convective modes of transport, the effects of physicochemical changes in the solid matrix on transport, and phase changes such as melting and evaporation-condensation. Evaporation/condensation is assumed to be distributed throughout the domain.

3.3.1 Problem description

The schematic description of a meat matrix as a porous medium is shown in Fig 1. The material is assumed to be homogenous. The first and most important step is to identify the distinct phases that are important and significantly affect transport. There can be three types of such phases: solid, liquid and gas. The

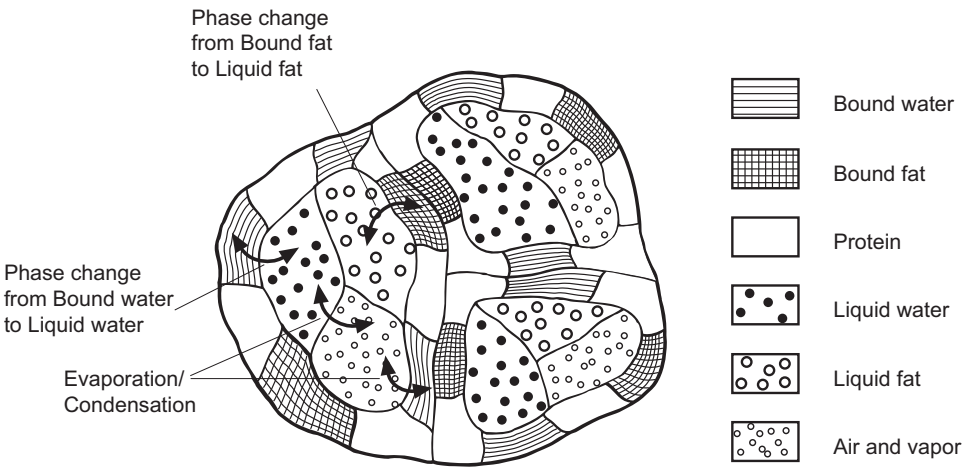

Figure 3.1: Schematic of a porous food material showing mass transfer between various phases

solid phase in food materials comprises a carbohydrates or proteins matrix with water and, possibly, fat physically and chemically bound to it. So, in all, there can be three components in the solid phase, i.e., the solid matrix, bound water and bound fat. The solid matrix is non-transportable. However, the bound water and fat can transport inside the matrix, even while remaining bound to the solid. In foods, the capacity of the solid matrix to hold water or fat (known as water [or fat] holding capacity in the food science literature) changes with temperature. Usually, as temperature rises, water (or fat) is gradually released from the matrix into the pore space. Thus, water (or fat) undergoes an interphase mass transfer from the solid phase to the pore liquid phase. Therefore, the mass balance of the solid phase is important where the phase change from solid to liquid is significant; otherwise, it can be ignored. In the pores, all immiscible liquids, such as fat and water, can be considered as separate liquid phases. The third and last type of phase is the gas phase. There cannot be more than one gas

phase, as gases are miscible and occupy the total available gas volume available to them. In most food applications, a gas phase is a mixture of air and water vapor.

3.3.2 Assumptions

The assumptions made while formulating this multiphase framework are: 1) All the phases (solid, liquids and gas) are in continuum; 2) local thermal equilibrium exists throughout the material between all phases; 3) pressure is shared by all phases, as the effects of capillary pressure have been included as diffusion terms [8, 13]; 4) there can be non-equilibrium between water in solid and water-vapor in gas phase, i.e., their concentrations are not given by the moisture isotherms; 5) deformation of the material during processing is not considered.

3.3.3 Governing equations

The mathematical model consists of conservation equations for all the phases and components discussed above. For the sake of generalization, we assume that there are n phases in all. Of these, there is one solid phase, one gas phase and $n-2$ liquid phases. There are b components inside the solid phase and two (vapor and air) inside the gas phase.

Mass balance equations

Porosity, ϕ, is defined as the fraction of the total volume occupied by pores, given by

$$\phi = \frac{V_g + \sum_{i=1}^{n-2} V_i}{V} \tag{3.1}$$

where V_i is the volume occupied by the i^{th} liquid phase in an elemental volume V. If, during a process, the solid matrix loses a bound fluid, such as water, then porosity, ϕ, does not remain constant. As the solid matrix loses water, the porosity increases. In such cases, porosity can be estimated as

$$\phi = 1 - \frac{V_s}{V} = 1 - \sum_{j=1}^{b} \frac{V_j}{V} = 1 - \sum_{j=1}^{b} \frac{c_j}{\rho_j} \tag{3.2}$$

where b is the number of components in the solid phase and c_j and ρ_j are the concentration and density of the j^{th} solid component, respectively. Here, it is assumed that the total volume of the solid can be estimated as the sum of the individual volumes of the solid phase components, with each component retaining its pure state density.

Saturation of a transportable phase is defined as the fraction of pore volume occupied by that particular phase:

$$\begin{aligned} S_i &= \frac{V_i}{\phi V} \\ S_g &= \frac{V_g}{\phi V} \end{aligned} \tag{3.3}$$

where i stands for any liquid phase. The summation of saturation of all transportable phases should lead to unity (Eq. 5.5).

The mass balance equation for a phase solves for saturation of the phase. There are $n-2$ liquid phases and one gas phase. So, $n-2$ mass balance equations

(Eq. 3.4) are solved to obtain the saturation (S_i) of each individual liquid phase. The saturation of gas, S_g, is calculated from Eq. 5.5:

$$\frac{\partial}{\partial t}(\phi \rho_i S_i) + \nabla \cdot \mathbf{n_i} = -\dot{R}_{i,j} - \dot{I} \tag{3.4}$$

$$S_g + \sum_{i=1}^{n-2} S_i = 1 \tag{3.5}$$

where $\dot{R}_{i,j}$ denotes interphase mass transfer from the i^{th} liquid phase to the j^{th} solid component. Similarly, $\dot{I}$ denotes the phase change from liquid water to water vapor.

The total flux of the liquid phase, $\mathbf{n_i}$, is due to the liquid pressure, $P - p_{i,cap}$, which is the difference between gas pressure and capillary pressure. This total flux term is given by Darcy's law [8] as:

$$\begin{aligned} \mathbf{n_i} &= -\rho_i \frac{k^p_{in,i} k^p_{r,i}}{\mu_i} \nabla (P - p_{i,cap}) \\ &= -\rho_i \frac{k^p_{in,i} k^p_{r,i}}{\mu_i} \nabla P + \rho_i \frac{k^p_{in,i} k^p_{r,i}}{\mu_i} \left(\frac{\partial p_{i,cap}}{\partial c_i} \nabla c_i + \frac{\partial p_{i,cap}}{\partial T} \nabla T \right) \end{aligned} \tag{3.6}$$

The first term in the right-hand side of the above equation represents flow due to gradients in gas pressure and is significant only in the case of intensive heating of food materials such as microwave heating, deep-fat frying and contact heating at high temperature. The second and third terms can be rewritten in terms of capillary diffusivity, $D_{i,cap}$, and diffusivity due to thermal gradients , $D_{i,T}$, given by:

$$D_{i,cap} = -\rho_i \frac{k^p_{in,i} k^p_{r,i}}{\mu_i} \frac{\partial p_{i,cap}}{\partial c_i} \tag{3.7}$$

$$D_{i,T} = -\rho_i \frac{k^p_{in,i} k^p_{r,i}}{\mu_i} \frac{\partial p_{i,cap}}{\partial T} \tag{3.8}$$

In most of the cases, the gas phase is a mixture of water vapor and air. Spatial variations in the concentration of these components during processing are obtained by solving the respective mass conservation equations in terms of their

mass fractions, ω_v and ω_a, with binary diffusion [7]:

$$\frac{\partial(\phi\rho_g S_g\omega_v)}{\partial t} + \nabla\cdot(u_g\rho_g\omega_v) = \nabla\cdot\left(\phi S_g\frac{C_g^2}{\rho_g}M_a M_v D_{eff,g}\nabla x_v\right) + \dot{I} \quad (3.9)$$

$$\omega_v + \omega_a = 1 \quad (3.10)$$

The concentration of components in the solid phase is determined by solving the mass conservation equation for each:

$$\frac{\partial c_j}{\partial t} = \nabla(D_{j,cap}\nabla c_j) + \nabla(D_{j,T}\nabla T) + \dot{R}_{i,j} \quad (3.11)$$

where $R_{i,j}$ is the rate of mass transfer from the liquid phase to the component j in the solid phase, $D_{j,cap}$ is the diffusivity due to concentration gradients and $D_{j,T}$ is the diffusivity due to temperature gradients. Details of $R_{i,j}$ are discussed later in the section in the discussion of phase change.

Therefore, $n-2$ number of Eq. 3.4, b number of Eq. 3.11, along with Eqs. 5.5, 5.10 and 5.11, constitute the set of $n+b+1$ equations from which the concentration variables c_1,c_2,...,c_b,S_1,S_2,...,S_{n-2},S_g, ω_v and ω_a can be found. Temperature and pressure at every point inside the material are determined by invoking gas phase mass conservation and energy conservation equations, as discussed later. Note, however, that there are additional unknowns in these equations for which auxiliary equations will be needed, as discussed later (Eq. 5.32 for the evaporation rate, $\dot{I}$, and Eq. 3.38 for the solid phase change rate, $\dot{R}$).

Momentum balance

The momentum balance equation for a phase solves for the velocity of that phase. In a porous medium with low permeabilities, Darcy flow is valid [8]. Therefore, Darcy's equation for each phase in porous media replaces the stan-

dard momentum conservation (Navier-Stokes) equation. However, some software applications do not support Darcy's law (Eq 4.5) directly and instead solve the modified Navier-Stokes equation (Eq. 4.8), which includes the Darcy's term, for momentum balance:

$$\frac{\partial((\phi S_i)\rho_i \mathbf{u_i})}{\partial t} + \nabla.((\phi S_i)^2 \rho_i \mathbf{u_i}\mathbf{u_i}) = -(\nabla P - \rho_i \mathbf{g}) - (\phi S_i)\frac{\mu_i}{k_{r,i}^p k_{in,i}^p}\mathbf{u_i} \tag{3.12}$$

Although Eq. 4.5 is different from Eq. 4.8 due to the additional terms, the inertial terms are shown to be negligible for low-permeability systems [30, 8], and Eq. 4.8 reduces to Eq. 4.5 for such systems. Solving Eq. 4.8 for each phase may involve numerous convergence issues as well as large computation times, and should be avoided when addressing low-permeability porous media problems. When there is no option in the software but to solve the Navier-Stokes equation, numerical complications can be reduced by assuming that all the transportable phases share the same pressure and velocity, thereby solving only one equation for the mixture. This is a simplified approach and may lead to erroneous results depending on the problem complexities.

Continuity equation to solve for pressure

The gas pressure, P, is calculated by solving the overall mass balance equation for the gas phase:

$$\frac{\partial}{\partial t}(\phi S_g \rho_g) + \nabla \cdot \mathbf{n_g} = \dot{I} \tag{3.13}$$

where

$$\mathbf{n_g} = -\rho_g \frac{k_{r,g}^p k_{in,g}^p}{\mu_g}\nabla P \tag{3.14}$$

The ideal gas law is used to relate gas phase density and pressure:

$$\rho_g = \frac{PM_g}{RT} \tag{3.15}$$

Pressure, P, is shared by all the phases (the capillary pressure of liquid phases have been included as diffusion). However, Eq. 5.13 cannot be used if saturation of the gas phase goes to zero in any region as pressure cannot be determined in the region— thus leading to the failure of the numerical solution (discussion follows). The gas phase can go to zero under various conditions, such as high condensation rate in a low porosity region or the accumulation of liquids due to favorable pressure gradients. One way to deal with the above problem is to prevent the gas phase from going to zero by forcing the gas phase saturation to a small value such that it does not affect the solution and at the same time does not require any further reformulations. The gas phase can be prevented from going to zero by introducing residual gas saturation or by giving high liquid capillary diffusivity values at low gas saturations [31]. Another method is to drop Eq. 5.13 from the system of equations and solve for pressure using the conservation equation for water. The latter is difficult to implement and used only in specialized porous media codes (e.g., TOUGH2 [32]).

Energy equation

Since thermal equilibrium is assumed to exist across all phases (e.g., all phases in a representative elemental volume have the same temperature), the energy balance equation of the mixture (Eq. 5.14) is solved to calculate T:

$$\rho_{eff} c_{p,eff} \frac{\partial T}{\partial t} + (c_p \mathbf{n})_{fluid} \cdot \nabla T = \nabla \cdot (k_{eff} \nabla T) - \lambda \dot{I} \tag{3.16}$$

The properties of the mixture are obtained by averaging those of the pure components, weighted by their mass or volume fractions (volume fraction is also

referred to as saturation in this manuscript) as appropriate:

$$\rho_{eff} = \sum_{j=1}^{b} c_j + \phi \left(\sum_{i=1}^{n-2} S_i \rho_i + S_g \rho_g \right) \tag{3.17}$$

$$c_{p,eff} = m_g(\omega_v c_{p,v} + \omega_a c_{p,a}) + \sum_{i=1}^{n-2} m_i c_{p,i} + \sum_{j=1}^{b} m_j c_{p,j} \tag{3.18}$$

$$(c_p \mathbf{n})_{fluid} = \sum_{i=1}^{n-2} \mathbf{n_i} c_{p,i} + \rho_g \mathbf{u_g} (\omega_v c_{p,v} + \omega_a c_{p,a}) \tag{3.19}$$

$$k_{eff} = \left(\sum_{j=1}^{b} \frac{c_j}{\rho_j} k_j \right) + \phi \left(\sum_{i=1}^{n-2} S_i k_i + S_g(\omega_v k_v + \omega_a k_a) \right) \tag{3.20}$$

Note that, in the energy equation, the melting of ice and fat is handled using the apparent specific heat method [33], in which the latent heat of fusion is incorporated by modifying the specific heat in the temperature range of melting.

3.3.4 Boundary conditions

Pressure at the boundary (which is open to the outside environment) in most food processes is the ambient pressure; hence the boundary condition for the continuity equation (Eq. 5.13) can be expressed as:

$$P_{surf} = P_{amb} \tag{3.21}$$

The flux at the boundary for any transportable phase can be due to a combination of phenomenon such as blowing or suction, surface evaporation, and convection outside the surface. By blowing or suction, it is meant that the phases have a normal velocity component at the surface and they either flow out (blowing) or flow into (suction) the porous medium.

If there is an insignificant pressure gradient at the boundary, then vapor can

leave the surface by surface convection only. The vapor flux, due to surface convection, will have contribution from evaporation from liquid water, evaporation from bound water in solid phase, and water-vapor already present at the surface. The total vapor flux leaving the surface will have the following expression:

$$n_{v,tot,surf} = h_m \left(\frac{V_w + V_g + V_{bw}}{V_{tot}} \right) (\rho_{g,surf} \omega_{v,surf} - \rho_{v,amb}) \tag{3.22}$$

The above expression is based on the assumption that total vapor flux from a surface when $\phi = 1$ and there is only one phase (gas phase), is given by:

$$n_{v,tot,surf} = h_m (\rho_{g,surf} \omega_{v,surf} - \rho_{v,amb}) \tag{3.23}$$

Accordingly, where only a part of the surface is contributing to vapor flux (in case of multiphase problem), the above expression should be multiplied by the fraction of the contributing surface area to the total area to get the total vapor flux. Therefore, Eq. 3.22 gives the total vapor flux for the present problem (multiphase problem) assuming that volume fraction is equal to the surface area fraction.

When there is insignificant pressure gradient at the boundary, flux for other liquid phases such as fat or cooking oil, which do not undergo phase change at the boundary, will be zero.

The other extreme can be the case when blowing at the surface dominates over other factors and boundary pressure is specified, in which case flux at the boundary for any i^{th} component will simply be:

$$\begin{aligned} n_{i,surf} &= -\rho_i \frac{k^p_{in,i} k^p_{r,i}}{\mu_i} \nabla (P - p_{i,cap})|_{surf} \\ &= -\rho_i \frac{k^p_{in,i} k^p_{r,i}}{\mu_i} \nabla P|_{surf} - D_{i,cap} \left(\nabla \phi \rho_{l,i} S_{l,i} \right)|_{surf} - D_{i,T} \nabla T|_{surf} \end{aligned} \tag{3.24}$$

For a gas phase component, such as water vapor, the second and third terms in the above equation (3.24) are zero.

However, if neither blowing nor convection at the boundary is dominating, then both phenomena contribute to the mass transfer at the boundary and the total flux of vapor going out is given by:

$$n_{v,surf} = -\rho_v \frac{k^p_{in,g} k^p_{r,g}}{\mu_g} \nabla P|_{surf} + h_m \left(\frac{V_g}{V_{tot}} \right) (\rho_{g,surf} \omega_{v,surf} - \rho_{v,amb}) \quad (3.25)$$

Similarly, for liquid water, if neither blowing nor surface evaporation is dominating, then both contribute to the mass transfer at the boundary and the flux of water going out is given by:

$$n_{w,surf} = -\rho_w \frac{k^p_{in,w} k^p_{r,w}}{\mu_w} \nabla (P - p_{w,cap})|_{surf} + h_m \left(\frac{V_w}{V_{tot}} \right) (\rho_{g,surf} \omega_{v,surf} - \rho_{v,amb}) \quad (3.26)$$

Note that the blowing phenomenon for any water phase becomes significant under conditions of large pressure-driven flow, when surface evaporation is insufficient to take away all the liquid coming out of the boundary [15, 34]. Ni et al. (1999) [15] used $S_w = 1$ as the condition at which blowing occurs, whereas Constant et al. (1994) [34] used $P - p_{cw} > P_{atm}$ in the cell adjacent to the boundary.

In simulating the frying process (discussed later) [13] for vapor transport at the boundary, neither blowing nor convective transfer at the surface were dominating throughout the process. No single boundary condition will work for the whole process. During the initial phase of the frying process, blowing is dominant but convection at the surface eventually takes over. So, a single lumped mass transfer coefficient was used to account for both blowing and convection at the surface. In that case, the boundary condition at the surface was gevin by Eqs. 3.25 and 3.26 but the equations resembled Eq. 3.22 with the mass transfer

coefficient as a lumped value of blowing and diffusion instead of diffusion only. These factors eventually lead to a changing mass transfer coefficient.

In the case of other liquids such as fat or cooking oil, there is no evaporation and therefore only blowing, and Eq. 3.24 gives the flux. For the energy equation, there is energy going out due to bulk flow, heat lost due to surface evaporation and convective heat transfer with hot air or oil or a heated plate:

$$q_{surf} = h(T_{amb} - T_{surf}) - T\sum_{i=1}^{n-1}(c_{p,i}n_{i,surf}) + \lambda h_m \left(\frac{V_w + V_{bw}}{V_{tot}}\right)(\rho_{g,surf}\omega_{v,surf} - \rho_{v,amb}) \tag{3.27}$$

3.3.5 Initial conditions

Typical initial conditions (I.C.s) are:

$$\text{I.C. for Eq. 5.13 :} \quad P = P_{amb} \tag{3.28}$$

$$\text{I.C. for Eq. 5.14:} \quad T = T_{amb} \tag{3.29}$$

$$\text{I.C. for Eq. 3.4:} \quad S_i = S_{0,i} \tag{3.30}$$

$$\text{I.C. for Eq. 5.10:} \quad \omega_v = \omega_{0,v} \tag{3.31}$$

$$\text{I.C. for Eq. 3.11:} \quad c_j = c_{0,i} \tag{3.32}$$

Initially the food material is at ambient pressure and temperature conditions. Depending on the composition of the food material, the initial phase saturation of the liquids ($S_{0,i}$) is estimated. The water vapor in air is in equilibrium with liquid water initially. Using a moisture sorption isotherm (Eq. 5.30 and 5.31), equilibrium water vapor pressure at ambient temperature is calculated. For example, the mass fraction of vapor in the gas phase, ω_v at 25°C, is calculated as 0.02.

3.3.6 Phase change

The evaporation rate, distributed spatially and over time, is a complex function of food material and process parameters. Phase change can be formulated in two ways, equilibrium and non-equilibrium.

Equilibrium formulation

In the equilibrium formulation of evaporation that is the most common in the literature [15, 13], vapor is always assumed to be in equilibrium with the water in the solid matrix:

$$p_v = p_{v,eq} \tag{3.33}$$

where $p_{v,eq}$ is the equilibrium vapor pressure at a particular temperature and moisture content and is given by the moisture isotherm equation:

$$\ln \frac{p_{v,eq}}{p_{sat}(T)} = f(S_w, T) \tag{3.34}$$

where $p_{v,eq}$ is the equilibrium vapor pressure and $p_{sat}(T)$ is the vapor pressure of pure water at temperature T and is given by the Clausius-Clapeyron equation:

$$\ln \frac{p_{sat}(T)}{p_0} = \frac{\Delta \overline{H}_{vap}}{R} \frac{(T - T_0)}{T T_0} \tag{3.35}$$

The relationship $f(S_w, T)$ is generally obtained from experiments and much data exists in the literature. As shown already in Eq. 3.33, in the equilibrium formulation, p_v is always equal to $p_{v,eq}$ and the vapor concentration, ω_v, can be calculated using this relationship. Therefore, the evaporation rate, $\dot{I}$, comes out of the solution as all the terms on the left-hand side of the mass balance equation of the vapor (Eq. 5.10) are known.

Non-equilibrium formulation

In a non-equilibrium formulation, Eq. 3.33 is not used and is replaced by an explicit expression for the evaporation rate, $\dot{I}$, as discussed in this section. To understand this, consider a beaker half filled with liquid water and half with pure nitrogen (with no water vapor). There is a partition between the two halves which prevents any mixing. At time $t = 0$, the partition between liquid water and nitrogen is removed and the system is allowed to come to equilibrium. The whole system comes to equilibrium after time $\triangle t$. This $\triangle t$ depends on the distance that the vapor has to diffuse and the diffusion rate. For this system, during the time $\triangle t$, the average evaporation rate over space and time is given as:

$$\dot{I} = \frac{(\rho_{v,f} - \rho_{v,i})}{\triangle t} = \frac{M_v}{RT}\frac{(p_{v,f} - p_{v,i})}{\triangle t} \tag{3.36}$$

where $\rho_{v,f}$ is the final vapor density after the equilibration time and is equal to the equilibrium vapor density, and $\rho_{v,i}$ is the initial vapor density. The same concept can be applied in the case of evaporation in the pores inside the food. A Representative Elemental Volume, shown in Figure 1, may consist of a number of pores and comes to equilibrium after time $\triangle t$ and the evaporation rate is given by Eq. 3.36. Equation 3.36 is identical to the non-equilibrium evaporation rate expression in porous hygroscopic solids used for modeling of phase change [35, 18] given by:

$$\dot{I} = K(\rho_{v,eq} - \rho_v)S_g\phi \tag{3.37}$$

where $\rho_v = \rho_g\omega_v$ is the vapor density at a location that comes from solution. Here K is a material and process-dependent parameter signifying the rate constant of evaporation and is the reciprocal of equilibration time $\triangle t$.

Choice of equilibration time. The equilibration time, $\triangle t$, depends on the ratio of the gas phase volume in the pore in which vapor has to diffuse and the surface area available for evaporation. For a simple cylindrical pore, this ratio scales as the radius of the pore. It has been shown that the time taken for a molecule to make a transition from liquid water to water vapor is 10^{-14} seconds [21]. Using this condition and pure diffusion of vapor from the evaporating surface, the time to equilibrium at one mean free path (1 μm) away from the liquid surface is less than 10^{-6} seconds and for 25 μm away is around 10^{-5} seconds. The time-scale analysis, shown in the Appendix, concludes that all the transport time scales within a pore are greater than the equilibration time scale for food materials with maximum pore size smaller than 25 μm (e.g., potato, meat, etc.). In that case, the non-equilibrium phenomenon is insignificant and an equilibration time that is one order of magnitude below the smallest transport time scale ensures equilibrium. But if pore sizes are on the order of 100 μm (e.g., bread), then the non-equilibrium phenomenon becomes significant and a reasonable value of K should be used. Estimation of precise values of K, by pore scale analysis or otherwise, can be a study in itself. However, high precision in K is not expected to significantly improve the model prediction [14] and, therefore, the value calculated from the pure diffusion approach is reasonable for the model.

Relationship of equilibration time to time step choice. In Halder et al. (2007b) [14], it is also shown that, as the equilibration time is decreased, the dependence of the solution on the equilibration time decreases, such that decreasing the equilibration time from 10^{-3} to 10^{-4} seconds caused negligible change in the solution. This is because, if the temperature and moisture transport time

scales are orders of magnitude higher, it is not necessary to use the accurate range of the equilibration time. Using a higher equilibration time than the actual value, but one still smaller than the transport scales, there is negligible change in the solution but the time elapsed to solve the problem is reduced significantly. For accuracy, the time step of the numerical solution should be smaller than the equilibration and transport time scales.

Coincidentally, an equilibrium formulation is difficult to implement in commercial software. Typically, commercial software application requires the source term (evaporation rate, $\dot{I}$, in the conservation equations) to be explicitly stated in terms of dependent variables in the model. A non-equilibrium formulation, given by Eq. 5.32, allows precisely this, i.e., the explicit expression of the evaporation rate and therefore would be preferred in commercial software application and is therefore used in our model. For infinitely large K, corresponding to instantaneously occurring phase change, Eq. 5.32 reverts back to Eq. 3.33, the equilibrium assumption, making it possible to simulate the equilibrium formulation as well.

Other phase changes

Analogous to the evaporation rate that relates water release from the liquid to the vapor phase, the release of liquids such as fat and liquid water from the solid matrix to the transportable phase, as temperature increases, can also be written in terms of rate expressions, similar to Eq. 5.32, given by:

$$\dot{R}_{i,j} = K_{i,j}(c_{s,j} - c_{s,j,eq}) \tag{3.38}$$

The holding capacity co-relation, $c_{s,j,eq}$, is experimentally determined [39]. It is assumed that the concentrations in the solid phase always remain at equi-

librium. Large values of $K_{i,j}$ were selected so that equilibrium is satisfied at each time step, similar to the use of large K to force equilibrium in the non-equilibrium formulation for evaporation discussed above.

3.4 Model implementation and validation

In the following section, the model developed is applied to two food processes, the frying of a restructured potato slab (made from dried potato flakes—see Figure 2) and contact heating of a hamburger patty (Figure 3), to demonstrate its effectiveness in describing different processes. The model is validated in each case using experimental results.

3.4.1 Deep-fat frying of restructured potato

Deep-fat frying can be defined as a process for cooking foods, by immersing them in an edible oil, at a temperature above the boiling point of water, usually between 150°C and 200°C.

Problem formulation

A schematic of the problem description is shown in Figure 3.2. The restructured potato slab is assumed to be a porous medium. There are four phases: solid, liquid water, oil and gas. The gas phase is a mixture of air and water vapor. Shrinkage during frying and the effects of gravity are ignored. To simulate a 1D heat and mass transfer, no flux conditions for mass species and energy are

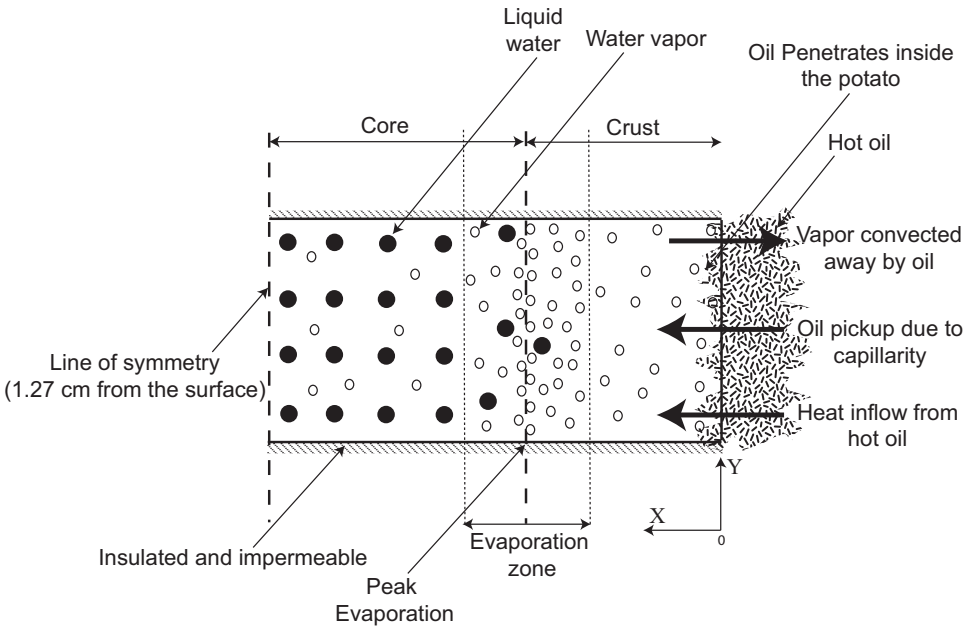

Figure 3.2: Schematic showing computational domain and boundary conditions. Two-dimensional geometry was implemented with the above boundary conditions to simulate an effective one-dimensional problem. For computation, the dimension in the y-direction was chosen to be 0.08 cm.

specified at boundaries other than $x = 0$. The problem is considered to be symmetric with $x = L$ as the line of symmetry. The left boundary ($x = 0$) is the frying surface where heat and mass exchange with the environment takes place. In a restructured potato, water in the solid matrix is negligible (as all the water is in the pore space), so interphase mass transfer from solid to liquid is ignored (it cannot be ignored in the case of contact heating of meat as shown later). This simplifies the overall model, as porosity can be assumed to be constant with time and mass balance of the solid is not required.

Mass balance equation

Saturation of liquid water and oil is calculated by solving the mass balance equations of the phases (Eq. 3.4). Saturation of gas is calculated from Eq. 5.5. The gas phase is a mixture of water vapor and air, so the mass balance equation of water vapor is solved using Eq. 5.10 and the mass fraction of air is calculated from Eq. 5.11.

Energy balance equation

Local thermal equilibrium exists between all the phases and, therefore, the energy balance equation for a mixture (Eq. 5.14) is solved to get the temperature, T.

Continuity and Momentum equation

The continuity equation of the gas phase (Eq 5.13) is solved to give the pressure, P. During frying, the gas phase never goes to zero, so solving Eq. 5.13 does not lead to numerical difficulties (discussion in Section 2.3.2). Darcy's law is assumed to be valid and gives the velocities of each phase (liquid water, oil and gas).

Boundary conditions and Initial conditions

Boundary conditions at $x = 0$ are given as:

$$\text{B.C. for Eq. 5.13:} \qquad P_{surf} = P_{amb} \tag{3.39}$$

$$\text{B.C. for Eq. 5.14:} \quad q_{surf} = h(T_{amb} - T_{surf}) - (\lambda + c_{p,w}T)n_{w,surf} - c_{p,v}Tn_{v,surf} - c_{p,o}T_{amb}n_{o,surf} \tag{3.40}$$

$$\text{B.C. for Eq. 3.4:} \quad n_{w,surf} = h_m S_w(\rho_{g,surf}\omega_{v,surf} - \rho_{v,amb}) \tag{3.41}$$

$$S_{o,surf} = S_{o1} \tag{3.42}$$

$$\text{B.C. for Eq. 5.10:} \quad n_{v,surf} = h_m S_g(\rho_{g,surf}\omega_{v,surf} - \rho_{v,amb}) \tag{3.43}$$

Initial conditions inside the potato before frying are:

$$\text{I.C. for Eq. 5.13:} \quad P = P_{amb} \tag{3.44}$$

$$\text{I.C. for Eq. 5.14:} \quad T = T_{amb} \tag{3.45}$$

$$\text{I.C. for Eq. 3.4:} \quad S_w = 0.3 \tag{3.46}$$

$$S_o = 0 \tag{3.47}$$

$$\text{I.C. for Eq. 5.10:} \quad \omega_v = 0.02 \tag{3.48}$$

Further details and explanations of boundary and initial conditions are given elsewhere [13].

Input parameters and numerical solution

Input parameters and other auxiliary equations used in this frying simulation are given in Table 3.4.1. A commercially available finite element software, COMSOL Multiphysics (Comsol Inc., Burlington, MA), was used to solve these equations. The computational domain, shown in Figure 3.2, is 0.0127 m $\times$ 0.0008 m and has a mesh consisting of 127×3 quadrilateral elements. Simulating 16 minutes of heating took approximately 6 hours of CPU time for a timestep size of 0.01 seconds on a Pentium 3.4 GHz PC with 2GB RAM.

Table 3.1: Input parameters used in the simulations of deep-fat frying

Parameter	Symbol	Value	Units	Source
Density				
water	ρ_w	998	kg/m^3	
vapor	ρ_v	Ideal gas	kg/m^3	
air	ρ_a	Ideal gas	kg/m^3	
oil	ρ_o	879	kg/m^3	[42]
solid	ρ_s	1528	kg/m^3	[5]
Specific heat capacity				
water	c_{pw}	4178	J/kg K	[7]
vapor	c_{pv}	2062	J/kg K	[7]
air	c_{pa}	1006	J/kg K	[7]
oil	c_{po}	2223	J/kg K	[7]
solid	c_{ps}	1650	J/kg K	[7]
Thermal conductivity				
water	k_w	0.57	W/m K	[7]
vapor	k_v	0.026	W/m K	[7]
air	k_a	0.026	W/m K	[7]
oil (corn)	k_o	0.17	W/m K	[44]
solid	k_s	0.21	W/m K	[7]
Intrinsic permeability				
water	$k^p_{in,w}$	5×10^{-14}	m^2	[15]
air and vapor	$k^p_{in,g}$	10×10^{-14}	m^2	[15]
oil	$k^p_{in,o}$	5×10^{-14}	m^2	[15]
Relative permeability				
water	$k^p_{r,w}$	$((S_w - 0.08)/0.92)^3$		[45]
air and vapor	$k^p_{r,g}$	$(1 - S_w - S_f)/0.92$		[45]
oil	$k^p_{r,o}$	$((S_f - 0.08)/0.92)^3$		[15]

Table 3.1: Input parameters used in the simulations of deep-fat frying continued

Parameter	Symbol	Value	Units	Source
Capillary diffusivity				
water	$D_{w,cap}$	$10^{-8}\exp(-2.8+2\mathrm{M})$		[15]
oil	$D_{o,cap}$	$10^{-8}\exp(-2.8+2\mathrm{M_o})$		[15]
Viscosity				
water	μ_w	0.988×10^{-3}	Pa s	
air and vapor	μ_g	1.8×10^{-5}	Pa s	
oil	μ_o	$5.05\times10^{-6}\exp(\frac{2725}{T})$	Pa s	[42]
Heat transfer coefficient				
Frying	h	graph	$\mathrm{W/m^2K}$	[13]
Post-frying cooling	h	20	$\mathrm{W/m^2K}$	[46]
Mass transfer coefficient	h_m	graph	m/s	[13]
Latent heat of vaporization	λ	2.26×10^6	J/kg	
Porosity	ϕ	0.928		[5]
Vapor diffusivity in air	$D_{eff,g}$	2.6×10^{-6}	$\mathrm{m^2/s}$	
Oil temperature	T_{oil}	180	°C	
Ambient pressure	P_{amb}	101325	Pa	
Surface oil saturation	S_{o1}	0.11 (frying)		[13]
		0.28 (cooling)		[13]

Results and validation

The simulation results are compared with the experimental data of Farkas et al. (1996b) [5], as shown in Figure 3.3a. The predicted temperatures at a distance of 0.05 cm from the surface are close to experimental values for the first two minutes but there is a considerable difference between them for the next 10 minutes and finally again matching closely for the last 4 minutes of frying. This difference is due to discrepancies in the temperature measurement technique for the depth of 0.05 cm, as discussed in Halder et al. (2007b) [14]. The temperature predictions for locations 0.42 cm and 0.85 cm from the frying surface compare well with the experimental measurements.

As shown in Figure 3.3b, the moisture content (dry-basis) of the potato slab dropped from its initial value of 2.50 to 1.56 after 16 minutes of heating. Our model prediction, with improved boundary conditions and evaporation formulation, matches very closely with the experimental results [5], making a better match than in other studies [15, 5]. Such close agreement between experimental measurements and model prediction confirms the effectiveness of the model and serves to validate it.

As can be seen in Figures 3.3c and 3.3d, the peak pressure occurs where the evaporation rate is maximum. The evaporation rate is distributed over a narrow zone near the surface, thus validating our assumption that evaporation does not occur at an interface (sharp boundary) but is distributed over a thin zone. In the region where rapid evaporation is taking place, the pressure is always above that of the ambient pressure. Initially, there is condensation in the core region, due to which the pressure falls below ambient pressure. This negative gauge pressure occurs because the gas phase has a negative rate of accumulation in the

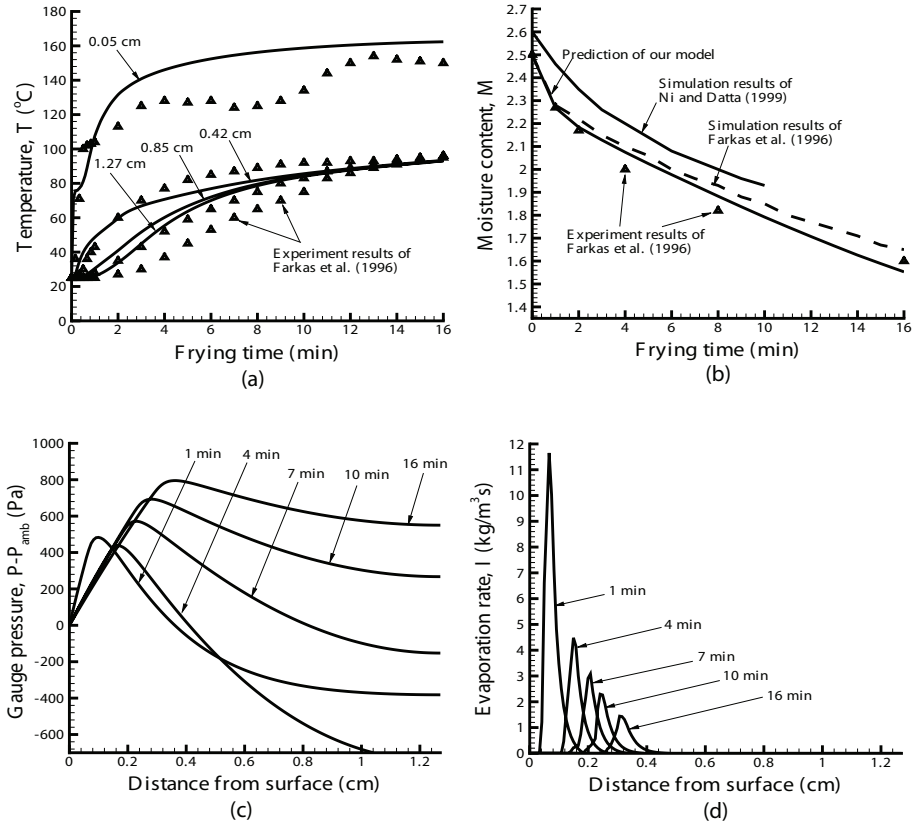

Figure 3.3: Comparison of model predictions for deep-fat frying with experimental data from literature for a)temperature; b) moisture content (dry basis). The spatial pressure and evaporation profiles during different times of frying are shown in (c) and (d), respectively.

core – the air present in the core is driven out due to binary diffusion and vapor reaching the core is condensed. As temperature rises and evaporation (and not condensation) starts to occur in the core region, the pressure starts rising and finally reaches around 600 Pa after 16 minutes of frying.

3.4.2 Contact heating of a hamburger patty

Meat can be processed and cooked in a variety of ways. For the purpose of this study, double-sided contact heating of hamburger patties [40] is selected, as shown in the schematic of Figure 3. A frozen hamburger patty of cylindrical shape (diameter 10 cm and height 1 cm), initially stored at $-22°C$, is placed between two hot plates. The gap between the top and bottom heating plates is kept fixed at 1 cm. As temperature rises, water and fat melt, but are still held strongly by the solid matrix. With further rise in temperature, denaturation of muscle proteins occurs, which causes the release of bound water and fat, making both liquids transportable. Mass transfer can also occur between water and vapor in the gas phase due to vaporization and condensation. Gradually, the region near the hot plates loses all the water due to evaporation and a dried crust region develops. The variables of interest for predicting quality and safety aspects of meat cooking are temperature, moisture content, fat content, evaporation rate and their histories.

Problem details

A schematic of the problem description is shown in Figure 3.4. To simulate a 1D heat and mass transfer in a cylindrical patty, it is assumed that the exchange of heat and mass with the outside environment takes place through the top and bottom surface of the patty only and the sides are insulated (i.e., radial transport is ignored so gradients are present only in the axial directions). Since the effect of gravity is small, and the top and the bottom plates are at the same temperature, symmetry is assumed at the centerline. The patty is assumed to comprise three transportable fluid phases: liquid water, liquid fat and gas (mixture of air and

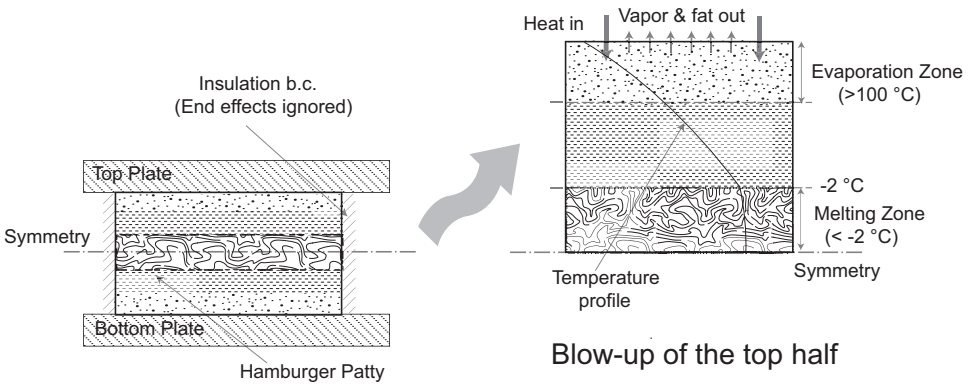

Figure 3.4: Schematic showing computational domain and boundary in the case of contact heating of a hamburger patty.

water vapor), and a solid phase comprising of protein, frozen water and fat.

Mass balance equation

As in frying, the saturations of the water and fat phases are calculated by solving the mass balance equations of the phases (Eq. 3.4). Saturation of gas is calculated from Eq. 5.5. The gas phase is a mixture of water vapor and air, so the mass balance equation of water vapor is solved using Eq. 5.10 and the mass fraction of air is calculated from Eq. 5.11. In meat cooking, where the solid releases water and fat, there are three additional mass balance equations for each component of the solid phase (Eq. 3.11).

Energy balance equation

Thermal equilibrium exists between all the phases and, therefore, the energy balance equation for a mixture (Eq. 5.14) is solved to get the temperature, T.

Continuity and momentum equation

Similar to frying, Eq. 5.13 is solved to obtain pressure, P, and Darcy's law provides the velocities of each phase.

Boundary and initial conditions

In the case of contact heating of meat, the heat transfer coefficient is very high (> 1000 W/m^2). This leads to high evaporation rates and thus large pressure gradients close to the heated surface. Under such conditions, blowing can be significant. Therefore, the boundary flux for water vapor is given by Eq 3.25. Following Ni et al. (1999) [17], $S_w = 1$ was used as the condition to kick in blowing for liquid water. However, this condition was never satisfied during 150 seconds of heating and liquid water left the patty by surface evaporation only. The time-dependent heat transfer coefficient and plate temperature data are taken from Pan et al. (2000) [40].

Initially frozen at -22 °C, the patty is composed of 60% water, 24% fat and 16% protein by weight and all are assumed to be in solid phase. The porosity of frozen patties is taken as 2% [41]. From this data, the initial concentrations for all the components can be calculated. Note that, at the initial temperature, all water and fat are assumed to be in the solid matrix and therefore concentrations of both bulk water and fat are zero. Initially, air is assumed to be saturated with vapor. The equilibrium mass fraction of vapor in the gas phase, ω_v at -22 °C, is 0.0015.

Input parameters and numerical solution

Input parameters used in the hamburger patty cooking simulation are given in Table 3.2. A commercially available finite element software, COMSOL Multiphysics (Comsol Inc, Burlington, MA), was used to solve these equations. The computational domain is 0.005 m in length and has a mesh consisting of 500 elements. Simulation of 150 seconds of heating took approximately 6 hours of CPU time for a timestep size of 0.01 second on a Pentium 3.4 GHz PC with 2GB RAM.

Results and validation

Predicted temperature profiles are compared with the experimental data from [40], as shown in Figure 3.5a. The temperatures at the core of the patty, i.e. the coldest point, follow the experimental results for around 100 seconds. After that the predicted heating rate is slightly lower than the experimentally observed value. The coldest-point temperature is around 70°C after 150 seconds, whereas the measured temperature is 85°C.

Once the ice is completely melted, the Biot number for the process is 250 (the heat transfer coefficient is greater than 1000 W/m^2K, patty thickness is 1 cm and thermal conductivity is around 0.4 W/m^2K, which means the heat transfer is internally limited). We compared our thermal conductivity values (estimated by volume averaging) with the values experimentally measured in Pan et al (2001) and found that there is a difference of about 10 %. The averaging correlations for transport property estimation may have an error of +/- 10% [7], which affects the results in the case of internally limited processes. The experimentally

Table 3.2: Input parameters used in the simulations of contact heating of a hamburger patty

Parameter	Symbol	Value	Units	Source
Patty dimensions				
Height		10	mm	[40]
Initial conditions				
Mass fractions				
water	x_{fw}	0.6	–	[40]
fat	x_f	0.24	–	[40]
protein	x_{pr}	0.16	–	[40]
Porosity	ϕ	.02	–	[41]
Temperature	T_{ini}	-22	°C	[40]
Pressure	P_{ini}	101325	Pa	–
Properties				
Water activity	a_w	–	–	[47]
Density				
water	ρ_w	997.2	kg/m^3	[7]
ice	ρ_i	917	kg/m^3	[7]
gas	ρ_v	Ideal gas	kg/m^3	[7]
fat	ρ_f	925.6	kg/m^3	[7]
protein	$\rho_p r$	1330	kg/m^3	[7]
Specific heat capacity				
water	$c_{p,w}$	4178	J/kg K	[7]
ice	$c_{p,i}$	2062	J/kg K	[7]
gas	$c_{p,g}$	1006	J/kg K	[7]
fat	$c_{p,f}$	1984	J/kg K	[7]
protein	$c_{p,pr}$	2008	J/kg K	[7]

Table 3.2: Input parameters used in the simulations of contact heating of a hamburger patty – continued.

Parameter	Symbol	Value	Units	Source
Thermal conductivity				
water	k_w	0.57	W/m K	[7]
ice	k_w	2.22	W/m K	[7]
gas	k_g	0.025	W/m K	[7]
fat	k_f	0.18	W/m K	[7]
protein	k_{pr}	0.18	W/m K	[7]
Intrinsic permeability				
water	$k^p_{in,w}$	5×10^{-16}	m^2	[11]
fat	$k^p_{in,f}$	1×10^{-15}	m^2	[11]
gas	$k^p_{in,g}$	5×10^{-16}	m^2	Same as fat
Relative permeability				
water	$k^p_{r,w}$	$((S_w - 0.08)/0.92)^3$	–	[45]
fat	$k^p_{r,f}$	$((S_f - 0.08)/0.92)^3$	–	Same as water
gas	$k^p_{r,g}$	$(1 - S_w - S_f)/0.92$	–	[45]
Capillary diffusivity				
water	$D_{w,cap}$	$10^{-10}\exp(-2.8 + 10S_w)$	m^2/s	[47]
fat	$D_{f,cap}$	$10^{-10}\exp(-2.8 + 10S_f)$	m^2/s	[47]

Table 3.2: Input parameters used in the simulations of contact heating of a hamburger patty – continued.

Parameter	Symbol	Value	Units	Source
Viscosity				
water	μ_w	0.988×10^{-3}	Pa s	
gas	μ_g	1.8×10^{-5}	Pa s	
fat	μ_f	0.02	Pa s	[49]
Holding capacities				
water	$c_{bw,eq}$	$c_{bw,ini}\exp(-.0132(\mathrm{T}-303))$	$\mathrm{kg/m^3}$	[39]
fat	$c_{bf,eq}$	$c_{bf,ini}\exp(-.0159(\mathrm{T}-303))$	$\mathrm{kg/m^3}$	[39]
Heat transfer coefficient	h	–	$\mathrm{W/m^2K}$	[40]
Mass transfer coefficient	h_m	0.015	m/s	[15]
Latent heat of vaporization	λ	2.26×10^6	J/kg	
Latent heat of fusion				
water		3.34×10^5	J/kg	
fat		1.5×10^5	J/kg	
Vapor diffusivity in air	$D_{eff,g}$	2.6×10^{-5}	$\mathrm{m^2/s}$	
Grill temperature	T_{surf}	–	°C	[40]
Ambient pressure	P_{amb}	101325	Pa	

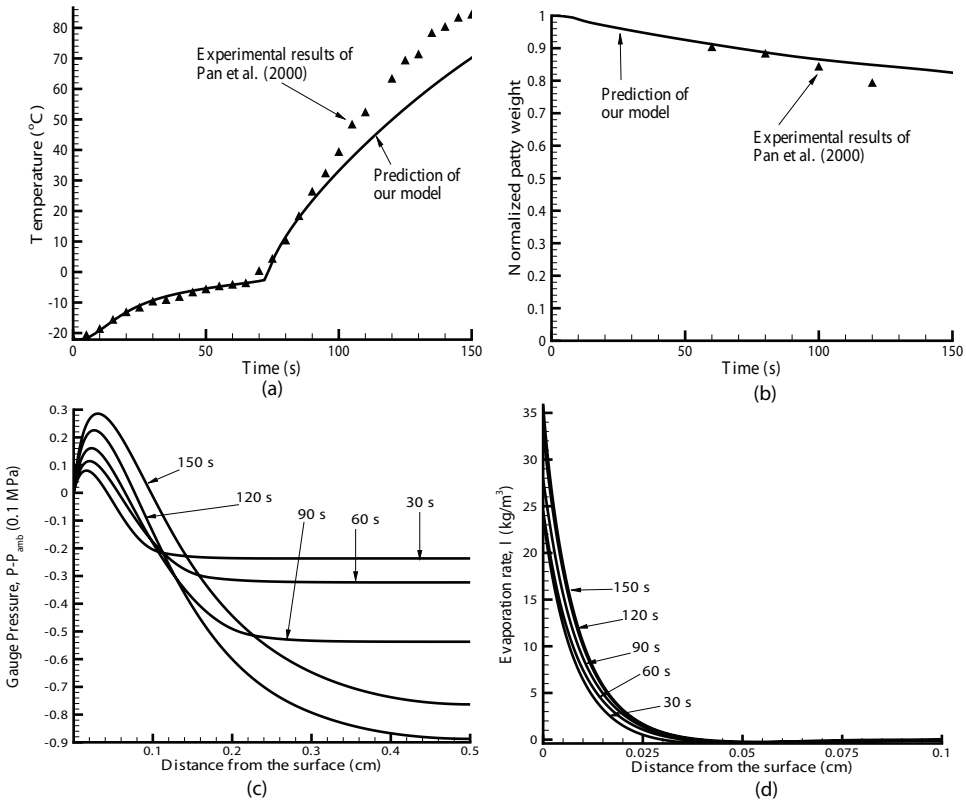

Figure 3.5: (a) Temperature at the center point, (b) average moisture content, (c) spatial pressure and (d) spatial evaporation rate profiles for contact heating of a hamburger patty at different times.

observed total weight loss (water and fat) after 150 seconds of heating time is around 22% after 120 seconds of heating [40]. The loss predicted from the simulation is around 18% (Figure 3.5b), which is pretty close.

Absolute comparison is difficult to achieve due to limitations in the property estimation correlations. However, the close results validate the more fundamental approach toward the modeling of food cooking. Following this approach, thermal processing of meat products can be simulated by applying the multiphase transport model. This is a major leap from the existing approach for modeling the meat-cooking process, under which bulk thermal properties

of meat (such as enthalpy and thermal conductivity) are measured as functions of temperature and, then, a simple conduction equation is used to fit the data.

Figures 3.5c and 3.5d show the spatial profiles of the pressure and evaporation rates, respectively, at different times. The evaporation rate and therefore the pressure are maximum near the heated surface. The interior of the patty has negative pressures, due to the diffusion, followed by the condensation, of vapor from the surface to the relatively cooler interior. Gradually, as the surface dries up, the evaporation and peak pressure zones are expected to move from the surface to the core, as was shown earlier (in Figure 3) for deep-fat frying.

3.5 Similarity in fundamental physics

As shown in deep-fat frying and contact heating of hamburger patties (Figures 3 and 5), the fundamental physics involved in different thermal food processes are similar. As the food (porous hygroscopic material) is heated from the boundary, the temperature inside rises. The rise in temperature causes a phase change, which in turn causes a rise in pressure. The pressure gradient causes the flow of phases toward the boundary where mass transfer takes place. If there is a fluid component absorbed in the solid, then with a rise in temperature and subsequent changes in solid matrix properties it changes into transportable phase. Therefore, a single model is able to solve distinct modes of cooking or processing where the physics is similar and distinct modes of heating are handled by distinct boundary conditions (e.g., frying, baking, etc) or in some cases by source terms (e.g., microwave heating).

3.6 Conclusion

The aim of this paper is to show that transport for many of the thermal processes in food (e.g., frying, baking, meat cooking and microwave heating) can be modeled using the comprehensive framework developed. The developed model includes all the important physics encountered in cooking or food processing (e.g., melting, bound phase, phase change, pressure-driven flow, capillary flow and binary diffusion). Depending on the food processing situation, this comprehensive model can be simplified by ignoring some physics that are irrelevant for that process and material. For example, in frying of restructured potato, it is assumed that there is no bound water and all the water is available for transport, thus, largely reducing complexities. In meat cooking, all of the physics is necessary and, therefore, it results in the most complex model. The two food processes, the frying of potato and the contact heating of hamburger patty, modeled in this paper demonstrate the effectiveness of the framework in solving different types of thermal processes.

Though meat and potato are completely different in terms of composition, and frying and contact cooking are completely different modes of cooking, transport in the case of frying of potato and meat cooking can be solved by the same model. This is because the developed model is not based on empirical relationships but is a fundamental-based model which can be generalized over a wide range of hygroscopic porous materials and different types of thermal processes. The input parameters required to solve the problem have a physical meaning and are inherent properties of either the process or the food material and can be determined experimentally.

A novel non-equilibrium evaporation formulation is used in the model to describe the evaporation and condensation processes. The non-equilibrium evaporation constant, K, is the reciprocal of the equilibration time and has been investigated in detail in this paper. Further, the same non-equilibrium formulation can be used to implement equilibrium by using a very large value of K. Time-scale analysis shows that the transport scales are much larger than the evaporation time scale for a typical food material. Therefore, a higher value for the equilibration time can be used in a simulation without affecting the solution.

The comprehensive model developed here can also simulate transport in other hygroscopic porous materials. Although the immediate applications shown here are to food processes, the model has applications in many different fields, for example, fuel cells, drug delivery through tissues, and nuclear waste treatment. For example, in fuel-cells simulation, there are two different phases (liquid and gas) which experience pressure-driven flow in porous media. There is a chemical reaction in fuel cells between liquid phases to form gaseous phase, which is analogous to evaporation in frying and meat cooking.

Another unique feature of the modeling framework is that it can be easily implemented in some general purpose CFD software. Most commercial software requires the evaporation rate to be explicitly expressed in terms of dependent variables of the model and the non-equilibrium formulation presented here allows precisely this, unlike the implicit evaporation formulations of the past. Use of the direct Darcy's law over Navier-stokes analog of Darcy flow reduces unnecessary numerical complexities. Because the model is versatile and easily implementable, it can be very useful in product, process and equipment design in the food sector and similar applications in other fields.

Acknowledgement

This research was partially supported by the United States Department of Agriculture Regional Project NC 1023 and the United States Department of Agriculture National Integrated Food Safety Project 2004-51110-02167.

APPENDIX

Transport time-scale analysis:

The minimum length scale (L) of significance for typical food materials is assumed to be 0.1 mm:

$$L \sim 10^{-4}\ [\mathrm{m}] \tag{3.49}$$

The time scale for capillary diffusion (t_{cap}):

$$t_{cap} \sim \frac{L^2}{D_{cap}} = \frac{10^{-8}\ [\mathrm{m}^2]}{10^{-6}\ [\mathrm{m}^2/\mathrm{s}]} = 10^{-2}\ [\mathrm{s}] \tag{3.50}$$

Note that a low value for the length scale and the highest possible value of D_{cap} is used to obtain the minimum relevant diffusion time scale.

The time scale for binary diffusion (t_g):

$$t_g \sim \frac{L^2}{D_{eff,g}} = \frac{10^{-8}\ [\mathrm{m}^2]}{10^{-5}\ [\mathrm{m}^2/\mathrm{s}]} = 10^{-3}\ [\mathrm{s}] \tag{3.51}$$

The time scale for pressure-driven flow (t_p):

$$\begin{aligned} v &\sim \frac{k}{\mu}\frac{\triangle P}{L} = \frac{10^{-15}\ [\mathrm{m}^2]}{10^{-3}\ [\mathrm{Pa\ s}]}\frac{10^{5}\ [\mathrm{Pa}]}{10^{-4}\ [\mathrm{m}]} = 10^{-3}\ [\mathrm{m/s}] \\ t_p &\sim \frac{L}{v} = \frac{10^{-4}\ [\mathrm{m}]}{10^{-3}\ [\mathrm{m/s}]} = 10^{-1}\ [\mathrm{s}] \end{aligned} \tag{3.52}$$

The time scale for heat flow (t_h):

$$t_h \sim \frac{L^2}{\frac{k_{eff}}{\rho_{eff} c p_{eff}}} = \frac{10^{-8}\ [\mathrm{m}^2]}{10^{-7}\ [\mathrm{m}^2/\mathrm{s}]} = 10^{-1}\ [\mathrm{s}] \tag{3.53}$$

Therefore, it can be seen that all the transport time scales are larger than the evaporation equilibrium time scale, which is 10^{-5} seconds for 25 μm-sized pores [21].

BIBLIOGRAPHY

[1] Ateba, P. and G. S. Mittal, 1994, Modeling the deep-fat frying of beef meatballs, *International Journal of Food Science and Technology*, 29(4), pp. 429-440.

[2] Ikediala, J. N., L. R. Correia, et al., 1996, Finite element modeling of heat transfer in meat patties during single-sided pan-frying, *Journal of Food Science*, 61(4), pp. 796-802.

[3] Bengtsson, N. E., B. Jakobsson, et al., 1976, Cooking of beef by oven roasting - study of heat and mass-transfer, *Journal of Food Science*, 41(5), pp. 1047-1053.

[4] Chau, K. V. and G. V. Snyder, 1988, Mathematical-model for temperature distribution of thermally processed shrimp, *Transactions of the Asae*, 31(2), pp. 608-612.

[5] Fowler, A. J. and A. Bejan, 1991, The effect of shrinkage on the cooking of meat, *International Journal of Heat and Fluid Flow*, 12(4), pp. 375-383.

[6] Dincer, I. and M. Yildiz, 1996, Modelling of thermal and moisture diffusions in cylindrically shaped sausages during frying, *Journal of Food Engineering*, 28(1), pp. 35-44.

[7] Williams, R. and G. S. Mittal, 1999, Low-fat fried foods with edible coatings: Modeling and simulation. *Journal of Food Science*, 64(2), pp. 317-322.

[8] Shilton, N., P. Mallikarjunan, et al., 2002, Modeling of heat transfer and evaporative mass losses during the cooking of beef patties using far-infrared radiation, *Journal of Food Engineering*, 55(3), pp. 217-222.

[9] Wang, L. and R. P. Singh, 2004, Finite element modeling and sensitivity analysis of double-sided contact-heating of initially frozen hamburger patty, *Transactions of the Asae*, 47(1), pp. 147-157.

[10] Kondjoyan, A., O. Rouaud, et al., 2006, Modelling coupled heat-water transfers during a decontamination treatment of the surface of solid food products by a jet of hot air. I. Sensitivity analysis of the model and first validations of product surface temperature under constant air temperature conditions, *Journal of Food Engineering*, 76(1), pp. 53-62.

[11] Farkas, B. E., R. P. Singh, et al., 1996a, Modeling heat and mass transfer in immersion frying .1. Model development, *Journal of Food Engineering*, 29(2), pp. 211-226.

[12] Farid, M. M. and X. D. Chen, 1998, The analysis of heat and mass transfer during frying of food using a moving boundary solution procedure, *Heat and Mass Transfer*, 34(1), pp. 69-77.

[13] Bouchon, P. and D. L. Pyle, 2005a, Modelling oil absorption during post-frying cooling - I: Model development, *Food and Bioproducts Processing*, 83(C4), pp. 253-260.

[14] Mascarenhas, W. J., H. U. Akay, et al., 1997, A computational model for finite element analysis of the freeze-drying process, *Computer Methods in Applied Mechanics and Engineering*, 148(1-2), pp. 105-124.

[15] Ni, H. and A. K. Datta, 1999, Moisture, oil and energy transport during deep-fat frying of food materials, *Food and Bioproducts Processing*, 77(C3), pp. 194-204.

[16] Yamsaengsung, R. and R. G. Moreira, 2002a, Modeling the transport phenomena and structural changes during deep fat frying - Part 1: model development, *Journal of Food Engineering*, 53(1), pp. 1-10.

[17] Halder, A., Dhall, A., et al., 2007a, An improved, easily implementable, porous media based model for deep-fat frying - Part I: Model development and input parameters, *Food and Bioproducts Processing*, 85(C3), pp. 209-219.

[18] Zhang, J., A. K. Datta, et al., 2005, Transport processes and large deformation during baking of bread, *Aiche Journal*, 51(9), pp. 2569-2580.

[19] Zhang, J., Datta, A.K. and Rakesh, V., 2005, Investigation of non-equilibrium in water evaporation, *3rd Inter-American Drying Conference*, Montreal, Canada.

[20] Farkas, B. E., R. P. Singh, et al., 1996b, Modeling heat and mass transfer in immersion frying .2. Model solution and verification, *Journal of Food Engineering*, 29(2), pp. 227-248.

[21] Ni, H., A. K. Datta, et al., 1999, Moisture transport in intensive microwave

heating of biomaterials: A multiphase porous media model, *International Journal of Heat and Mass Transfer*, 42(8), pp. 1501-1512.

[22] Yamsaengsung, R. and R. G. Moreira, 2002b, Modeling the transport phenomena and structural changes during deep fat frying - Part II: model solution and validation, *Journal of Food Engineering*, 53(1), pp. 11-25.

[23] Rutqvist, J., Y. S. Wu, et al., 2002, A modeling approach for analysis of coupled multiphase fluid flow, heat transfer, and deformation in fractured porous rock, *International Journal of Rock Mechanics and Mining Sciences*, 39(4), pp. 429-442.

[24] Buscheck, T. A. and J. J. Nitao, 1993, Repository-heat-driven hydrothermal flow at Yucca Mountain .1. modeling and analysis, *Nuclear Technology*, 104(3), pp. 418-448.

[25] Abriola, L. M. and G. F. Pinder, 1985, A Multiphase approach to the modeling of porous-media contamination by organic-compounds .1. Equation development, *Water Resources Research*, 21(1), pp. 11-18.

[26] Arbogast, T., S. Bryant, et al., 1996, Computational methods for multiphase flow and reactive transport problems arising in subsurface contaminant remediation, *Journal of Computational and Applied Mathematics*, 74(1-2), pp. 19-32.

[27] Khanafer, K. and K. Vafai, 2006, The role of porous media in biomedical engineering as related to magnetic resonance imaging and drug delivery, *Heat and Mass Transfer*, 42(10), pp. 939-953.

[28] Datta, A. K., 2007a, Porous media approaches to studying simultaneous heat and mass transfer in food processes. I: Problem formulations, *Journal of Food Engineering*, 80(1), pp. 80-95.

[29] Curtiss, C. F. and R. B. Bird, 2001, Multicomponent diffusion, *Industrial and Engineering Chemistry Research*, 40(7), pp. 1791-1791.

[30] Vafai, K. and C. L. Tien, 1981, Boundary and inertia effects on flow and heat-transfer in porous-media, *International Journal of Heat and Mass Transfer*, 24(2), pp. 195-203.

[31] Perre, P., and Moyne, C., 1991, Processes related to drying .2. Use of the

same model to solve transfers both in saturated and unsaturated porous-media, *Drying Technology*, 9(5), pp. 1153-1179.

[32] Pruess, K., 2004, The TOUGH codes - a family of simulation tools for multiphase flow and transport processes in permeable media, *Vadose Zone Journal*,3, pp. 738-746.

[33] Pham, Q.T., 1995, Comparison of general-purpose finite-element Methods for the Stefan problem, *Numer Heat Tranf. B-Fundam.*, 27(4), pp. 417-435.

[34] Constant, T., Moyne, C., and Perre, P., 1996, Drying with internal heat generation: Theoretical aspects and application to microwave heating, *Aiche Journal*, 42(2), pp. 359-368.

[35] Le, C. V., Ly, N. G., and Postle, R., 1995, Heat and mass-transfer in the condensing flow of steam through an absorbing fibrous medium, *International Journal of Heat and Mass Transfer*, 38(1), pp. 81-89.

[36] Scarpa, F. and G. Milano, 2002, The role of adsorption and phase change phenomena in the thermophysical characterization of moist porous materials, *International Journal of Thermophysics*, 23(4), pp. 1033-1046.

[37] Ward, C. A. and G. Fang, 1999, Expression for predicting liquid evaporation flux: Statistical rate theory approach, *Physical Review E*, 59(1), pp. 429-440.

[38] Halder, A., A. Dhall, et al., 2007b, An improved, easily implementable, porous media based model for deep-fat frying - Part II: Results, validation and sensitivity analysis, *Food and Bioproducts Processing*, 85(C3), pp. 220-230.

[39] Pan, Z. and R. P. Singh, 2001, Physical and thermal properties of ground beef during cooking, *Lebensmittel-Wissenschaft Und-Technologie-Food Science and Technology*, 34(7), pp. 437-444.

[40] Pan, Z., R. P. Singh, et al., 2000, Predictive modeling of contact-heating process for cooking a hamburger patty. *Journal of Food Engineering*, 46(1), pp. 9-19.

[41] Boukouvalas, C. J. and M. K. Krokida, et al. 2006, Density and porosity: Literature data compilation for foodstuffs. *International Journal of Food Properties*, 9(4), pp. 715-746.

[42] Tseng, Y.C., Moreira, R. and Sun, X., 1996, Total frying-use time effects on soybean-oil deterioration and on tortilla chip quality, *International Journal of Food Science and Technology*, 31, pp. 287-294.

[43] Choi, Y. and Okos, M. R., 1986, Thermal properties of liquid foods – review, in *Physical and Chemical Properties of Food*, Okos, M. R. (editor), American Society of Agricultural Engineers, St Joseph, MI, USA, pp. 35-77.

[44] Lewis, M.J., 1987, Physical properties of foods and food processing systems. Deerfield Beach, FL: VCH.

[45] Bear, J., 1972, Dynamics of fluids in porous media, American Elsevier Publishing company, Inc., New York.

[46] Hanreich, G. and Nicolics, J., 2001, Measuring the natural convective heat transfer coefficient at the surface of electronic components, *IEEE Instrumentation and Measurement Technology Conference*, pp. 1045-1050.

[47] Hallstrom, B., 1990, Mass transport of water in foods a consideration of the engineering aspects, *Journal of Food Engineering*, 12(1), pp. 45-52.

[48] Oroszvari, B. K., C. S. Rocha, et al., 2006, Permeability and mass transfer as a function of the cooking temperature during the frying of beefburgers. *Journal of Food Engineering*, 74(1), pp. 1-12.

[49] Goodrum, J. W. and D. P. Geller, et al., 2002, Rheological characterization of yellow grease and poultry fat. *Journal of the American Oil Chemists Society*, 79(10), pp. 961-964.

CHAPTER 4

BOUNDARY CONDITIONS IN MULTIPHASE, POROUS-MEDIA, TRANSPORT MODELS OF THERMAL PROCESSES WITH RAPID EVAPORATION

4.1 Abstract

Multiphase transport models of food processes require surface heat and mass transfer coefficients as boundary conditions that are traditionally assumed. A conjugate heat and mass transfer model is solved for simple microwave heating of food as a porous medium (from which vapor blows out) with air flow over it, such that there is no need to provide the boundary conditions at the food-air interface. Surface fluxes due to diffusion and flow (blowing) are computed for both vapor and heat from which transfer coefficients are obtained. As evaporation increases with heating, vapor flux due to pressure-driven flow increases but remains small compared with diffusive flux. Vapor accumulation at the interface increases the diffusive flux, leading to an 8% increase in mass transfer coefficient. Heat transfer at the interface occurs through both conduction and flow, and the heat transfer coefficient shows a slight decrease (10%) as blowing increases with heating. The rate of heating had a minimal effect on the transfer coefficients.

Keywords: porous-media, boundary conditions, suction/injection, conjugate

Nomenclature

c_p	specific heat capacity, J $kg^{-1}K^{-1}$
C_g	molar density, kmol m^{-3}
$D_{eff,g}$	effective gas diffusivity, m^2s^{-1}
D	diffusivity, m^2 s^{-1}
h	heat transfer coefficient, W m^{-2} K^{-1}
$h^{'}$	lumped heat transfer coefficient, W m^{-2} K^{-1}
h_m	mass transfer coefficient of vapor, m s^{-1}
$h_m^{'}$	lumped mass transfer coefficient of vapor, m s^{-1}
$\dot{I}$	volumetric evaporation rate, kg m^{-3} s^{-1}
$\mathbf{J}$	mass flux, kg m^{-2} s^{-1}
k	thermal conductivity, W m^{-2} K^{-1}
k^p	permeability, m^2
K	non-equilibrium evaporation constant, s^{-1}
m	overall mass fraction
M_a, M_v	molecular weight of air and vapor
$\mathbf{n}$	total flux, kg m^{-2} s^{-1}
P	gas pressure, Pa
p_v	vapor pressure, Pa
$\mathbf{q}$	heat flux, J m^{-2} s^{-1}
R	universal gas constant, J $kmol^{-1}$ K^{-1}
S	saturation

t	time, s
T	temperature
u	velocity in the x-direction, ms^{-1}
v	velocity in the y-direction, ms^{-1}
V	volume, m^3
x	mole fraction

Greek Symbols

ρ	density, kg m^{-3}
λ	latent heat of vaporization, J kg^{-1}
ω_v, ω_a	mass fraction of vapor and air in relation to total gas
ϕ	porosity
μ	dynamic viscosity, Pa s

Subscripts

amb	ambient
a, g, v, w	air, gas, vapor, water
cap	capillary
eff	effective
eq	equilibrium
in	intrinsic
0	at time $t = 0$
r	relative, residual

sat	saturation
$surf$	surface
T	temperature
tot	total

4.2 Introduction

Boundary conditions are an integral part of a transport model and they are as important as the governing equations themselves. The governing equations of a transport model describe the physical phenomena occurring inside the solution domain. The interaction of the solution domain with the outside environment is expressed by the boundary conditions. Therefore, various thermal food processes can be modeled using the same set of governing equations but varying boundary conditions (e.g., frying and hot air drying). Hence, it is extremely important to have proper representative boundary conditions for accurate prediction.

Boundary conditions for heat and mass transfer can be of different types, representing different situations, as outlined here. In the case of heat transfer inside a solid surrounded by air, heat flux reaching the surface from inside the solid by conduction is convected away by the flowing air at the surface (forced convection). The heat transfer coefficient of the air, flowing over the surface, is a function of its velocity over the porous surface. A similar analogy can be made for mass transfer where a species transports to the surface due to diffusion inside the solid and is convected away by the flowing air at the surface. Another type of boundary condition, used in simulating the flow of a fluid in a pipe, is outlined next. In this case, no boundary condition is required at the exit. Such

a boundary condition is referred to as a convective flux boundary condition. Fluid reaching the pipe exit with a velocity (u) leaves the pipe with the same velocity. There is no further resistance to the flow at the exit.

In food systems, an enormous range of thermal processes can be viewed as involving transport of energy, moisture and, in some cases, fat through a hygroscopic porous medium. The phases move through the capillaries similar to a flow in a pipe. Heat is transferred due to the bulk flow of phases and also due to conduction inside the solid. Liquid phases do not diffuse but they move due to pressure driven flow. The gas components have binary diffusion within the gas phase and also pressure-driven flow. Therefore, a porous medium can be visualized as a combination of a solid matrix and pipes (capillaries) and, therefore, the boundary condition for heat and mass transport should be a combination of the two boundary conditions mentioned above. The combination of two boundary conditions means that diffusive heat and mass flux experience resistances at the surface but the convective flux goes out without any further resistance.

In modeling thermal food processes, boundary conditions for various processes have not been explored properly. Either the same boundary condition is used for different processes without any fundamental basis, or one of the diffusive or convective fluxes is ignored. For example, in the case of frying, there are various models with varying boundary conditions. In a moving boundary problem (Farkas et al., 1996; Pyre and Bouchan, 2006), the porous medium surface is treated like a pipe exit and the convective flux boundary condition is applied. The diffusive flow of water vapor is ignored inside the porous medium. In a distributed evaporation model (Ni and Datta, 1999; Yamsaesung and Moreira, 2002), the convective heat and mass transfer boundary condition is applied. In-

side the porous medium, there is both diffusion and bulk flow of mass species but the velocity of species at the surface is ignored in these models. In such situations, a lumped heat and mass transfer coefficient, which includes the effects of both diffusive and convective flow, can be used, but such a coefficient is not expected to be constant over time and will increase with bulk flow at the surface. Hubbard and Farkas (2000) showed this effect during the frying process through experiments. Halder et al. (2007) gave a time-varying heat and mass transfer coefficient to account for this effect during frying based on the experiments of Hubbard and Farkas (2000). Although such a boundary condition gave a better match with experimental results, it is an empirical relation and cannot be used for different situations. Therefore, there is an urgent need for a general formulation of boundary conditions that represents the physics accurately and can be used for a wide range of processes.

Several attempts (Eichhorn, 1960; Sparrow et al., 1959; Murthy, 2000; Volchkov, 2006; Bansod, 2005) have been made to understand the effects of injection (blowing out of the porous medium) or suction (blowing into the porous medium) at the porous surface in the overall heat and mass transfer at the surface. In each case, only the outside atmosphere was solved by providing a constant injection or suction velocity at the porous medium surface. It was shown that the suction velocity increased heat and mass transfer and injection velocity decreased them. Erriguible et al. (2005) solved the porous medium and the outside environment as a conjugate problem. In a conjugate problem, no boundary condition at the porous medium surface (an internal boundary) is required. In this study, however the porous medium problem was solved in one software application and the outside environment in another software application. Therefore, a boundary condition for momentum conservation was required at the

porous medium surface. This model is the first attempt to avoid giving boundary conditions at the porous medium surface by solving a conjugate model but due to solver limitations it was not able to avoid the problem completely. Specifying a boundary condition for momentum conservation equations changed the velocity profile, thus solving a different situation. Curcio et al. (2008) solved a conjugate model of hot air drying but did not use a porous medium model to describe the heat and mass transfer inside the food, thereby, simplifying the overall problem, which does not give an accurate picture of how heat and mass transfer coefficients vary during the process.

Therefore, there is a need for a fundamental understanding of boundary conditions at the porous surface and of how the injection/ suction velocity affects the heat and mass transfer coefficients over processing time. Thus, the objective of the present study is to solve a conjugate problem of microwave heating, containing both the porous material and the outside environment, and to discuss and quantify the factors on which the heat and mass transfer coefficients at the porous media surface depends.

The outline of this manuscript is as follows: First, a mathematical model of microwave heating where a conjugate model containing both a porous medium and the outside atmosphere is shown. This is followed by results from the conjugate problem and discussion of the boundary layer and the heat and mass transfer coefficients at the porous medium surface.

4.3 Mathematical model of conjugate system

For the microwave heating simulation, the porous food material and the outside atmosphere are solved together such that there is no need to provide any boundary conditions at the porous medium surface. Therefore, a multiphase porous medium model is developed that describes heat and mass transfer inside a porous material during microwave heating in conjugate with the air flow outside the porous material. Mass and energy conservation equations are developed and they include binary diffusion, capillary and convective modes of transport, and phase change such as evaporation-condensation. Evaporation is considered distributed throughout the porous domain. Outside the porous medium, there is binary diffusion between air and vapor and pressure-driven flow and there is no evaporation-condensation.

4.3.1 Problem description

A schematic of the problem description is shown in Figure 4.1. The restructured potato slab is assumed to be a porous medium. There are three phases: solid, liquid-water and gas. In a restructured potato, bound water is negligible so phase change from solid to liquid is ignored. This simplifies the overall model as porosity can be assumed to be constant and mass balance of the solid is not required. The gas phase is a mixture of air and water-vapor. A 2D heat and mass transfer problem is simulated. The problem is considered symmetric with $x = 0$ as the line of symmetry. No flux conditions for mass species and energy are specified at boundaries $y = 0$ and $y = 0.01$ m. The right-most boundary of the porous medium ($x = 0.01$ m) is the exposed surface where heat and mass

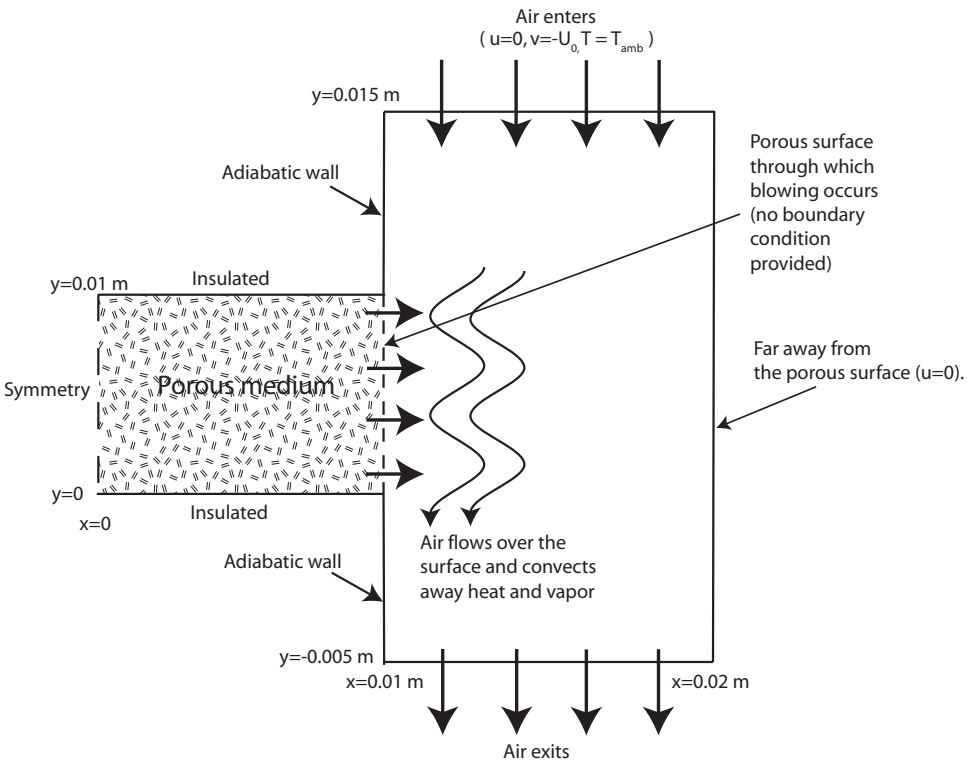

Figure 4.1: Schematic showing the computational domain of the conjugate problem of microwave heating (porous medium and outside atmosphere). The porous surface is an internal boundary and does not require any boundary conditions.

exchange with the environment takes place. The environment surrounding the restructured potato is in the gas phase (a mixture of water vapor and air) only. The air (gas phase) flows over the surface of the porous medium convecting away water-vapor and energy from the surface.

4.3.2 Assumptions

The assumptions made while formulating the developed multiphase framework are: 1) All the phases (solid, liquid and gas) are in continuum; 2) local ther-

mal equilibrium exists between all phases throughout the material; 3) pressure is shared by all phases as the effects of capillary pressure have been included as a diffusion term (Datta, 2007; Halder et al., 2007); 4) there can be a state of non-equilibrium between water in the solid and water-vapor in the gas phase, i.e., their concentrations are not given by the moisture isotherms; 5) deformation of the material during processing is not considered; 6) effects of gravity have been ignored.

4.3.3 Governing equations

The mathematical model consists of conservation equations for all the phases and components discussed above.

Mass balance of liquid water

Liquid-water is present inside the porous domain only. Therefore, the mass balance equation for liquid-water is solved in the porous domain only. In the porous domain, the porosity, ϕ, is defined as the fraction of the total volume occupied by pores, given by

$$\phi = \frac{V_g + V_w}{V} \tag{4.1}$$

where V_g and V_w are the volumes occupied by the gas and the liquid water phases, respectively, in an elemental volume V. Saturation of a phase is defined as the fraction of pore volume occupied by that particular phase. Saturation of the liquid-water and the gas phase are given by

$$S_w = \frac{V_w}{\phi V}$$

$$S_g = \frac{V_g}{\phi V} \tag{4.2}$$

The summation of saturation of the liquid-water and the gas phase should lead to unity (Eq. 5.5).

The mass balance equation for a phase solves for saturation of the phase. Equation 5.3 is solved to obtain the saturation of the liquid-water phase, S_w. The saturation of the gas phase, S_g, is calculated from Eq. 5.5.

$$\frac{\partial}{\partial t}(\phi \rho_w S_w) + \nabla \cdot \mathbf{n_w} = -\dot{I} \tag{4.3}$$

$$S_g + S_w = 1 \tag{4.4}$$

where $\dot{I}$ denotes the phase change from liquid-water to water-vapor in the gas phase.

The total flux of the liquid-water phase, $\mathbf{n_w}$, is due to the liquid pressure, $P - p_{i,cap}$, which is the difference between the gas pressure and the capillary pressure. The total flux term is given by Darcy's law (Datta 2007a) as

$$\begin{aligned}
\mathbf{n_w} &= -\rho_w \frac{k^p_{in,w} k^p_{r,w}}{\mu_w} \nabla (P - p_{w,cap}) \\
&= -\rho_w \frac{k^p_{in,w} k^p_{r,w}}{\mu_w} \nabla P + \rho_w \frac{k^p_{in,w} k^p_{r,w}}{\mu_w} \left(\frac{\partial p_{w,cap}}{\partial c_w} \nabla c_w \right) \\
&= -\rho_w \frac{k^p_{in,w} k^p_{r,w}}{\mu_w} \nabla P - D_w \nabla c_w
\end{aligned} \tag{4.5}$$

The first term in the right-hand side of the above equation represents flow due to gas pressure gradients and is significant in cases involving intensive heating of food materials such as microwave heating, deep fat frying, and contact heating at high temperature. The second term is rewritten in terms of capillary diffusivity, D_w.

Mass balance of water-vapor and air

The gas phase is a mixture of water-vapor and air and it is present both in the porous medium and in the outside environment. Therefore, it needs to be solved in both domains. Spatial variations in concentrations of water-vapor and air during microwave heating are obtained by solving the respective mass conservation equations in terms of their mass fractions, ω_v and ω_a, with binary diffusion (Bird et al., 2001):

$$\frac{\partial(\phi S_g \rho_g \omega_v)}{\partial t} + \nabla \cdot (u_g \rho_g \omega_v) = \nabla \cdot \left(\phi S_g \frac{C_g^2}{\rho_g} M_a M_v D_{eff,g} \nabla x_v \right) + \dot{I} \quad (4.6)$$

$$\omega_v + \omega_a = 1 \quad (4.7)$$

where $\phi S_g = 1$ and $\dot{I} = 0$ outside the porous medium. Inside the porous medium, they are given by Eq. 5.5 and 5.32 (discussed later). Because the same equations (Eq. 5.10 and 5.11) are solved in both the domains with different properties (ϕ and S_g), no boundary conditions are required at the porous medium surface ($x = 0.01\ m$).

Therefore, Eqs. 5.3 to 5.11 constitute the set of 4 equations from which the saturation S_w and S_g and mass fractions of components inside the gas phase, ω_v and ω_a can be obtained. Pressure and temperature inside the material are determined by invoking the gas phase mass conservation and energy conservation equations respectively, as discussed later. Note, however, that there are additional unknowns in these equations for which auxiliary equations will be needed, as discussed later (Eq. 5.32 for the evaporation rate, $\dot{I}$).

Momentum balance of gas phase

The momentum balance equation for a phase solves for the velocity of that phase. In a porous medium with low permeabilities, Darcy flow is valid (Bear, 1972). The air flowing outside the porous surface needs to be described by the Navier-Stokes equation as the inertia terms cannot be ignored. Since, a single equation needs to be solved for both the domains, such that no boundary condition is required at the porous surface, the modified Navier-Stokes equation (Eq. 4.8) for momentum balance, which includes the Darcy's term, is solved.

$$\frac{\partial((\phi S_g)\rho_g \mathbf{u_g})}{\partial t} + \nabla.((\phi S_g)^2 \rho_g \mathbf{u_g}\mathbf{u_g}) = -(\nabla P - \rho_g \mathbf{g}) + \mu \nabla^2 \mathbf{u_g} - (\phi S_g)\frac{\mu_g}{k^p_{r,g} k^p_{in,g}}\mathbf{u_g} \tag{4.8}$$

Although Eq. 4.8 is different from Darcy's equation, due to the additional terms, the inertial terms are shown to be negligible for low-permeability systems (Vafai and Tien, 1981; Datta, 2007a), so Eq 4.8 reduces to Darcy's equation inside the porous media. In the outside environment, the permeability is pushed to a very high value such that Darcy's term becomes negligible and Eq. 4.8 becomes a standard Navier-Stokes equation.

Continuity Equation to solve for pressure

The gas pressure, P, is calculated by solving the overall mass balance equation for the gas phase

$$\frac{\partial}{\partial t}(\phi S_g \rho_g) + \nabla \cdot (\rho_{\mathbf{g}} \mathbf{u_g}) = \dot{I} \tag{4.9}$$

where $\phi S_g = 1$ and $\dot{I} = 0$ outside the porous medium and inside the porous medium, as given by Eq. 5.5 and Eq. 5.32 (discussed later).

Ideal gas law is used to relate gas phase density and pressure

$$\rho_g = \frac{PM_g}{RT} \tag{4.10}$$

The pressure, P, is shared by all phases (the capillary pressure of liquid-water has been included as diffusion). However, equation 5.13 cannot be used if the saturation of the gas phase goes to zero in any region, as pressure then cannot be determined in the region, leading to the failure of the numerical solution (discussion follows). The gas phase can go to zero under various conditions: high condensation rate in any region, accumulation of liquids due to favorable pressure gradients, etc. One way to deal with the above problem is to prevent the gas phase from going to zero by forcing the gas phase saturation to a small value such that it does not affect the solution and at the same time does not require any further reformulations. In this problem, the gas phase is prevented from going to zero by introducing the drip flow of liquid-water (discussed later in the section on boundary conditions).

Energy Equation

Since thermal equilibrium is assumed to exist across all phases (e.g., all phases have the same temperature), the energy balance equation of the mixture (Eq. 5.14) is solved to calculate T:

$$\rho_{eff} c_{p,eff} \frac{\partial T}{\partial t} + (c_p \mathbf{n})_{fluid} \cdot \nabla T = \nabla \cdot (k_{eff} \nabla T) - \lambda \dot{I} + Q \tag{4.11}$$

Again, a single energy equation is used in both domains (the porous medium and the outside atmosphere) such that no boundary condition is required at the porous media surface. Inside the porous medium, the properties of the mixture are obtained by averaging those of the pure components, weighted by their

mass or volume fractions as appropriate:

$$\rho_{eff} = \sum_{j=1}^{b} c_j + \phi \left(\sum_{i=1}^{n-2} S_i \rho_i + S_g \rho_g \right) \tag{4.12}$$

$$c_{p,eff} = m_g(\omega_v c_{p,v} + \omega_a c_{p,a}) + \sum_{i=1}^{n-2} m_i c_{p,i} + \sum_{j=1}^{b} m_j c_{p,j} \tag{4.13}$$

$$(c_p \mathbf{n})_{fluid} = \sum_{i=1}^{n-2} \mathbf{n_i} c_{p,i} + \rho_g \mathbf{u_g} (\omega_v c_{p,v} + \omega_a c_{p,a}) \tag{4.14}$$

$$k_{eff} = \left(\sum_{j=1}^{b} \frac{c_j}{\rho_j} k_j \right) + \phi \left(\sum_{i=1}^{n-2} S_i k_i + S_g(\omega_v k_v + \omega_a k_a) \right) \tag{4.15}$$

Outside the porous medium for the surrounding atmosphere, the properties of the mixture are

$$\rho_{eff} = \rho_g \tag{4.16}$$

$$c_{p,eff} = \omega_v c_{p,v} + \omega_a c_{p,a} \tag{4.17}$$

$$(c_p \mathbf{n})_{fluid} = \rho_g \mathbf{u_g} (\omega_v c_{p,v} + \omega_a c_{p,a}) \tag{4.18}$$

$$k_{eff} = \omega_v k_v + \omega_a k_a \tag{4.19}$$

The volumetric heat source term, Q, in microwave heating is given by Lambert's law (Ni et al., 1999):

$$Q = \frac{Q_{surf}}{\delta(x)} \exp\left(- \int \frac{dx}{\delta(x)} \right) \tag{4.20}$$

where Q_s is the microwave flux at the surface and $\delta(x)$ is the penetration depth of microwaves at a distance x from the surface. The penetration depth is a function of of moisture content and is given in Table 1.

4.3.4 Boundary conditions

The whole intent of solving the conjugate problem was to avoid giving a boundary condition at the porous surface that becomes an internal boundary. There-

fore, no boundary condition is required for the energy equation (Eq. 5.14), the water-vapor conservation equation (Eq. 5.10), the gas continuity equation (Eq. 5.13) and the momentum conservation equation (Eq. 4.8) at the internal boundary $x = 0.01$ m. At other boundaries, insulated boundary conditions (with flux at zero) is imposed for the energy equation and the water-vapor conservation equation. For the gas momentum conservation and continuity equations, the boundaries $y = 0.015$ m and $y = -0.005$ m are treated as the inlet and the outlet, respectively. At the inlet, the air velocity is required. No boundary condition is required at the outlet. A symmetry boundary condition, at zero normal velocity and with stress at zero, is imposed at $x = 0.02$ m.

Since, liquid-water is present and solved only in the porous medium, a boundary condition needs to be given for the liquid-water conservation equation (Eq. 5.3) at the porous media surface ($x = 0.01$m). For microwave heating, it is assumed that liquid water can leave the surface in two ways: (1) vaporizing to water-vapor and being carried away by the outside air; (2) leaving the surface under pressure-driven flow when the surface is completely saturated with liquid-water (Ni and Datta, 1999). Therefore, the boundary condition for liquid water is:

$$\mathbf{n_w} = \begin{cases} 0 & S_w < 0.98 \\ -\rho_w \frac{k^p_{in,w} k^p_{r,w}}{\mu_w} \nabla P - D_w \nabla c_w & S_w > 0.98 \end{cases} \tag{4.21}$$

$$\tag{4.22}$$

The transition from no flux to drip flow of liquid water occurs at $S_w = 0.98$ instead of $S_w = 1$ (completely saturated) to prevent the gas phase from going to zero. If the gas phase goes to zero then Eq. 5.13 cannot be used because the pressure cannot be determined in the region, leading to the failure of the numerical solution. Therefore, by allowing drip flow to occur at $S_w = 0.98$, the

gas phase is prevented from going to zero and at the same time the solution is not affected.

4.3.5 Initial conditions

Initial conditions (I.C.s) are:

$$\text{I.C. for Eq. 5.13 :} \quad P = P_{amb} \tag{4.23}$$

$$\text{I.C. for Eq. 5.14:} \quad T = T_{amb} \tag{4.24}$$

$$\text{I.C. for Eq. 5.3:} \quad S_w = S_{0,w} \tag{4.25}$$

$$\text{I.C. for Eq. 5.10:} \quad \omega_v = \omega_{0,v} \tag{4.26}$$

Initially the restructured potato is at ambient pressure and temperature conditions. Depending on the composition of the food material, the initial phase saturation of water ($S_{0,w}$) is estimated. The water-vapor in air is in equilibrium with liquid-water initially. Using a moisture sorption isotherm, equilibrium water-vapor pressure at ambient temperature is calculated. For example, the mass fraction of vapor in the gas phase, ω_v at 25°C, is calculated as 0.02.

4.3.6 Phase change

The evaporation rate, distributed spatially and over time, is a complex function of food material and process parameters. Phase change is implemented using a non-equilibrium formulation, as explained in this section. In a non-equilibrium formulation, vapor may or may not be in equilibrium with water in the liquid and the solid phase. Therefore, the equilibrium relation, $p_v = p_{v,eq}$,

is replaced by an explicit expression for the evaporation rate, $\dot{I}$, for modeling of phase change (Le et al., 1995; Scarpa and Milano, 2002; Halder et al., 2007; Halder et al., 2010), given by:

$$\dot{I} = K(\rho_{v,eq} - \rho_v)S_g\phi \tag{4.27}$$

where $\rho_v = \rho_g\omega_v$ is the vapor density at a location that comes from solution. Here K is a material and process-dependent parameter signifying the rate constant of evaporation.

4.3.7 Input parameters and Numerical solution

Equations 5.3, 5.10, 5.13 and 5.14 are solved for the variables S_w, ω_v, P and T respectively, with boundary and initial conditions (Equations 4.23-4.26). Auxiliary conditions, such as Eq. 5.5, are used to compute the remaining variables. Input parameters are given in Table 1. A commercially available finite element software, COMSOL Multiphysics 3.5a (Comsol Inc, Burlington, MA), was used to solve these equations. The computational domain is shown in Fig. 4.1 . Simulation of microwave heating over a duration of 7 minutes took approximately 36 hours of CPU time for a timestep size of 0.01 second on a Intel Xeon 3.0 GHz PC with 16GB RAM.

4.3.8 Computation of heat and mass transfer coefficients

Heat and mass transfer coefficients are computed from the temperature and vapor flux profiles obtained from the solution process. The heat flux at the porous surface has two components: conductive flux, $\mathbf{q}_{cond}$, and convective flux, $\mathbf{q}_{conv}$. The lumped heat transfer coefficient, $h^{'}$, is calculated as:

$$h^{'} = \frac{\mathbf{q}_{cond} + \mathbf{q}_{conv}}{T_{surf} - T_{amb}} \tag{4.28}$$

The heat transfer coefficient, h, is calculated from the conductive heat flux only and the Nusselt number, Nu, is estimated from the calculated heat transfer coefficient.

$$h = \frac{\mathbf{q}_{cond}}{T_{surf} - T_{amb}} \tag{4.29}$$

$$Nu = \frac{hx}{k} \tag{4.30}$$

where T_{surf} is the temperature at the porous surface and T_{amb} is the temperature of the air flowing over the surface.

Similarly, for mass transfer, the vapor flux consists of two components: the binary diffusion flux, $\mathbf{J}_{bin}$, and the convective flux, $\mathbf{J}_{conv}$. The lumped mass transfer coefficient, $h_m^{'}$, is calculated as:

$$h_m^{'} = \frac{\mathbf{J}_{bin} + \mathbf{J}_{conv}}{\rho_g(\omega_v - \omega_{v,surf})} \tag{4.31}$$

The mass transfer coefficient, h_m, is calculated from the binary diffusion flux only, shown as:

$$h_m = \frac{\mathbf{J}_{bin}}{\rho_g(\omega_v - \omega_{v,surf})} \tag{4.32}$$

where ω_v is the vapor mass fraction at the porous surface and $\omega_{v,surf}$ is the vapor mass fraction of the air flowing over the surface.

Table 4.1: Input parameters used in the simulations of microwave heating

Parameter	Symbol	Value	Units	Source
Density				
water	ρ_w	998	kg/m^3	
vapor	ρ_v	Ideal gas	kg/m^3	
air	ρ_a	Ideal gas	kg/m^3	
solid	ρ_s	1528	kg/m^3	Farkas et al. (1996b)
Specific heat capacity				
water	c_{pw}	4178	J/kg K	Choi and Okos (1986)
vapor	c_{pv}	2062	J/kg K	Choi and Okos (1986)
air	c_{pa}	1006	J/kg K	Choi and Okos (1986)
solid	c_{ps}	1650	J/kg K	Choi and Okos (1986)
Thermal conductivity				
water	k_w	0.57	W/m K	Choi and Okos (1986)
vapor	k_v	0.026	W/m K	Choi and Okos (1986)
air	k_a	0.026	W/m K	Choi and Okos (1986)
solid	k_s	0.21	W/m K	Choi and Okos (1986)
Intrinsic permeability				
water	$k^p_{in,w}$	5×10^{-14}	m^2	Ni and Datta (1999)
air and vapor	$k^p_{in,g}$	10×10^{-14}	m^2	Ni and Datta (1999)
Relative permeability				
water	$k^p_{r,w}$	$((S_w - 0.08)/0.92)^3$		Bear (1972)
air and vapor	$k^p_{r,g}$	$(1 - S_w)/0.92$		Bear (1972)
Capillary diffusivity				
water	$D_{w,cap}$	$10^{-8} \exp(-2.8 + 2M)$		Ni and Datta (1999)
Viscosity				
water	μ_w	0.988×10^{-3}	Pa s	
air and vapor	μ_g	1.8×10^{-5}	Pa s	
Latent heat of vaporisation	λ	2.26×10^6	J/kg	
Porosity	ϕ	0.928		Farkas et al. (1996)
Vapor diffusivity in air	$D_{eff,g}$	2.6×10^{-6}	m^2/s	
Ambient pressure	P_{amb}	101325	Pa	
Microwave surface flux	Q_{surf}	30000	W/m^2	Ni et al. (1999)
Free stream velocity	U_0	0.1	ms^{-1}	

4.4 Results and Discussion

Predicted temperature, moisture and pressure are computed as functions of position and time for the conjugate problem (the porous medium (potato), together with the surrounding gas). Results based on boundary layer theory for non-porous and porous plates are compared with analytical solutions. The effects of blowing on the boundary layer thickness is shown. The contributions of pressure-driven flow, diffusion, and evaporation on heat and mass transfer at the surface are discussed next. Sensitivity analysis with respect to the free stream velocity, U_0, and the heating rate, by changing Q_{surf}, is shown next. Finally, the implications of the study for food processes are discussed.

4.4.1 Temperature, moisture and pressure profiles for the conjugate problem

Figure 4.2 shows the temperature profiles at various times during microwave heating of the porous medium. The temperature at the porous medium surface rises rapidly to 73°C during the first 4 minutes of microwave heating, and then slowly to 90°C during the next 6 minutes, starting from the initial value of 20°C. During the initial 4 minutes of heating, the evaporation rate is not high (as discussed later in connection with Figure 4.17c) and a major portion of the microwave heat source goes to increase the temperature of the domain. During the next 6 minutes of heating, as the temperature of the domain rises above 70°C, evaporation becomes significant and a major portion of the microwave heat source is used as latent heat of vaporization, which explains the slow rate

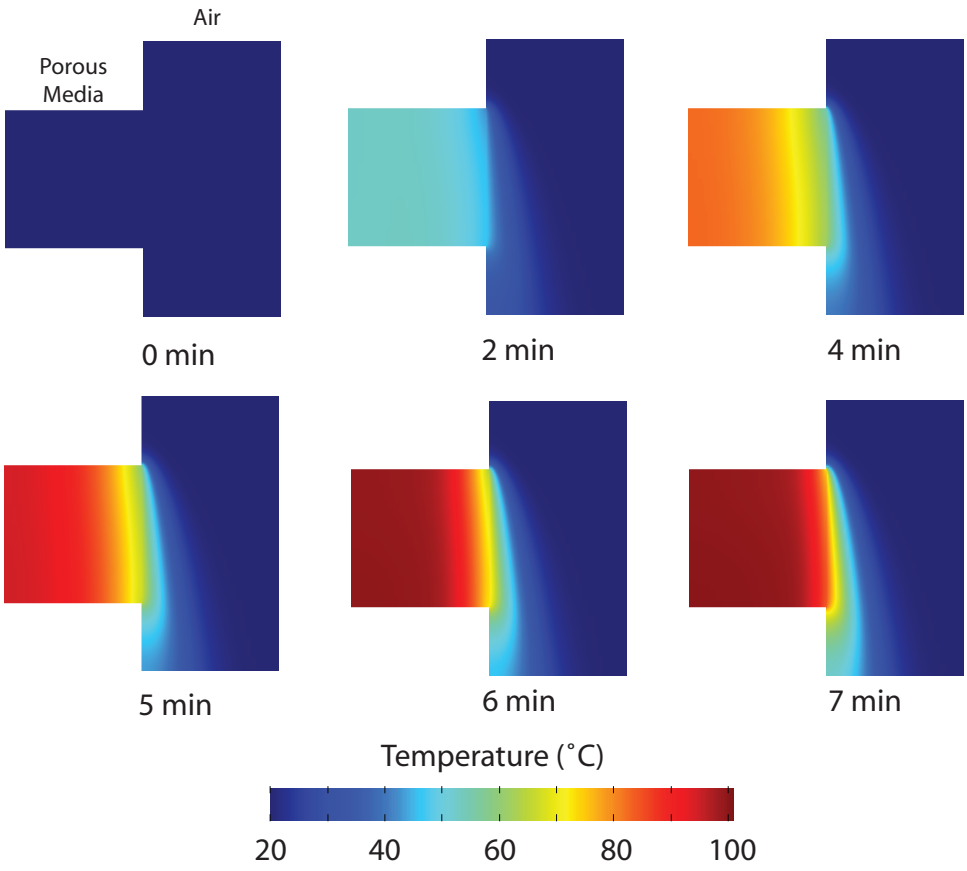

Figure 4.2: Spatial temperature profiles at various times obtained from the simulation of the conjugate problem with microwave heating of the porous medium. The initial temperature of the domain was 20°C.

of temperature rise in the porous domain in the latter part of the heating process. The surface temperature is slightly less than the core temperature as the air flowing over the porous medium surface is at a lower temperature (20°C) and thereby cools the surface.

Figures 4.3 and 4.4 show the liquid-water saturation and the water-vapor mass fraction at various times. The initial liquid water saturation of the sample is 0.5, which rises to 0.69 near the surface after 7 minutes of heating (Figure 4.6a). As the sample is heated, liquid-water evaporates inside the domain, leading to

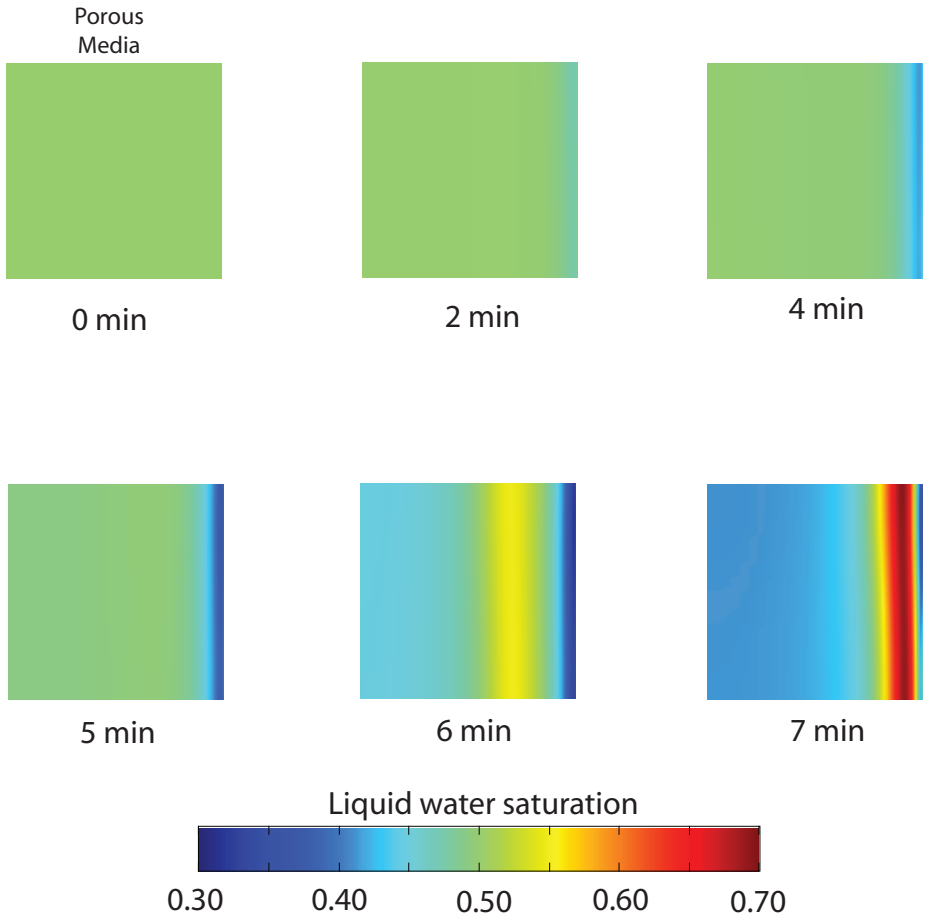

Figure 4.3: Spatial liquid-water saturation (S_w) profiles at various times obtained from the simulation of the conjugate problem with microwave heating of the porous medium. Only the porous domain is shown as liquid-water is present in the porous domain only. The initial liquid-water saturation in the porous medium domain was 0.5.

an increase in pressure (shown in Figure 4.6b), causing liquid-water and gas to move towards the surface. The amount of water removed from the surface is less than that coming to the surface, so there is a buildup of water at the surface, as shown in Figure 4.6a. There is continuous evaporation of liquid-water to water-vapor at the surface and the water-vapor is carried away by dry air flowing over the surface.

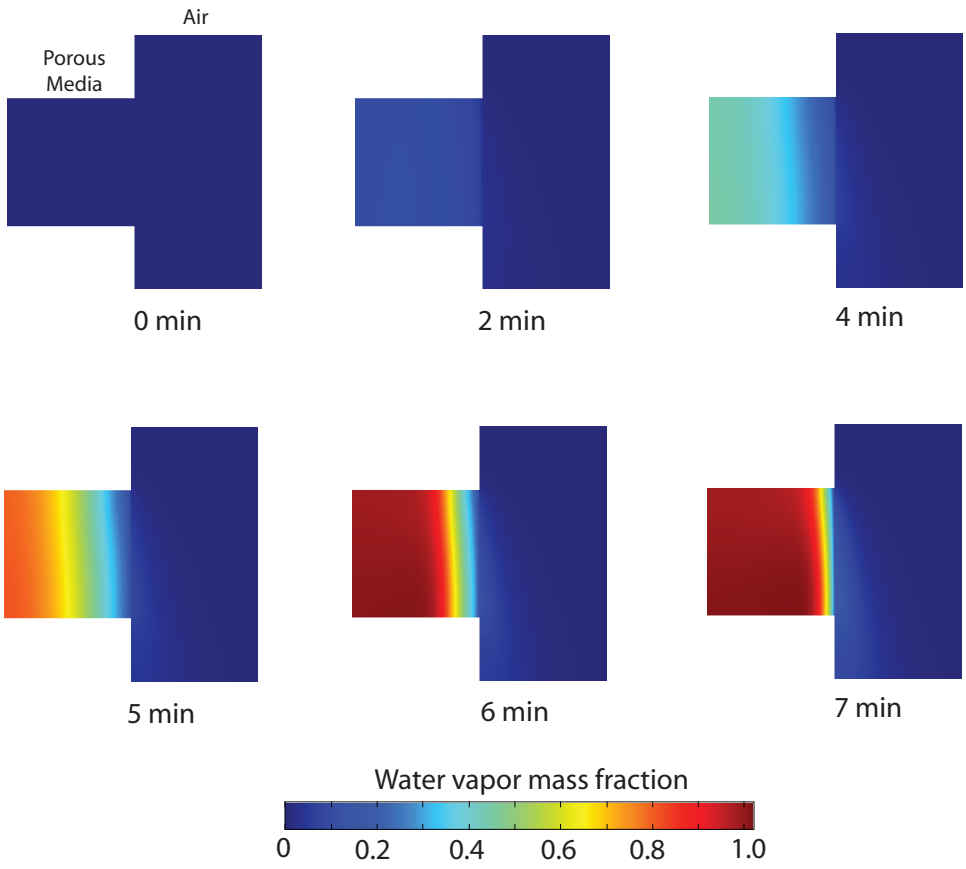

Figure 4.4: Spatial water-vapor mass fraction (ω_v) profiles at various times obtained from the simulation of the conjugate problem with microwave heating of the porous medium. The initial vapor mass fraction in the domain was 0.02.

Figure 4.5 shows the evolution of gas pressure in the porous domain during heating. As the sample is heated, evaporation causes the gas pressure inside the sample to rise slowly to 1450 Pa after 5 minutes of heating and then rapidly to 4000 Pa over the next 2 minutes of heating. The slow initial rise is due to slow evaporation at lower temperatures, whereas the rapid pressure rise after 5 minutes of heating is due to higher temperatures and the continued low rate of water-vapor removal from the surface.

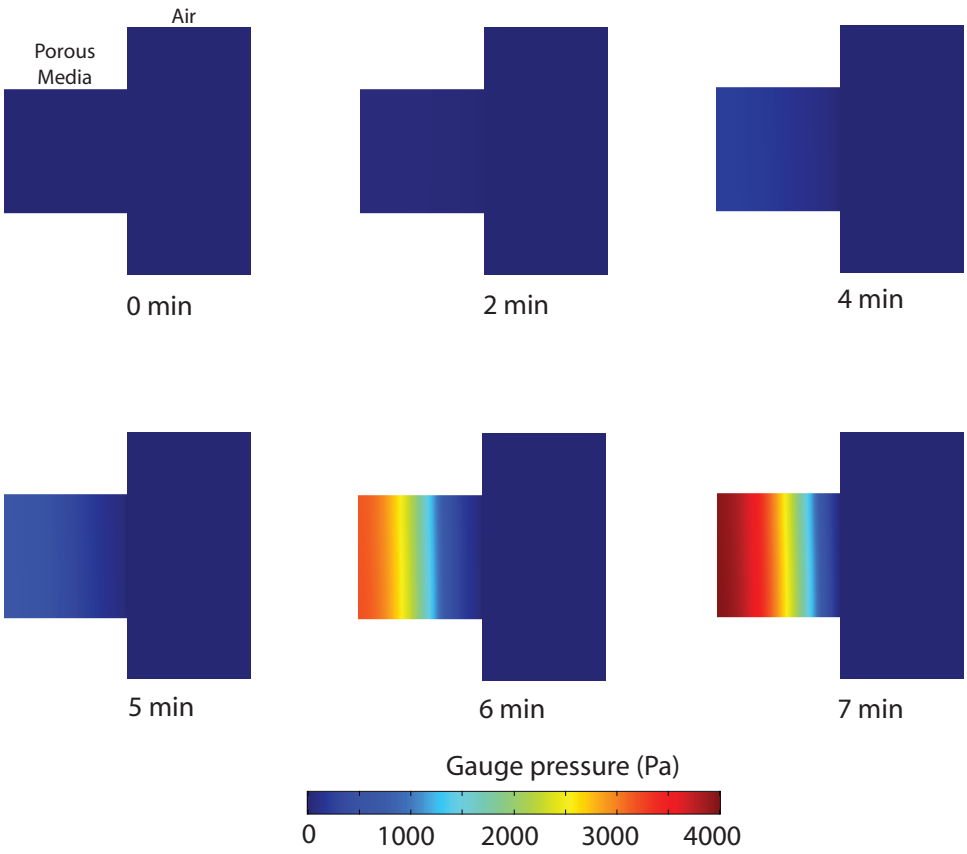

Figure 4.5: Spatial gauge pressure ($P - P_{atm}$) profiles at various times obtained from the simulation of the conjugate problem with microwave heating of the porous medium. The initial pressure in the domain was 101325 Pa (atmospheric pressure).

4.4.2 The boundary layer hypothesis cannot be used in this problem

The boundary layer theory is valid if the slenderness postulate is satisfied (Bejan, 1991). The postulate states that the thickness of the boundary layer (d) should be very small compared with the length along the flow (L). As can be seen in Figure 4.7, the thickness of the thermal gradient zone for this problem is comparable to the length of the surface. Therefore, boundary layer theory

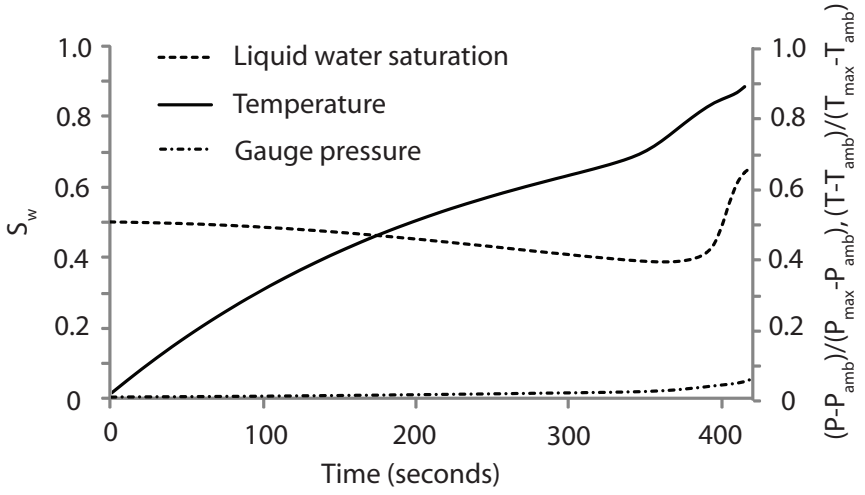

(a)

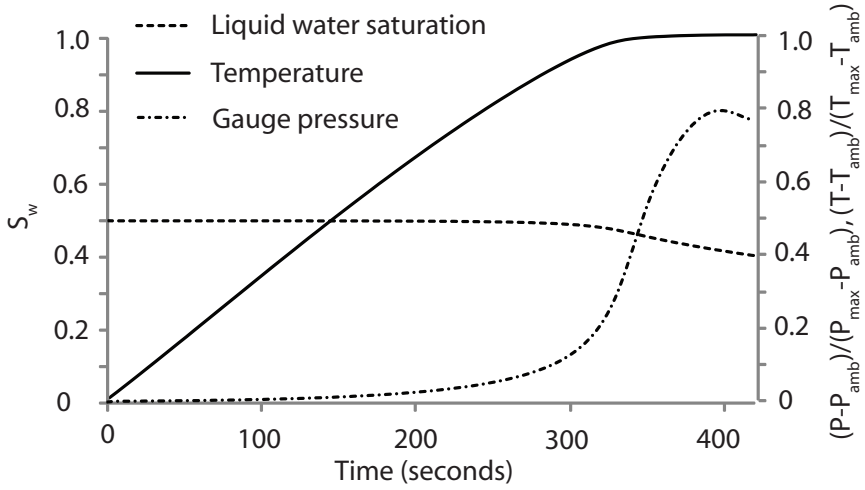

(b)

Figure 4.6: History profiles of temperature, T, water saturation, S_w, and pressure, P, obtained from the simulation of the conjugate problem with microwave heating of the porous medium for (a) near the surface (0.0005 m from the surface) and (b) near the center (0.0095 m from the surface). The saturation, temperature and pressure are divided by their maximum values (P_{max}=106325 Pa and T_{max}=373 K)

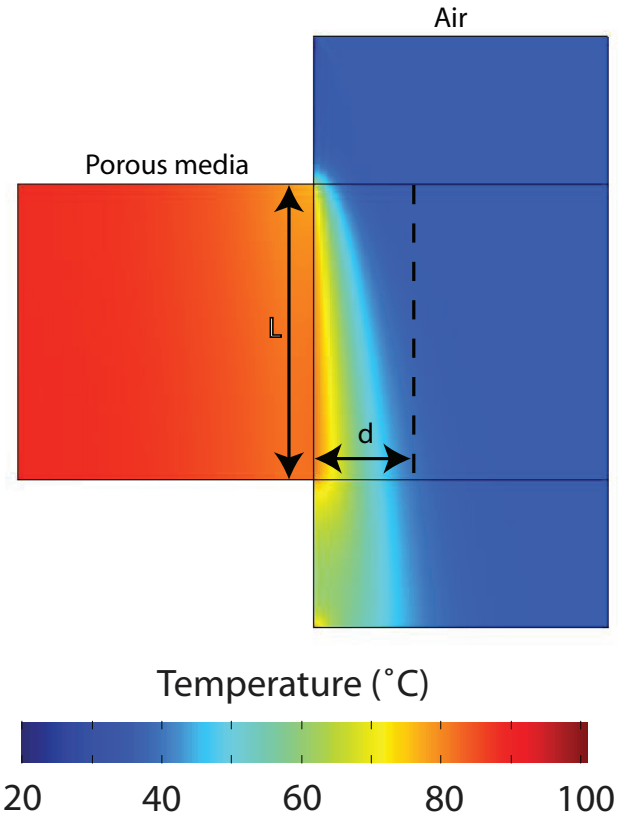

Figure 4.7: Illustration of boundary layer thickness at the porous surface for heat transfer. The boundary layer hypothesis implies that the thickness of the gradient zone (d) must be smaller than the characteristic length (L) of the sample ($d << L$). The above figures show that d is comparable with L, and hence the boundary layer assumption is not valid for the present situation.

cannot be applied to this problem.

4.4.3 Validations of the simulation process

Direct comparison with experimental results for the conjugate problem of microwave heating of a porous medium with air flow over it was not possible due to lack of availability of such data. In order to build confidence in the numerical

solution process, we compare three related situations for which limited analytical solutions are available. First, we simulate flow over a flat plate with no blowing (Figure 4.8, with $u = 0$ at $x = 0$) and compare it against the boundary layer solution (in regions where such a solution is valid). Figure 4.9a shows the comparison of the local Nusselt number versus the local Reynolds number obtained from the analytical solution from boundary layer theory and our simulation for a flat plate without blowing. The simulation results do not match with the analytical solution at the low local Reynolds number, since the boundary layer theory is not valid near the leading edge (low local Reynolds number). At the high local Reynolds number, the analytical and the simulation results match closely, showing the accuracy of the model in predicting boundary layer results for a flat plate. Figure 4.9b compares the heat transfer coefficient along the surface obtained from the analytical solution and our simulation. Again, the analytical solution is not valid near the leading edge and therefore the simulation results are off in this region. Far away from the leading edge, the heat transfer coefficient obtained from our simulation matches very closely to that obtained from the analytical solution.

Next, flow over a flat porous plate with blowing (Figure 4.8) was simulated and the results were compared in Figure 4.10 with the analytical solutions obtained from Bejan (1991). The blowing velocity at the porous surface is 1.6×10^{-3} ms^{-1} and the free stream velocity is 0.1 ms^{-1}. The figure shows the variation in $Nu_x/Re_x^{0.5}$, with the blowing parameter, $u_{surf}\,Re_x^{0.5}/U_0$, for the analytical solution and our simulation. Here again the analytical solution and the simulation results do not match closely since the velocity profiles obtained from the simulation (Figure 4.11, with blowing) do not match the expected velocity profile from boundary layer theory (Blasius profile). Boundary layer theory

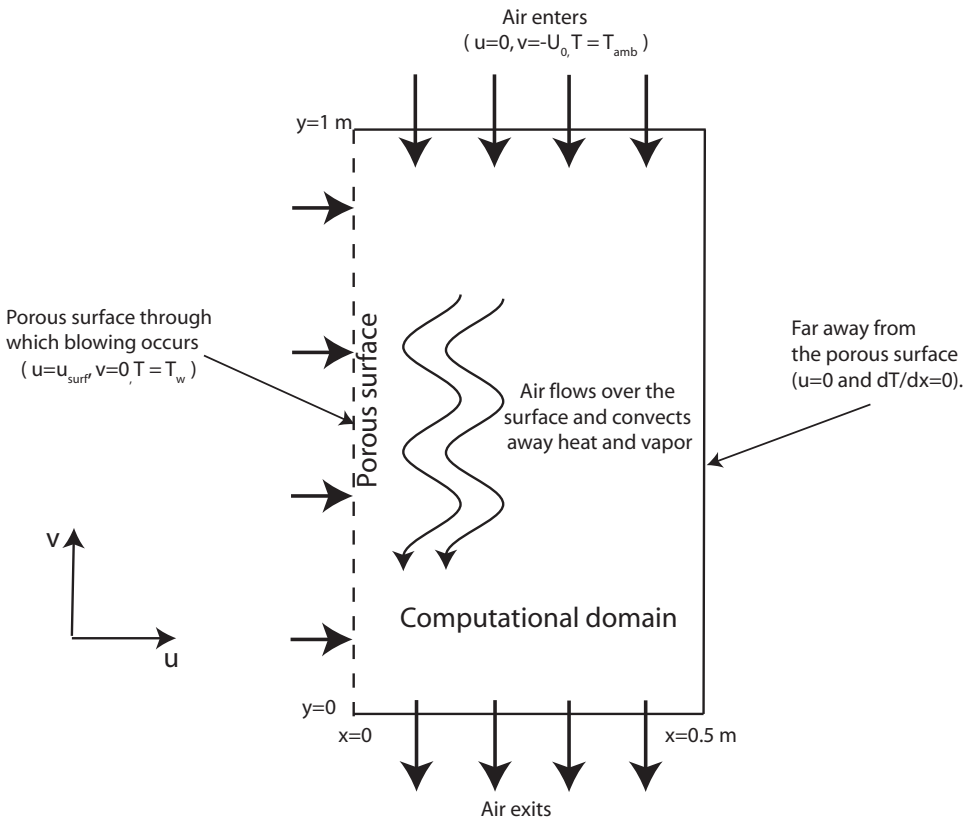

Figure 4.8: Schematic showing the computational domain of the non-conjugate problem where air is flowing over a permeable surface. A constant injection/ suction velocity is given at the porous medium surface to study its effect on the heat transfer coefficient. To simulate flow over a flat plate, the surface velocity, u_{surf}, is put to zero.

does not assume that there is a reduction in mass flow due to the presence of a boundary layer compared with an inviscid case with slip at the wall. When such an assumption is not made, as in case of Navior-Stokes equations, a hook develops in the velocity profile to accommodate the mass displaced by the boundary layer, as shown in Figure 4.11. The hook is real and the numerical solution, without the assumptions in the analytical solution, shows the hook. The formation of the hook affects all the gradients (velocity, thermal and mass transfer)

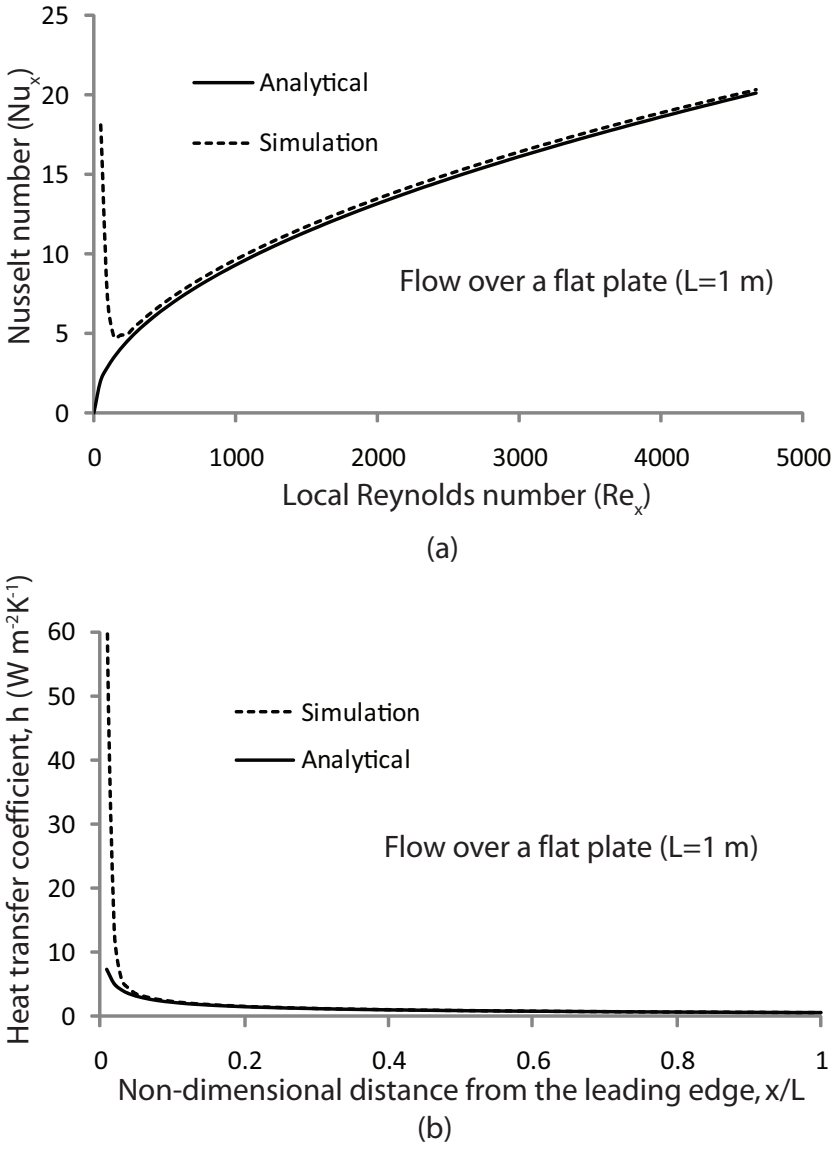

Figure 4.9: Results from simulation of the non-conjugate problem without blowing (Figure 4.8) are compared with the analytical solution from the boundary layer theory for flow over a flat plate (without blowing): (a) Local Nusselt number obtained for the corresponding local Reynolds number; (b) Heat transfer coefficient along the distance from the leading edge.

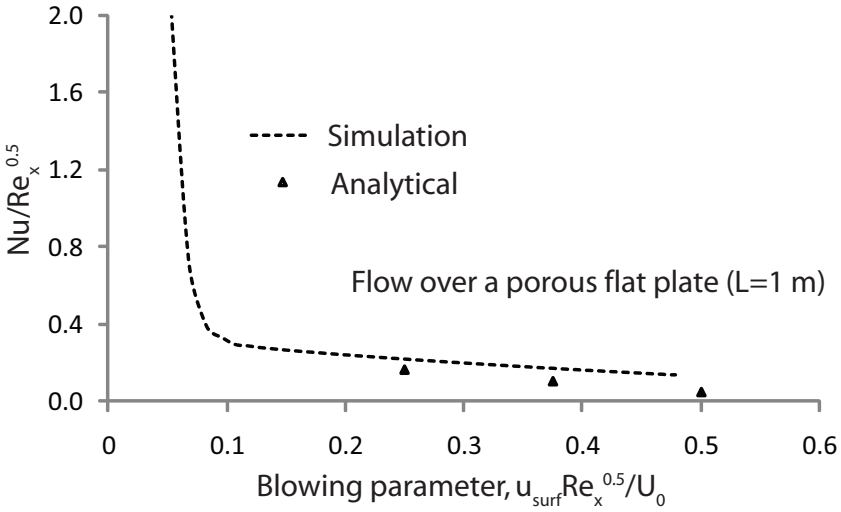

Figure 4.10: Simulation results for flow over a porous flat plate with blowing (Figure 4.8) are compared with the analytical solution from the boundary layer theory that includes blowing (Bejan, 1991). The blowing velocity at the porous surface is 1.6×10^{-3} ms^{-1} and the free stream velocity is 0.1 ms^{-1}.

and therefore the calculated Nusselt number (in Figure 4.10) does not match as closely with the analytical solution even far from the leading edge. The hook in Figure 4.11 is more pronounced for blowing than when there is no blowing due to the accommodation of additional mass coming from the porous surface. Therefore, we obtained a better match in the case of flow over a flat plate than when blowing is included. Although the analytical solutions have limitations, comparison with analytical solutions helped establish some level of trust in our numerical simulations.

Finally, another possible avenue toward validation of our computations would be to compare the results from the conjugate problem at an instant of time with results from blowing over a flat plate (Figure 4.12, with unheated lengths before and after the porous surface, comparable to the geometry for conjugate

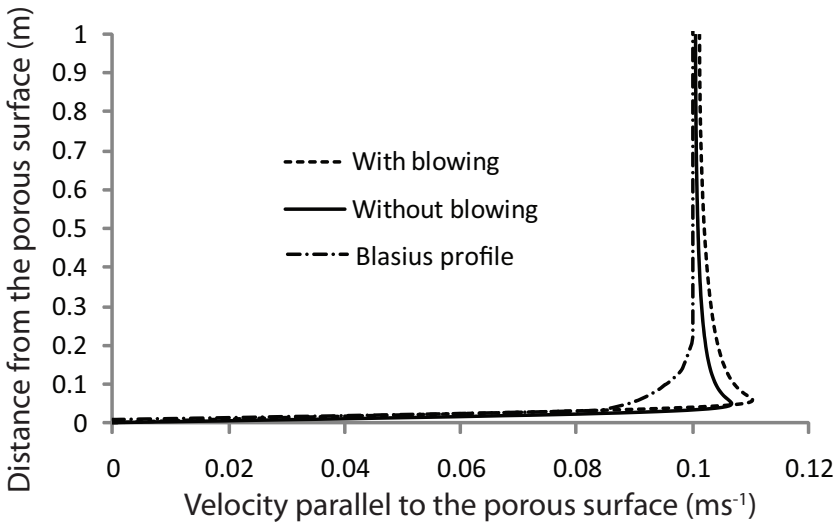

Figure 4.11: Velocity profiles obtained from the simulations (both lines above) do not match those from the Blasius solution (boundary layer theory). The hook (sharp peak near the wall) in the figure is due to the displacement effect caused by the boundary layer, an effect ignored in the boundary layer theory.

case) with the same instantaneous blowing velocity obtained from the conjugate problem (i.e., 1.6×10^{-3} ms^{-1} after 7 minutes of heating). In Figure 4.13, the ratio, $Nu_x/Re_x^{0.5}$, plotted against the blowing parameter, $u_{surf}\,Re_x^{0.5}/U_0$, matches very closely for the two cases, the conjugate (Figure 4.1) and the non-conjugate problem (Figure 4.12) with the same blowing velocity as the conjugate problem.

4.4.4 The effect of blowing velocity on the boundary layer

Figure 4.14 shows that the velocity of gas coming out of the porous medium (blowing velocity) increases from 0 to 1.6×10^{-3} ms^{-1} during the first 7 minutes of heating. The increase in blowing velocity at the surface is due to the increased pressure gradient from evaporation inside the porous domain. For flow through

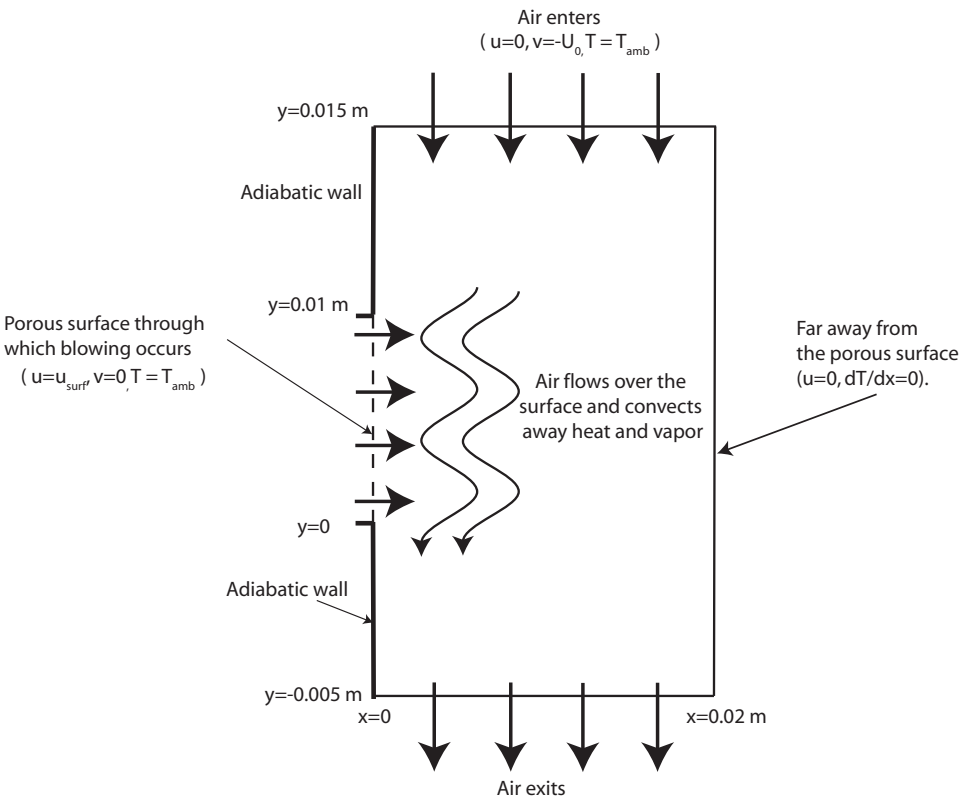

Figure 4.12: Schematic showing the computational domain of the non-conjugate problem where air is flowing over a permeable surface. A constant injection/ suction velocity, obtained from the conjugate problem after 7 minutes of heating, is given at the porous medium surface.

a porous surface, the Nusselt number, Nu_x, decreases as the blowing parameter, $u_{surf}\,Re_x^{1/2}/U_0$, increases (Bejan, 1991). Therefore, the effect of blowing on a longer surface, where the local Reynolds number, Re_x, is high far from the leading edge, would be to make the local Nusselt number even smaller. For the conjugate problem in this study, the surface is short (the length is 1 cm) and the maximum blowing velocity reached after 7 minutes of heating is 1.6×10^{-3} ms^{-1}. Therefore, in the transient simulation, there should be a decrease in the Nusselt number with time and hence a decrease in the heat transfer coefficient

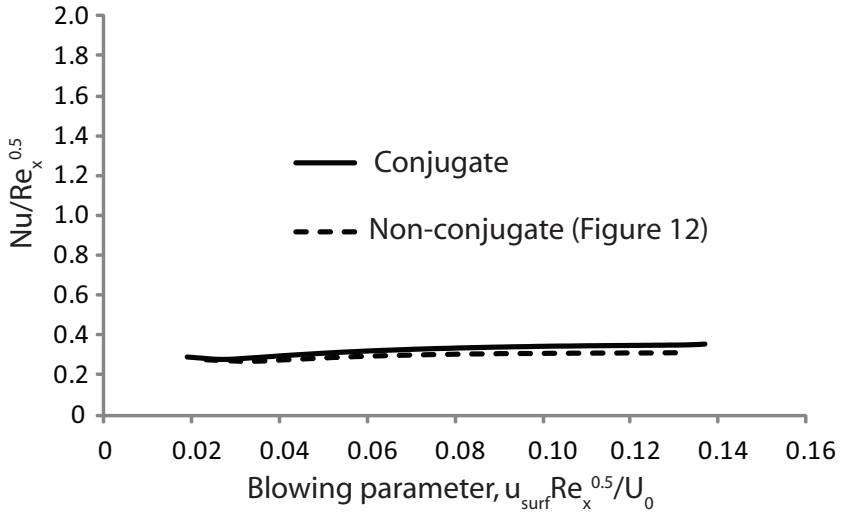

Figure 4.13: Simulation results from a simpler case (the non-conjugate problem without the porous medium, shown in Figure 4.12) is compared with that from the conjugate problem after 7 minutes of heating. The blowing velocity at the porous surface of the flat plate is 1.6×10^{-3} m/s, which is same as that obtained from the conjugate problem after 7 minutes of heating.

with time. This is indeed observed in Figure 4.15 although the decrease cannot be seen in Figure 4.15a but can be seen in the enlarged Figure 4.15b. The observed decrease in heat transfer coefficient is approximately 10%.

4.4.5 Heat and Mass transfer coefficients

The heat transfer coefficient, h, at the porous medium surface, shown in Figure 4.15a, varies significantly along the surface. At the entry point, h is very high but decreases with distance from the entry point and asymptotes between 8 $\mathrm{Wm^{-2}K^{-1}}$ and 9 $\mathrm{Wm^{-2}K^{-1}}$. The heat transfer coefficient varies by approximately 10% with time far from the leading edge, where the local Reynolds number is highest and therefore the blowing parameter is highest.

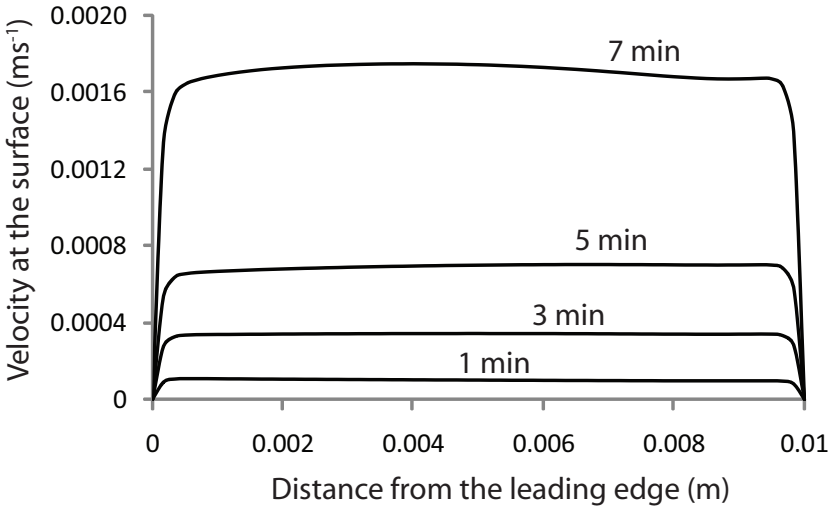

Figure 4.14: Velocity of gas normal to the porous medium surface at various times when the ambient air speed is 0.1 ms^{-1}, plotted as a function of distance from the leading edge of the porous surface. The gas velocity increases with time as the pressure inside the porous domain increases.

The mass transfer coefficient at the porous medium surface, shown in Figure 4.16, also varies significantly along the surface, similar to the heat transfer coefficient. At the entry point, h_m is high and decreases along the length of the surface, and finally asymptotes between 0.011 and 0.010 m/s for different times. Away from the leading edge, however the mass transfer coefficient increases with time, unlike the heat transfer coefficient. The binary diffusion flux is given by: $\phi S_g C_g^2 M_a M_v D_{eff,g} \nabla x_v / \rho_g$, where C_g is the molar density of gas. Due to the high rate of evaporation near the surface and the low rate of vapor removal, the molar density increases, thereby increasing the diffusion rate and mass transfer coefficient. As the blowing parameter increases with time, it should decrease the mass transfer coefficient. But as shown in Figure 4.17c, evaporation increases significantly with time and this will cause the mass transfer coefficient to increase. The increase due to evaporation is more than the

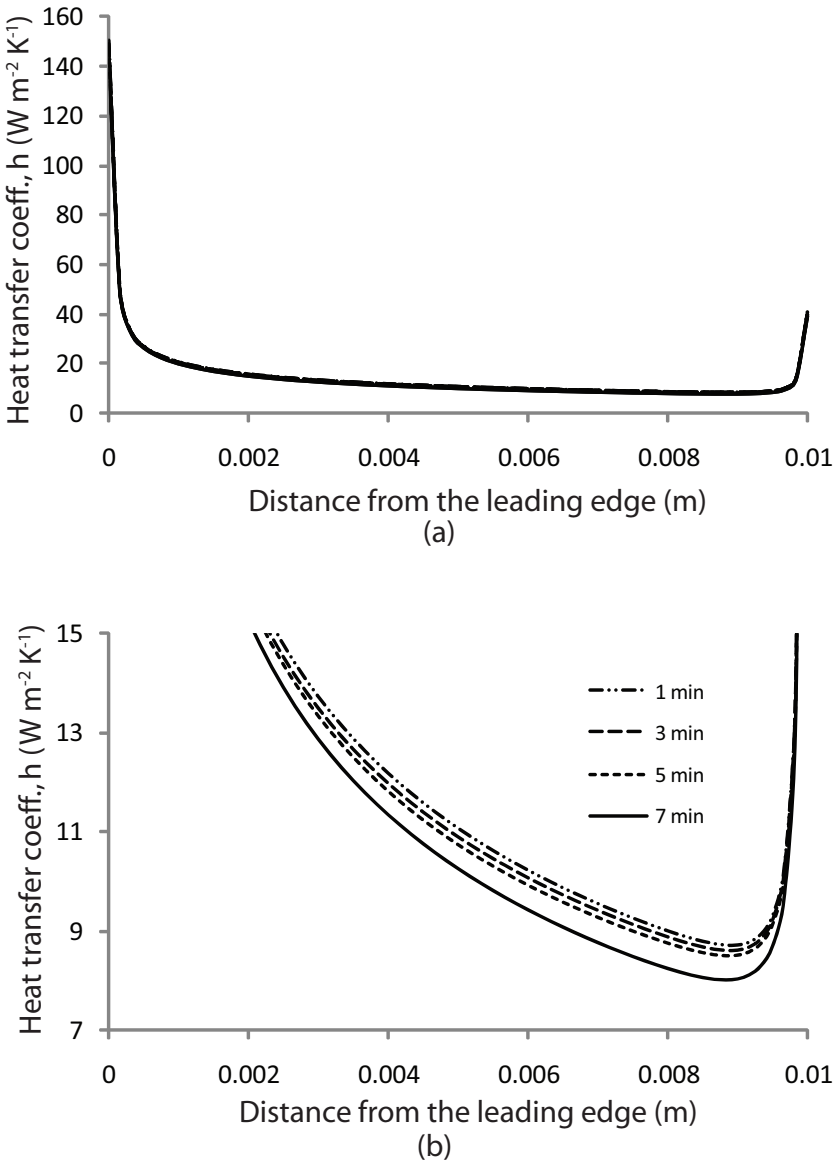

Figure 4.15: The heat transfer coefficient along the porous surface at various times when the ambient air speed is 0.1 ms^{-1} showing how the heat transfer coefficient decreases with time. Magnified image near the trailing edge is shown in (b). Distances are measured from the leading edge of the porous surface.

decrease due to blowing, causing an overall increase in mass transfer coefficient with time.

4.4.6 Contributions of convection, diffusion and evaporation to water-vapor transfer at the boundary

Figures 4.17a and 4.17b show the diffusive and convective vapor fluxes at the porous medium surface, respectively. Both fluxes increase with time, but the diffusive vapor flux is the dominant one at all the times (at least ten times more than the convective vapor flux). Figure 4.17c shows the evaporation rate at the surface at various times. A high rate of continuous generation of vapor causes an increase in the diffusion rate, as explained in the previous section. Therefore, evaporation at the surface also dominates the vapor transfer at the surface and this shows up in the diffusion term. This is why the mass transfer coefficient increases with time as opposed to decreasing due to blowing.

With diffusive flux at the surface being at least ten times greater than the convective flux at all times, a lumped mass transfer coefficient at the porous surface will be affected by a 10% or lower contribution by the convective flux. The use of a constant (e.g., as opposed to varying with time) value of the lumped mass transfer coefficient (e.g., Ni et al., 1999) can be justified as the contribution of convective flux is low.

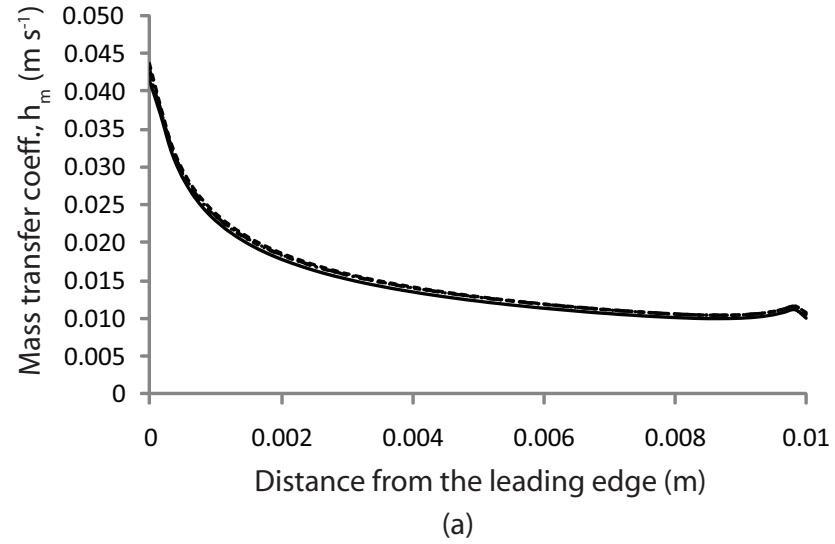

Figure 4.16: The mass transfer coefficient along the porous surface at various times when the ambient air speed is 0.1 ms^{-1} showing how the mass transfer coefficient increases with time due to evaporation. Magnified image near the trailing edge is shown in (b). Distances are measured from the leading edge of the porous surface.

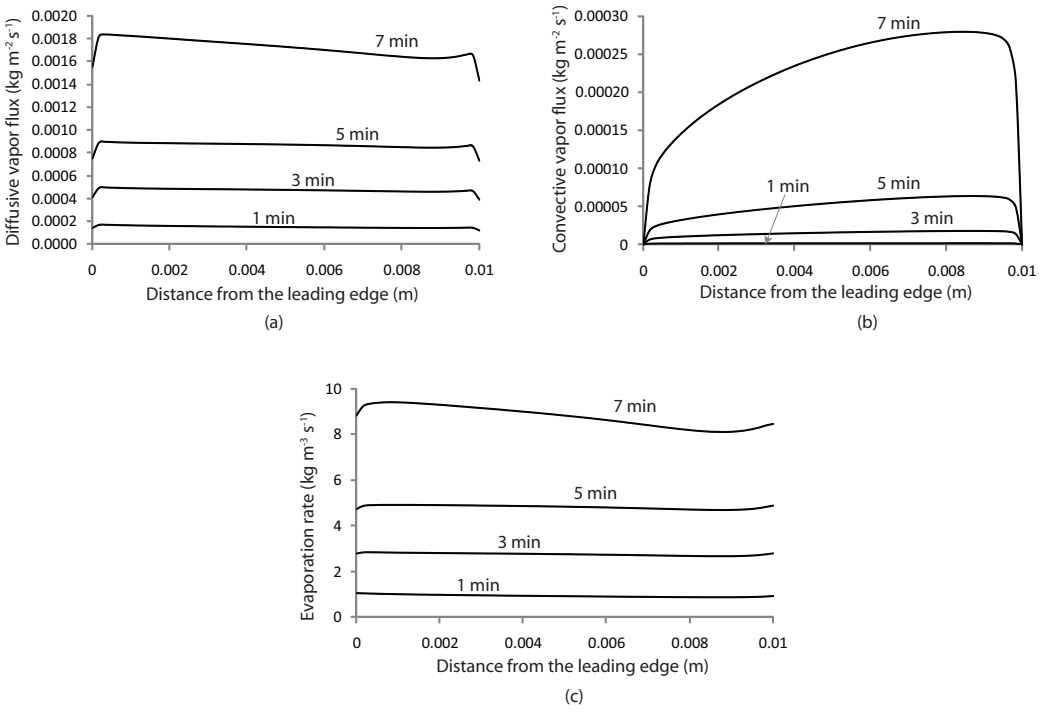

Figure 4.17: (a) Diffusive vapor flux (b) convective vapor flux and (c) evaporation rate along the porous surface at various times when the ambient air speed is 0.1 ms^{-1}. Distances are measured from the leading edge of the porous surface.

4.4.7 Contributions of convection, conduction and evaporation to heat transfer at the boundary

As shown in Figure 4.18, both the conductive and convective heat fluxes at the surface are more comparable, unlike mass transfer. There is no exchange of energy with the outside atmosphere due to evaporation. The liquid water takes heat from the porous surface to evaporate and this is accounted for in the governing equations. Therefore, there is no contribution of evaporation to heat transfer at the boundary. Since the conductive flux at the surface is comparable to the convective vapor flux at the surface, a constant (over time) value of

lumped heat transfer coefficient at the porous surface cannot be justified. The heat transfer coefficient should change with time as the blowing at the surface becomes significant. The best approach in such problems is to separate out the conductive and convective heat fluxes. The convective heat flux leaves the surface without further resistance, while there is a heat transfer coefficient to account for the conductive heat flux.

4.4.8 Effects of free stream velocity and heating rate (of the porous medium) on the heat transfer coefficient

As the free stream velocity is increased from 0.1 ms^{-1} to 1 ms^{-1}, the flowing air takes away more heat from the porous surface, showing an increase in the heat transfer coefficient. Boundary layer theory predicts that the heat transfer coefficient is directly proportional to the square root of the Reynolds number. Therefore, the heat transfer coefficient should increase by 3.28 times when the Reynolds number goes up by a factor of 10. Similar results have been obtained from our simulations (shown in Figure 4.19a) where the heat transfer coefficient increases by three times as the free stream velocity increases by a factor of 10. Another interesting observation made from the simulation is that the peak blowing velocity at the surface decreased from 1.6×10^{-3} ms^{-1} to 1.2×10^{-3} ms^{-1} as the free stream velocity increases ten times. The increased free stream velocity caused faster removal of vapor from the surface, which reduced the pressure development and therefore, the pressure-driven flow. Due to the decreased blowing velocity that accompanies the increased free stream velocity in this conjugate problem, the blowing parameter decreases by more than ten fold, making

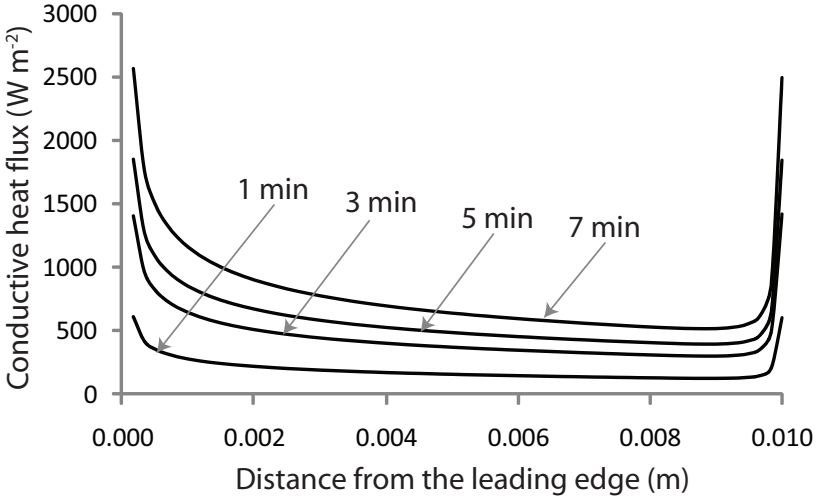

(a)

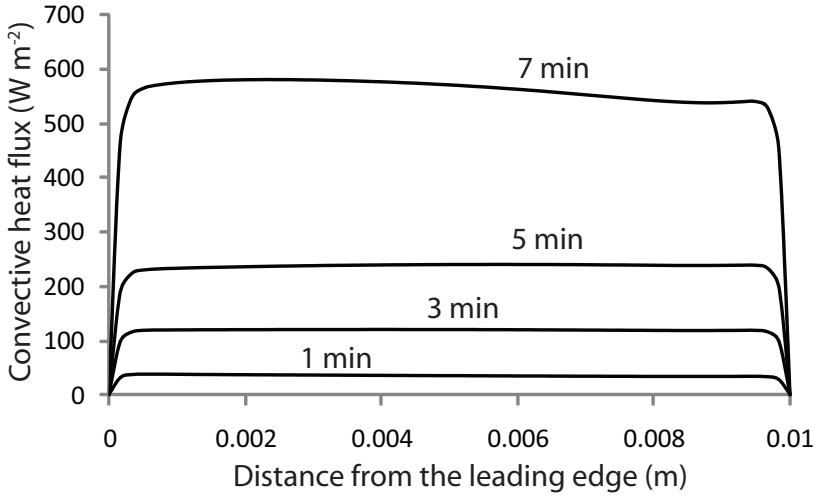

(b)

Figure 4.18: (a) The conductive heat flux and (b) the convective heat flux along the porous surface at various times when the ambient air speed is 0.1 ms^{-1}. Distances are measured from the leading edge of the porous surface.

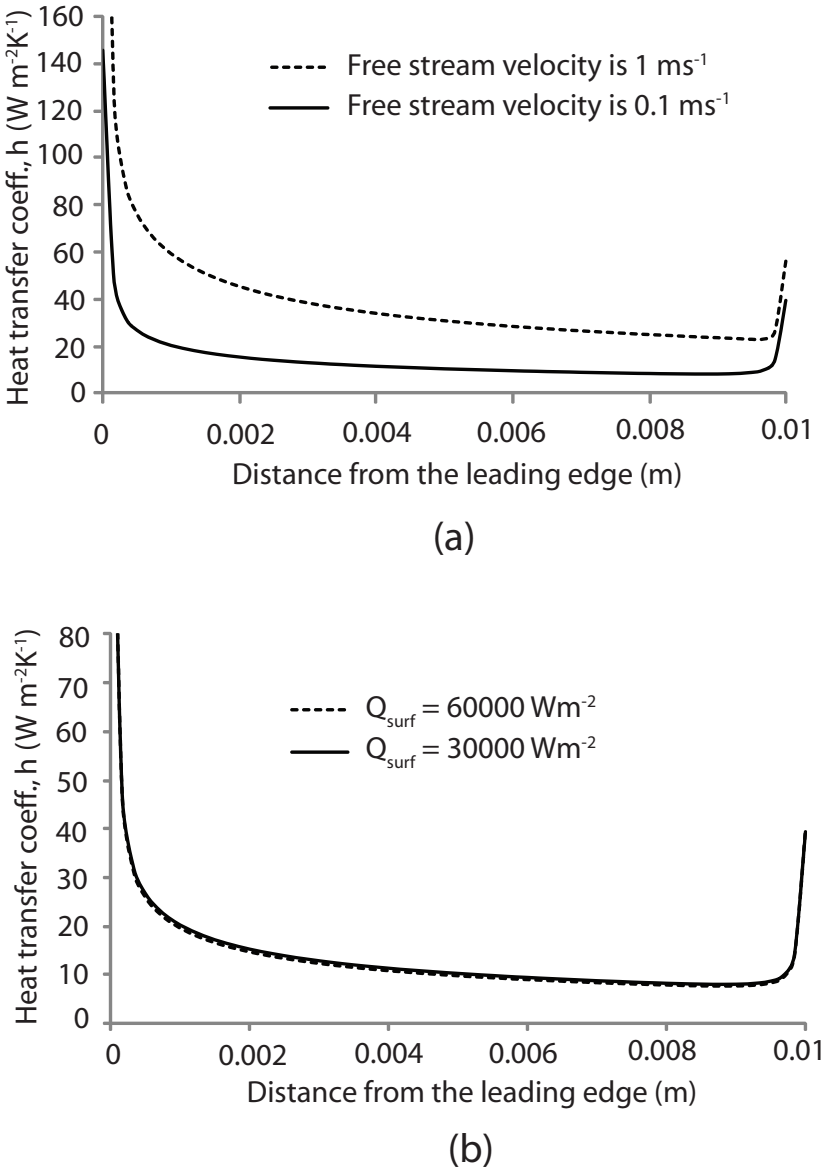

Figure 4.19: Sensitivity analysis of a) free stream velocity and b) heating rate on the heat transfer coefficient at the porous surface.

the effect of blowing velocity on the heat transfer coefficient even smaller.

As the heating rate is doubled (Q_{surf} in Eq. 5.14 increased from 30000 $\mathrm{Wm^{-2}}$ to 60000 $\mathrm{Wm^{-2}}$), the temperature in the core reached 100°C in 160 seconds as opposed to 420 seconds for the lower heating rate. The peak blowing veloc-

ity at the higher heating rate is 1.5×10^{-3} ms^{-1}, reached at 160 seconds during heating. This value is very close to the peak blowing velocity obtained for the lower heating rate (1.6×10^{-3} ms^{-1}) reached at 420 seconds during heating. As shown in Figure 4.19b, when the temperature in the core reaches 100^{o}C, the heat transfer coefficient obtained for the higher heating rate (after 160 seconds of heating) overlaps that with the lower heating rate (420 seconds of heating). This shows that, although the food temperature reaches 100^{o}C sooner (as expected) as we increase the heating rate, the blowing velocity and heat transfer coefficients do not show significant change with heating rates. The dependence of blowing velocity on heating rate, as reported here, can change depending on the permeability of the porous medium.

4.5 Implications for food processes

Correlations based on boundary layer theory have been used frequently to calculate heat and mass transfer coefficients over a food surface. Boundary layer theory is not valid near the leading edge and its predictions are true only for high Reynolds numbers (more than 5000, as shown in this work). In general, food materials have smaller dimensions, and therefore high Reynolds numbers can be obtained if the density of the fluid flowing over the surface is high (e.g., water) or the free stream velocity is high, or both. In the case of hot air drying, the density (of air) is small, and therefore boundary layer theory can be used only when the free stream velocity is high. For cases with lower free stream velocity, boundary layer theory cannot be used, as shown in the present work.

Another important thing to note is that the heat and mass transfer coeffi-

cients near the leading edge are higher than those predicted by boundary layer theory. Therefore, an average heat and mass transfer coefficient along the food surface is larger than that predicted by boundary layer theory. For example, in the conjugate problem with the surface length of 0.01 meters, the average value of the heat transfer coefficient obtained from the simulation is 13.38 $Wm^{-2}K^{-1}$, while that obtained from boundary layer theory is 11.94 $Wm^{-2}K^{-1}$. The difference between the numerical solution (no boundary layer assumptions) and that predicted by boundary layer theory depends on the length of the surface, decreasing for a larger surface.

From the literature, typical heat transfer coefficients measured inside baking ovens (these would be lumped heat transfer coefficients, $h^{'}$) are in the range of 10 to 80 $Wm^{-2}K^{-1}$ (Hallstrom et al., 1988). The lumped heat transfer coefficient, $h^{'}$, obtained through our simulations (shown in Figure 4.20) falls within the range, reported in the literature. The lumped heat transfer coefficient, which contains the effects of both conduction and convection, increases with time as the convective flux at the surface increases. Similar observations have also been made in the case of frying (Hubbard and Farkas, 1999) where the heat transfer coefficient increases during the intense evaporation period (from 300 to 1000 $Wm^{-2}K^{-1}$) and again drops down to 300 $Wm^{-2}K^{-1}$ when the convection at the surface sharply reduces.

4.6 Conclusion

A conjugate model, including both the porous medium food and the outside environment during microwave heating, is solved such that there is no need to

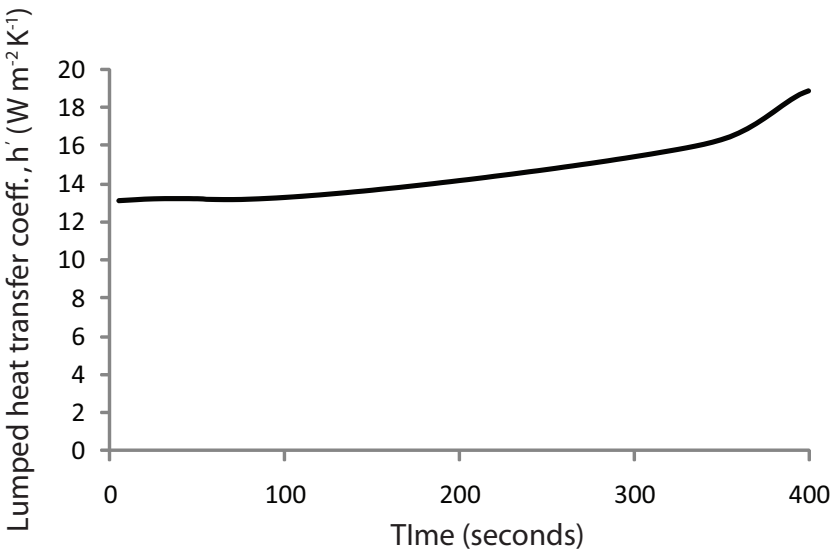

Figure 4.20: The lumped heat transfer coefficient, h', increases with time as the blowing velocity at the surface increases.

provide separate boundary conditions at the porous medium surface. From the simulation results, the heat and mass transfer at the porous surface is investigated. Fluxes at the surface due to diffusion and flow (blowing) are computed for both vapor and heat, from which transfer coefficients are obtained. As evaporation increases with heating, vapor flux due to pressure-driven flow increases but remains small compared with that of diffusive flux. Vapor accumulation at the interface increases the diffusive flux, leading to an 8% increase in the mass transfer coefficient. Heat transfer at the interface is caused equally by conduction and flow, and the heat transfer coefficient shows a slight decrease (10%) as blowing increases with heating. The rate of heating had a minimal effect on the transfer coefficients.

Acknowledgement

This research was partially supported by the United States Department of Agriculture National Integrated Food Safety Project 2004-51110-02167 and Regional Project NC 1023. The authors would like to thank Professor Thomas Avedisian in Mechanical and Aerospace Engineering, Cornell University, and Dr. Rajesh Bhaskaran, Swanson Laboratories at Cornell University, for assistance with the discussion on the boundary layer theory.

BIBLIOGRAPHY

[1] Ateba, P. and G. S. Mittal, 1994, Modeling the Deep-Fat Frying of Beef Meatballs, *International Journal of Food Science and Technology*, 29(4): 429-440.

[2] Bansod, V. J., The effects of blowing and suction on double diffusion by mixed convection over inclined permeable surfaces, *Transport in porous media*, 60: 301-317.

[3] Bear, J., 1972, Dynamics of fluids in porous media, American Elsevier Publishing company, Inc., New York.

[4] Bejan, A., 1995, Convective heat transfer, John Wiley and Sons, Inc., New York.

[5] Bouchon, P. and Pyle, D.L., 2005a, Modelling oil absorption during post-frying cooling - I: Model development, *Food and Bioproducts Processing*, 83(C4): 253-260.

[6] Curcio, S., Aversa, M, Calabro, V and Iorio, G., 2008, Simulation of food drying: FEM analysis and experimental validation, *Journal of Food Engineering*, 87: 541-553.

[7] Curtiss, C. F. and R. B. Bird, 2001, Multicomponent diffusion, *Industrial and Engineering Chemistry Research*, 40(7): 1791-1791.

[8] Datta, A. K., 2007a, Porous media approaches to studying simultaneous heat and mass transfer in food processes. I: Problem formulations, *Journal of Food Engineering*, 80(1): 80-95.

[9] Datta, A. K., 2007b, Porous media approaches to studying simultaneous heat and mass transfer in food processes. II: Property data and representative results, *Journal of Food Engineering*, 80(1): 96-110.

[10] Eichhorn, R., 1960, The effect of mass transfer on free convection, *Journal of heat transfer*, 260-263.

[11] Erriguible, A., Bernada, P., Couture, F. and Roques, M., 2006, Simulation of convective drying of a porous medium with boundary conditions provided by CFD, *Trans IChemE, Part A*, 84(A2): 113-123.

[12] Farkas, B. E., R. P. Singh, et al., 1996a, Modeling heat and mass transfer in immersion frying .1. Model development, *Journal of Food Engineering*, 29(2): 211-226.

[13] Halder, A., A. Dhall, et al., 2007a, An improved, easily implementable, porous media based model for deep-fat frying - Part I: Model development and input parameters, *Food and Bioproducts Processing*, 85(C3): 209-219.

[14] Halder, A., A. Dhall, et al., 2007b, An improved, easily implementable, porous media based model for deep-fat frying - Part II: Results, validation and sensitivity analysis, *Food and Bioproducts Processing*, 85(C3): 220-230.

[15] Halder, A., A. Dhall, et al., 2010, Modeling transport in porous media with phase change: Applications to food processing, Submitted in *Journal of Heat Transfer*, HT-2009-1055.

[16] Murthy, P.V.S.N., 2000, Effect of double dispersion on mixed convection heat and mass transfer in non-darcy porous media, *Journal of Heat Transfer*, 122: 476-484.

[17] Ni, H., A. K. Datta, et al., 1999, Moisture transport in intensive microwave heating of biomaterials: A multiphase porous media model, *International Journal of Heat and Mass Transfer*, 42(8): 1501-1512.

[18] Scarpa, F. and G. Milano, 2002, The role of adsorption and phase change phenomena in the thermophysical characterization of moist porous materials, *International Journal of Thermophysics*, 23(4): 1033-1046.

[19] Sparrow, E.M., Eichhorn, R., and Gregg, J.L., 1959, Combined forced and free convection in a boundary layer flow, *The Physics of Fluids*, 2(3): 319-328.

[20] Volchkov, E.P., 2006, Concerning heat and mass transfer features on permeable surfaces, *International journal of heat and mass transfer*, 49: 755-762.

[21] Ward, C. A. and G. Fang, 1999, Expression for predicting liquid evaporation flux: Statistical rate theory approach, *Physical Review E*, 59(1): 429-440.

[22] Yamsaengsung, R. and R. G. Moreira, 2002a, Modeling the transport phenomena and structural changes during deep fat frying - Part 1: Model development, *Journal of Food Engineering*, 53(1): 1-10.

[23] Zhang, J., Datta, A.K. and Rakesh, V., 2005, Investigation of non-equilibrium in water evaporation, *3rd Inter-American Drying Conference*, Montreal, Canada.

CHAPTER 5

APPLICATION TO DEEP-FAT FRYING. PART I: MODEL DEVELOPMENT AND INPUT PARAMETERS

5.1 Abstract

A fundamental-based model of the frying process that can also be solved in a commercially available software would provide tremendous benefit to design of fried food products and frying processes by making the power of simulation available for design. Quality and safety issues such as crust development, oil pickup and acrylamide formation can be addressed with such a model. However to achieve the above without sacrificing the fundamental physics behind the process, significant reformulations are needed, that require mathematical as well as physical insight into the process. An improved multiphase porous media model involving heat and mass transfer has been developed and solved numerically with careful consideration given to selection of input parameters. Non-equilibrium formulation for evaporation is used which describes the physics better and is easier to implement in a typical CFD software as it can explicitly express the evaporation rate in terms of concentration of vapor and temperature. External heat transfer and mass transfer coefficients are estimated to accurately reflect the different frying phases, i.e., the non-boiling phase and surface boiling and falling rate stages in the boiling phase. This paper discusses model development, while the results, validation and the sensitivity analysis are presented in the companion paper.

Keywords: transport phenomena, multiphase, porous media, evaporation, non-equilibrium, oil pickup, acrylamide.

Nomenclature

a	acrylamide content, ppm
c	concentration, kg m^{-3}
c_p	specific heat capacity, J $kg^{-1}K^{-1}$
C	molar density, kmol m^{-3}
$D_{eff,g}$	effective gas diffusivity, m^2s^{-1}
D	diffusivity, m^2 s^{-1}
h	heat transfer coefficient, W m^{-2} K^{-1}
h_m	mass transfer coefficient of vapor, m s^{-1}
$\dot{I}$	volumetric evaporation rate, kg m^{-3} s^{-1}
k	thermal conductivity, W m^{-2} K^{-1}
k^p	permeability, m^2
K	non-equilibrium evaporation constant
m	overall mass fraction
$M = \phi S_w \rho_w / ((1-\phi)\rho_s)$	moisture content (d.b.)
M_a, M_v	molecular weight of air and vapor
n	total flux, kg m^{-2} s^{-1}
P, p	total pressure and partial pressure, respectively, Pa
R	universal gas constant, (J $kmol^{-1}$ K^{-1})
S	saturation
t	time, s
T	temperature
u	velocity, m s^{-1}
V	volume, m^3
x	mole fraction

Greek Symbols

ρ	density, kg m^{-3}
λ	latent heat of vaporization, J kg^{-1}
ω_v, ω_a	mass fraction of vapor and air in relation to total gas
ϕ	porosity
μ	dynamic viscosity, Pa s

Subscripts

amb	ambient
a, g, o, s, v, w	air, gas, oil, solid, vapor, water
cap	capillary
eff	effective
eq	equilibrium
in	intrinsic
r	relative, residual
sat	saturation
$surf$	surface

5.2 Introduction

The popularity of fried foods make deep-fat frying an important industrial food process. Design and optimization of large scale industrial deep-fat frying processes require comprehensive understanding of the process. Mathematical modeling can provide a level of understanding that complements experimenta-

tion in ways that are impossible to achieve with experiments alone. Improved understanding of deep-fat frying (hereafter referred to as frying) can also help in reducing some health risks associated with fried food consumption, namely co-consumption of oil picked up by the food during frying and the formation of acrylamide, a carcinogen, during frying. Fundamental based modeling of the frying process, however, remains a major challenge due to the complex nature of the process, particularly the presence of rapid evaporation. Difficulties arise both in formulating the physical problem into mathematical equations, and in numerical complexities associated with solving the resulting mathematical equations. Combination of rapid evaporation, changing material properties and other complexities make a food frying process distinct from most processes in other industries. As a result, commercial modeling software that is developed primarily in the context of processes in other engineering disciplines cannot readily accommodate the physics of frying. Implementing frying in a commercial software has the major advantage of enabling modeling as a design tool in industry and its wider use in research. Such implementation, without sacrificing the fundamental physics behind the process, can require significant reformulation of the mathematical problem. This manuscript discusses the literature models and puts forth a model which is complete from the point of view of physics and associated input parameters, and is implementable in commercial software.

Frying models from literature are categorized and discussed. A multiphase porous media model of transport with distributed evaporation is developed and solved using a commercially available software. The critical question of equilibrium between water in solid phase and water vapor in gas phase is addressed. Two different formulations of evaporation, equilibrium and non-equilibrium,

are compared. Temperature, pressure, saturation of different phases and evaporation rate profiles are calculated and validated with experimental results in the companion paper, along with sensitivity of the model to mass transfer coefficients, evaporation rate constant and oil diffusivity.

5.2.1 Comparison of published models

Frying models can be grouped together or categorized as: 1) Totally lumped with no information on spatial variation; 2) Simple diffusional transport of energy and moisture with evaporation of water; 3) Diffusional and sometime pressure driven transport with evaporation at sharp boundary; 4) Evaporation distributed throughout the domain with diffusional and pressure driven flow.

Totally lumped models (Ateba and Mittal, 1994; Ikediala et al.,1996) are empirical curve fits of experimental data and are not physics-based. They are suited for a particular food material and specific processing conditions and cannot be applied for a general class of food or process. Ikediala et al. (1996) included evaporative loss in the model but that was based on experimental data of evaporative loss in meat patties. The prediction of these models would be greatly affected if there is any change in physical property or environmental conditions. Also the transient temperature and moisture profiles inside the food during frying cannot be studied.

Models in the second category are slightly improved that have treated frying as a simple heat conduction and moisture diffusion process and ignored evaporation altogether in the domain (Dincer and Yildiz, 1996; Williams and Mittal, 1999). Evaporation was included using a surface boundary condition in the

diffusional heat and mass transfer model of Moreira et al.(1995). Evaporation inside the food domain was ignored in this study even though temperatures in the core reached 80°C. These simple diffusion-based frying models provide very limited understanding of the frying process as complex processes such as pressure driven flow are lumped into effective "diffusivities" and other empirical parameters. The empirical nature of these parameters also make it harder to translate them from one study to another.

A significantly improved formulation, compared to simple diffusion models, is a two region model with a sharp boundary separating the core and the crust region (Farkas et al., 1996a). A sharp boundary model of frying is a moving boundary problem where the interface between crust and core moves. It is analogous to sharp front model of freezing and thawing (Mascarenhas et al., 1997) of a pure material where a sharp front separates the frozen and unfrozen regions. These models have separate conservation equations for two regions - crust and the core with a moving boundary. Farkas et al. (1996a) is perhaps the first one to include pressure-driven flow, although restricting such flow to the crust region and for vapor phase only. Ignoring vapor flux in the core and liquid flux in the crust reduced mathematical complications but sacrificed important physics (discussed later in 'Our implementation vs Sharp boundary formulation' in Results and Discussion of the companion paper). A moving boundary model solving only the heat transfer equation and no mass transport have also been reported (Farid and Chen, 1998; Bouchon and Pyle, 2005a).

In contrast to sharp boundary models, distributed evaporation models consider evaporation to be distributed over a zone (Ni and Datta, 1999; Yamsaengsung and Moreira, 2002a). For a given frying situation, it is possible that real

evaporation zone is very narrow, closer to the sharp interface and distributed evaporation formulation will, in fact, predict such narrow evaporation zone. At high rates of internal evaporation, significant pressure driven flows can be present for all phases and throughout the material. The model of Ni and Datta (1999) and Yamsaengsung and Moreira (2002a) have not considered frying as combination of different stages (e.g., boiling and non-boiling stages) and therefore used a constant convective heat and mass transfer coefficient through the process. But Hubbard and Farkas (1999) showed through experiments that both heat and mass transfer coefficients vary significantly during different stages of frying and need to included in modeling. Furthermore, the distributed evaporation models are very difficult to implement in many commercial software due to complexities involved in calculating the evaporation rate.

5.2.2 Implementation of evaporation

Evaporation of water in frying or other drying like processes has been implemented using an equilibrium formulation where water in the solid matrix is assumed to be in equilibrium with water-vapor in the surrounding air. This may not always be true, as has been conjectured (e.g., see Labuza, 2001) and demonstrated for pure water by Ward and Fang (1999). Furthermore, the equations resulting from an equilibrium formulation cannot be implemented in any direct manner in the framework of most commercial software. As will be explained later, a non-equilibrium formulation describes the physics better and is also easier to implement in a software, and thus appears to be the obvious alternative. Although few experimental studies have been done to estimate the non-equilibrium evaporation rate constant of food materials (Zhang et al., 2005), no

accurate estimate of non-equilibrium evaporation constant in hygroscopic materials is available. In this manuscript, non-equilibrium formulation is shown to be an improved approach and, using sensitivity analysis, probable range of non-equilibrium evaporation rate constant has been estimated.

5.2.3 Oil pickup

During deep-fat frying, oil imparts flavor and texture to the fried food. However, oil uptake in food during frying needs to be reduced for health reasons and this is a major concern in food industry. Experimentally most of the oil uptake was shown to take place during post-frying cooling (Ufheil and Escher, 1996). This was quantified by Moreira et al. (1997) where it was shown that 20% of the oil pickup takes place during immersion frying and rest during post-frying cooling. Uptake of oil during frying was implemented as a diffusion term (represents capillarity) by Ni and Datta (1999) with a constant oil concentration boundary condition but the cooling process was not included. While oil uptake during the cooling process was simulated in Bouchon and Pyle (2005a), they ignored heat and mass transfer of other phases (liquid water and gas) and assumed that pressure inside the potato is due to vapor only (e.g., no air). At low temperatures, air contributes significantly to the total pressure and ignoring its effects would cause over-prediction of oil-pickup. Yamsaengsung and Moreira (2002b) assumed that oil absorption during cooling is only due to capillary pressure and ignored pressure gradient developed inside the potato due to condensation of water-vapor. Further, they did not consider post-frying cooling process as a continuation of the frying process where the initial conditions for post-frying cooling should be the end condition of the frying process. They

gave separate initial conditions and ignored the presence of liquid water inside the food during cooling. This gives an over-prediction of oil-pickup. A more complete model of oil-pickup where contribution of all phases are taken into account should improve the prediction of this important quantity.

5.2.4 Acrylamide formation during frying

Acrylamide is a neurotoxin and is classified as a probable carcinogen to humans by the International Agency for Research on Cancer. Highest levels of acrylamide were found in carbohydrate-rich food, such as potato chips and French fries, which had been cooked at high temperatures (Claeys et al., 2005). Tareke et al. (2002) showed that the formation of acrylamide was temperature-dependent, increasing with rising temperatures. Raw or unheated foods did not exhibit any acrylamide formation. Mottram et al. (2002) indicated that acrylamide formation increases with temperature from about 120^{o}C to 170^{o}C and then decreases. Surdyk et al. (2004) found that not only temperature (above 200^{o}C) but also heating time increased the acrylamide content.

Granda and Moreira (2005) studied the formation of acrylamide during traditional and vacuum frying of potato chips. Vacuum frying of potatoes were found to produce 94% less acrylamide than traditional frying because of lower temperatures in vacuum frying. Using a first-order model with temperature dependence, acrylamide content was calculated using experimental frying temperature profiles. Similarly, Claeys et al. (2005) also described the formation and elimination of acrylamide as first-order kinetics. Corradini and Peleg (2006) found that acrylamide formation and degradation model based on Fermi model,

a logistic kinetic model, is able to capture the main features better than any other empirical model. None of the acrylamide kinetic models were coupled with a transport model for frying.

The model developed in the present work is a good one to study acrylamide formation during frying as all the factors (temperature, moisture migration, oil pickup and evaporation) that effect acrylamide formation are being solved in this model.

5.2.5 Use of commercial software

Previous detailed physics-based models of frying (Ni and Datta, 1999; Yamsaengsung and Moreira, 2002b) have been solved by user developed codes. These codes are either publicly unavailable, have limited capabilities or are difficult to use by anyone other than the creator. Implementation of the same process in commercial code will make the power of simulation capability more widely available for design of products and processes. However, the governing equation and boundary conditions for frying require significant reformulations when implementing in a typical CFD software, which has not been accomplished.

5.2.6 Objectives and overview

The objectives of this present study are 1) To develop a multiphase model of deep-fat frying and post-frying cooling which includes all the important physics and which can be implemented in a commercially available software; 2) To com-

pare predictions using a non-equilibrium evaporation model with those from the equilibrium evaporation model of published literature; 3) To estimate the amount of oil pickup during deep-fat frying and post-frying cooling; 4) To estimate the acrylamide formation during the frying process.

5.3 Model Development

A multiphase porous media model is developed that describes heat and mass transfer inside a restructured potato slab during deep-fat frying. Mass and energy conservation equations are developed that include diffusion, capillary and convective modes of transport. Model would include post-frying cooling through change in boundary condition of the energy equation and oil transport. Evaporation is considered distributed throughout the domain. Kinetics for acrylamide formation is introduced.

5.3.1 Problem description

A schematic of the problem description is shown in Figure 1. The potato slab is assumed to be a porous media. During frying, the pores may be filled with liquid water, oil, water-vapor and air depending on processing history. Three transportable phases are considered: liquid water, oil and gas (mixture of air and water-vapor). To simulate a 1D heat and mass transfer, no flux conditions for mass species and energy are specified at boundaries other than $x = 0$. The problem is considered symmetric with $x = L$ as the line of symmetry. The left boundary ($x = 0$) is the frying surface where heat and mass exchange with the

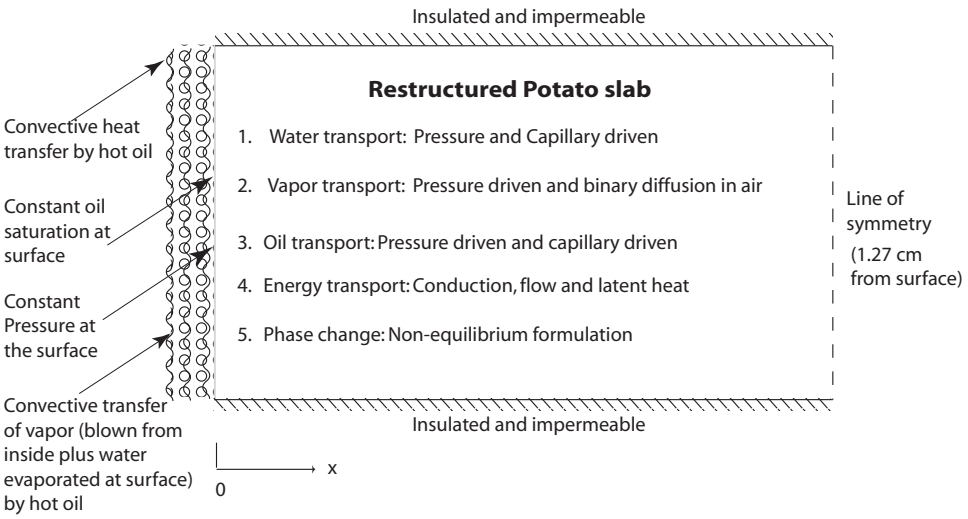

Figure 5.1: Schematic showing computational domain and boundary conditions. Two-dimensional geometry was implemented with the above boundary conditions to simulate an effective one-dimensional problem. For computation, the dimension in the other direction was chosen to be 0.08 cm.

environment takes place.

5.3.2 Assumptions

A number of assumptions need to be made in formulating the frying problem. There are four phases in continuum: solid, liquid water, oil and gas. Pressure is shared by all phases as effects of capillary pressure have been included as diffusion term (discussed in detail in Input Parameters section). Thermal equilibrium exists between all phases. There is *non-equilibrium* between water in solid and water-vapor in gas phase, i.e., their concentrations are not given by the moisture isotherms. Bound water is ignored so all the liquid water is available for transport. Shrinkage during frying due to removal of bound water is not considered. The effects of gravity have been ignored.

5.3.3 Governing equations

Conservation equations are developed for all phases and components inside any phase, energy and Darcy flow in a porous media.

Mass balance equations

Porosity, ϕ, is defined as the fraction of the total volume occupied by pores, given by

$$\phi = \frac{\sum_{i=w,g,o} \triangle V_i}{\triangle V} \tag{5.1}$$

where $\triangle V_i$ is the volume occupied by the i^{th} phase in an elemental volume $\triangle V$. Saturation of a phase is defined as the fraction of volume of the pore occupied by a particular phase

$$S_i = \frac{\triangle V_i}{\phi \triangle V} \tag{5.2}$$

where i stands for water, oil or gas. The summation of saturation of all phases should lead to unity as shown in Eq. 5.5.

Mass balance equation for a phase solves for saturation of the phase in an element. Saturations S_w and S_o are obtained from mass balance equations (Eq. 5.3 and 5.4) for liquid water and oil, respectively. Saturation of gas, S_g, is calculated from Eq. 5.5.

$$\frac{\partial}{\partial t}(\phi \rho_w S_w) + \nabla \cdot (u_w \rho_w) = \nabla \cdot (D_{w,cap} \nabla (\phi \rho_w S_w)) - \dot{I} \tag{5.3}$$

$$\frac{\partial}{\partial t}(\phi \rho_o S_o) + \nabla \cdot (u_o \rho_o) = \nabla \cdot (D_{o,cap} \nabla (\phi \rho_o S_o)) \tag{5.4}$$

$$S_w + S_g + S_o = 1 \tag{5.5}$$

In Eqns. 5.3 and 5.4, the total flux of the liquid (water or oil) is due to the liquid pressure, $P - p_{cap}$, which is the difference between gas pressure and capillary

pressure. This total flux term can be rewritten (e.g., see Datta, 2007), for example, for water as

$$n_w = -\rho_w \frac{k^p_{in,w} k^p_{r,w}}{\mu_w} \nabla (P - p_{cap}) \tag{5.6}$$

$$= -\rho_w \frac{k^p_{in,w} k^p_{r,w}}{\mu_w} \nabla P + \rho_w \frac{k^p_{in,w} k^p_{r,w}}{\mu_w} \frac{\partial p_{cap}}{\partial S_w} \nabla S_w \tag{5.7}$$

The first term in this equation is rewritten in terms of velocity, u_w, as explained later. The second term is rewritten in terms of capillary diffusivity, $D_{w,cap}$, given by:

$$D_{w,cap} = -\frac{k^p_{in,w} k^p_{r,w}}{\phi \mu_w} \frac{\partial p_{cap}}{\partial S_w} \tag{5.8}$$

Similarly, capillary diffusivity of oil is defined by

$$D_{o,cap} = -\frac{k^p_{in,o} k^p_{r,o}}{\phi \mu_o} \frac{\partial p_{cap}}{\partial S_o} \tag{5.9}$$

The gas phase is a mixture of water-vapor and air. Spatial variations of concentration of water-vapor and air during frying are obtained from solving the respective mass conservation equations in terms of their mass fractions, ω_v and ω_a, with binary diffusion (Bird et al., 2001):

$$\frac{\partial (\phi \rho_g S_g \omega_v)}{\partial t} + \nabla \cdot (u_g \rho_g \omega_v) = \nabla \cdot \left(\phi S_g \frac{C_g^2}{\rho_g} M_a M_v D_{eff,g} \nabla x_v \right) + \dot{I} \tag{5.10}$$

$$\omega_v + \omega_a = 1 \tag{5.11}$$

As can be seen in Figure 2, Eqs 5.3, 5.4, 5.5, 5.10 and 5.11 constitute the set of five equations from which the concentration variables S_w, S_o, S_g, ω_v and ω_a can be found. Note, however, there are additional unknowns in these equations for which auxiliary equations will be needed as discussed later (Eq. 5.12 for velocities, u_w, u_g and u_o, and Eq. 5.32 for the evaporation rate, $\dot{I}$).

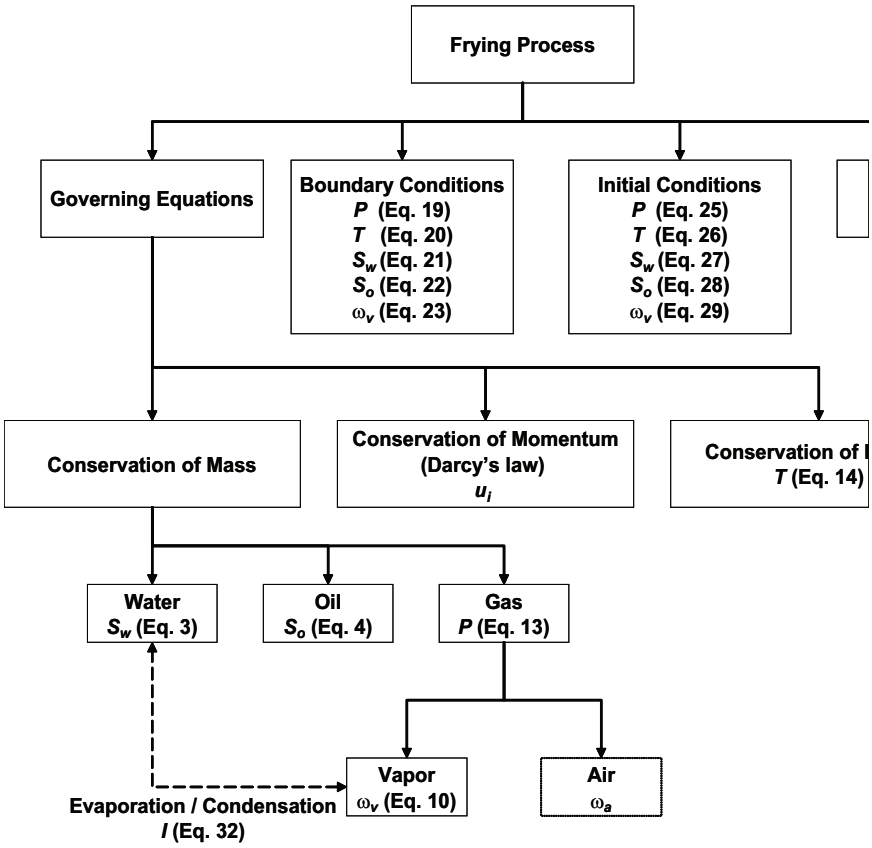

Figure 5.2: Summary of the model showing the the Governing equations, Boundary conditions, Initial conditions and Input data. S_g in Eq. 5.13 comes from Eq. 5.5. ω_a and u_i appear in the governing equations and are calculated from Eq. 5.11 and 5.12, respectively.

Momentum balance equation

Darcy's equation for each phase in porous media replaces the standard momentum conservation equation (Navier-Stokes equation). Since the effect of capillary pressure is included as a diffusion term, velocity of each phase is due to total pressure gradient as given by

$$u_i = -\frac{k^p_{r,i} k^p_{in,i}}{\mu_i} \nabla P \tag{5.12}$$

where i stands for water, oil or gas. The components of a phase (e.g., air and water vapor in gas phase) share the same velocity.

Mass balance equation for gas phase

The total pressure, P, is calculated by solving the overall mass balance equation for the gas phase

$$\frac{\partial}{\partial t}(\phi S_g \rho_g) + \nabla \cdot (-\rho_g \frac{k_{r,g}^p k_{in,g}^p}{\mu_g} \nabla P) = \dot{I} \tag{5.13}$$

Total pressure is shared by all the phases (capillary pressure of liquid water and oil have been included as diffusion).

Energy balance equation

Since thermal equilibrium is assumed to exist between all phases (e.g., all phases have the same temperature), energy balance equation of the mixture (Eq. 5.14) is solved to calculate T:

$$\frac{\partial}{\partial t}(\rho_{eff} c_{p,eff} T) + \nabla \cdot ((\rho c_p u)_{fluid} T) = \nabla \cdot (k_{eff} \nabla T) - \lambda \dot{I} \tag{5.14}$$

The properties of the mixture are averages of phase properties weighted by their mass or volume fractions:

$$\rho_{eff} = (1-\phi)\rho_s + \phi(S_w \rho_w + S_g \rho_g + S_o \rho_o) \tag{5.15}$$

$$c_{p,eff} = m_g(\omega_v c_{p,v} + \omega_a c_{p,a}) + m_w c_{p,w} + m_o c_{p,o} + m_s c_{p,s} \tag{5.16}$$

$$\begin{aligned}(\rho c_p u)_{fluid} = {} & \left(\rho_w u_w - D_{w,cap} \nabla(\phi S_w \rho_w)\right) c_{p,w} + \rho_g u_g (\omega_v c_{p,v} + \omega_a c_{p,a}) \\ & + \left(\rho_o u_o - D_{o,cap} \nabla(\phi S_o \rho_o)\right) c_{p,o}\end{aligned} \tag{5.17}$$

$$k_{eff} = (1-\phi)k_s + \phi(S_w k_w + S_g(\omega_v k_v + \omega_a k_a) + S_o k_o) \tag{5.18}$$

5.3.4 Boundary and initial conditions

As shown in Figure 1, to simulate a 1D situation, no flux conditions for mass species and energy are specified at boundaries other than $x = 0$. The problem is considered symmetric with $x = L$ as the line of symmetry. The left boundary ($x = 0$) is the frying surface where heat and mass exchange with the environment takes place. Boundary conditions at $x = 0$ are given as

$$\text{B.C. for Eq. 5.13:} \quad P_{surf} = P_{amb} \tag{5.19}$$

$$\text{B.C. for Eq. 5.14:} \quad q_{surf} = h(T_{amb} - T_{surf}) - (\lambda + c_{p,w}T)n_{w,surf} - c_{p,v}Tn_{v,surf} - c_{p,o}T_{amb}n_{o,surf} \tag{5.20}$$

$$\text{B.C. for Eq. 5.3:} \quad n_{w,surf} = h_m\phi S_w(\rho_{g,surf}\omega_{v,surf} - \rho_{v,amb}) \tag{5.21}$$

$$\text{B.C. for Eq. 5.4:} \quad S_{o,surf} = S_{o1} \tag{5.22}$$

$$\text{B.C. for Eq. 5.10:} \quad n_{v,surf} = h_m\phi S_g(\rho_{g,surf}\omega_{v,surf} - \rho_{v,amb}) \tag{5.23}$$

and are now explained. The total pressure at the frying surface is equal to the ambient pressure and remains constant throughout the frying and the post-frying cooling processes as shown by Eq. 5.19. During frying, it is assumed that convective heat transfer occurs between the surrounding oil and the frying surface given by Eq. 5.20. Immersion frying can be broken into two phases (Hubbard and Farkas, 1999): 1) boiling phase; 2) Non-boiling phase. During the non-boiling phase there is no water vaporization and is for a short duration ($5 - 10$ seconds). It is followed by the boiling phase when rapid evaporation starts. The boiling phase can be further divided into 2 stages: 1) surface boiling stage which is characterized by the sudden loss of free moisture at the surface, increased surface heat transfer, and inception of crust formation; 2) falling rate stage where there is continued thickening of the crust region, decreased heat transfer and a steady decrease in vapor mass transfer from the material.

Thus, surface heat transfer coefficient varies during the process, which has been shown experimentally. Hallstrom (1979) reports that convective heat transfer coefficient during non-boiling phase of frying is $250 - 300\ \mathrm{W/m^2K}$ and during the boiling phase is near to $1000\ \mathrm{W/m^2K}$. Detailed variation of h with time, shown in Figure 5.3a, is reported by Hubbard and Farkas (1999) and is used in this model.

Another important term that needs to be included in the energy boundary condition (Eq. 5.20) is the energy lost as latent heat of vaporization due to evaporation of liquid water at the surface. It is assumed that the liquid water at the surface first evaporates and is then convected away as vapor. During post-frying cooling, natural convection heat transfer occurs between the frying surface and the ambient air at 25°C and the corresponding heat transfer coefficient is $20\ \mathrm{W/m^2K}$ (Hanreich and Nicolics, 2001).

Mass transport at the frying surface with oil is considered to be convective mass transfer where the vapor is convected away by the oil and is expressed by Eq. 5.21 and 5.23. The liquid water is first evaporated to vapor and then convected away by the oil. As shown in Figure 5.3b, the convective mass transfer coefficient for vapor is not constant throughout the frying process but varies with time. Hubbard and Farkas (1999) experimentally measured the mass of vapor leaving the frying surface. If the mass transfer coefficient remained constant throughout the frying process then the mass of vapor lost from the frying surface should increase initially and then become constant as the surface vapor concentration increases with time and then becomes constant. But the mass of vapor exiting the frying surface decreases with time which can only be explained if mass transfer coefficient decreases with time. This can be explained

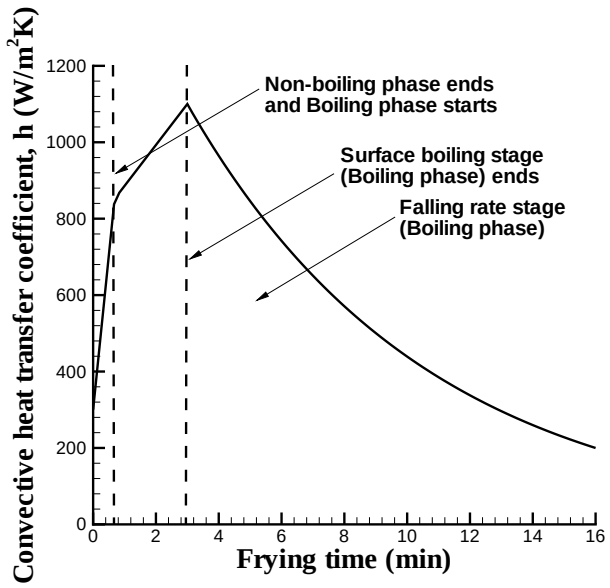

(a)

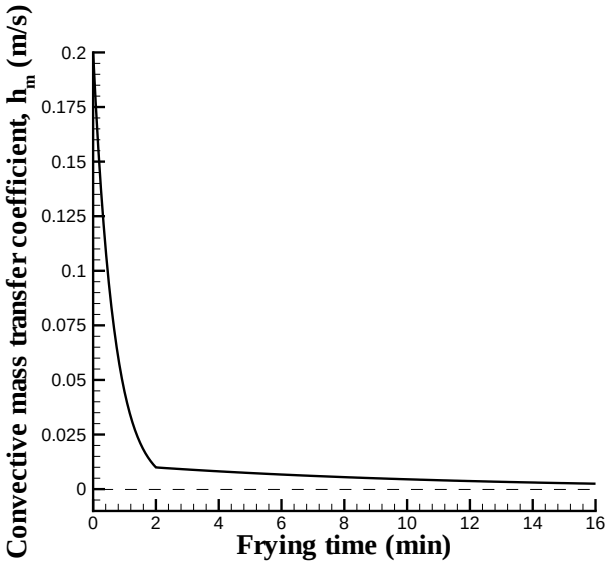

(b)

Figure 5.3: (a) Variation of convective heat transfer coefficient, h, with time (plotted using the data of Hubbard and Farkas, 1999) (b) Variation of convective mass transfer coefficient, h_m, with time used in this study based on discussion in Input parameters section.

by the fact that the mass transfer coefficient used in this model includes the effect of both, the mass of vapor lost due to bulk flow (velocity from blowing) and that due to diffusion. Initially, during the surface boiling stage, significant amount of vapor is transported from the surface due to bulk flow and therefore the mass transfer coefficient is high (transport due to diffusion remains nearly constant during the boiling phase). After all the water is lost from the surface and evaporation front starts moving inward, the bulk flow reduces sharply and therefore the mass transfer coefficient also reduces. During the surface boiling stage, the water transport is heat transfer limited which means that all the heat that is coming in is used up in evaporation and all the vapor produced is convected away. Therefore, the maximum mass transfer coefficient can be calculated by a simple heat balance as shown in Eq. 5.24, where all the convective heat coming inside the system is taken up for evaporation of liquid water to water-vapor and all the vapor produced is convected away.

$$\begin{aligned} hA(T_{oil} - T_{surf}) &= \lambda h_m A(c_{v,surf} - c_{v,0}) \\ h_m &= \frac{h(T_{oil} - T_{surf})}{\lambda(c_{v,surf} - c_{v,0})} \end{aligned} \tag{5.24}$$

This gives a maximum h_m of 0.2 m/s for $T_{oil} = 180°C$, $T_s = 100°C$, $h = 1100\ W/m^2K$, $c_{v,0} = 0$ and $c_{v,s} = 0.2\ kg/m^3$. Note that in a multiphase system, the vapor concentration at the surface is lower than the vapor density. After 16 minutes of frying time when the core temperatures are above 90°C, there is negligible air in the potato and the water-vapor density at the surface is equal to water-vapor density at that surface temperature ($0.5\ kg/m^3$ at 170°C). From the experimental results (Hubbard and Farkas, 1999) , the mass transfer coefficient after 16 minutes can be calculated and is 0.0013 m/s. Based on this analysis of experimental data and heat transfer limitation during surface boiling stage, a likely description of mass transfer coefficient is shown in Figure 5.3b and is

used here.

It is assumed that the volume fraction of oil at the surface, S_{o1}, is constant and is equal to 0.11 during frying and 0.28 during post-frying cooling (Chen and Moreira, 1997; Yamsaengsung and Moreira, 2002b). Volume fraction of oil at the boundary during frying is less than that during cooling because of vigorous bubbling that occurs during frying and impedes oil inflow. From the previous experiments (Chen and Moreira, 1997), it has been shown that total amount of oil absorbed during frying is 8% w.b. which through simulation (Yamsaengsung and Moreira, 2002b) has been found to correspond to 0.11 oil saturation. Similarly, during cooling, 27% w.b. of oil is absorbed which translates to 0.28 of oil saturation at the boundary. This boundary condition (constant volume fraction of oil at the boundary) may over predict the oil pickup but there is also a self-limiting mechanism— the oil pickup stops when there is no void space left inside the potato, even if a higher concentration of oil exists at the boundary. A constant oil concentration at the boundary, as shown above, is an empirical estimate but since no data is available on interaction of oil with the potato surface during immersion frying or post-frying cooling, the above approach seems to be the best possible for now. Possible future availability of a more mechanistic model of surface adsorption of oil may enhance the transport model presented here.

Initial conditions inside the potato before frying are:

$$\text{I.C. for Eq. 5.13:} \quad P = P_{amb} \tag{5.25}$$

$$\text{I.C. for Eq. 5.14:} \quad T = T_{amb} \tag{5.26}$$

$$\text{I.C. for Eq. 5.3:} \quad S_w = 0.3 \tag{5.27}$$

$$\text{I.C. for Eq. 5.4:} \quad S_o = 0 \tag{5.28}$$

$$\text{I.C. for Eq. 5.10:} \qquad \omega_v = 0.02 \tag{5.29}$$

Initially the potato is at ambient pressure and temperature conditions. The material used in this study, restructured potato, was made using a paste of 70/30 mixture of water and dehydrated potato powder (Farkas et al., 1996b). This gives an initial water saturation of 0.3 for a sample with bulk density of 386 kg/m^3 and moisture content of 2.5. Since, before frying there is no oil inside the potato so oil saturation is zero. The water vapor in air is in equilibrium with liquid water initially. Using Eq. 5.30 and 5.31, equilibrium water-vapor pressure at 25°C is calculated. Using the equilibrium water-vapor pressure, mass fraction of vapor in gas phase (ω_v) is calculated as 0.02.

5.3.5 Phase change

The evaporation rate distributed spatially and over time is a complex function of food material and process parameters. Phase change can be formulated in two ways, equilibrium and non-equilibrium. In the equilibrium formulation of evaporation that has been used in the literature (Ni and Datta, 1999; Yamsaengsung and Moreira, 2002a), vapor is always assumed to be in equilibrium with the water in the solid and the vapor pressure at a particular moisture content and temperature is given by the moisture isotherm equation (e.g., Ratti et al., 1989):

$$\ln \frac{p_{v,eq}}{p_{sat}(T)} = -0.0267 M^{-1.656} + 0.0107 e^{-1.287M} M^{1.513} \ln(p_{sat}(T)) \tag{5.30}$$

where $p_{v,eq}$ is the equilibrium vapor pressure and $p_{sat}(T)$ is the vapor pressure of pure water given by Clausius-Clapeyron equation:

$$\ln \frac{p_{sat}(T)}{p_0} = \frac{\Delta \overline{H}_{vap}}{R} \frac{(T - T_0)}{T T_0} \tag{5.31}$$

Moisture content (dry basis), M, is related to saturation by $M = \phi S_w \rho_w / ((1 - \phi)\rho_s)$. In the equilibrium formulation, p_v is always equal to $p_{v,eq}$ and is given by Eq. 5.30. For this situation, the evaporation rate, $\dot{I}$, is part of the solution and cannot have an explicit expression (as Eq. 5.32 discussed later).

However, recent studies (Fang and Ward, 1999a; Minkowycz et al., 1999; Zhang et al., 2005) have shown that evaporation is not instantaneous and non-equilibrium exists during rapid evaporation between water-vapor in gas phase and water in solid phase. A discontinuity in temperature between the liquid surface and the water-vapor just above the surface has been observed through experiments on pure water (Fang and Ward, 1999b). Using statistical rate theory approach, an expression for predicting liquid evaporation flux for pure water surface was given by Ward and Fang (1999) but this expression cannot be used for hygroscopic solid. A more general expression of non-equilibrium evaporation rate used for modeling of phase change in porous media (Le et al., 1995; Scarpa and Milano, 2002), that is consistent with studies on pure water just mentioned, is given by:

$$\dot{I} = K(\rho_{v,eq} - \rho_v) \tag{5.32}$$

where $\rho_v = \rho_g \omega_v$ is the vapor density at a location that comes from solution. Here K is a parameter signifying the rate constant of evaporation. Coincidentally, an equilibrium formulation (use of Eq. 28) is difficult to implement in commercial software which requires the source term (evaporation rate, $\dot{I}$, in the conservation equations) to be explicitly expressed in terms of dependent variables of the model. A non-equilibrium formulation, given by Eq. 5.32, allows precisely this, i.e., can express the evaporation rate explicitly and therefore would be preferred in a commercial software and is therefore used in our model.

The rate constant parameter K has the dimension of reciprocal time in which phase change occurs. A large value of K signifies that phase change occurs in a small time. For the assumption of equilibrium, K is infinitely large or phase change occurs instantaneously. A very high value of K, however, makes the convergence of the numerical solution difficult. Independent ways of estimating K (in Eq. 5.32) for a hygroscopic material are still unavailable but was recently estimated in our group to be of the order of 1 for evaporation of pure water (Zhang et al., 2005).

5.3.6 Acrylamide formation in potato

Kinetics of acrylamide formation and degradation have been described by mathematical models of varying degrees of complexities (Claeys et al., 2005b; Knol et al., 2005; Corradini and Peleg, 2006). Acrylamide formation and degradation model based on Fermi model, a logistic kinetic model, is able to capture the main features better than any other empirical model (Corradini and Peleg, 2006). Kinetics of acrylamide formation and degradation modeled using a Fermi model is given by:

$$\begin{aligned} a(t) &= \left[\frac{A(T)}{1+\exp(-k''_g(T)(t-t_{cg}(T)))} - \frac{A(T)}{1+\exp(k''_g(T)t_{cg}(T))}\right] \\ &\quad \times \frac{1}{1+\exp(k''_d(T)(t-t_{cd}(T))} \end{aligned} \tag{5.33}$$

where da/dt is acrylamide concentration at time t. The parameters in the above equation are functions of temperature:

$$A(T) = 94363259\exp(-5705.95/T) \tag{5.34}$$

$$k''_g(T) = 3069003\exp(-8459.12/T) \tag{5.35}$$

$$t_{cg}(T) = 6.97 \times 10^{-6} \exp(6673.09/T) \quad (5.36)$$

$$k''_d(T) = 160238.71 \exp(-8649.90/T) \quad (5.37)$$

$$t_{cd}(T) = 1.93 \times 10^{-20} \exp(23794.27/T) \quad (5.38)$$

The above expressions (Eq. 5.35-5.39) were obtained by curve fitting an Arrenhius equation to the acrylamide data obtained from Knol et al. (2005). The intuitive meaning of the parameters in Eq. 5.34 are as follows: $A(T)$ is the equilibrium acrylamide content or the amount of acrylamide that is formed after a long time; t_{cg} is the time taken to generate an acrylamide concentration that is half of $A(T)$; k_g is the rate of formation of acrylamide; t_{cd} is the time taken to decrease acrylamide concentration to half of $A(T)$; k_d is the rate of degradation of acrylamide.

The acrylamide degradation becomes significant at very high temperatures (more than 180°C). This is when $t_{cd} << t_{cg}$ and $k_d >> k_g$, and acrylamide is degraded faster than it is generated (Corradini and Peleg, 2006). But in frying when the oil temperature is 180°C, the temperature values at the surface and inside the potato do not go beyond 170°C after 16 minutes of frying. At these temperatures $t_{cd} >> t_{cg}$ and the degradation taking place is very small compared to the generation. Thus, in our model degradation is ignored which simplifies Eq. 5.34 to

$$a(t) = \frac{A(T)}{1 + \exp(-k_g(T)(t - t_{cg}(T)))} - \frac{A(T)}{1 + \exp(k_g(T)t_{cg}(T))} \quad (5.39)$$

The simplification of Eq. 5.34 to Eq. 5.40 reduces numerical complexities and can be easily solved. To solve Eq. 5.40 for variable temperature, da/dt is obtained from Eq. 5.40 given as

$$\frac{da}{dt} = \frac{A(T)k_g(T)\exp[k_g(T)(t + t_{cg}(T))]}{(\exp[k_g(T)t] + \exp[k_g(T)t_{cg}(T)])^2} \quad (5.40)$$

This expression for da/dt is then numerically integrated using small time steps.

5.4 Numerical solution

Equations 11, 12, 3, 4 and 8 are solved for the variables P, T, S_w, S_o and ω_v, respectively, with boundary conditions (Equations 17-21) and initial conditions (Equations 23-27). Auxiliary conditions, such as Eq. 5, are used to compute the remaining variables. Knowing $T(t)$, acrylamide concentration is computed using Eq. 5.41. It is difficult to solve such a system using many of the general purpose computational fluid dynamics (CFD) solvers. Multi-phase models in such software solve Navier-Stokes and heat balance equation for each phase, which will lead to unnecessary numerical complications as in this case three different phase exist in a porous media of very low permeability. Further difficulties lie in implementing thermal equilibrium condition for all the phases and the solid matrix, and adjusting the default flow boundary conditions to model the complex boundary conditions encountered in our case. A commercially available finite element software, COMSOL Multiphysics (Comsol Inc, Burlington, MA), was used to solve these equations. In COMSOL Multiphysics, we are able to replace Navier-Stokes equations with Darcy's equation and solve a mixture energy equation. The computational domain, shown in Figure 5.1, is $0.0127\ \text{m} \times 0.0008\ \text{m}$ and has a mesh consisting of 127×3 quadrilateral elements. Simulation of heating duration of 16 minutes took approximately 6 hours and post-frying cooling of duration of 3 minutes took approximately 2 hours of CPU time for a timestep size of 0.01 second on a Pentium 3.4 GHz PC with 2GB RAM.

5.5 Input parameters

Input parameters used in this study are listed in Table 1. The physical and thermal properties used for potato are those for a restructured potato, used in the study of Farkas et al. (1996) to minimize sample variability (details of making such a sample are discussed in that publication). A restructured potato is different from a raw potato as it has more air spaces in it and the bulk density is 386 kg/m^3 which is less than the value of 1050 kg/m^3 for a typical potato. Similar bulk densities have been observed for apples (Feng et al., 2004). The experimentally determined intrinsic permeability value in the raw potato (Datta, 2006) is very low (around 1×10^{-17}m^2) and is applicable for potatoes with void air space fraction of around 0.11. But for the restructured potatoes with void air space fraction of around 0.50, permeability values of apples is more suitable. Kozeny-Carman equation which gives the permeability-porosity relationship (Feng et al., 2004) also predicts a three orders of magnitude difference in intrinsic permeability when void air space fraction changes from 0.11 to 0.50. So, a higher intrinsic permeability value for the restructured potato (compared to raw potato) is used in this model and is given in Table 3.4.1. The intrinsic permeability values for gas and liquid are assumed to be two different ones, with intrinsic permeability for gas being higher, based on discussions in earlier work (Ni and Datta, 1999). The relative permeabilities of gas and liquid water are given by Bear (1972):

$$k^p_{r,g} = \begin{cases} 1 - 1.1 S_w & S_w < 1/1.1 \\ 0 & S_w > 1/1.1 \end{cases} \tag{5.41}$$

$$k^p_{r,w} = \begin{cases} (\frac{S_w - S_r}{1 - S_r})^3 & S_w > S_r \\ 0 & S_w < S_r \end{cases} \tag{5.42}$$

Data on permeability values for oil are unavailable, so oil is treated the same as water and permeability values of water is used in the model (Ni and Datta, 1999).

Liquid water and oil transport due to capillary effects have been modeled as diffusion. The capillary diffusivity of water used in the model is a function of moisture content (Ni and Datta, 1999) and given by:

$$D_{w,cap} = 1 \times 10^{-8} \exp(-2.8 + 2.0M) \tag{5.43}$$

The effective diffusivity of water in the potato reported in the published literature is in the range of 10^{-7} to 10^{-11}m^2/s (Goring, 1958; Ruan et al., 1991). Equation 5.44 is an empirical equation that covers the entire region from low to high moisture content and was arrived at from literature data on effective diffusivity (Ni, 1997).

The effective diffusivity of oil reported in literature shows a wide range from 1.321×10^{-5}m^2/s in tortilla chips (Moreira et al., 1995) to 4.9×10^{-8}m^2/s in restructured potatoes (Rubnov and Saguy, 1996). These diffusivity values unfortunately include effects of both the capillary flow and the pressure driven flow. Further, these values include both frying and post-frying oil pickup. So, the magnitude of these diffusivity values are higher than capillary diffusivity (as defined in this manuscript). The capillary oil diffusivity should be a function of local moisture content and oil content but no literature data is available for oil capillary diffusivity as a function of oil saturation or moisture content. The effective diffusivity of oil during frying as a function of initial moisture content is given by Moreira et al. (1997) and is the only expression available which indirectly relates to moisture content. Therefore, in our model, expression for capillary diffusivity of oil chosen after much analysis (Eq. 5.45) is a function of

oil content (same form of dependence as given by Eq. 5.44) and predicts a value which falls within the range reported in past literature:

$$D_{o,cap} = D_o \exp(-2.8 + 2.0\gamma) \tag{5.44}$$

where γ is the oil content (dry basis) given by $\phi S_o \rho_o / ((1-\phi)\rho_s)$ and $D_o = 1.22 \times 10^{-8}$ m^2/s as used in the model. The maximum diffusivity predicted by the above expression is same as that predicted by Moreira et al. (1997) for the initial moisture content of the model ($M = 2.5$). Sensitivity analysis of capillary oil diffusivity is done in the companion paper where its effects on oil pickup have been discussed in detail.

The specific heat capacity of liquid water and water-vapor are functions of temperature given by (Lewis, 1987):

$$c_{p,w} = 4176.2 - 0.0909(T-273) + 5.4731 \times 10^{-3}(T-273)^2 \tag{5.45}$$

$$c_{p,v} = [32.22 + 0.192 \times 10^{-2}(T-273) + 1.054 \times 10^{-5}(T-273)^2 - 3.594 \times 10^{-9}(T-273)^3]\frac{10^3}{M_v} \tag{5.46}$$

The thermal conductivity of liquid water as a function of temperature is given by (Choi and Okos, 1986):

$$k_w = 0.57109 + 1.762 \times 10^{-3}(T-273) - 6.7036 \times 10^{-3}(T-273)^2 \tag{5.47}$$

5.6 Conclusion

A multiphase porous media model of deep-fat frying has been developed, which can be applied to both frying and post frying cooling to predict important industrial food quality parameters such as crust thickness, oil pickup

and acrylamide content. Existing equilibrium vapor pressure model is replaced by non-equilibrium evaporation rate expression for a better approximation of evaporation kinetics. Heat and mass transfer coefficients used include the effect of different frying phases — the non-boiling phase, surface boiling and falling rate stages in the boiling phase. This model can be extended to processes like baking, convection drying, meat cooking with relatively minor changes, as basic physics behind all these processes is the same. Such a model has been implemented in a commercial software for the first time without sacrificing any fundamental physics and this opens up possibilities for simulation as a design tool for frying process, fried product and fryer development.

Acknowledgement

This research was partially supported by the United States Department of Agriculture Regional Project NC 1023 and the United States Department of Agriculture National Integrated Food Safety Project 2004-51110-02167.

BIBLIOGRAPHY

[1] Ateba, P. and Mittal G.S., 1994, Modeling the Deep-Fat Frying of Beef Meatballs, *International Journal of Food Science and Technology*, 29(4): 429-440.

[2] Bear, J., 1972, Dynamics of fluids in porous media, American Elsevier Publishing company, Inc., New York.

[3] Bird, R.B., Stewart, W.E. and Lightfoot, E.N., 2001, Transport phenomena, Second Edition, *John Wiley and Sons, Inc.*, Chapter 17, 513-542.

[4] Bouchon, P. and Pyle, D.L., 2005a, Modelling oil absorption during post-frying cooling - I: Model development, *Food and Bioproducts Processing*, 83(C4): 253-260.

[5] Bouchon, P. and Pyle, D.L., 2005b, Modelling oil absorption during post-frying cooling - II: Solution of the mathematical model, model testing and simulations, *Food and Bioproducts Processing*, 83(C4): 261-272.

[6] Chen, Y. and Moreira, R.G., 1997, Modelling of a batch deep-fat frying process for tortilla chips, *Food and Bioproducts Processing*, 75(C3):181-190

[7] Choi, Y. and Okos, M. R., 1986, Thermal properties of liquid foods – review, in Physical and Chemical Properties of Food, Okos, M. R. (editor), American Society of Agricultural Engineers, St Joseph, MI, USA, pp 35-77.

[8] Claeys, W.L., Vleeschouwer, K. De and Hendrickx, M.E., 2005, Quantifying the formation of carcinogens during food processing: acrylamide, *Trends in Food Science and Technology*, 16(5): 181-193.

[9] Corradini, M.G. and Peleg, M., 2006, Linear and non-linear kinetics in the synthesis and degradation of acrylamide in foods and model systems, *Critical Reviews in Food Science and Nutrition*, 46(6):489-517

[10] Datta, A.K., 2006, Hydraulic permeability of food tissues, *International Journal of Food Properties*, 9(4):767-780

[11] Datta, A.K., 2007, Porous media approaches to studying simultaneous heat and mass transfer in food processes. I: Problem formulations, *Journal of Food Engineering*, 80(1):80-95

[12] Dincer, I. and Yildiz, M., 1996, Modelling of thermal and moisture diffusions in cylindrically shaped sausages during frying, *Journal of Food Engineering*, 28(1): 35-44.

[13] Fang, G. and Ward, C.A., 1999a, Examination of the statistical rate theory expression for liquid evaporation rates, *Physical Review E*, 59(1):441-453

[14] Fang, G. and Ward, C.A., 1999b, Temperature measured close to the interface of an evaporating liquid, *Physical Review E*, 59(1):417-428

[15] Farid, M.M. and Chen, X.D., 1998, The analysis of heat and mass transfer during frying of food using a moving boundary solution procedure, *Heat and Mass Transfer*, 34(1): 69-77.

[16] Farkas, B.E., Singh, R.P. and Rumsey, T.R., 1996a, Modeling heat and mass transfer in immersion frying. Part 1. Model development, *Journal of Food Engineering*, 29(2): 211-226.

[17] Farkas, B.E., Singh, R.P. and Rumsey, T.R., 1996b, Modeling heat and mass transfer in immersion frying. Part 2. Model solution and verification, *Journal of Food Engineering*, 29(2): 227-248.

[18] Feng, H., Tang, J., Plumb, O.A. and Cavalieri, R.P., 2004, Intrinsic and relative permeability for flow of humid air in unsaturated apple tissues, *Journal of Food Engineering*, 62(2):185-192

[19] Gorling, P., 1958, Physical phenomenon during the drying of foodstuffs. Fundamental Aspects of the dehydration of foodstuffs, Society of chemical industry, London, S.W.1.

[20] Granda, C. and Moreira, R.G., 2005, Kinetics of acrylamide formation during traditional and vacuum frying of potato chips, *Journal of Food Process Engineering*, 28(5): 478-493.

[21] Hanreich, G. and Nicolics, J., 2001, Measuring the natural convective heat transfer coefficient at the surface of electronic components, *IEEE Instrumentation and Measurement Technology Conference*, 1045-1050.

[22] Hallstrom, B., 1979, Heat and mass transfer in industrial cooking, *Food Process Engineering*, 1: 457-465.

[23] Hubbard, L.J. and Farkas, B.E., 1999, A method for determining the convective heat transfer coefficient during immersion frying, *Journal of Food Process Engineering*, 22(3):201-214

[24] Ikediala, J.N., Correia, L.R., Fenton, G.A. and BenAbdallah N., 1996, Finite element modeling of heat transfer in meat patties during single-sided pan-frying, *Journal of Food Science*, 61(4): 796-802.

[25] Knol, J.J., Van Loon, W.A.M., Linssen, J.P.H., Ruck, A.L., Van Boekel, M. and Voragen, A.G.J., 2005, Toward a kinetic model for acrylamide formation in a glucose-asparagine reaction system, *Journal of Agricultural and Food Chemistry*, 53(15):6133-6139

[26] Le, C.V., Ly, N.G. and Postle, R., 1995, Heat and mass-transfer in the condensing flow of steam through an absorbing fibrous medium, *International Journal of Heat and Mass Transfer*, 38(1):81-89

[27] Labuza, T. P. 2001. The water in food panel: What do we know and what do we agree on? On the web at http://fscn.che.umn.edu/Ted_Labuza/tpl.html.

[28] Lewis, M.J., 1987, Physical properties of foods and food processing systems. Deerfield Beach, FL: VCH.

[29] Mascarenhas, W.J., Akay, H.U. and Pikal, M.J., 1997, A computational model for finite element analysis of the freeze-drying process, *Computer Methods in Applied Mechanics and Engineering*, 148(1-2): 105-124.

[30] Minkowycz, W.J., Haji-Sheikh, A. and Vafai, K., 1999, On departure from local thermal equilibrium in porous media due to a rapidly changing heat source: the Sparrow number, *International Journal of Heat and Mass Transfer*, 42(18):3373-3385

[31] Moreira, R.G., Palau, J.E. and Sun, X., 1995, Deep-fat frying of tortilla chips - an engineering approach, *Food Technology*, 49(4): 146-150.

[32] Moreira, R.G., Sun, X.Z. and Chen, Y.H., 1997, Factors affecting oil uptake in tortilla chips in deep-fat frying, *Journal of Food Engineering*, 31(4): 485-498.

[33] Mottram, D.S., Wedzicha, B.L. and Dodson, A.L., 2002, Acrylamide is formed in the Maillard reaction, *Nature*, 419(6906): 448-449.

[34] Ni, H., 1997, Multiphase moisture transport in porous media under intensive microwave heating. Ph.D. thesis, Cornell University, 1997

[35] Ni, H. and Datta, A.K., 1999, Moisture, oil and energy transport during deep-fat frying of food materials, *Food and Bioproducts Processing*, 77(C3): 194-204.

[36] Ratti, C., Crapiste, G.H. and Rotstein, E., 1989, A New Water Sorption Equilibrium Expression for Solid Foods Based on Thermodynamic Considerations, *Journal of Food Science*, 54(3):738-&

[37] Rubnov, M. and Saguy, I.S., 1996, Fractal analysis and crust diffusivity affect oil uptake during deep-fat frying, *IFT Annual Meeting*, Paper No. 74-2.

[38] Ruan, R., Schmidt, S.J., Schmidt, A.R. and Litchfield, J.B., 1991, Nondestructive measurement of transient moisture profiles and the moisture diffusion coefficient in a potato during drying and absorption by NMR imaging, *J. Food Process Engineering*, 14: 297-313.

[39] Scarpa, F. and Milano, G., 2002, The role of adsorption and phase change phenomena in the thermophysical characterization of moist porous materials, *International Journal of Thermophysics*, 23(4):1033-1046

[40] Surdyk, N., Rosen, J., Andersson R. and Aman, P., 2004, Effects of asparagine, fructose, and baking conditions on acrylamide content in yeast-leavened wheat bread, *Journal of Agricultural and Food Chemistry*, 52(7): 2047-2051.

[41] Tseng, Y.C., Moreira, R. and Sun, X., 1996, Total frying-use time effects on soybean-oil deterioration and on tortilla chip quality, *International journal of food science and technology*, 31:287-294.

[42] Tareke, E., Rydberg, P., Karlsson, P., Eriksson, S. and Tornqvist, M., 2002, Analysis of acrylamide, a carcinogen formed in heated foodstuffs, *Journal of Agricultural and Food Chemistry*, 50(17): 4998-5006.

[43] Ufheil, G. and Escher, F., 1996, Dynamics of oil uptake during deep-fat frying of potato slices, *Food Science and Technology-Lebensmittel-Wissenschaft and Technologie*, 29(7): 640-644.

[44] Ward, C.A. and Fang, G., 1999, Expression for predicting liquid evaporation flux: Statistical rate theory approach, *Physical Review E*, 59(1):429-440

[45] Williams, R. and Mittal, G.S., 1999, Low-fat fried foods with edible coatings: Modeling and simulation, *Journal of Food Science*, 64(2): 317-322.

[46] Yamsaengsung, R. and Moreira, R.G., 2002a, Modeling the transport phenomena and structural changes during deep fat frying - Part 1: model development, *Journal of Food Engineering*, 53(1): 1-10.

[47] Yamsaengsung, R. and Moreira, R.G., 2002b, Modeling the transport phenomena and structural changes during deep fat frying - Part II: model solution and validation, *Journal of Food Engineering*, 53(1): 11-25.

[48] Zhang, J., Datta, A.K. and Rakesh, V., 2005, Investigation of non-equilibrium in water evaporation, *3rd, Inter-American Drying Conference*, Montreal, Canada.

CHAPTER 6

APPLICATION TO DEEP-FAT FRYING. PART II: RESULTS, VALIDATION AND SENSITIVITY ANALYSIS

6.1 Abstract

The multiphase porous media model, developed in the companion paper, has been applied to frying of a restructured potato slice to obtain temperature, pressure, moisture, oil content, acrylamide content and evaporation rate profiles, providing valuable insight into the frying process. The model is validated by comparing temperature, moisture content and crust thickness profiles from literature experimental results. A novel non-equilibrium formulation, different from the existing food literature, is able to describe well the evaporation process. Post-frying cooling is included through appropriate changes in boundary conditions. It is seen that the oil pickup mostly takes place during post-frying cooling and is due to capillary suction created by the negative pressures from condensation of water-vapor. Acrylamide is formed primarily in the crust region where temperature exceeds 100°C. Sensitivity analyses of the process to surface mass transfer coefficient, evaporation rate constant and oil diffusivity show that they all have significant effects on the process. Development of this mechanistic model that is also more easily implementable than previous models should make computer-aided design and optimization of frying processes closer to reality.

Keywords: non-equilibrium, potato, crust formation, oil pickup, acrylamide.

Nomenclature

c_p	specific heat capacity, J $kg^{-1}K^{-1}$
D	diffusivity, m^2 s^{-1}
h	heat transfer coefficient, W m^{-2} K^{-1}
h_m	mass transfer coefficient of vapor, m s^{-1}
$\dot{I}$	volumetric evaporation rate, kg m^{-3} s^{-1}
k	thermal conductivity, W m^{-2} K^{-1}
k^p	total permeability, m^2
K	non-equilibrium evaporation constant
P, p	total pressure and partial pressure respectively, Pa
S	saturation
T	temperature, K
u	velocity, m s^{-1}
w	acrylamide content, ppm

Greek Symbols

ρ	density, kg m^{-3}

Subscripts

amb	ambient
a, g, o, s, v, w	air, gas, oil, solid, vapor, water
cap	capillary
eff	effective
eq	equilibrium
in	intrinsic

r	residual
sat	saturation
$surf$	surface

6.2 Introduction

Design and optimization of a frying process can greatly benefit from mathematical model of the process that provides in-depth understanding of the physics, as was noted in the companion paper. The multiphase porous media based model developed in the companion paper can provide spatial and transient temperature, pressure, water and oil saturation, and evaporation rate profiles. Transient and spatially varying evaporation rate, for example, has not been available in the past and can provide significant insight into the process. Many of the literature models treat evaporation at a sharp boundary and it would be useful to contrast the sharp boundary model with the distributed evaporation model in this study. Finally, a complex physics-based model such as this one has many input parameters not all of which have been measured or readily available. A mathematical model is very effective in understanding the sensitivity of model predictions to the various input parameters. This serves dual purpose— it provides insight into which parameters are critical and need to be manipulated in a design process; it also guides further research by isolating the most significant parameters for which more accurate data may be necessary. The objectives of this research are as follows: 1) To numerically solve the multiphase porous media based frying model developed in the companion paper and obtain quantities such as temperature, pressure and evaporation rate; 2) To relate these quanti-

ties to quality parameters, i.e., crust thickness, moisture content, oil pickup and acrylamide formation; 3) To determine the sensitivity of the model to various input parameters.

6.3 Results and Discussion

Predicted temperature, moisture, pressure and evaporation rate are computed as functions of position and time. Distributed evaporation model used in this paper is contrasted with sharp evaporation front model from literature. Quality parameters of crust formation, oil pickup and acrylamide formation are computed as function of space and time. Finally, sensitivity of the computations to mass transfer coefficient, evaporation rate constant, oil diffusivity and intrinsic permeability is shown.

6.3.1 Temperature distribution

One of the important factors affecting crust formation and acrylamide generation is temperature. The higher the temperature in the domain, more is the crust thickness and acrylamide generation. As shown in Figure 6.1a, temperature rises sharply at the heating surface and reaches a temperature of 170°C within 1 minute of frying. Initially there is a sharp increase in surface temperature because of the large temperature difference (155°C) between the potato surface and the oil which amounts to a high energy flux. The temperature difference between the surface and the oil decreases with time and rise in temperature inside the potato slab slows down. As shown in Figure 6.3a, at a distance of 0.05

cm from the surface, temperature rises sharply to 105°C in one minute and then gradually reaches 160°C after 16 mins. Deep inside the core, heating starts after some time as evaporation uses up a lot of energy at the surface and insulates the core (e.g., at a distance of 0.85 cm from the surface, heating starts after 30 seconds). The simulation results are compared with the experimental data of Farkas et al. (1996a) as shown in Figure 6.3a. The predicted temperatures at a distance of 0.05 cm from the surface are close to experimental values for the first two minutes but there is a considerable difference between them for next 10 minutes and finally again matching closely for the last 4 minutes of frying. One of the limitations of the experiment as reported by Farkas et al. (1996a) is that there is a tendency of the thermocouple to shift during frying. In the crust region where large temperature gradients exist, a small shift in thermocouple's position will lead to large changes in temperature. In a subsequent study of Hubbard and Farkas (1999), the measured surface temperatures showed similar values as obtained by our model and there was no drop in temperature between 2 and 12 minutes at the 0.05 cm location. This further strengthens the point that temperature measurement technique for the depth of 0.05 cm has some discrepancy. The temperature prediction for 0.42 cm and 0.85 cm from the frying surface compares well with the experimental measurements. The temperature gradients at these depths are small and a slight shift in position of thermocouple during frying would not give significant errors. The predicted temperatures at the depth of 1.27 cm matches closely with the experimental results initially for the first 1 minutes but are higher than the experimental results between 4 and 12 minutes. Again the profiles match closely with the experimental results for the last 4 minutes of frying.

Although our model is based on distributed evaporation and not a sharp

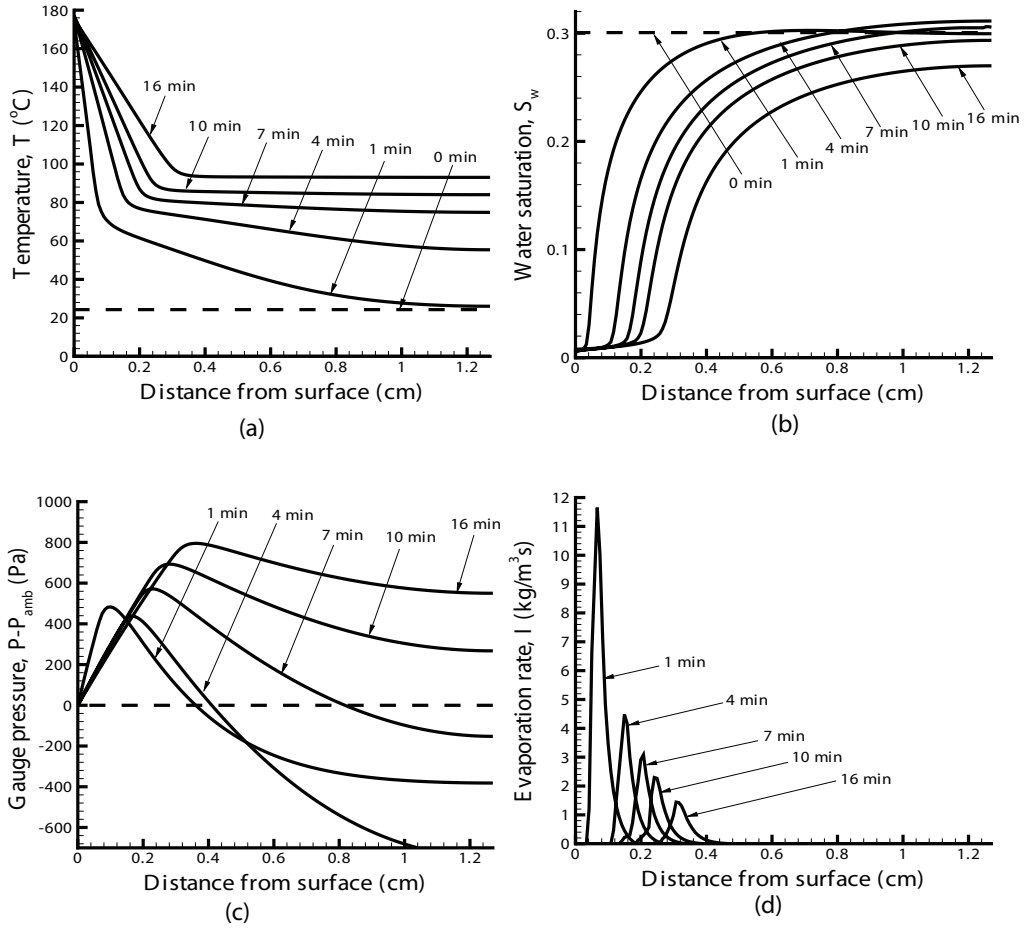

Figure 6.1: Spatial profiles in a potato slab at various times during frying: a) Temperature, T; b) Water saturation, S_w; c) Gauge Pressure, $P - P_{amb}$; and d) Evaporation rate, $\dot{I}$.

boundary formulation, a fairly distinct crust region (dry with no liquid water) develops as shown in Figure 6.1a and 6.1b. The rest of the domain is termed as the core region. The crust region is heated up more quickly than the core region because the effective heat capacity, $\rho c_{p,eff}$, of the crust is much lower due to the absence of liquid water. There is a sharp bend in the temperature profiles (Figure 6.1a) at around 90°C. This region is the crust-core interface where rapid evaporation is taking place (Figure 6.1d and 6.2) and a pseudo-steady state is

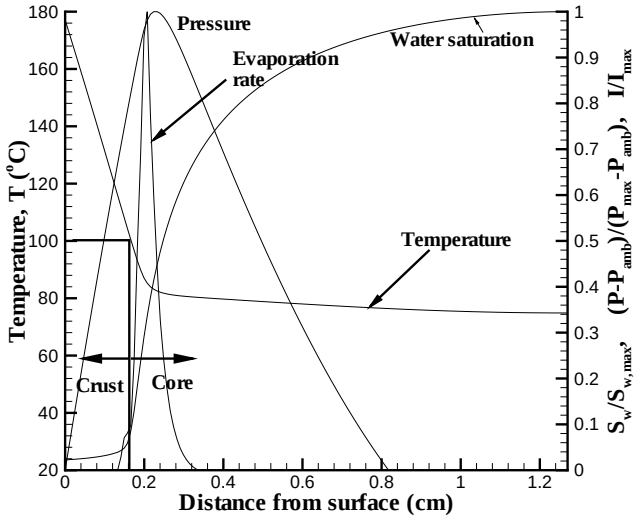

Figure 6.2: Spatial profiles in a potato slab after 7 minutes of frying: Temperature, T, Water saturation, S_w, Gauge pressure, p, and Evaporation rate, $\dot{I}$, superimposed for improved understanding. The saturation, pressure and evaporation rate are divided by their maximum values ($S_{max} = 0.305$, $P_{max} = 550$ Pa, $\dot{I}_{max} = 3.08$ kg/m^{3}s).

reached where significant amount of heat is going into latent heat of vaporization, making temperature rise slow. Also, the temperature at which this rapid evaporation is taking place is sensitive to the magnitude of the mass transfer coefficient.

6.3.2 Moisture distribution

Moisture, in form of vapor, is convected away from the frying surface. The liquid water that reaches the surface first evaporates and is then convected away. Initially, high rate of evaporation near the surface produces large amounts of vapor that cannot escape from the surface due to surface mass transfer limitations,

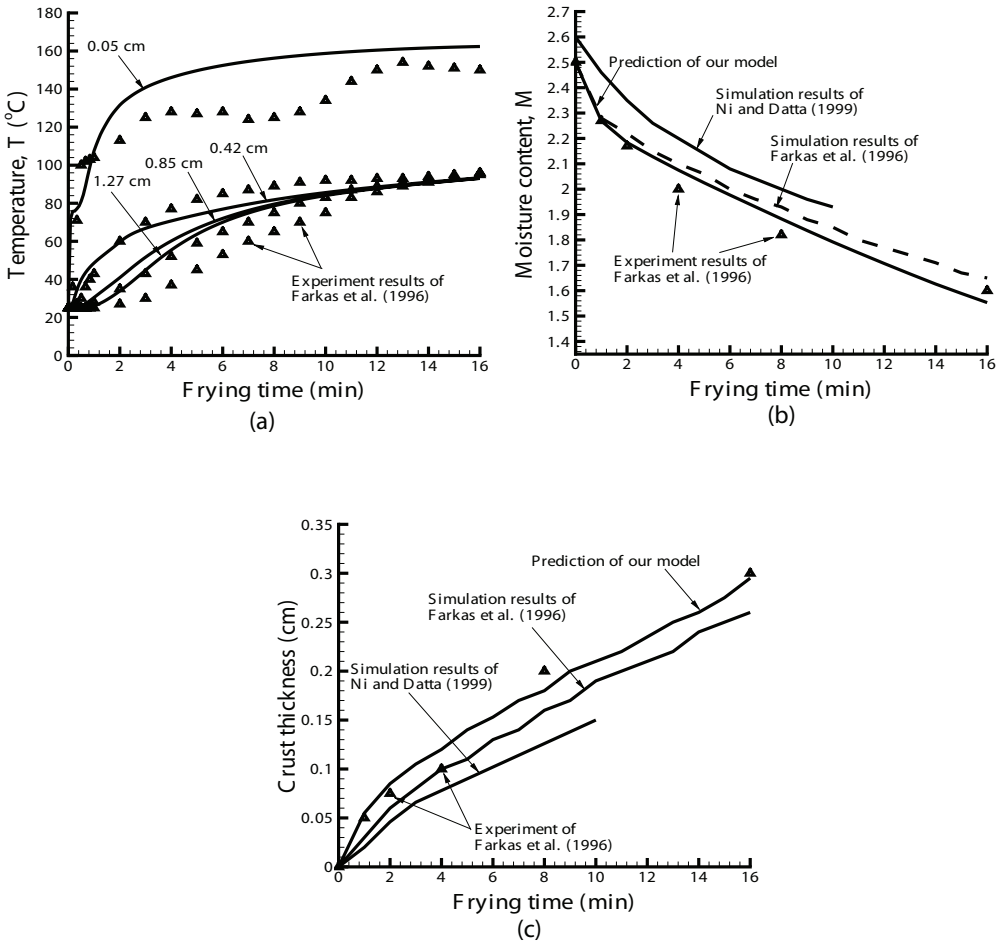

Figure 6.3: Comparison of model predictions with literature experimental data for a) Temperature; b) Moisture content (dry basis); and c) Crust thickness (region having temperature $T > 100$°C).

so excess vapor moves towards the core. Since the core is a cooler region, the vapor coming from the surface condenses there, reducing the pressure below ambient pressure. Therefore, as can be seen in Figure 6.1b, the liquid saturation in the core increases from 0.3 to 0.32 in the first four minutes. Similar migration of liquid water from or near the surface to the core has been observed in experiments done on meat (e.g., Oroszvari et al., 2006). After 4 minutes, as the evaporation inside the core becomes significant and the core pressure rises, movement

of water vapor from the surface toward the core decreases. Capillary migration of liquid water out of the core into the crust decreases water saturation at the core from 0.32 to 0.27 during the next 12 minutes of frying. On and near the surface, liquid water saturation decreases rapidly and becomes negligible after 60 seconds of frying.

As shown in Figure 6.3b, moisture content (dry-basis) of the potato slab dropped from its initial value of 2.50 to 1.56 after 16 minutes of heating. Our model prediction matches very closely with the experimental results of Farkas et al. (1996), a better match than that achieved by Ni and Datta (1999) and the modeling work of Farkas et al. (1996). Such close agreement between experimental measurements and model prediction confirms the effectiveness of the model and serves to validate the model.

6.3.3 Pressure distribution

No measurement of dynamic pressure inside the food during frying has been reported due to obvious difficulties in such measurements. Pressure buildup during frying has been computed (Ni and Datta, 1999; Yamsaengsung and Moreira, 2002). Ni and Datta (1999) predicted a gauge pressure of around 1000 Pa after 10 minutes of frying. Yamsaengsung and Moreira (2002) predicted an average pressure of 2.84×10^5 Pa inside the tortilla chips after 60 seconds of frying. Such high pressure is unlikely to exist during frying as it will blow up the potato. Thus, pressures predicted by Ni and Datta (1999) seem more reasonable.

As shown in Figure 6.1c, the peak pressure occurs at the crust-core interface. The peak pressure reached 500 Pa within 1 minute of frying and 800 Pa after 16

minutes of frying. As evaporation slows down with time, pressure buildup reduces. In the crust, the gauge pressure always remained positive as rapid evaporation is taking place in this region. In the core, gauge pressure is negative for the first 8 minutes of frying because water-vapor coming from the surface condenses in the cooler core region. As the core temperature starts to rise, evaporation rate increases and so does the pressure. The gauge pressure in the core rises from -800 Pa after 4 minutes to 600 Pa at the end of 16 minutes of frying. The pressure prediction by our model and by Ni and Datta (1999) are similar but experiments need to be done to validate the above reported pressures.

6.3.4 Distributed evaporation rate

As shown in Figure 6.1d, evaporation rate is maximum at the core-crust interface and reduces sharply on either side. More discussion on this is provided in the following section. Initially, the evaporation rate is high (has a higher peak) because of both larger temperature difference between the oil and the surface, and also the higher heat transfer coefficient. Later, both the temperature difference and the heat transfer coefficient reduce and, in addition, the thermally insulating crust layer forms, all contributing to lower rate of heat transfer. Another important observation is that the zone of evaporation is of the order of 2 mm. Whether this is small enough so that a sharp boundary assumption (see discussion below) is valid, needs further investigation. Spatial distribution of evaporation has not been available in the past and is a major contribution of this study.

6.3.5 Distributed evaporation (this study) contrasted with a sharp boundary formulation for evaporation

In a sharp-boundary formulation (Farkas et al., 1996), phase change occurs at the interface only. But as can be seen in Figure 6.1d, significant phase change extends to inside the crust (defined as region having temperature above 100°C) and the core, although the total distance is somewhat small (about 2 mm). Thus, a distributed evaporation model can predict a narrow evaporation zone where rapid evaporation is taking place. A sharp boundary formulation can over-predict the core temperature as it ignores any phase change in the core that would act as heat sink. Since transport of water vapor toward the core is ignored in a sharp boundary formulation, migration of water vapor from the interface to the core (Figure 6.1b), an experimental fact (Oroszvari et al., 2006), is not seen in a sharp boundary formulation.

Another limitation of the sharp boundary model by Farkas et al. (1996) is that it ignores the presence of air inside the food domain. It assumes that the vapor pressure is driving the flow of vapor toward the surface. The vapor pressure at the interface is assumed to be 1 atmosphere and negligible at the surface. So, according to a sharp boundary formulation, a pressure difference of 1 atmosphere between the crust-core interface and the surface drives the vapor. This would have been true if the partial pressure of air at the boundary and at the surface were the same. But as evaporation takes place, the vapor produced expels the air and occupies its space. This is not a closed system where the pressure rise is completely due to the vapor produced but the pressure rise during frying is the net result of increase due to vapor produced and decrease due to vapor and air leaving from the surface. At the interface, the total pressure due to vapor and

air is much less than 2 atmospheres and at the surface, total pressure is 1 atmosphere due to air alone. Therefore, a sharp boundary problem will over predict the vapor flux in the crust region as the pressure difference between the surface and the interface is never as high as 1 atmosphere. The pressure difference between the crust-core interface and the surface, as observed from simulation results in Figure 6.1d, is around 1000 Pa in contrast to 10^5 Pa as used by Farkas et al. (1996).

6.3.6 Variations in effective transport properties during processing

Since the composition of the food material changes (water moves out and oil moves in) during processing, transport and other properties at a location in the food go through constant variation based on the amount of different phases present and the temperature, all of which change with time. Knowledge of such changes can provide great insight into the process. Since it is hard to visualize the quantitative variations of a property based on algebraic expressions (such as Eq. 5.15-5.18 from the companion paper) alone, a snapshot of such changes at a location 0.1 cm from the surface are plotted in Figure 6.6. As can be seen in Figure 6.6a, effective thermal conductivity, k_{eff}, decreases from its initial value of 0.21 W/mK to 0.05 W/mK during the first 6 minutes of frying. During this time liquid water saturation in the region decreases and gas saturation (having lower thermal conductivity) increases, thus decreasing k_{eff}. After 6 minutes, k_{eff} increases slightly as oil from the surface reaches this region. Figure 6.6b shows that the capillary diffusivity of water decreases with time because the water

saturation in the region decreases from 0.3 to zero in 6 minutes. The diffusivity of oil increases as the oil saturation increases with time. In Figure 6.6c, the changes of permeability of water and oil with time is shown. The water permeability decreases sharply from 10^{-15} to 10^{-25} in approximately 4 minutes as water saturation decreases from 0.3 to near zero, since the relative permeability follows a cubic power of water saturation.

6.3.7 Crust thickness

During frying, two distinct zones develop in the potato slab: the crust and the core, with the crust being defined as a dry region with no liquid water. Farkas et al. (1996) defined crust as the region with temperatures above 100°C. Since, negligible liquid water exists above 100°C, this definition of crust is acceptable and has been used in our model to estimate the crust thickness. As can be seen in Figure 6.1d, maximum evaporation takes place at the crust-core interface. Crust movement is slow because in a pore until all the phase change from liquid water to water vapor with absorption of latent heat of vaporization has occurred, the interface does not move forward. From Figure 6.3c, it can be seen that the crust thickness after 16 minutes of frying is 0.3 cm. The model prediction of crust thickness matches very closely with the experimental results of Farkas et al. (1996). The good agreement between experimental measurements and model prediction again confirms the effectiveness of the model in predicting various safety and quality factors.

6.3.8 Oil pickup

Oil pickup is a major concern during frying. Though oil imparts necessary flavor and texture to the product but consumption of excess oil is unhealthy. Oil pickup can be due to the separate mechanisms of capillary action and pressure driven flow. During the times of rapid evaporation during frying, the flow of oil from outside to inside is impeded by the vigorous outflow of vapor and liquid water. Effect of this is implemented in the model using different surface concentrations during frying and post-frying cooling. As can be seen in Figure 6.4b (and later in 6.10b), significant amount of oil still diffuses (through capillarity) during frying. The oil content, defined as kg of oil absorbed per kg of dry solid, after 16 minutes of frying is 0.106.

During post-frying cooling, evaporation reduces and no vigorous escape of vapor takes place at the surface. The temperature at the surface decreases from 173°C to 37°C within 5 minutes of cooling (Figure 6.4a) and there is a pressure drop inside the potato due to condensation of water-vapor. This causes pressure driven flow of oil from outside to inside. The pressure driven flow and capillary flow together cause rapid oil-pickup (Figure 6.10b) and within 5 minutes of cooling, the oil content in the potato reaches 0.44. Thus, 24% of the total oil pickup takes place during frying and rest during post-frying cooling. Similar observations were made by Moreira et al. (1997) where they found that 20% of the total oil pickup takes place during frying and rest during post-frying cooling.

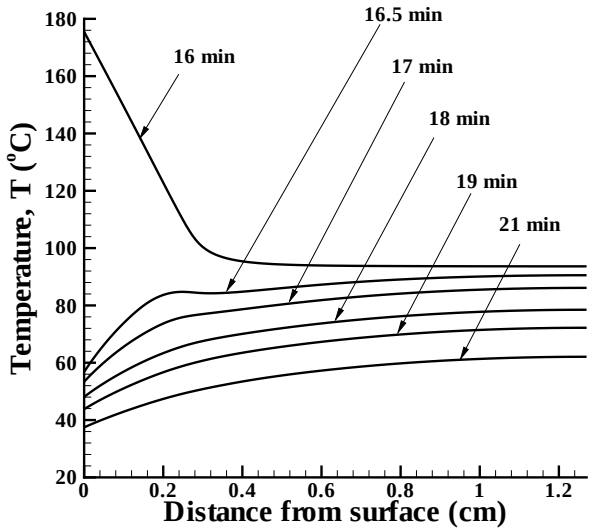

(a)

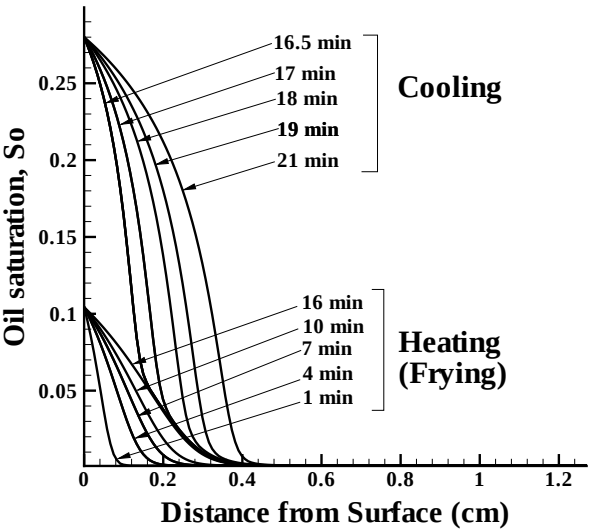

(b)

Figure 6.4: Spatial profiles of a) Temperature, T, at various times during post-frying (16 minutes of frying) cooling of a potato slab; b) Oil saturation, S_o, at various times during frying and post-frying cooling.

6.3.9 Acrylamide formation

As has been mentioned, acrylamide content in fried potato chips is highly undesirable because it is carcinogenic. Acrylamide formation is assisted by high temperatures. Figure 6.5a shows the predicted acrylamide content as a function of position during the frying process. Such spatial distributions of acrylamide have not been available in the past and is a novel contribution of this study. The total acrylamide content, computed as $(\int_A w dA')/A$, where A is 0.0127 m $\times$ 0.0008 m (area of computational domain), is shown in Figure 6.5b. After 16 minutes of frying, computed value of acrylamide content is 14.8 ppm which compares well with experimental data in published literature (also plotted in the same figure). Similarly, Granda and Moreira (2005) experimentally measured an acrylamide content of 1.1 ppm after 4 minutes of frying of potato chips in oil at 180°C. This compares well with the prediction by our model of 1.6 ppm. Claey's et al. (2005) reported that acrylamide formed after 10 minutes of frying is approximately 6.5 ppm for a glucose-asparagine model system heated at 185°C, which again compares well with our model prediction of 8.5 ppm. Acrylamide formation in glucose-asparagine model system is not same as ours but it closely resembles that in a potato (Corradini and Peleg, 2006) and therefore can serve as additional validation of our model.

6.3.10 Sensitivity of the model to convective mass transfer coefficient

As can be seen in Figure 6.7, temperature, moisture and pressure predictions depend significantly on the convective mass transfer coefficient of vapor, h_m.

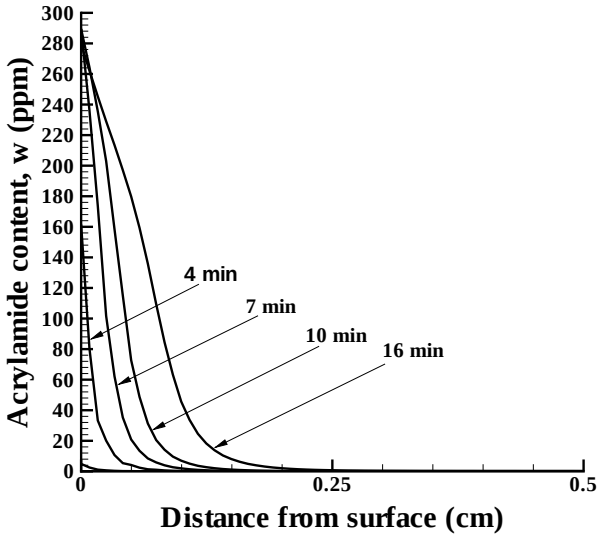

(a)

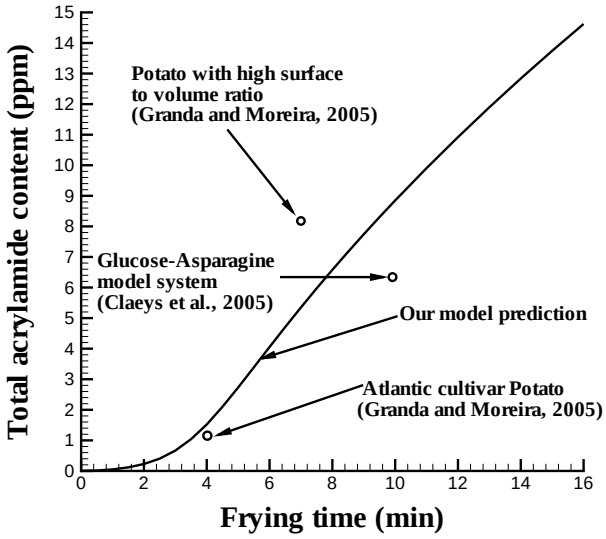

(b)

Figure 6.5: a) Spatial profiles of acrylamide content in a potato slab at various times during frying; b) Total acrylamide content in the potato slab during frying with literature experimental data superimposed

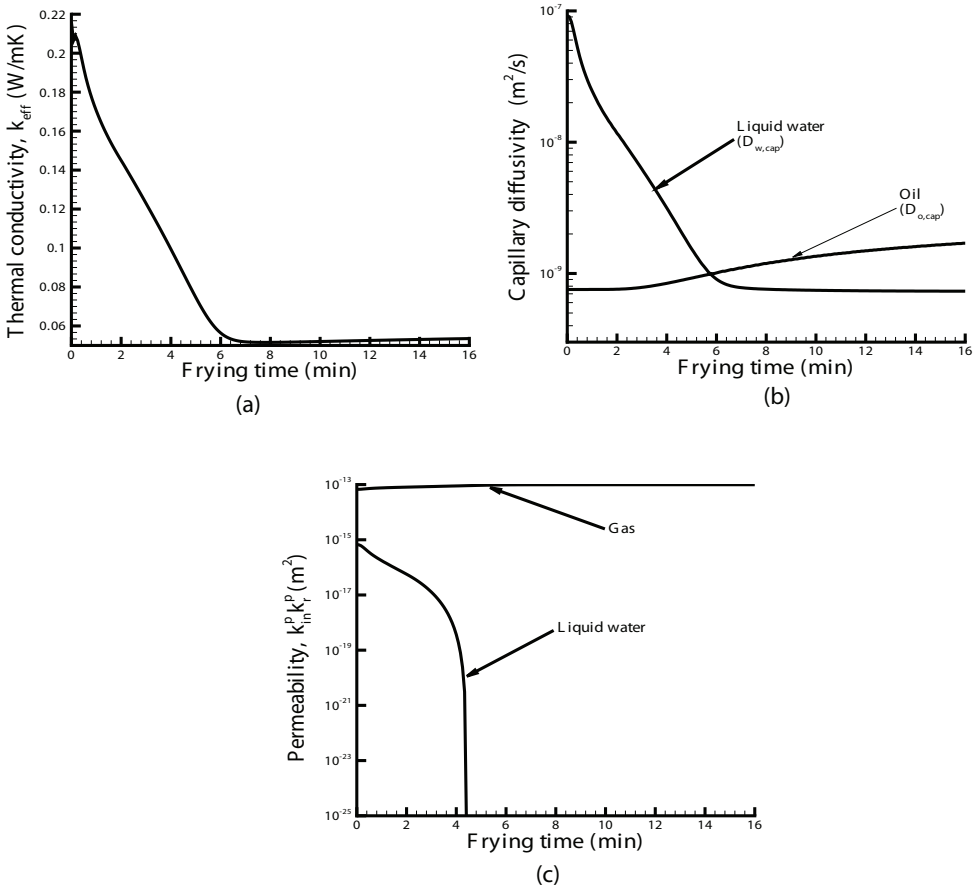

Figure 6.6: Representative curves showing how the various transport properties of potato at a location change over time due to changes in mass concentrations and temperature. Shown are: a) Effective thermal conductivity, k_{eff}; b) Capillary diffusivity of liquid water, $D_{w,cap}$, and that of oil, $D_{o,cap}$; c) Permeability, $k_{in}^p k_r^p$, of water and oil. The location chosen is 0.1 cm from surface.

Although a time varying h_m has been used in our model for better understanding of the effect of h_m in frying, sensitivity analysis in Figure 6.7 uses values of h_m which are constant over time. A higher value of h_m leads to lower temperature, higher pressure and increased moisture loss.

A high value of h_m means a low resistance to the surface vapor transfer. As a

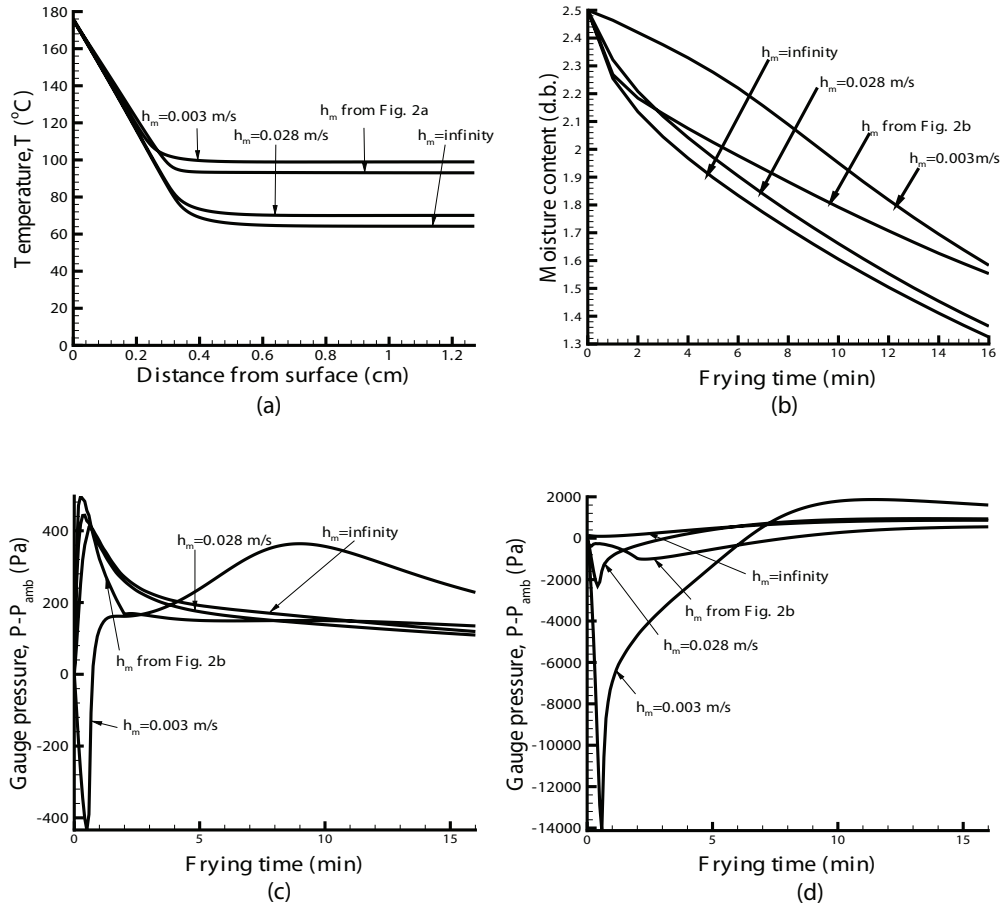

Figure 6.7: Sensitivity of frying process to the convective mass transfer coefficient, h_m, as measured by: a) Spatial temperature profiles after 16 minutes of frying; b) Transient moisture content; Transient pressure profiles at two depths— c) 0.05 cm (crust) and d) 1.27 cm (core)

result, more vapor is removed from the surface and evaporation rate inside adjusts to a higher value. Higher rate of evaporation (for larger h_m) leads to lower temperature rise (Figure 6.7a) due to large amount of energy going into latent heat of vaporization. Higher evaporation rate also leads to increased pressure development, as can be seen in Figures 6.7b and 6.7d. Similarly, the moisture content is lower for higher h_m (Figure 6.7c) as more vapor is being convected

away from the surface.

A higher resistance to the surface vapor transfer (lower h_m) causes excess vapor to move toward the core and condense in the cooler region which causes a drop in pressure. As shown in Figure 6.7c and d, for high values of h_m, there are no negative gauge pressures in the core region as all the vapor produced is convected away at the surface and no vapor is moving toward the core and therefore no condensation. But for lower values of h_m, there is negative gauge pressures in the core region as there is significant condensation of vapor.

In Figure 6.7a, a sharp bend appears in the spatial profiles of temperature and this is the region where maximum evaporation is taking place. The temperature at which these profiles bend is very sensitive to h_m. A high mass transfer coefficient will cause a large amount of vapor to exit from the surface and this is compensated by more evaporation inside the potato. The higher the h_m, lower the temperature where maximum evaporation takes place. When a constant surface concentration is given (or mass transfer coefficient of infinite value), the maximum evaporation takes place at 70^oC while at a mass transfer coefficient of 0.003 m/s, the maximum evaporation takes place at 100^oC. Oil pickup is not affected by h_m, signifying that pressure gradient opposing oil inflow (due to vigorous vapor outflow) is insignificant when compared to capillary forces driving the oil inside the potato.

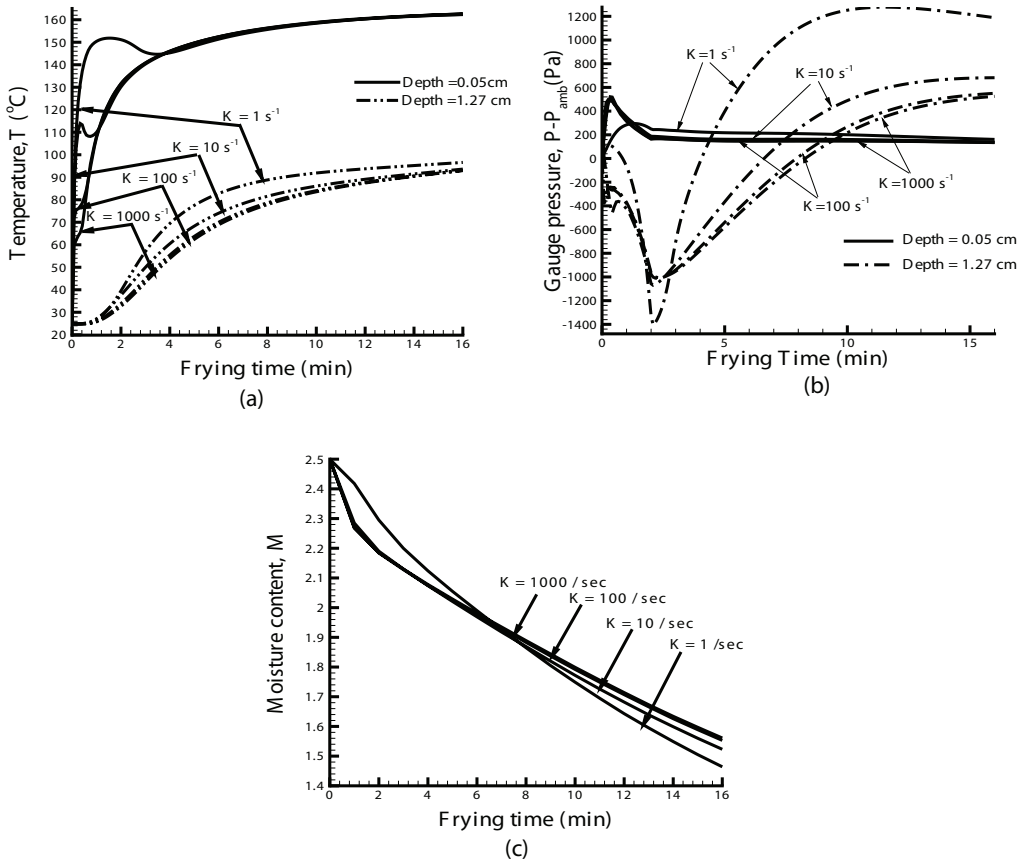

Figure 6.8: Sensitivity of the frying process computations to the evaporation rate constant, K: a) Transient temperature at two depths, 0.05 cm (crust) and 1.27 cm (core); b) Transient pressure at two depths, 0.05 cm (crust) and 1.27 cm (core); c) Transient moisture content.

6.3.11 Sensitivity of the model to non-equilibrium evaporation constant

Another important model parameter is the non-equilibrium evaporation constant, K. Figures 6.8a, b and c, show the effect of choice in K on temperature, moisture and pressure profiles.

As can be seen in Figure 6.8a, for low values of K, the evaporation rate is small and thus higher temperatures are seen in the core region because less energy is going into vaporization of liquid water. Similarly, higher moisture content is observed for high values of K (Figure 6.8c), because evaporation rate is low due to lower temperature in the core compared to lower values of K. As can be seen in Figure 6.9a, at a depth of 0.2 cm from the surface, maximum evaporation rate occurs for $K = 1000\,\mathrm{s}^{-1}$ and minimum for $K = 1\,\mathrm{s}^{-1}$ as K directly affects the evaporation rate. For $K = 1000\,\mathrm{s}^{-1}$, for the first 4 minutes there is condensation at the depth of 0.2 cm. This is because rapid evaporation is occurring near the surface and excess vapor move towards the cooler regions as they are not convected away due to the surface mass transfer resistance. The vapor moving to colder regions condenses and causes pressure drop. After 4 minutes, evaporation starts at the depth of 0.2 cm, peak evaporation rate occurs at about 6 minutes and evaporation ends after 7 minutes of frying. After 7 minutes, all the water is lost from this depth or this is the extent of the crust. For lower values of K, initially there is less condensation at this depth compared to $K = 1000\,\mathrm{s}^{-1}$ because less evaporation is taking place between this depth and the surface and therefore less vapor is moving towards the core and condensing. The time interval for which evaporation takes place at this depth is smallest for $K = 1000\,\mathrm{s}^{-1}$ and increases as K is decreased. For $K = 1\,\mathrm{s}^{-1}$, significant evaporation is present even after 16 minutes of frying as evaporation rate with this rate constant value is severely limited.

As can be seen in Figure 6.9b and c, the vapor pressure in the potato is at equilibrium in most of the potato slab except at the crust-core interface where rapid evaporation is taking place. The deviation of vapor pressure from equilibrium condition at the interface decreases as K is increased. This suggests

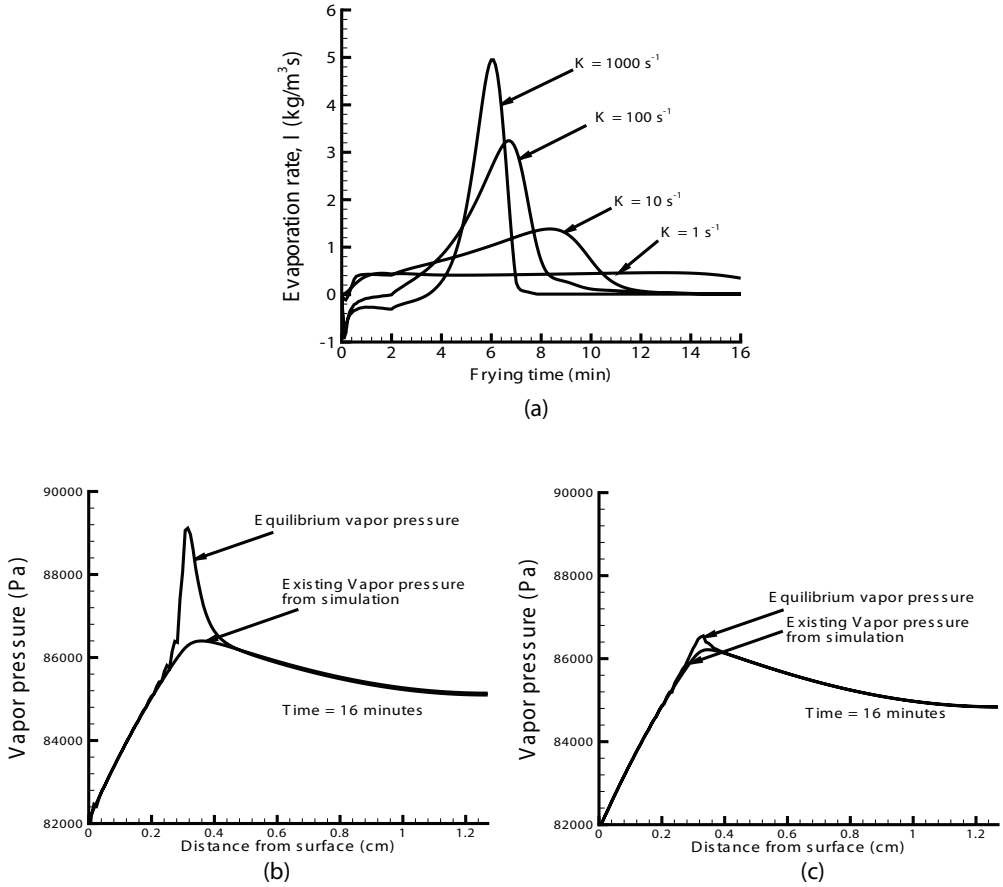

Figure 6.9: Sensitivity of the frying process computations to the evaporation rate constant, K: a) Transient evaporation rate at a distance of 0.2 cm from the surface. Negative value of evaporation rate denotes condensation; b) Deviation of vapor pressure from equilibrium vapor pressure for $K = 100$; and c) Same deviation for $K = 1000$.

that with high values of K, we can simulate an equilibrium problem. But from Figure 6.8a, b and c, it can be seen that changes in temperature, moisture content and pressure is very small as K is increased from $100\ s^{-1}$ to $1000\ s^{-1}$ and even $10000\ s^{-1}$ (omitted here for clarity). This suggests that we can simulate a case which is very close to equilibrium with $K = 100\ s^{-1}$. Even though we get closer to equilibrium by taking higher values of K (more than $100\ s^{-1}$) but

large source terms give numerical convergence problems. So, $K = 100\,\mathrm{s}^{-1}$ is an optimum value which keeps the system very close to equilibrium and is low enough to avoid convergence problems while solving.

6.3.12 Sensitivity of the model to capillary diffusivity of oil

Capillary diffusivity of oil is unavailable. Thus, it is important to know how the choice of capillary diffusivity affects the solution, particularly oil pickup. This will also tell us the importance of capillary flow as compared to pressure driven flow in oil pickup.

The sensitivity analysis of capillary diffusivity of oil was done by taking three values of D_o (see Eq. 44 in companion paper). As can be seen in Fig. 6.10a and 6.10b, diffusivity of oil affects oil pickup significantly. Higher the oil diffusivity, greater is the oil pickup. For $D_o = 1.22 \times 10^{-7}\mathrm{m}^2/\mathrm{s}$, the oil pickup is the maximum during frying as well as during post-frying cooling. Oil penetration inside the potato is also maximum for higher diffusivity value. But the use of such a high diffusivity value ($1.22 \times 10^{-7}\mathrm{m}^2/\mathrm{s}$) leads to oil penetration deep inside the core that contradicts previous studies (Ufheil and Escher, 1996; Moreira et al., 1997) that have reported oil pickup primarily in the crust region and only slightly inside the core. A diffusivity value of $1.22 \times 10^{-8}\mathrm{m}^2/\mathrm{s}$ seems more appropriate as the oil fills the crust region and also slightly inside the core as reported in the literature.

It can be concluded that the main mechanism behind oil pickup is capillary action. As we decrease the capillary diffusivity, oil pickup decreases and for $D_o = 1.22 \times 10^{-9}\mathrm{m}^2/\mathrm{s}$ oil pickup is only 0.1 (d.b.) which is one-fifth of the

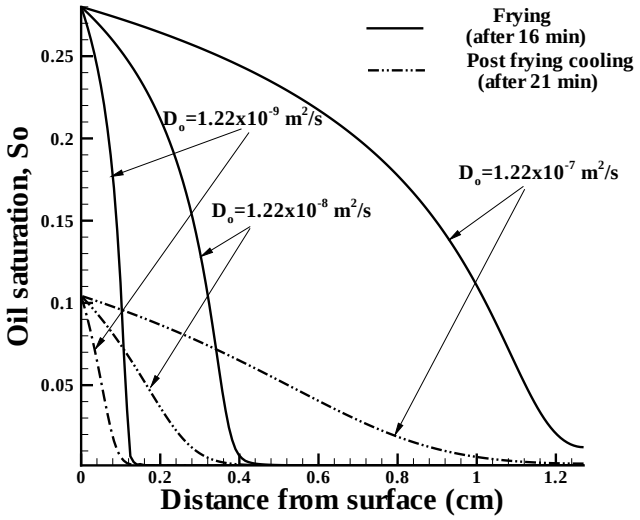

(a)

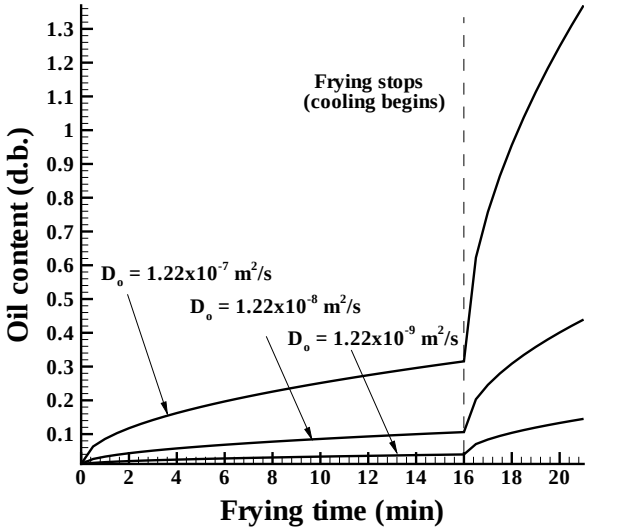

(b)

Figure 6.10: Sensitivity of oil pickup to the diffusivities of oil: a) Spatial distribution of oil after 16 minutes of frying and after post-frying cooling (at 21 minutes); b) Total oil content during frying and post-frying cooling.

pickup when $D_o = 1.22 \times 10^{-8} \mathrm{m}^2/\mathrm{s}$. These observations imply that the effect of pressure driven flow in oil pickup is insignificant.

6.4 Conclusions

A multiphase porous media model of frying, developed in the companion paper, has been solved to predict temperature, moisture, pressure, evaporation rate, and important food quality parameters of crust thickness, oil pickup and acrylamide content. The model has been validated with literature experimental data. A novel non-equilibrium formulation of the phase-change (evaporation and condensation), that is a more realistic representation, describes well the physics of frying process and is easier to incorporate in a numerical model. However, the rate constant, K, needed for such a non-equilibrium formulation of phase change in a hygroscopic material is currently not available and was determined in this study through sensitivity analysis. It was found that the simulation results match better with experimental results when using a high value of K, i.e., when vapor pressure is close to equilibrium. Spatial profiles of evaporation during frying and post-frying cooling process are available for the first time. They provide more insight into the process by relating to moisture loss and crust formation.

Furthermore, sensitivity analysis of convective mass transfer coefficient and capillary diffusivity of oil showed that they affect the model significantly. For accurate prediction of crust thickness and moisture content, it is critical to have accurate estimates of the time-varying mass transfer coefficient and experimentation to directly measure this should be tried. The oil pickup mainly takes place

during post frying cooling due to capillary action and not so much through pressure driven flow. Only 24 % of oil pickup takes place during frying and rest during post-frying cooling. Spatial profiles of acrylamide, available for the first time, show that acrylamide forms primarily in the crust region.

Acknowledgement

This research was partially supported by the United States Department of Agriculture Regional Project NC 1023 and the United States Department of Agriculture National Integrated Food Safety Project 2004-51110-02167.

BIBLIOGRAPHY

[1] Claeys, W.L., Vleeschouwer, K. De and Hendrickx, M.E., 2005, Quantifying the formation of carcinogens during food processing: acrylamide, *Trends in Food Science and Technology*, 16(5): 181-193.

[2] Corradini, M.G. and Peleg, M., 2006, Linear and non-linear kinetics in the synthesis and degradation of acrylamide in foods and model systems, *Critical Reviews in Food Science and Nutrition*, 46(6):489-517

[3] Farid, M.M. and Chen, X.D., 1998, The analysis of heat and mass transfer during frying of food using a moving boundary solution procedure, *Heat and Mass Transfer*, 34(1): 69-77.

[4] Farkas, B.E., Singh, R.P. and Rumsey, T.R., 1996, Modeling heat and mass transfer in immersion frying. Part 1. Model development, *Journal of Food Engineering*, 29(2): 211-226.

[5] Farkas, B.E., Singh, R.P. and Rumsey, T.R., 1996, Modeling heat and mass transfer in immersion frying. Part 2. Model solution and verification, *Journal of Food Engineering*, 29(2): 227-248.

[6] Feng, H., Tang, J., Plumb, O.A. and Cavalieri, R.P., 2004, Intrinsic and relative permeability for flow of humid air in unsaturated apple tissues, *Journal of Food Engineering*, 62(2):185-192

[7] Granda, C. and Moreira, R.G., 2005, Kinetics of acrylamide formation during traditional and vacuum frying of potato chips, *Journal of Food Process Engineering*, 28(5): 478-493.

[8] Hubbard, L.J. and Farkas, B.E., 1999, A method for determining the convective heat transfer coefficient during immersion frying, *Journal of Food Process Engineering*, 22(3):201-214

[9] Moreira, R.G., Sun, X.Z. and Chen, Y.H., 1997, Factors affecting oil uptake in tortilla chips in deep-fat frying, *Journal of Food Engineering*, 31(4): 485-498.

[10] Ni, H. and Datta, A.K., 1999, Moisture, oil and energy transport during deep-fat frying of food materials, *Food and Bioproducts Processing*, 77(C3): 194-204.

[11] Oroszvari, B.K., Bayod, E., Sjoholm, I. and Tornberg, E., 2006, The mechanisms controlling heat and mass transfer on frying of beefburgers. III. Mass transfer evolution during frying, *Journal of Food Engineering*, 76(2):169-178

[12] Ufheil, G. and Escher, F., 1996, Dynamics of oil uptake during deep-fat frying of potato slices, *Food Science and Technology-Lebensmittel-Wissenschaft and Technologie*, 29(7): 640-644.

[13] Yamsaengsung, R. and Moreira, R.G., 2002, Modeling the transport phenomena and structural changes during deep fat frying - Part 1: model development, *Journal of Food Engineering*, 53(1): 1-10.

[14] Yamsaengsung, R. and Moreira, R.G., 2002, Modeling the transport phenomena and structural changes during deep fat frying - Part II: model solution and validation, *Journal of Food Engineering*, 53(1): 11-25.

CHAPTER 7

A USER-FRIENDLY GENERAL-PURPOSE PREDICTIVE SOFTWARE PACKAGE FOR FOOD SAFETY

7.1 Abstract

Computer-aided engineering tools can help speed up food product, process and equipment design by making it easier to check 'what if' scenarios, much like how such tools have improved productivity in other industries. In particular, food safety is a critical area where such predictive tools can have great impact. A realistic, integrated and comprehensive software has been developed that can simulate a food process and its safety by combining fundamental, physics-based model of the process with the kinetics of microbiological and chemical changes during processing to provide needed information at any time and at any location in the food during processing. Composition-based prediction of thermophysical properties, needed for the models are built-in. Compositions for a large number of foods are integrated into the software. Microbiological and chemical kinetic databases are also built-in that can cover many practical situations, based on grouping of foods. An intuitive graphical user interface has been built for those in the food sector in mind.

Keywords: Food safety, predictive software, process modeling, GUI

7.2 Introduction

To increase the efficiency and competitiveness of food product, process and equipment design, computer-aided engineering (CAE) tools, where the physical reality is replaced by its equivalent computer model, and which allows checking 'what if' scenarios quicker, can go a long way. However, CAE tools that are customized to food processing and integrates several disciplines (engineering, food science), need to be appropriately developed (Datta, 2008; Sablani, 2008; Marks, 2008; van Boekel, 2008; Banga, 2008; Jousse, 2008). CAE tools can improve safety and quality, reduce costs and decrease "time to market." The same tools that have made automobile, airplane and chemical process designs impressively more efficient (Ivester, 2008) are potentially available to the food sector. However, the quality and safety aspects of food processes, and the characteristics of food materials have many unique features compared to any other manufacturing. To make computer-aided product and process engineering more of a reality for food, so that the food sector can reap the benefits of this technology, an integrated, robust and user-friendly CAE tool has to be developed. This has been an underlying desire in the food community, as expressed in many specialized international conferences and workshops (IFT, 2006; Model-It, 2005; Eurotherm Seminar 77, 2005; FOODSIM, 2004; IFT Annual Meeting Symposia, 2003; AFoT, 2003; ISFTFPFFS ,2003).

In order for food sector to increase the CAE use, available generic simulation software needs to be customized for food applications, e.g., by delivering solutions to sets of equations of relevance to food processing. Need for food sector is not unique in this sense—such customization is required for other industries and has very significant developmental time and cost. However, the

current user base for the food industry is small enough that the software companies are reluctant to invest the resources needed to develop specific capabilities of interest to food processing. The user base, of course, cannot increase until ready-to-use tools are available. This is a chicken-and-egg situation and the only solution is to start somewhere. The work presented here is such an attempt and it became possible with funding from the United States Department of Agriculture's National Integrated Food Safety Program for development of a software package to simulate food safety.

7.2.1 Physics based models in CAE software

Typically, CAE software is based on physics-based models (of processes) as opposed to observation-based models. Relative advantages of these two broad types of models have been discussed at length (Datta and Sablani, 2008; Datta, 2008; Sablani, 2008). The phenomenal growth in computing power and its associated userfriendliness have allowed physics-based models to be highly realistic by including more and more of the detailed physics and have fueled rapid growth in the use of models in product, process, and equipment design and research in other sectors. Advantages of a physics-based model include (Datta, 2008): 1) reduction of number of experiments, thus reducing time and expenses; 2) providing great insight into the process that may not even be possible with experimentation; 3) process optimization; 4) predictive capability, such as ways of performing "what if" scenarios; and 5) providing improved process automation and control capabilities. On the downside, physics-based models are more restricted to the food process itself rather than food quality or food safety, since physics-based models require precise relationships between quality/safety and

the process parameters, which are generally unavailable. Observation-based models can relate quality/safety to processing parameters more easily as they do not require detailed knowledge of the underlying physical process. However, observation-based models are primarily ”blackbox” models that would not provide the insight and they are difficult to be generalized into a framework for use in multiple processes. As mechanistic models for quality and safety are continually improved (e.g., van Boekel, 2008) these improvements can be easily integrated with physics-based process models to provide quality and safety parameters that are readily usable by the food designer.

Modeling food quality and safety requires addressing issues such as (Datta, 2008): 1) Complex multiphase heat and mass transfer such as evaporation and multiphase flow as in aseptic processing; 2) Multiphysics such as combined microwave or microwave-infrared heating; 3) Significant changes in material property during processing; 4) Significant dimensional changes and associated physics; 5) Considerable variation (batch to batch or within the same material) in material properties due to its biological origin; 6) Large number of new processes continually being introduced; 7) Lack of kinetic data for final variables of interest (quality and safety) as they relate to temperature and moisture. Additional characteristics of the food industry are that the scientists who are often in charge of these issues in an industrial setting have their training in chemistry and microbiology as opposed to physics-based mathematical modeling. By training, the technical persons in the food industry are more likely to be used to observation-based models. These characteristics of food processing point to the requirements of a food CAE software in two broad directions—the useful software would need to consider the complexities in food and processes that are unique; and the software should integrate many of the details and at the same

time hide it under an user interface that is as simple as possible. For computer-aided food process engineering (CAE applied to food processes), it would be ideal to have a scenario where a technical person, with minimal knowledge of the physics of the process and computational aspects, can use a few clicks of a mouse to define a practical food process. For example, such a user could click and choose between various container types, food material, and heating systems and ask the computer to provide the heating temperature needed for optimum quality in a sterilization process. The computer would need to formulate the physical problem (sterilization) into a mathematical one (equations), decide the best solution method, and finally do an optimization. For food processing applications, this has not yet been a reality.

Most of the modeling or CAE effort is at the research stage (e.g., Mittal, 199; Scott and Richardson, 1997; Datta, 1998; Tijskens et al., 2001; Irudayaraj, 2001; Welti-Chanes et al., 2003; Sun, 2007) and does not migrate to production or mass use in design by practicing scientists and engineers in industry, Extension or education. Available software (mostly the computational fluid dynamics (CFD) software that solves fluid flow, heat transfer and mass transfer problems) cannot be readily used for food for several reasons (Datta, 2008). First, the detailed first-principle-based and experimentally validated formulations of more complex processes such as frying are generally unavailable. Second, when the problem formulations can be made, there are unique aspects of food processes (such as strong evaporation in the food matrix) that can be hard to implement in a typical commercial software. Third, when the formulation is available and the software can solve it, we often run into difficulties obtaining the appropriate material properties for specific condition of the food. Until these items are resolved and hidden from the user through user friendly interface, simulation

will continue to be research rather than design project.

7.2.2 Current status of CAE in food processing

The current state of introduction of CAE into food industry can be stated as follows: Larger food companies that can invest more resources are doing this (Joussee, 2007) but, for other than the largest multinationals, modeling is often not seen as an efficient alternative. Smaller companies that do not maintain the CAE or simulation infrastructure, can and some do utilize consultants to contract out their simulation work. Such consultants can be those specialized for food industry (e.g., www.airflowsciences.com) or the generic CAE software companies themselves. Customized software, of the type described in this manuscript can go a long way toward a more widespread use of CAE in the food sector. Some efforts are underway to develop customized software (Torres, 2003; CFDfood, 2004; Otles and Onal, 2004; Banga, 2006; Verdurmen, 2006; PRO FOOD, 2009). To the best of the authors' knowledge, these software are still quite limited in terms of the physics they include. For example, they may include only diffusional heat and mass transfer. There are microbiological modeling software (e.g., ComBASE-PMP, 2003) but they typically do not include the process model. In a related area, kinetic modeling of food quality has been extensively studied (van Boekel, 2008) but not integrated in simulation software with process models.

Thus, a comprehensive software package that integrates realistic processes, products and microbiological aspects had not been available. However, such a software package has now been developed and this manuscript presents the

underlying scientific principles for a fundamental-based, easy-to-use, universal software predictive tool that is useful in a broad range of situations in the food sector (production, processing, distribution, preparation). The developed software can 1) simulate a large variety of food processes, and 2) integrates the process models with the microbiological and chemical safety models in order to predict safety information for a wide variety of food processes. The manuscript is organized as follows: first the outline of the software is provided which is followed by discussion on the development steps of the software - 1) problem formulation for food processes; 2) integration of food type, composition and property estimation; 3) integration of microbiology and chemical safety simulation; 4) model validation; and finally 5) a short overview of software implementation and the user interface.

7.3 Outline of the software package

A custom-developed Graphical User Interface (GUI) takes various product and process related inputs from the user (Figure 7.1). The user first selects the food process, the geometry and the dimensions of the food product to be modeled. User then selects the food type is selected either from the built-in database (that is based on the USDA National Nutrient Database (USDA-ARS, 2006) and contains the composition of the food) or directly inputs the food composition. The thermal properties (density, thermal conductivity, specific heat) are then estimated from the composition. Here also, the user has a choice of specifying properties that would bypass the computer-based estimation process. Other properties required to run the process models are also entered at this step. User then specifies the microbiological or chemical safety data or both, following by

the processing conditions. The final step in the process is to specify the solver settings. All these user inputs are then automatically fed into a commercial Finite Element solver, COMSOL Multiphysics 3.5a - which simulates the appropriate process and safety. The results of the simulation can then be processed in various ways by using the user-friendly post-processing interface of COMSOL Multiphysics.

7.4 Food processes

The food processes included in the software are grouped into two categories (Figure 7.2) based on the physics, the computation level and the knowledge required to solve the process.

7.4.1 Simple process models

The first category comprises of simple processes, which solve for only heat transfer (and, optionally, diffusion moisture transfer). It is assumed that the food is solid, and there can only be diffusion mass transfer of moisture inside or at the surface of the food. The only variables of interest are temperature and moisture content, and all the safety or quality analysis for these processes are associated with these variables only. The models in the simple process category cannot be used in case where intensive heating of the food takes place and there is significant vapor generation and pressure driven flow inside the food matrix. Currently, three industrially important thermal food process modules have been included in the simple process category - refrigeration/ storage/ trans-

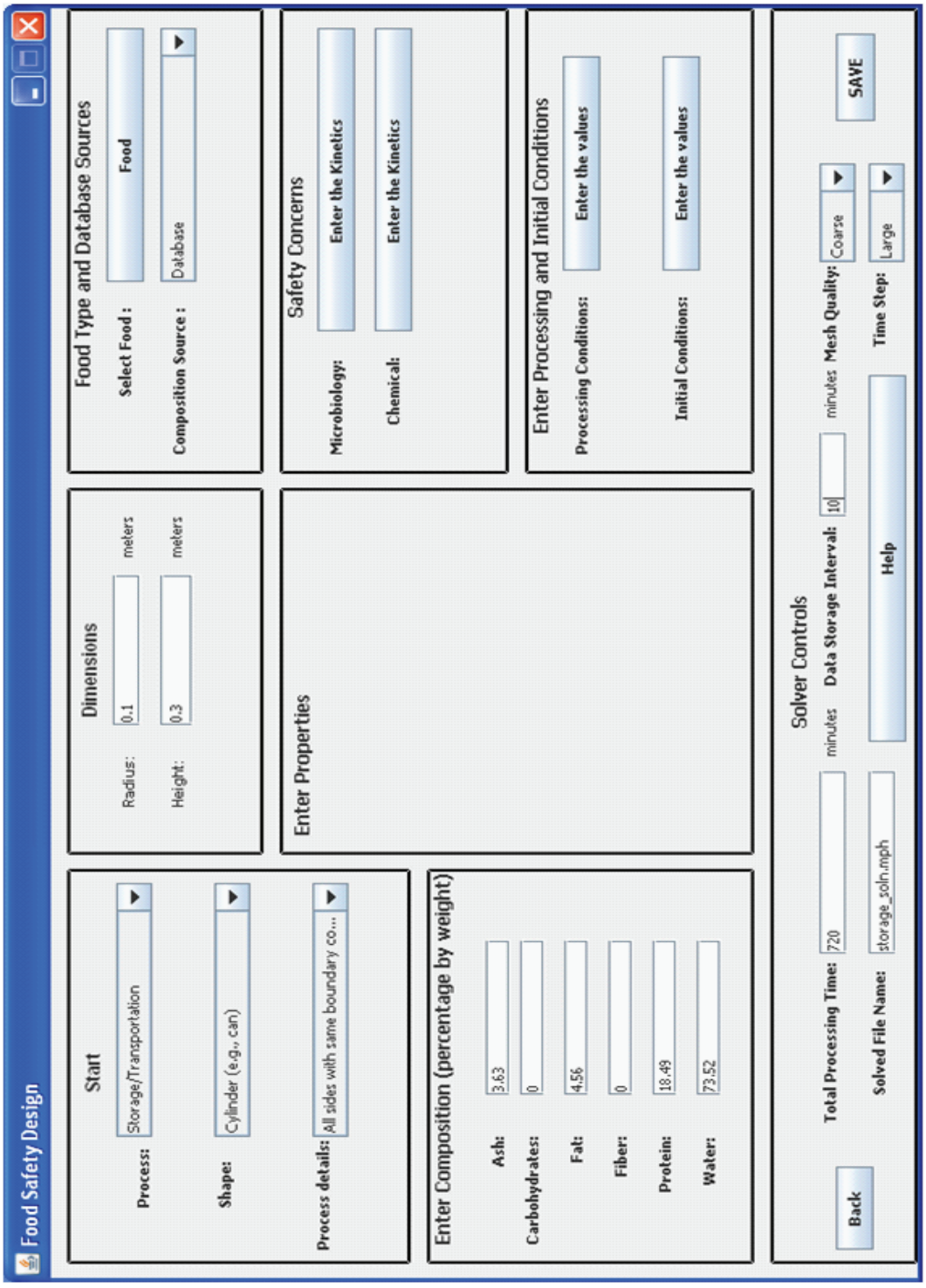

Figure 7.1: The screenshot of the software GUI.

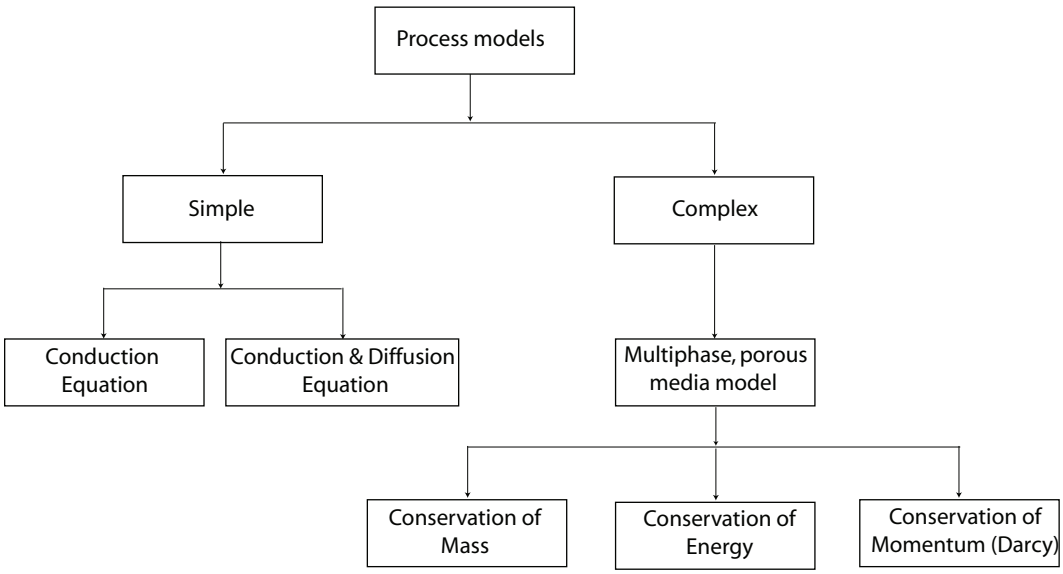

Figure 7.2: Categorization of the processes depending on their level of complexities involved.

portation/ general heating or cooling, sterilization of solid foods, and drying of solid foods. In the future versions, software would be extended to important non-thermal processes also.

Refrigeration/ storage/ transportation/ general heating or cooling

The module for these processes models conduction heating or cooling, without any evaporation/condensation (latent heat) and without any moisture loss. The governing equation is as follows:

$$\rho C_p \frac{\partial T}{\partial t} = \nabla.(k \nabla T) \tag{7.1}$$

where ρ is the density, C_p is the specific heat capacity and k is the thermal conductivity of the solid medium. The process module, as implemented in the

software, can be applied to check the possible microbial load when there is a temperature abuse. For example, it can be used to monitor the effect of temperature abuse (resulting in bacterial growth) for a chilled product by providing any expected temperature change as a function of time. It can also estimate maximum allowed time for a chilling process (see section 7.9.1) during which bacterial growth inside the food is within the safety limit.

Drying

This module can be applied for slow heating or cooling of food materials, where significant moisture loss occurs. The drying module solves for heat conduction (Eq. 7.2) along with moisture loss by solving for diffusion inside the food and evaporation at the surface. The moisture diffusion equation is:

$$\frac{\partial M}{\partial t} = \nabla.(D\nabla M) \tag{7.2}$$

where D is the moisture diffusivity through the medium and can be a function of moisture content of the medium. The safety applications of the module are similar to that for heating or cooling situations, the only difference being moisture transport is also important in this case.

Sterilization of solid foods

The sterilization module models heating of solid foods to high enough temperature using steam or hot water to inactivate microorganism contained in the food such that it is safe to eat. The module for these processes models conduction heating (Eq. 7.1), without any evaporation and moisture loss.The information

from such a mathematical model can help a process designer in deciding the sterilization time that retains the maximum quality and safety, or planning for corrections in the processing time for unintended increase or decrease in the processing temperature.

7.4.2 Multiphase porous media models

In the difficult process category, food is considered as a porous medium and a multiphase, porous media problem is solved. Mass conservation equations are solved for the relevant phases inside the food (e.g., in case of deep-fat frying of potato, in Halder et al. (2007), the pores inside the potato may be filled with water or gas or oil anytime during frying). So, the phases identified are solid potato, liquid water, oil and gas (mixture of vapor and air). The solid phase conservation is not solved as the solid mass remains unchanged. The mass conservation equation for any component, i can be written as

$$\frac{\partial}{\partial t}(\phi \rho_i S_i) + \nabla . n_i = \dot{R} \tag{7.3}$$

where ϕ is the porosity of the porous medium, S is the volume saturation, n is the mass flux, $\dot{R}$ is the appropriate source term due to evaporation.

Local thermal equilibrium is assumed, which means that at a given location in the food, all the phases have a same temperature. Therefore, only one energy conservation equation is solved for the system given as:

$$\rho_{eff} c_{p,eff} \frac{\partial T}{\partial t} + n_{fluid} . \nabla \left(c_{p,fluid} T \right) = \nabla . (k_{eff} \nabla T) - \lambda \dot{I} \tag{7.4}$$

where subscripts eff refers to mixture properties including the contribution by solid and $fluid$ refers to mixture properties due to fluids (transportable

phases). Currently, two industrially important thermal food process modules have been included in the difficult process category - microwave heating and deep-fat frying.

Microwave heating

The microwave heating module solves for change in temperature, liquid water, water vapor and pressure (from evaporation) inside the food during the microwave heating process. A multiphase porous media model, as implemented by Ni et al. (1999), has been used to simulate the process. In this problem, food geometry has been restricted to 1-dimension only. The model can be applied to observe the effect of microwave power level, penetration depth, product composition, surrounding temperature on the temperature and moisture accumulation near the surface. Since, the temperature can stay colder at the surface than slightly inside, safety issues such as trichinosis from undercooked pork, can also be checked.

Deep-fat frying

The deep fat frying model solves for change in temperature, liquid water, water vapor and pressure (from evaporation) inside the food over the deep-fat frying duration. A multiphase porous media model, as implemented by Halder et al. (2007) has been used to simulate the process, in which food geometry has been restricted to 1-dimension only. In addition to observing the temperature, moisture, pressure and oil profiles, the model can be used to obtain the effect of oil temperature, product properties, product thickness etc. on the frying time

and oil pickup. Amount of acrylamide formation can also be calculated for potato frying.

7.5 Composition and property estimation

7.5.1 Composition

After selecting the process, geometry of the food and its dimensions, the user is asked to select the food. The software gives the user a choice of either specifying a user defined food or selecting a food from an inbuilt database. The inbuilt foods' database of the software is based on the USDA National Nutrient Database for Standard Reference, Release 19, which contains data for 7293 food items for up to 140 nutrients and other components. These 7293 food items are divided into 24 food groups based on the food product type. Out of the 140 nutrients, only 6 major food proximates dictate the thermal properties of a food product (discussed below). These proximates are: ash, carbohydrates, fat, fiber, proteins and water. On selection of a food from the inbuilt food database, the composition values are obtained from the USDA National Nutrient database, and are used to calculate the property values based on the work of Choi and Okos (1987), as described in the following section. The user can also choose to define a food outside of the database. In such a case, the user should either know the composition (in terms of the above-mentioned proximates) of the food so that the properties can be estimated or should enter the properties directly.

7.5.2 Property estimation

The complex and highly heterogeneous nature of foods make their property estimation from fundamental principles a highly improbable task. For almost all types of foods, the physical properties are experimentally determined. Over the last several decades, efforts have been made to compile the huge property data of all the foods into an organized structure (Saravacos and Maroulis, 2001; Rao et al., 1995; Rahman, 2005, Nesvadba et al., 2003). However, using this huge compilation of data in software is a humongous task and cannot be extended to any new food products. Another way to approach this issue is assuming that the properties of a food are a weighted average of the properties of its constituent proximates (Miles et al., 1983; Choi and Okos, 1987). The weighing strategy is dependent on the nature of the property itself. This software follows the work done by Choi and Okos (1987) on predicting food properties from its composition. They compared the predicted values from the averaging technique with experimental measurements and found that the error was within 10% for all the food that were tested.

Density

The bulk density of the food material is estimated by assuming that the volumes of the different proximates simply add up. So, the density for a food material which does not have any air pockets will be:

$$\rho = \frac{1}{\sum \frac{X_i^w}{\rho_i}} \tag{7.5}$$

where X_i^w is the weight fraction and ρ_i is the density of the i^{th} component. If air is present with volume fraction, ϵ, then the density of the food material is

modified to include the effect of air volume:

$$\rho = \frac{1-\epsilon}{\sum \frac{X_i^w}{\rho_i}} \tag{7.6}$$

Specific heat capacity

The net specific heat of the food material is simply the mass average of specific heat of individual components:

$$C_p = \sum C_{p,i} X_i^w \tag{7.7}$$

The is based on the principle that the total heat required to raise the temperature of the food material by a given amount is equal to the sum of heats required to raise the temperatures of its individual components by the same amount. Here, it is assumed that there are no phase changes involved.

Thermal conductivity

The net thermal conductivity, k, of the food material is the volume average of individual conductivities, k_i, given as:

$$k = \sum k_i X_i^w \tag{7.8}$$

where k_i is the thermal conductivity of the i^{th} component. This is based on the fact that the thermal conductivity is a property of the volume rather than the mass. More complex models for thermal conductivity exist in literature (Sarvacos and Maroulis 2001), but help accuracy only incrementally. Therefore, we selected the simplest formulation which gives reasonable approximation of thermal conductivity.

Process specific properties

In addition to thermal properties of food, which are required for all food processes selected, deep fat frying requires porosity of the food material and thermal properties of cooking oil used. Similarly, the microwave heating process requires the user to specify porosity of the food material, microwave power supplied to the food and the penetration depth of the microwaves in the food material. The power absorbed by a food during microwave heating depends on a number of factors, which can be divided into two categories: food factors and oven factors (Zhang and Datta 2003). The main food factors are volume, surface area and dielectric properties of food. The main oven factors are oven size, geometry, location of food inside the oven cavity, presence of special features like turntable and mode stirrer, location of microwave feed etc. The dependence of power absorption on so many factors makes experimental determination of the power absorbed necessary. Ni et al. (1999) used 30000 W/m^2 as the power absorbed by the surface of a cylindrical food of radius 0.5 cm and height 2 cm in a domestic microwave oven (SHARP Carousal, Rated Power 1.5 kW). By default, this value is used in the microwave heating problem in the software. The user can scale this value to any value by using the Microwave power scaling factor. The other input, penetration depth, is a measure of how deep microwaves can penetrate into a food material. It is defined as the depth at which the intensity of the microwaves inside the material falls to 1/e (about 37%) of the original value at the surface. For a given food material, it is a function of moisture content and temperature. The microwave heating model requires this value as an input. By default, the penetration depth of a potato is used.

7.6 Microbiological safety prediction

Quantitative microbiological modeling in the literature is generally not coupled to spatial variation (e.g., temperature, moisture and pH) in a food material during a process. Models typically assume one temperature for the food material or implicitly refer to one location (e.g., cold spot) in the food material. In a typical food process, time-temperature history would vary spatially depending on process and food thermal parameters. Lack of availability of such growth and inactivation profiles within a food is obviously a major limitation of microbiology-only models (Marks, 2003). To overcome this, process model (that provides spatial temperature-time histories) has been integrated with predictive microbiological models to provide a comprehensive prediction concerning food safety for many production-to-consumption situations. But integrating the process models with microbiological growth/ inactivation models is not all. The availability of a comprehensive database containing microbiological growth/ death kinetic parameters is also important. In this present work, a comprehensive database of microbial inactivation and growth kinetic parameters for different food types has been developed through extensive regression analysis of decades of experimental data from literature to facilitate predictive modeling and make the software user-friendly. The user with a basic knowledge of food processing and no specialized background in predictive microbiological modeling can use the software. All the user needs to do is select the target microorganism (with built-in guidance) from the GUI and the software takes care of the rest (it provides, for example, the kinetic parameters as a function of temperature for the selected microorganism and food group from the inbuilt microbiological kinetic database).

7.6.1 Food groups/ types from USDA National Nutrient Database

The availability of a comprehensive database containing microbiological growth/ death kinetic parameters is far from reality. There are several issues in trying to compile comprehensive microbiological kinetic information 1) limited availability of data for many specific situations; 2) correlation issues between laboratory conditions and real foods; 3) variability of data on microbial inactivation reported by various researchers; 4) variability among microbial populations; and 5) evolving knowledge of appropriate predictive models that describe the data. In this present work, to overcome many of the issues just mentioned in building a comprehensive database, a holistic approach was taken by first using a database of food products (USDA National Nutrient database) and associating pathogens with those foods. The foods having similar composition, intrinsic characteristics and shown similar association with pathogens (based on outbreak history) have been grouped together. All the foods within the food group will have same growth/ inactivation kinetic parameter values. In all, 7294 food products from USDA National Nutrient database were grouped into 17 food groups. Table 7.1 gives the USDA National Nutrient Database food groups and Table 7.2 gives the rearranged food product database for the purpose of predictive microbiological modeling. After forming the food groups, decades of experimental data on growth and inactivation from published literature (over 1000 datasets) were extensively analyzed using regression technique to obtain kinetic parameters for developed food groups using the chosen models (how the model was chosen is discussed in the next section).

Table 7.1: USDA National Nutrient Database Food Groups

Category	General Types of Foods	Number of items
1	Dairy and Egg Products	183
2	Spices and Herbs	60
3	Baby Foods	261
4	Fats and oils	205
5	Poultry Products	337
6	Soups, Sauces and Gravies	399
7	Sausage and Luncheon Meats	213
8	Breakfast Cereals	409
9	Fruits and Fruit Juices	312
10	Pork Products	289
11	Vegetables and Vegetable	776
12	Nut and Seed Products	128
13	Beef Products	576
14	Beverages	251
15	Finfish and Shellfish Products	249
16	Legumes and Legume Products	211
17	Lamb, Veal and Game Products	343
18	Baked Products	487
19	Sweets	421
20	Cereal Grains and Pasta	168
21	Fast Foods	309
22	Meals, Entrees, and Side dishes	102
23	Beef (2)	213
25	Snacks	15
35	Ethnic Foods	132
42	Miscellaneous	84
43,44,47,48,80,83, 90,93	Miscellaneous (2)	161
Total		7294

Table 7.2: Rearranged Food Product Database

Original Categories	New Food Group Categories	Number of items
1,4,19,35,42,43,44	Dairy Products	224
3,42,43	Baby Food	288
4,35,42,44	Fats and oils	240
1,5,7,35,42,43	Poultry and eggs	440
6,35	Soups and Sauces	401
8,20,42,43	Cereal products	594
9,19,35,43	Fruits	327
7,10,13,17,19,23,35,42,43	Red meat products	1629
11,16,35,42,43,48	Vegetables	1012
12,16,42	Nuts and seeds	155
14,35,42,43,44,47	Beverages	276
15,35,43,80,83,90,93	Fish and seafood	294
18,35,43	Baked products	492
19,25,42,43,44	Snacks	447
21	Fast foods	309
22	Entrees	102
2,43,44	Spices and Herbs	63
Total		7294

7.6.2 Mathematical models

For microbial inactivation, it is not practical to provide the kinetic parameters for all of the possible models in the database. After careful analysis, the first order model was selected for the following reasons: 1) the first-order model for inactivation has been used extensively and kinetic parameter values (e.g. D-values) are available for this model for a significant number of microorganisms in specific food products; 2) there are models (Baranyi model, Hills model, etc.) which can predict both tail and shoulder effects during inactivation, but applying data from the literature to such models would be an arduous task and is not feasible given the limited presentation of the baseline data used in many studies; 3) the compilation of numerous inactivation parameters, such as D-values, over like experiments for specific microorganisms acts to normalize the impact of non-log linear effects seen in individual experiments. The important trend becomes the rate of response relative to specific food types for individual organisms under defined process conditions.

First-order inactivation model

An inactivation curve following first-order kinetics (Ball, 1929) is written as:

$$log_{10}\left(\frac{N}{N_0}\right) = -\frac{1}{D_T}\int 10^{\frac{T(t)-T_{ref}}{z}}dt \tag{7.9}$$

where D_T is the time taken to reduce the concentration of microorganism by a factor of 10 at temperature T, and z is the temperature change required to reduce the D-value by a factor of 10. The database for first-order inactivation model contains the mean D_T and z values for different microorganisms in different food types. In addition to the mean kinetic values, the database also

contains the upper 95% confidence interval values of D_T and infectious dose.

First-order growth model

The sequential stages of a bacterial growth are the lag phase, exponential phase, stationary phase and death phase. The lag phase is the stage when the microorganism adapts to a new environment and the lag time (L) is the time taken by the microorganism to adapt to that environment prior to exponential growth. Exponential phase is followed by stationary phase when the conditions are no longer favorable for rapid growth (e.g., due to lack of nutrients or change in pH). As conditions become unfavorable and/or lethal for bacteria, the death phase begins. A growth model describes the first three stages of growth, lag phase, exponential phase and stationary phase. The predictive model for lag phase and exponential phase using a first-order growth model is given for two different situations, isothermal and non-isothermal. A first order model cannot predict stationary phase. Lag times (L_T) are available for different temperatures from published literature. So, in a first-order model, for isothermal situations, the growth rate is zero until lag time is over and k_T, the growth rate at temperature T, is used after the lag time has elapsed. The model is given as:

$$\frac{dN}{dt} = \begin{cases} 0 & t < L_T \\ k_T N & t > L_T \end{cases} \tag{7.10}$$

Methodology to predict microbial growth under fluctuating temperature conditions has been developed by Li et al. (1988). The total adaption under fluctuat-

ing temperature conditions is given by:

$$\frac{dA}{dt} = \frac{1}{L_T} \tag{7.11}$$

where A is the total adaptation during the lag phase. An adaptation rate can be defined as the reciprocal of lag time. When A equals 1, adaptation is complete and growth starts. Therefore, the growth is given by:

$$\frac{dN}{dt} = \begin{cases} 0 & A < 1 \\ k_T N & A > 1 \end{cases} \tag{7.12}$$

Equations 7.10, 7.11 and 7.12 resemble equation Eq. 7.2 (a diffusion equation) with zero diffusivity and a non-zero source term. Therefore, the above mentioned equations are implemented as diffusion equations in COMSOL Multiphysics, where diffusivity is zero and the terms on the right hand side of Eqs. 7.10, 7.11 and 7.12 are added as source terms to the respective equations. The model parameters, such as k_T and L_T, are functions of temperature, and are specified as such in the software.

7.7 Software platform

The software package graphical user interface is built using Java script with the process, microbiological and chemical kinetic models (Equations in Sections 3, 4 and 5) solved in the background using COMSOL Multiphysics (Burlington, MA), a finite element based commercial modeling package. Some of the reasons for choosing the software COMSOL Multiphysics as the computational engine

were: 1) ease at which we could implement food processes with rapid evaporation and resulting Darcy flow, for example, of water and vapor. Implementing such processes in some other software required solution of Navier-Stokes equivalent of fluid momentum equation for porous media that is computationally far more intensive; 2) Flexibility with which the transport equations and their boundary conditions can be programmed; and 3) A more user-friendly interface of the software itself.

7.8 Implementation details

7.8.1 Geometry

For simpler processes, a 2-dimensional heat transfer model has been implemented and the geometry has been restricted to cylindrical or rectangle shapes. Simulation of frying and microwave heating in 2 or 3-dimensions is much more involved than a 1-dimensional problem. Such simulations are very sensitive to parameters for solution convergence and require a lot of computational time. Due to these reasons, complex processes, like frying and microwave problems, are restricted to solving 1-dimensional heat and mass transfer. For these two processes, we have used the 2-dimensional shape (rectangle) for better visualization, and have insulated one direction so that all the changes happen in the other direction only.

7.8.2 Meshing

Since a finite element method is used to solve the governing equations, the relevant geometry is discretized into elements and the equations are solved at the vertices of the elements (called nodes). The discretized geometry is called a mesh and the meshing of the geometry is done automatically with the help of COMSOL Multiphysics. For all the processes and geometries, structured meshing with quadrilateral elements is used. The user gets the option of having a coarse, medium or fine mesh. Finer the mesh, more accurate is the solution but at the expense of increased computation time.

7.8.3 Solver

The direct UMFPACK solver of COMSOL Multiphysics has been used for all processes. The time stepping has been decided for each process after careful analysis. Similar to meshing, the user gets a choice of large, medium or small time step, with the recommendation that small time step should be used for processes that involve rapid changes of variables such as temperature and pressure, for example in deep-fat frying and microwave heating processes. In slower processes, such as storage, small time step is recommended when the processing conditions such as ambient temperature is changing rapidly.

7.8.4 Postprocessing

COMSOL Multiphysics has a well developed post-processing module, which is very intuitive, and does not require modeling expertise for its use. Therefore,

the built-in COMSOL Multiphysics post-processing module was used for the software package. Although, this may be seen as a disadvantage of the software being reported here, the user-friendliness and functionalities offered by COMSOL combined with tutorial-type directions developed by us for food-specific quantities are deemed very adequate for a non-specialized user. Some of the examples of postprocessing capabilities of the software are (Datta and Rakesh, 2010):

Information at a location (Temporal history) At a given location, value of a parameter of interest (temperature, moisture content, microbial concentration etc.) or its variation with time are basic forms of information that may be necessary.

Spatial Variation A simple form of spatial variation is the information of maximum and minimum value. A more comprehensive way of getting spatial information is to plot contours of the parameter of interest.

Spatial Integration and Averaging Integration or averaging over a region can give useful information such as average temperature or moisture content of the food or total microbial load in the food.

Secondary Quantities Secondary quantities such as heat or mass fluxes at a surface location and variation of such quantities with time can give the information about rates of heat or moisture loss (or gain) from (or by) the food.

Apart from the quantities mentioned above, any kind of customized parame-

ter which is a function of parameters being solved for can be defined and plotted in various ways in COMSOL Multiphysics.

7.9 Software validation

Validation is essential for any modeling effort. In the context of predictive microbiological modeling, a model is evaluated on the basis of how well the model predictions match with the observed phenomena. Often, the model is applied only to make predictions in the experimentally studied range of conditions only. However, if the predictive capabilities are applied only to the experimentally verified conditions, the use of modeling will be seriously limited. The power of modeling technology can really be leveraged by making predictions for wide variety of condition, of course, after we have gained confidence in the model by applying it to available experimental observations. In this section, we validate the approach by applying the model to two different food processes:

7.9.1 Growth of *Clostridium perfringens* during air chilling of ready-to-eat ham

Clostridium perfringens bacterium is of particular concern in cooked meat products. *C. perfringens* is a spore former and is one of the most rapidly growing bacteria, with doubling time as short as 7.1 minutes at around 44°C. In this case study, the chilling process of boneless cooked cured ham is modeled along with the growth of *C. perfringens*, to check if the concentration of *C. perfringen*s would be kept sufficiently low during the process. The ham is in the shape of a cylin-

der (radius 10 cm and height 30 cm) and being cooled by air at 7°C. Blowing of the air over the ham leads to a surface heat transfer coefficient of 50 Wm^{-2}. The flow chart (Figure 7.4) shows the sequence of the solution process using the software. The specific food, boneless cooked cured ham, is selected by the user from the USDA composition database from within the software. From the composition, thermal properties needed for the simulation is estimated by the software following discussion in Section 4. Heat conduction equation (Eq. 7.1) is solved to describe the temperatures inside the ham at any point and at any time. Non-isothermal first order growth model (Eq. 7.11 and 7.12) is solved using the temperature history at any location inside the ham to obtain the growth of *C. perfringens* with the lag phase equation (Almonacid-Merino and Torres, 1993). The kinetic data for the growth of *C. perfringens* is obtained by the software from the microbiological database contained in it (Table 7.3). In the database, growth kinetics data for ham belongs to a red meat group (pH 5.5; beef, pork and ham), and is the most conservative estimate within this group. Figure 7.4 shows the comparison of predicted and observed *C. perfringens* growth during cooling of the ham, following the cooling process is in compliance with FSIS stabilization performance standards for cured products. The prediction made by taking the database value for red meat group (pH 5.5; beef, pork and ham) is always on the conservative side (can be seen in Figure 7.4), which is acceptable for evaluation of safety of the process. Difference between experimental and predicted values can be attributed partly to the selection of the kinetic data as the most conservative value in the food group. This serves as the validation of predictions related to microbiological safety.

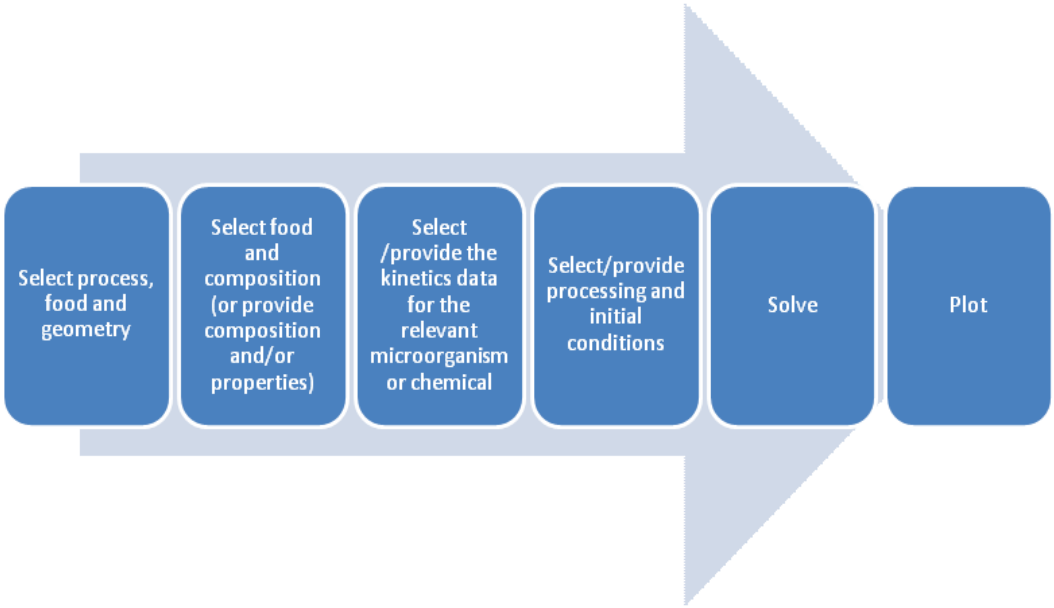

Figure 7.3: Flowchart of the approach.

Table 7.3: First-order growth kinetic data for *Clostridium perfringens* in various food groups, as stored in the inbuilt microbial kinetic database of the software

Food groups	Temp. range (°C)	Rate (CFU/hr)	r^2/N	Lag (hr)	r^2/N
Poultry, eggs and red meat	15-18	0.067		39	
	18-24	0.0305T-0.504	0.991/7	158.54-6.49T	
	24-35	0.0305T-0.504	0.991/7	12.44-0.341T	0.900/3
	35-40	0.0305T-0.504	0.991/7	0	0.712/4
	40-50	0.75		0	
Soups, sauces, spices, herbs	15-18	0.073		55	
	18-24	0.0376T-0.641	0.988/8	223.86-9.21T	
	24-35	0.0376T-0.641	0.988/8	15.81-0.442T	0.892/3
	35-45	0.0376T-0.641	0.988/8	0	0.725/4
	45-50	0.94		0	

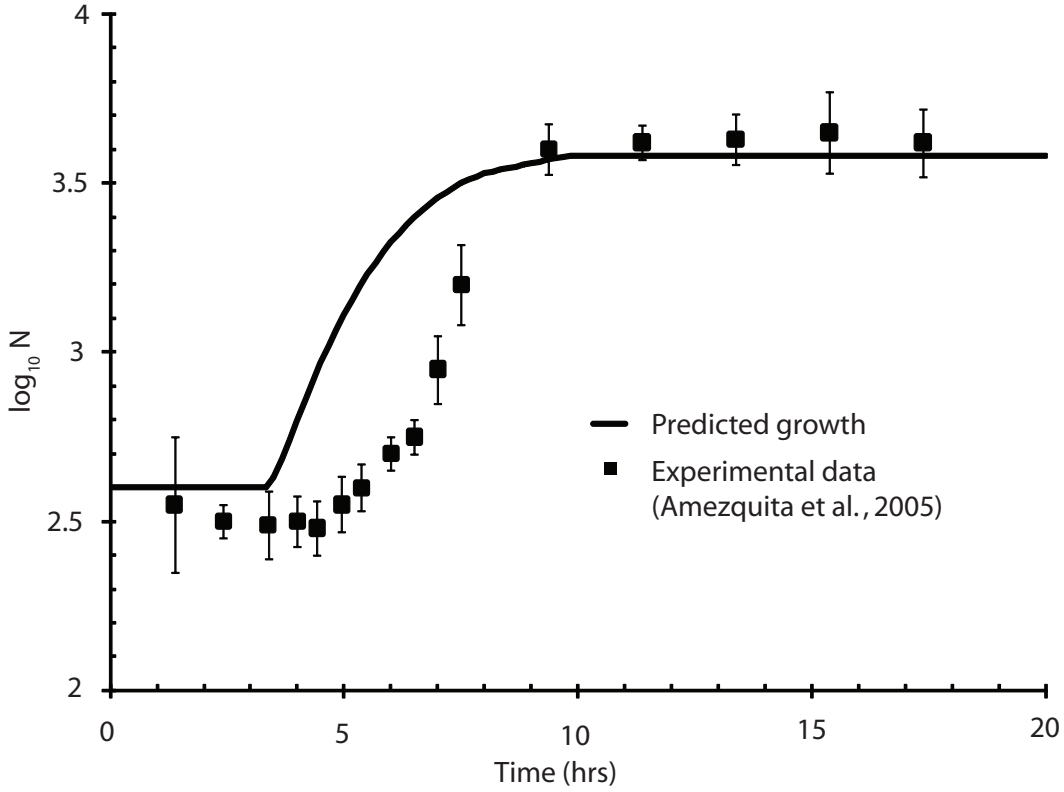

Figure 7.4: Predicted and observed *C. perfringens* growth during cooling of boneless cooked and cured ham.

7.9.2 Safety prediction during deep-fat frying of a potato slice

Deep fat frying is one of the most important industrial processes, with crust thickness and oil pickup being two quality parameters of importance associated with frying. In this case study, the goal is to estimate the total oil picked up and thickness of the crust developed during deep fat frying of potato slice. Formation of acrylamide, a probable carcinogen, is also modeled as the food safety parameter. The potato slice is 3 cm thick. It is being heated equally from both sides by oil at 180°C. The surface heat transfer coefficient for frying is taken as 300 $Wm^{-2}K^{-1}$. The flow chart (Figure 7.3) shows the sequence of the solution process using the software. The user selects the type of potato from the database.

The thermal properties of the slice are estimated by the software following discussion in Section 4. The oil properties are input by the user. Processing conditions and initial conditions are then specified. Multiphase porous media model developed by Halder et al. (2007) is solved to describe the temperature, moisture and oil content inside the potato slice at any point and at any time. Figure 7.5 shows the comparison of predicted and temporal history of temperature at different locations and overall moisture content during potato frying. Also, the total concentration of acrylamide with time is plotted. Such close agreement between experimental measurements and model prediction confirms the effectiveness of the model and serves to validate it.

7.10 Limitations of the predictive software

Although the software is based on fundamental models and is intended to cover a large range of processes, there are limitations to its predictive capabilities. Some of the limitations are:

Process models Modeling of complex food processes such as those involving shrinkage (Mayer and Serano, 2004; Katekawa and Silva, 2006) is still in research stage. The models in the software do not include shrinkage, but the transport properties used in the models are obtained from experiments and they contain some of the effects of shrinkage in their values. Therefore, the error due to not including shrinkage is balanced to some extent by using these transport properties.

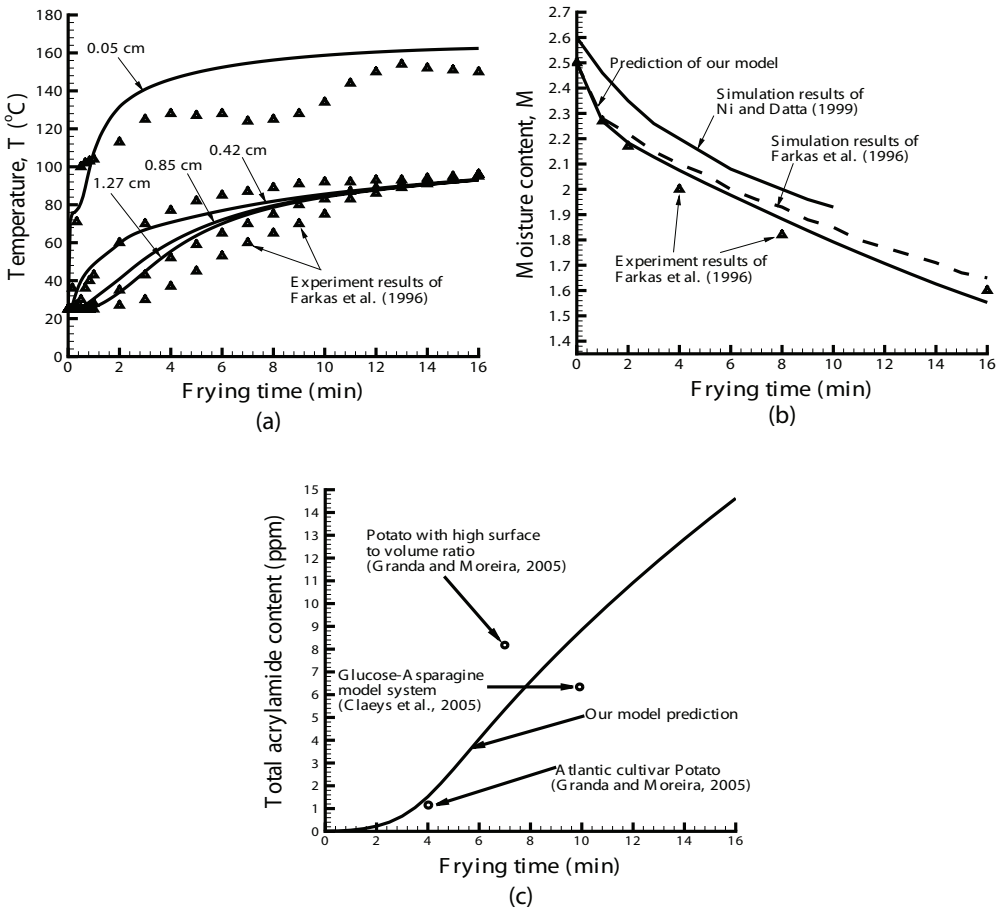

Figure 7.5: Comparison of model predictions with the experimental data from literature for a) Temperature; b) Moisture content (dry weight basis); c) Total acrylamide concentration.

Geometry of the food The simpler processes (such as refrigeration or sterilization) are limited to 2-dimensional geometries and the more complex multiphase porous media models are limited to 1-dimensional geometry. These limitations either arise from the need to make the software available to a user with little knowledge of simulation (restrictions on geometry) or to restrict the computational time.

Property estimations The Choi and Okos (1987) relations used to estimate the food properties are based on compositions, may have an error of around 10%. Also, there can be significant variation in compositions of different samples of the same food material. An estimation of implications of this variability (e.g. by Monte Carlo techniques applied by Halder et al., 2007) cannot be performed from within the GUI developed here, but can be performed using COMSOL Multiphysics interface directly.

Microbial models The microbiological kinetics database developed here has some drawbacks as has been discussed in detail in Halder et al. (2010). There can be instances when there is difference in composition within a food group, and therefore, likely differences in kinetic parameters. For example, some foods may not clearly belong to any one group. The decision to put them in a particular group was made on the basis of outbreak history and association literature and pH or other intrinsic or extrinsic factors. Further, the estimated growth/ inactivation kinetic parameters are the conservative estimates but there can be situations when kinetic parameters will vary significantly due to formation of micro-environments, which protects the microorganisms against extreme conditions. Effects of such variability can be included using the COMSOL Multiphysics interface directly, as already mentioned under property estimation.

7.11 Summary and Expected Benefits

A software has been developed that can simulate food safety by combining physics-based model of food processes with the kinetics of microbiological and

chemical changes in foods during processing to provide bacterial or chemical amounts at any time and any location in the food during processing. Physics-based models range from simple conduction or diffusion to multiphase porous media model that can keep track of multiple components such as moisture and oil, and multiple phases such as water and water vapor. The thermophysical properties needed for the models are predicted from composition, based on available correlations. Compositions themselves, available from published sources, are integrated into the software. Microbiological kinetic data corresponds to that for a food group, as opposed to individual foods, available from published sources. Similarly for data for kinetics of chemical changes. An intuitive graphical user interface has been built for those in the food sector in mind. This interface sits on top of a general purpose commercial computational software, thus delegating the detailed computation to the software. This enabled the development of this highly versatile software over a relatively short period of time. Because of the fundamentals-based framework on which the computations are built, it will be somewhat routine to extend to newer processes or combinations of processes.

The software is intended to be a comprehensive tool for speeding up food product, process and equipment design for improved safety and quality. With the help of the simple interface of the software, it is now easier and quicker to check 'what if' scenarios. A food scientist with little knowledge of simulation engineering can use the software with the help of documentation provided and thus have this potential tool available. Apart from direct use by the food industry, beneficiaries of such a comprehensive software tool can include food extension educators, university food science/engineering courses, and food science researchers. Such a tool can be incorporated in a food science/food engineering

curricula following details outlined in Datta and Rakesh (2010). Extension will benefit by having customized instruction capabilities of microbiological safety for arbitrary products, processes and handling situations. The tool, with the ability to present highly detailed visualizations, will make difficult concepts of process more easily comprehensible. In university classroom education, advantages of the proposed tool would be 1) to incorporate safety issues for more realistic food product/process/equipment situations; 2) to gain much greater insight into processes; and 3) to introduce a concept that is rapidly becoming part of design process. To tool also has the potential to increase productivity in food research in academia.

Acknowledgement

We acknowledge the USDA Cooperative State Research, Education, and Extension Service (CSREES) National Integrated Food Safety Initiative (2004-51110-02167) for funding this project.

BIBLIOGRAPHY

[1] AFoT, Second International Workshop on Mathematical and Computing Technologies for Agro-Food Technologies, Barcelona, Spain, Nov. 27-28, 2003.

[2] Almonacid-Merino, S.F., Simpson, R. and Torres, J.A., 1993, Time-variable retort temperature profiles for cylindrical cans: batch process time, energy consumption, and quality retention model, *Journal of Food Process Engineering*, 16: 271-287.

[3] Amezquita, A, Weller, CL, Wang, L, Thippareddi, H and Burson, DE, 2005, Development of an integrated model for heat transfer and dynamic growth of Clostridium perfringens during the cooling of cooked boneless ham, *International Journal of Food Microbiology*, 101: 123-144.

[4] Arvidsson P., van Boekel M.A.J.S., Skog K., Solyakov A. and Jagerstad M., 1997, Kinetics of formation of polar heterocyclic amines in a meat model system, *Journal of Food Science* 62: 911-916.

[5] Arvidsson P., van Boekel M.A.J.S., Skog K., Solyakov A. and Jagerstad M., 1997, Formation of heterocyclic amines in a meat juice model system, *Journal of Food Science* 62: 216-221.

[6] Ball, C.O., 1929, Food preservation by canning, *Food Industries*, 1:262-263.

[7] Burnham, G.M., Schaffner, D.W. and Ingham, S.C., April 2008, Predict Safety, *Food Quality*, 15(2): 14-22.

[8] CFDfood, 2004, The site of Engineering thermodynamics for the evolution of AgriFood Systems, On the web at http://www.unibas.it/cfdfood/top_eng.htm.

[9] Choi Y. and Okos, M.R., 1987, Effects of temperature and composition on thermal properties of foods. In: *M. Le Maguer and P. Jelen, Editors, Food Engineering and Process Applications*, Elsevier Applied Science, London, UK.

[10] ComBase-PMP, 2003, Combined Database and Predictive Microbiology Program, On the web at http://www.ifr.ac.uk/combase.

[11] Datta, A.K., 1998, Computer-aided engineering in food process and product design, *Food Technology*, 52(10):44-52.

[12] Datta, A.K., 2008, Status of physics-based models in the design of food products, processes and equipment, *Critical Reviews in Food Science and Food Safety*, 7(1):114-116.

[13] Datta, A.K. and Rakesh, V., 2010, An introduction to modeling of transport processes: Applications to biomedical systems, Cambridge University press, Cambridge, UK.

[14] Jousse, F., 2008, Modeling to improve the efficiency of product and process development, *Critical Reviews in Food Science and Food Safety*, 7(1):175-181.

[15] Datta, A. K., Editor. 2008. Models for Safety, Quality, and Competitiveness of the Food Processing Sector. Comprehensive Reviews in Food Science and Food Safety. IFT Press, Chicago, Illinois. On-line at http://www.blackwell-synergy.com/toc/crfs/7/1.

[16] Eurotherm Seminar 77, June 20-22, 2005, Heat and Mass Transfer in Food Processing, Parma, Italy, On the web at http://ied.eng.unipr.it/fisicatecnica/seminar77/inglese/menu.htm.

[17] FOODSIM, 2004, June 16-18, 2004, WICC-WIR, Wageningen, The Netherlands.

[18] Halder, A., Datta, A.K. and Geedipalli, S.S.R., 2007, Uncertainty in thermal process calculations due to variability in first-order and Weibull kinetic parameters. *Journal of Food Science*, 72: E155-E167.

[19] Halder, A., Dhall, A. and Datta, A.K., 2007, An improved, easily implementable, porous media based model for deep-fat frying. Part 1: Model development and input parameters, *Transactions of IChemE*, 85(C3), 1-11.

[20] Halder, A., Dhall, A. and Datta, A.K., 2010, Modeling Transport in Porous Media with Phase Change: Applications to Food Processing, *Submitted in Journal of Heat Transfer*, Manuscript ID: HT-09-1055.

[21] Halder, A., Black, D.G., Davidson, P.M. and Datta, A.K., 2010, Development of Associations and Kinetic Models for Microbiological Data to be Used in Comprehensive Food Safety Prediction Software, *Submitted in Concise Reviews and Hypotheses in Food Science*, Manuscript ID: JFS-2009-0867.R1.

[22] IFT Annual Meeting, Chicago, Illinois, July 13-16, 2003, Symposia on

'Computer-Aided Engineering to Enhance Food Product, Process and Equipment Design', Co-organized by Ashim K. Datta and Kumar M. Dhanasekharan of Fluent, Inc.

[23] ISFTFPFFS, International Symposium on Future Technologies for Food Production and Future Food Scientists, Gteborg, Sweden, June 2-4, 2003.

[24] Irudayaraj, J, 2001, Food processing operations modeling: Design and analysis, Marcel Dekker, New York.

[25] Ivester, R.W., 2008, Productivity improvement through modeling: An overview of manufacturing experience for the food industry, Critical Reviews in Food Science and Food Safety, 7(1):182-191.

[26] Jackson, L.S. and Hargraves, W.A., 1995, Effects of Time and Temperature on the Formation of Meiq(X) and Dimeiq(X) in a Model System Containing Threonine, Glucose, and Creatine. *Journal of Agricultural Food Chemistry*, 43(6):1678-1684.

[27] Jakszyn, P., Agudo, A., Ibanez, R., Garcia-Closas, R., Pera, G., Amiano, P. and Gonzalez, C.A., 2004, Development of a food database of nitrosamines, heterocyclic amines, and polycyclic aromatic hydrocarbons, *Journal of Nutrition*, 134: 2011-2014.

[28] Katekawa, M.E. and Silva, M.A.A., 2006, A review of drying models including shrinkage effects, *Drying Technology*, 24(1): 5-20.

[29] Li, K.Y., 1988, The microbial stability of refrigerated intermediate moisture foods. PhD thesis. Oregon State University, Corvallis, OR.

[30] Marks, B.P., 2003, Food safety beyond guidelines and regulations, *Thermal processing of ready-to-eat meat products*, Editors: Knipe, C.L. and Rust, R.E., Wiley-Blackwell, Ames, Iowa, USA.

[31] Mayor, L. and Sereno, A.M., 2004, Modelling shrinkage during convective drying of food materials: a review, *Journal of Food Engineering*, 61(3): 373-386.

[32] Model-It, The third international symposium on Applications of Modelling as an Innovative Technology in the Agri-Food Chain, May 29 - June 2, 2005, Leuven, Belgium.

[33] Miles, C.A., Van Beek, G. and Veerkamp, C.H., 1983, Calculation of Thermophysical Properties of Foods. In: Physical Properties of Foods. Applied Science Publishers, New York, 269-312.

[34] Mittal, G. S., 1997, Computerized Control Systems in the Food Industry, Marcel Dekker, Inc.

[35] Nesvadba, P., Houska, M., Wolf, W., Gekas, V., Jarvis, D., Sadd, P.A. and Johns, A.I., 2003, Database of physical properties of agro-food materials, *Journal of Food Engineering*.

[36] Ni, H., Datta, A.K. and Torrance, K.E., 1999, Moisture transport in intensive microwave heating of biomaterials: a multiphase porous media model, *International Journal of Heat and Mass Transfer*, 42(8): 1501-1512.

[37] Otles, S. and Onal, A., November 2004, Computer-aided engineering softwares in the food industry, *Journal of Food Engineering*, 65(2): 311-315.

[38] Persson, E., Oroszvari, B.K., Tornberg, E., Sjoholm, I. and Skog, K., 2008, Heterocyclic amine formation during frying of frozen beef burgers, *International Journal of Food Science and Technology*, 43: 62-68.

[39] PROFOOD, 2009, The site for advanced tools for simulation, optimization and control of food preservation processes. On the web at http://www.cimne.com/profood/default.asp.

[40] Rahman, S., 1995, Food properties handbook, CRC, Boca Raton, Florida.

[41] Rao, M.A., Rizvi, S.S.H., and Datta, A.K., 2005, Engineering Properties of Foods, 3rd edition, CRC Press, New York, pp. 175-201.

[42] Sablani, S.S., Datta, A.K., Rahman, M.S. and Mujumdar, A.S. editors, 2007, Handbook of Food and Bioprocess Modeling Techniques, CRC Press, Taylor and Francis Group, Boca Raton, Florida.

[43] Sablani, S.S., 2008, Status of observational models used in design and control of food products and processes. *Critical Reviews in Food Science and Food Safety*, 7(1):130-143.

[44] Saravacos, G.D. and Maroulis, Z.B., Transport Properties of Foods, Marcel Dekker: New York, 2001.

[45] Scott, G. and Richardson, P., 1997, The application of computational fluid dynamics in the food industry, *Trends in Food Science and Technology*, 8:119-124.

[46] Sun, D.W., 2007. Computational fluid dynamics in food processing, Edited. Taylor and Francis, Boca Raton, Florida.

[47] Tijskens, L.M.M., Hertog, M.L.A.T.M. and Nicolai, B.M., Editors, 2001, Food Process Modelling, CRC Press, Boca Raton, Florida.

[48] Torres JA, 2003, Personal communication, Oregon State University, Corvallis, Oregon.

[49] U.S.D.A - Agricultural Research Service. 2006. USDA National Nutrient Database for Standard Reference, Release 19. Nutrient Data Laboratory Home Page, On the web at http://www.ars.usda.gov/ba/bhnrc/ndl.

[50] Van Boekel, M.J.A.S., 2008, Kinetic modeling of food quality: A critical review, *Critical Reviews in Food Science and Food Safety*, 7(1):144-158.

[51] Verdurmen REM, Van Houwelingen G., Gunsing G., Verschueren M. and Straatsma J., 2006, Agglomeration in spray drying installations (The EDECAD Project): Stickiness measurements and simulation results, *Drying Technology*, 24: 721-726.

[52] Welti-Chanes, J. and Velez-Ruiz, J.F. and Barbosa-Canovas, G.V., Editors. Transport Phenomena in Food Processing, CRC Press, Boca Raton, Florida.

[53] Zhang, H. and Datta, A.K., 2003, Microwave power absorption in single and multi-component foods, *Transactions of the Institution of Chemical Engineers*, 81(C): 257-266.